



Position Self-Sensing of Permanent-Magnet Machines using High-Frequency Signal Injection

Thesis submitted in fulfillment of the requirements for the award of the degree of
Doctor in de ingenieurwetenschappen (Doctor in Engineering) by

Fabien Gabriel

January 10, 2013

Promoters: Prof. Philippe Lataire, VUB
Prof. Xavier Neyt, RMA
Advisers: President: Em. Prof. Jacques Tiberghien,
VUB
Vice-presidency: Prof. Rik Pintelon, VUB
Secretary: Prof. Johan Deconinck, VUB
Dr. Frederik De Belie, UGent
Em. Prof. Marc Acheroy, RMA
Prof. Ralph Kennel, TUM



Summary

Rotating electric machines play an increasing role in our daily lives and in all power levels such as power generation, boats, submarines and vehicles propulsion, industrial machinery, medical robotics, space module actuators, door actuators, etc., for civil applications as well as military applications. Their small size, their robustness and their life time, their high dynamic performances, their energy efficiency and their reduced noise levels are some of the many advantages compared to traditional combustion engines and hydraulic actuators.

In recent decades, designs such as *permanent-magnet (PM) machines* have emerged thanks to the manufacturing progress and the reduction of rare-earth magnet costs. In some applications, such as vehicle propulsion, the polyphase PM machines present important benefits compared to other machine types: high-torque density (ratio between the peak torque and the required machine mass), no rotor electrical-circuit (that would introduce manufacturing costs and that would require a connection system such as brushes and slip rings) resulting to compactness gain, and simple control methods. An optimal and stable torque, with small losses, can be reached by the use of a *digital controller* commanding a polyphase *voltage-source inverter* (VSI). The optimal control requires however the knowledge of the *rotor position*. This position can be measured by dedicated position sensors mechanically mounted on the rotor shaft (such as encoders or resolvers) or placed in the rotor iron-block (such as hall-effect sensors or field-measurements windings). These additional sensor devices are often fragile (relative to mechanical vibrations and temperature variations, resulting to early aging) and they introduce a risk of failure (leading to possible invalid control and dramatic damages), they require space (cabling and processing in addition to the sensor device) and they have a cost (purchase price and maintenance costs).

Intensive research is therefore performed in order to remove these sensors and replace them through the development of so-called *position-sensorless* methods, also called *position-self-sensing* methods. The latter terminology is preferred in this document since it reflects the principle: some electromagnetic phenomena in the machine, that vary with the rotor position, are used to estimate that position. These phenomena can be observed and the position can be tracked from measurable electrical variables, such as currents and voltages at the machine terminals. Most of the methods use the same sensors as those used by for the control. Some other methods use additional current or voltage sensors dedicated to the self-sensing op-

erations. All these self-sensing methods also benefit to hostile environment applications thanks to their increased reliability or can be used for emergency operations in case of sensor failures.

Many of the self-sensing strategies are based on the *back-electromotive force* (back-EMF), that is defined as the voltage induced by the magnetic field produced from the rotor side. In synchronous machines, such as PM machines, the back-EMF is a reliable source for the estimation since it is closely related to the rotor position. The magnitude of this phenomenon is however related to the rotation speed. Therefore, the position information becomes inaccurate at low speed, and completely vanishes at standstill.

Latest and promising self-sensing strategies make use of *high-frequency voltage signals*, injected in the terminals in addition to the power signals used for the *rotation-drive* control (also called *fundamental-signal* control). They are reliable over a wide speed range from standstill. The measurements of the related high-frequency current response allows to identify the orientation of a phenomenon called *magnetic anisotropy*, that is generally related to the rotor position. This anisotropy is particularly pronounced in many PM machines, mainly due to magnetic saturation effects in the iron, and in many other machines with salient poles. These strategies however come with several new problems and issues that are, for many, still in the top of the research topics.

This Ph.D. thesis summarizes a research work focusing on the anisotropy-based self-sensing methods using high-frequency signal-injections without additional sensors. Different types of signals were implemented, such as the so-called *test pulses*, *rotating* and *pulsating* signals, at different frequencies. The progress was closely related to the issues faced during the implementation of the methods on a challenging experimental *Brushless DC* (BLDC) motor, that is a specific type of PM machine. Among them, we have the *misalignment* between the rotor position and the anisotropy, whose orientation is identified by the high-frequency signals. This can be due to significant load currents in the stator or to space harmonics in the magnetic field and in the stator winding distribution. This misalignment causes errors in the estimated position, to be considered or compensated before its use in the rotation-drive control. The theory of this misalignment is largely developed in this thesis. Another important issue is consequent to *nonlinearities* in the voltage supplied by the VSI, resulting in identification errors. Compensation of some nonlinearities and prevention strategies from other non compensable ones is introduced in this thesis. Another issue comes from the impact of the *resistor* and the *eddy currents* in the identification operations. Their analysis are combined with a last issue related to the separation between the signals for the self-sensing operations and the signals for the rotation-drive operations. It is shown that these issues are significantly improved using the highest possible frequency for the signal injection, that is one third of the sampling frequency (for rotating signals) or half the sampling frequency (for pulsating signals) used for the digital operations.

Many of these issues are often neglected, or partially considered, in most of the self-sensing control methods found in the recent state-of-the-art. Due to their sig-

nificance during the research experimentation, it was however required to consider all of them together. This lead to many questionings and analysis of the phenomena in order to propose efficient solutions. These solutions are largely detailed in this thesis. Note that they can be generalized to other machine characteristics and many machine types. This is the contribution of this work.

Contents

1	Introduction	15
1.1	The Research Context	15
1.1.1	Overview of the applications	15
1.1.2	The optimal control issue	16
1.1.3	Self-sensing solutions	17
1.1.4	Self-sensing in position/speed controls	19
1.2	Technical Overview	20
1.2.1	Main issues and contributions	20
1.2.2	Experimental bench	23
1.2.3	Flow chart of the self-sensing control	24
1.3	Thesis Plan	26
2	Electromagnetic Model	29
2.1	Introduction	29
2.2	Electric Machine Designs	31
2.3	Electromagnetic Relations	34
2.3.1	Function of the radial air-gap magnetic-field	35
2.3.2	Function of the conductor distribution	36
2.3.3	Relation between the flux linked by a coil and the magnetic field	37
2.3.4	Relation between the magnetic field and the magnetomotive forces	38
2.3.5	Contributions to the magnetomotive force	42
2.3.6	Relations between the fluxes and the magnetic contributions	44
2.3.7	Electrical torque	44
2.4	Relations using Space Vectors	45
2.4.1	Fourier transforms	46
2.4.2	Relation between space vectors and coefficients of the flux	48
2.4.3	Relation between the flux and the B-field	49
2.4.4	Relation between the B-field and the magnetomotive forces	51
2.4.5	Contribution of the currents to the magnetomotive force	52
2.4.6	Relation between the flux space vectors and the magnetic sources	52

2.4.7	Electrical torque	53
2.5	Three-Phase Machines	55
2.5.1	Space vector computations	55
2.5.2	The incremental self-inductances	56
2.5.3	The harmonic incremental self-inductances	57
2.5.4	The anisotropy definition	57
2.5.5	Impact of the harmonics on the anisotropy	59
2.5.6	Impact of the currents on the anisotropy	60
2.6	Experimental Brushless-DC Motor	61
2.6.1	Simplified design model	63
2.6.2	Estimation of the PM field	67
2.6.3	Simulation Results	70
2.6.4	Experimental Results	73
2.7	Summary	77
3	Electrical Circuit Model	79
3.1	Introduction	79
3.2	Space Vectors in Different Frames	80
3.2.1	The Stationary Frame	80
3.2.2	The Synchronous Frame	82
3.2.3	The Anisotropic Relation	84
3.3	Continuous-time models	86
3.3.1	Induced Voltages	86
3.3.2	The Resistive Voltage Drop	86
3.3.3	Back-electromagnetic force	88
3.3.4	Current Contribution To The Induced Voltage	88
3.3.5	Electrical Circuit Model Without Eddy Currents	91
3.3.6	Electrical Circuit Model Including Eddy Currents	91
3.4	Discrete-Time Models	93
3.4.1	Electrical Circuit Model Without Eddy Currents	94
3.4.2	Electrical Circuit Model Including Eddy Currents	98
3.5	Machine Impedance	109
3.5.1	Continuous-time parameters	110
3.5.2	Discrete-time parameters	111
3.5.3	Experiments and Simulations	114
3.6	Summary	116
4	Voltage-Source Inverter	119
4.1	Introduction	119
4.2	Pulse-Width Modulated Voltage	120
4.2.1	The Two-Level Design	121
4.2.2	Modulation techniques	122
4.2.3	Semiconductor Voltage Drop	125
4.2.4	Switching Dead Time	128

4.3	Zero-Crossing Issues and Prevention	131
4.3.1	Space Vector of Switching State Voltages	132
4.3.2	The Current Ripples	137
4.3.3	The Margin Estimation - previous method	142
4.3.4	The Margin Estimation - simplified method	146
4.3.5	Zero-Crossing Prevention	150
4.4	Experimental Analysis	151
4.4.1	Estimation of the Margins	151
4.5	Summary	154
5	Signal Processing	159
5.1	Introduction	159
5.2	Self-Sensing Field-Oriented Vector-Control	160
5.2.1	The Vector-Control Principle	160
5.2.2	The Field-Oriented Control	161
5.2.3	Conventional BLDC Control	163
5.2.4	Regulators in Closed-Loop Controls	163
5.2.5	Sources of Position Information	164
5.2.6	Back-EMF-Based Self-Sensing	164
5.2.7	Anisotropy-Based Self-Sensing	165
5.2.8	High-Frequency Sources	169
5.2.9	Types of Signal Injections	171
5.2.10	Position Estimation From The Anisotropy Angle	172
5.3	High-Frequency Signal Injection	173
5.3.1	The Discrete-Time Model	173
5.3.2	The z-Transform of the Model	174
5.3.3	The Fourier-Transform of the Model	175
5.3.4	Principle and Assumptions	177
5.3.5	Filtering Operations and Spectrum Dispersions	178
5.3.6	Filter Implementation	179
5.3.7	Operations with Rotating Signals	180
5.3.8	Operations with Pulsating Signals	183
5.3.9	Operations with Alternating Signals	185
5.3.10	Signal-to-Noise Ratio Issue	188
5.3.11	Issue regarding the PWM-VSI	191
5.3.12	Discussion on the Signal Characteristics	192
5.4	Experiments	193
5.4.1	Self-Sensing Using Rotating Signals	193
5.4.2	Self-Sensing Using Alternating Signals	199
5.5	Summary	203
6	Conclusions and Future Works	205
6.1	Summary and Contributions	205
6.2	Future Works	208

Notations, symbols and abbreviations

Abbreviations

PM	Permanent-Magnet(s)
PMSM	PM-synchronous machine
BLDC motor	Brushless DC motor
MMF	Magnetomotive Force
EMF	Electromotive Force
VSI	Voltage Source Inverter
PWM	Pulse-width modulation
HF	High-frequency
LPF	Low-pass filter
PI	Proportional-Integral

Symbols

Θ	physical angle centered on the rotation axis
θ	electric angle periodic on 2π in a single-pole-pair
$B(\theta)$	radial magnetic B-field
$H(\theta)$	radial magnetic H-field
ϕ	elementary linked magnetic flux
$n_p(\theta)$	conductor distribution related to the phase p
$\psi_p(\theta)$	magnetic flux linked by $n_p(\theta)$
$N_p(\theta)$	linking distribution related to the phase p
i_p	electrical current flowing in the phase p
$F(\theta)$	magnetomotive force
$m(\theta)$	factor between the magnetomotive force and the B-field
T	electrical torque
C	Clark-transformation matrix
v	supply voltage applied to the stator circuit terminals
i	electrical current flowing through the terminals
ψ	magnetic flux linked by the stator coils
e	voltage induced by a flux variation
e_{PM}	back-electromagnetic force (back-emf)
ν_s	sampling frequency
ν_{pwm}	PWM frequency
ν_c	frequency of the rotation-drive operations
ν_i	high-frequency of the signal-injection operations
s	PWM switching signal
S	VSI level connection
\mathcal{S}	multiphase level connections
v_{dc}	DC-bus voltage
v_{sc}	Semi-conductor voltage drop
v_{th}	threshold voltage
Δt_{on}	turn-on delay
Δt_{off}	turn-off delay
Δt_{lag}	lag time
Δt_{dt}	dead time
Δi_m	zero-crossing margin

Notations

\vec{X}	spatial vector of a electromagnetic phenomenon X
$a(\theta)$	value a as a function of θ
$a_{\text{PM}}(\theta)$	contribution from the permanent-magnets (PM)
$a_{\text{S}}(\theta)$	contribution from the stator currents/coils (S)
$a_{\text{E}}(\theta)$	contribution from the eddy current/circuit (E)
$a_p(\theta)$	contribution from the stator phase p
$a_t(\theta)$	incremental contribution, i.e. from small signals
$\mathbf{a}^{(k)}$	k^{th} rank coefficient of the Fourier series-development of $a(\theta)$
x_p	value linked by the phase p
$\underline{x}_{(p')}$	p'^{th} rank complex space-vector related to x_p
x_o	homopolar component = $\underline{x}_{(p')}/2$ where $p' = 0$
\underline{x}	fundamental complex space-vector = $\underline{x}_{(p')}$ where $p' = 1$
$\underline{x} _{\alpha\beta}$	space vector represented in the $\alpha\beta$ complex reference-frame
x_α, x_β	projection of \underline{x} along the α and β -axis
\underline{X}	matrix space vector = column matrix containing x_α, x_β
\mathbf{a}	complex parameter between space vectors
a_+	positive contribution of the parameter \mathbf{a}
\mathbf{a}_-	negative contribution of the parameter \mathbf{a}
$x(t)$	continuous-time value
$x(t^{[k]})$	value sampled at the time $t^{[k]}$
$x^{[k]}$	discrete-time value
$\delta x^{[k]}$	backward difference between two consecutive samples
$\bar{x}^{[k]}$	average between two consecutive samples
$\tilde{x}^{[k]}$	mean of $x(t)$ between two consecutive samples
\bar{a}	parameter substituting a in a discrete-time model
ν, ω, T	frequency, pulsation (radial frequency) and period
\underline{x}^*	instruction value
$\mathcal{Z}\{x\}$	z-transform of x
$\mathcal{F}\{x\}$	Fourier-transform of x
$\underline{X}(z)$	= $\mathcal{Z}\{x\}$ in chapter 5

Parameters

j	imaginary unit
e	Euler number
P	number of pole-pairs
l_m	machine length
R	mean radius of the stator coils
δ_o	air-gap length
μ_o	permeability constant in the void
κ	leakage factor
n	number of phases
a, b, c	phase numbering for the case $n = 3$
$\alpha\beta$ -frame	stationary frame, i.e. linked to the stator
qd-frame	frame linked to the orientation of the permanent-magnets
xy-frame	anisotropy frame, i.e. linked to an anisotropy
φ_q	angle of the q-axis with respect to α
φ_d	angle of the d-axis with respect to α
ω_d	$= \omega_q$ rotation speed of the qd-frame
r	resistance
l	self-inductance
l_m	mutual inductance
l_σ	leakage inductance
τ	transient time-constant
k_{pwm}	PWM distortion factor
K_{c2d}	discretization distortion factor
z	impedance
Z	integral-impedance
Y	derivative-admittance

Chapter 1

Introduction

1.1 The Research Context

1.1.1 Overview of the applications

We are surrounded by rotating electric machines of all powers and all types in a lot of applications [1]. The highest powers of hundreds of MW (Mega Watt) are delivered by huge alternators in the power production plants. The wind turbines deliver some MW, generally produced by induction machines, possibly double-fed in order to remove the gearbox, or increasingly by permanent-magnets (PM) machines through AC/AC converters. Medium powers of tens of kW (kilo Watt) are found in electric and hybrid vehicles, submarines and boats propulsions, for civil and military applications. They were previously powered by DC motors or induction motors, but more and more by PM synchronous motors. Similar power levels are also found in industrial machinery, pumping or compressing applications, etc. Low powers of hundreds or tens of Watts are found in robotics and in small actuators, found in transportation, domotics, medical, entertainment sectors. They are generally powered by DC, Brushless-DC or stepper motors. We see here the huge fields of applications of the electric machines, explaining the intensive researches performed on their design and their control methods.

In contrast with most of the large power generators and many industrial applications with constant rotation speeds, many of the mentioned applications require variable speed controls. This means that the machines have to operate smoothly and efficiently at different speeds defined by the user. This is required for the vehicle traction, high-precision robotic applications, but also for the aleatory operating conditions of the wind turbines. These variable speed operations have been largely improved by the use of power inverters and, more recently, digital controls, offering an important flexibility in the implementations.

In the context of energy savings and cost reductions, the efficiency and the maintenance costs are two critical factors in the choice of the machine type for medium and higher powers in civil applications. Thanks to their high robustness and reliability, the induction machines with squirrel cages substituted the brushed

DC-motors in many variable-speed applications [2]. In low speed conditions however, they offer generally lower efficiency rates, mainly due to the power losses in the rotor. In comparison, the motors with permanent-magnets (PM) allow to reach higher efficiencies, assuming optimal control methods, while benefiting of similar robustness and reliability levels due to the absence of rotor electrical-circuit (that would introduce manufacturing costs and that would require a connection system such as brushes and slip rings). Another strong benefit of the PM motors are their relative high-torque density (ratio between the peak torque and the required machine mass) [2]. The price of rare-earth magnets was however an important drawback until recent decades. Nowadays, the PM machines have become good candidates in applications where the efficiency increase and the weight reduction are crucial points, such as in electric vehicles. Many of the criteria for civil applications are also valid for military applications [3]. In that context, PM motors also present strong advantages in terms of robustness and reliability in hostile environments [4].

1.1.2 The optimal control issue

The so-called *optimal control* of machines is defined as a control point delivering a constant torque with the lowest losses for a fixed torque instruction. This definition is valid for any type of machine. This optimal point can be reached using advanced digital controllers and efficient power inverters. These units allow to regulate accurately the currents in the machine in order to control the produced torque following the desired user instruction. In case of some AC machines, such as the PM machines, this solution however requires the knowledge of the *rotor position* (i.e. the rotor angle with respect to a reference orientation) in order to adjust the currents as a function of the magnetic field produced from the rotor. Traditionally, this position is measured by dedicated position sensors mounted mechanically on the rotor shaft (such as encoders or resolvers) or placed in the rotor iron-block (such as hall-effect sensors or field-measurements windings). These dedicated sensors present however many disadvantages [5, 6, 2, 1, 7]:

- due to their proximity with the machine, they must endure mechanical vibrations, temperature variations and possible corrosive or hostile environments, although they are often quite fragile regarding the machine itself, resulting to early aging and risk of failures. These failures may lead to invalid control operations, mainly blocking suddenly the rotation or leading to blinded control, that can result in dramatic damages ;
- if they are mounted on shaft, they inevitably require dedicated space, what is not always possible or recommended in applications such as for wheel motors. Moreover, dedicated cabling and processing are required, which brings an additional risk of failure and noise ;
- finally, all these tools have a purchase price. They also require maintenance

that have costs and that may interrupt the drive.

In order to maintain the advantages that the AC of machine, or simply to improve their reliability with respect to the demands, intensive research is therefore performed in order to remove these sensors and replace them through the development of so-called *position-sensorless* methods, also called *position-self-sensing* methods. In our opinion, the expression *sensorless* can be confusing, since only the position sensor is removed, while other voltage and current sensors are still needed. These voltage and current sensors are generally made with simpler technologies, resulting in more robustness, and can be placed on the side of the power supply, distant from the machine and its environment. Moreover, the latter terminology “*self-sensing*” better reflects the principle: some electromechanical phenomena in the machine vary with the rotor position. Some of these phenomena can be observed from measurable electrical variables, such as currents and voltages at the machine terminals, and used to provide an estimation of the position position. Thanks to their increased reliability, the self-sensing methods are strongly advised in hostile environment applications [2], such as many military applications [3]. But they can also be used in combination with traditional position sensors for emergency operations in case of sensor failures [7], called *fault-tolerant operations*.

1.1.3 Self-sensing solutions

Technically, the simplest solution consist to perform the position estimation using the same current and voltage sensors as those used for the optimal control. This can be quite easy to implement without modification of the drive setup. By consequence, it can be implemented in existing applications without much effort. Moreover, different possible self-sensing strategies can be quickly tested and compared. Some methods however use additional current, current-derivative or voltage sensors dedicated to the self-sensing operations. If feasible, the main advantage is that the accuracy of these dedicated sensors can be especially selected for the measurements of the signals used for the self-sensing operations. But their disadvantages are very similar to those described for the traditional position sensors. Other methods use the same current and voltage sensors as the optimal control, but require additional samplings or modified operations of the power converter. The implementation of these solutions heavily depend on the existing hardware specifications. In the frame of this thesis work, in order to optimize the research and the time, we decided to focus on the first type of solutions, using the control current and voltage sensors without any hardware modification or any special requirements. Note that the quality of the sensors use in our experiments were quite poor, leading to reduced resolutions. This constraint forced us to develop extremely robust methods with respect to the measurement resolutions.

In PM machines, there are mainly two phenomena that can be used as sources of position information:

1. the *back-electromotive force* (back-EMF), defined as the voltage induced

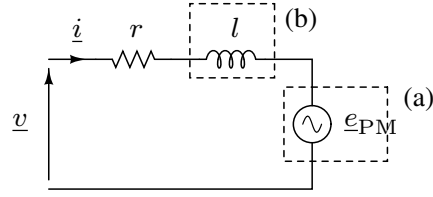
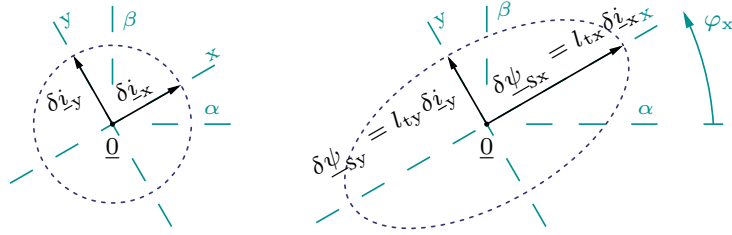


Figure 1.1: Schema of the electrical-circuit model.

Figure 1.2: Illustration of $\delta\psi_s$ related to $\delta\vec{i}$: (I) along the x-axis; (II) along the y-axis. The blue dashed lines represent the path drawn by the space vectors when $\delta\vec{i}$ rotates.

by the PM contribution to the magnetic field and produced from the rotor side. It is written e_{PM} using *complex space-vectors* (the concept of complex space-vectors is largely introduced in this thesis and offers very powerful mathematical tools) and it is illustrated in an equivalent electrical-circuit model in Figure 1.1. The back-EMF is a reliable source for the estimation since it is closely related to the rotor position. This phenomenon is not restricted to PM machines, but it exists in any synchronous machine, where the back-EMF is defined as the voltage induced by the rotor-circuit contribution. The back-EMF however suffers from an important limitation: it vanishes at standstill, making any direct attempt to estimate the position impossible (excepted through predictions based on dynamic models, for a limited period of time). However, the knowledge of the rotor position is essential for smooth startup operations, or simply when a load torque must be maintained constant at standstill, or at very low speed. For these situations, another source of position information is therefore required ;

2. the *magnetic anisotropy*, defined as variable inductive relations depending on the orientation the current signals in a *space vector* frame. From a phase point of view, the magnetic anisotropy is related to differences in the inductive behaviour along the different phases. The self-inductance l is illustrated in an equivalent electrical-circuit model in Figure 1.1. In practice, most of the anisotropy-based self-sensing methods use variations of the *incremental self-inductance* l_t , linking small stator-currents $\delta\vec{i}$ to their small contributions to the magnetic flux $\delta\psi_s$ in the space-vector complex frame. Figure 1.2 illustrates the difference of the incremental self-inductance between two ex-

trema directions, denoted by the axes x and y . The *anisotropy angle* φ_x provides an approximation of the rotor-PM orientation. The magnetic anisotropy is mainly due to two characteristics:

- to physical variations of the air-gap space between the rotor and the stator parts of the machine. These variations can be due to a design saliency of the rotor or to teeth between conductors slots. The saliency is generally pronounced in synchronous machines, but it can be very small in some PM machines, for example in machines where the PM are placed on a smooth rotor surface, such as the Brushless-DC motors ;
- to variations of saturation levels of the iron. Most of the PM produce noticeable saturations that is linked to their location in the rotor.

It is assumed that the anisotropy yields reliable information about the rotor position. In practice however, it is not so simple and significant deviations between the anisotropy angle and the rotor position can be observed. We propose to refer to this by *anisotropy misalignment*. This issue constitutes a large part of this thesis. Beside some issues in signal processing, the anisotropy should not be affected by the rotation speed. Solutions based on anisotropies should thus be reliable over a wide speed range from standstill.

Since the back-EMF-based methods are already sufficiently mature to our opinion, we focused in this study on the second source of information that is the magnetic anisotropy. Much work remains to be done for that, since the identification of the rotor position based on the anisotropy brings many new issues that remain to be solved and to be validated for industrial applications.

In order to identify the magnetic anisotropy for the position estimation, one strategy consists to inject *high-frequency voltage signals* in the terminals in addition to the low-frequency power signals used for the control. In order to distinct both signal types, authors refer to the control signals as *fundamental*-signals. We prefer however to refer to them as *rotation-drive* control-signals, since it may content a larger spectrum than a simple fundamental: other harmonics in the spectrum can be added due to transitory operations (such as variations in the load torque or in the torque instruction, required for example in the case of an acceleration) or also due to phenomenons such as nonlinearities in the power source. The high-frequency signals required for the anisotropy identification are simply referred to as *signal injection*.

1.1.4 Self-sensing in position/speed controls

We addressed the self-sensing from the point of view of optimal torque control. Another control aspect must also be to point out concerning the speed and the position control. Some drives, such as many robotic applications, require an accurate control of the speed or the position of the machine. The self-sensing solutions can also be applied in that case instead of using dedicated speed and position sensors.

The position estimation is therefore not only used to compute the optimal torque, but it is used in feed-back loops controlling speeds and positions. The speed is generally obtained from an observer using, in input, the estimated rotor position. The observer can eventually include dynamic models of the machine in order to improve the speed estimation. This benefit of the self-sensing is valid for any type of machine [5], that can be PM machines, but also induction machines and DC-motors [8]. The solution to track the rotor position in case of induction machines and DC-motors are however limited to small magnetic anisotropies mainly related to rotor teeth. The small amplitude and the high-harmonic content of the anisotropies in these cases bring some further issues that are not met in PM machines. Some references focus on these questions and are mentioned in this thesis, but it is not further addressed.

Let us highlight here a third source of rotor-position information specific to double-fed asynchronous machines: thanks to their double circuits, one at the rotor and the other at the stator, the relative shift between these circuits provide an additional source of information, used by [9]. This source exists in any machine with connection to the rotor and can certainly be used in synchronous machine with wound rotor, but we did not find references about this. Note that these machines are generally less robust because of the slip rings required for the rotor connection. Other types of connections using the coupling of two machines also exist, but these solutions greatly deviate from the studied applications of the PM machines.

1.2 Technical Overview

1.2.1 Main issues and contributions

As introduced previously, this Ph.D. thesis summarizes a research work focusing on the anisotropy-based self-sensing methods using high-frequency signal-injections without additional sensors. Different types of signals were implemented, such as the so-called *test pulses*, *rotating* and *pulsating* signals, at different frequencies. All these types of signals have their advantages and their drawbacks, depending on the application.

The progress of the work was closely related to the issues faced during the implementation of the methods on a challenging experimental *Brushless DC* (BLDC) motor, that is a specific type of PM machine described in the next subsection. Among the issues, we have the significant *misalignment* between the rotor position and the anisotropy, whose orientation is identified by the high-frequency signals. This is firstly due to significant load currents in the stator that leads to an error shift with respect to the real position of the rotor, but also to space harmonics in the magnetic field and in the stator winding distribution leading to an oscillating error in the position estimation. This last error is illustrated in Figure 1.3 by the anisotropy angle φ_x as a function of the rotor position located by its quadratic angle φ_q . These misalignments can be neglected in certain machine designs, but they are highly pronounced in the the experimental BLDC motor. They can significantly affect the

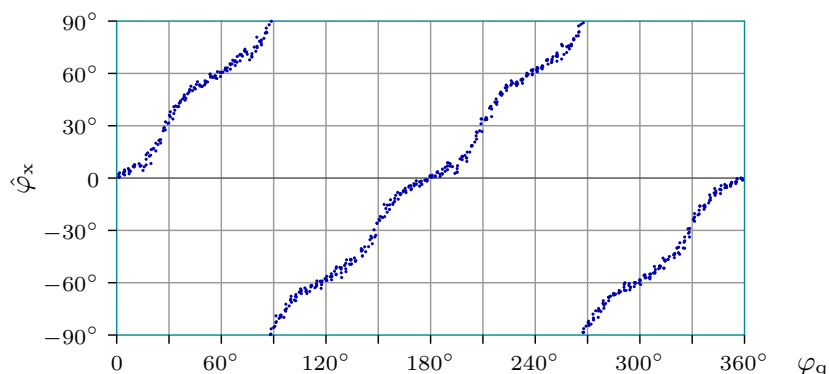


Figure 1.3: Results with the experimental BLDC motor: anisotropy angle $\hat{\varphi}_x$ estimated using signal-injection, as a function of the PM-rotor orientation, related to φ_q .

optimal torque control, reducing its efficiency. They should therefore be assessed and compensated. Many publications analyze the misalignment through finite-element simulations and address approximate technical solutions. But the theory of this misalignment is not greatly beloved by the community of researchers. To bridge this gap, we largely studied the possibility to develop a simple analytical model that could give instructive information about the phenomenon of the anisotropy. This development was rather long, providing very interesting models to be used. But it did unfortunately not leave much time to concretely implement a solution. Possible solutions are however suggested in this thesis.

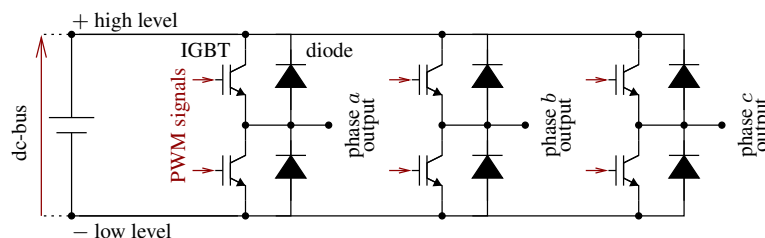


Figure 1.4: Design of the two-level three-phase VSI

Another important issue is due to *nonlinearities* in the voltage supplied by the voltage-source inverter, corresponding to deviations between the expected voltage and the real output voltage. The topology of the two-level three-phase voltage source inverter (VSI) used in the experiments is shown in Figure 1.4. This type of inverter operates by switching each phase output between a high-level voltage and a low-level voltage from the dc-bus input, commanded by pulsewidth modulated (PWM) signals. The self-sensing methods require an accurate knowledge of the supplied voltage. For cost and reliability reasons however, the voltage is often not directly measured. In that case, self-sensing operations rely on the command voltage sent to the ship generating the PWM. The behavior of the VSI is however not

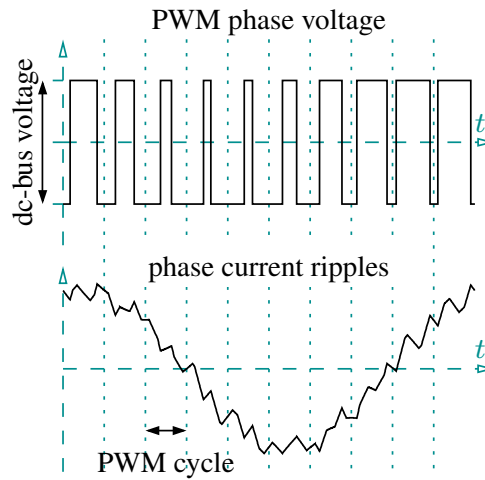


Figure 1.5: PWM voltage signal and the current ripples

perfectly linear. The two main nonlinearities are the voltage drops that exist across the semiconductor devices and the inherent commutation times of the switching devices to turn on and to turn off. In order to avoid that the switching devices of the two levels are simultaneously conducting, and so to prevent dc-bus short-circuit, it is indispensable to add a delay to the turn on moments of the switching devices. As a result during a short period of time called dead time, both switching devices remain blocking. Both voltage drops and dead times can be compensated by using approximate estimation values. But these compensations are however not valid when the current of one phase crosses zero. The *zero-crossing* reveals an important nonlinear effect referred to as *zero-clamping effect*: if the current reaches zero during the dead time, it is clamped to zero for the rest of the dead time. This phenomenon is not easy to model as the topology of the machine is changed with one disconnected phase. Moreover, the pulse-width modulation (PWM) technique used to command most of the VSI results in small current ripples between two samples, illustrated in Figure 1.5. These ripples are generally not measured and they complicate any attempt to predict the zero-crossings and, by consequence, to compensate for the zero-clamping effect. This problem was amplified due to the relatively low voltage operations required for the experimental BLDC motor and due to significant dead times in the supply operations. This has two consequences: firstly on the rotation-drive operations, leading to strong disturbances in the control signals and in the optimal operations. Secondly, on the self-sensing operations that became inaccurate. The problem was very annoying in our experimental setup and could probably be solved by adding dedicated voltage sensors. But the addition of sensors however brings all the issues addressed about the traditional position sensor. Moreover, voltage sensing could reduce the problem, but cannot removed it. No satisfying solution was found in the literature for our experimental conditions. In order to overcome this problem, the solution proposed in this thesis consists to

estimate the amplitude of the current ripples and to add an offset in the current reference in order to maintain the current ripples far enough from zero. This offset is selected in order to minimize its impact on the torque and the performances of the machine.

Another issue comes from the impact of the *resistor* and the *eddy currents* in the identification operations. They are generally neglected in self-sensing operations using high-frequency signals, assuming a purely inductive behaviour of the machine circuit. In practice however, they can lead to estimation errors. This topic is addressed in some publications, but we propose a further analysis based on a discrete-time model that we develop in this thesis. The issue of the resistance can be combined with a last issue related to the separation between the signals for the self-sensing operations and the rotation-drive operations. It is shown that these issues are significantly reduced using the highest possible frequency for the signal injection, that is one third of the sampling frequency (for rotating signals) or half the sampling frequency (for pulsating signals) used for the digital operations. We proposed a very simple and very reliable solution based on discrete-time operations and FIR filters. The efficiency and the robustness are verified in the drive of the experimental BLDC motor, including all the problems due to the low sensor resolution, due to anisotropy misalignment and due to the nonlinearities of the voltage-source inverter. This is the most relevant contribution of this work.

1.2.2 Experimental bench



Figure 1.6: Experimental BLDC motor.

The experiments are performed on a 3 kW three-phase in-wheel motor brushless-DC (BLDC) motor with $P = 14$ pairs of surface-mounted permanent-magnets in an outer rotor, presented in Figure 1.6. It was developed by the company *Technicréa*, France, for the propulsion of small vehicles and initially intended for the project *Vélapac* of the company *SERA* (Société d'Etude et de Recherche Automobile). This is a 14 inch diameter cylindrically shaped motor and it weighs 13.5 kg. The yoke is made of sheet of FeSi (type Ugine 250-35HA) and the PM are made of

Nd-Fe-B, producing peak magnetic fields of 0.66 T in the air-gap. It is cooled by forced air convection. The rated torque is 150 Nm from standstill to 191 rpm, corresponding to a rated stator current of 134 A. The maximum torque decreases down to 57.3 Nm, corresponding to a rated stator current of 55 A, when the rated rotation speed is of 500 rpm is reached, corresponding to a rotation electrical-frequency of $14 \times 500/60 = 116$ Hz. The motor performance is 91 % at 500 rpm.

The motor is fed with an IGBT voltage-source inverter (VSI) from *SEMIKRON* (model *SKM 50GB123D* with a rated current of 50 A), which is supplied by a DC-bus voltage set around $v_{dc} = 50$ V. Owing to the relatively small inductance of the motor, the manufacturer *Technicréa* recommends not exceed a DC voltage of $v_{dc} < 72$ V. This voltage is supplied by a thyristor power rectifier from *ACEC* (model *REDACEC S*, that is initially a power driver for DC-motor). The pulse-width modulated (PWM) signals commanding the IGBT of the VSI are generated by a DSP controller unit from *Texas Instruments* (model *TMS320F240DSP*) set in a *dSpace* card (model *DSP103 PPC Controller Board*).

The same *dSpace* card is used to measure the phase currents at the machine terminals, the DC-link voltage of the power rectifier and to perform the digital control operations. The maximum sampling frequency for the current measurements is $\nu_s = 13$ kHz (obtained experimentally). This frequency is mainly limited by the time required to perform the computations, that must be lower than the sampling period $T_s = 1/\nu_s$ minus all the delays of the input/output operations. The self-sensing control method has been implemented using partly *Simulink* codes (*Matlab R13* with *Simulink 5.0.2*) and mainly *C* codes, compiled and loaded in the card (*Real-Time Workshop 5.0.1*).

The BLDC motor is equipped by *hall-effect sensors* from *Honeywell* (*400SS Series*), but they are not used in this study. The position estimated by the self-sensing operations are compared to the position given by a 8192-pulses incremental encoder from *Sick|Stegmann* (model *DRS61-A4A08192*).

1.2.3 Flow chart of the self-sensing control

The anisotropy angle φ_x can be estimated by the injection of high-frequency signals in addition to the low-frequency voltage computed by the normal rotation-drive operations. The resulting high and low-frequency contents of the current response are filtered for self-sensing and rotation-drive operations.

Figure 1.7 gives an overview of the self-sensing control operations using signal-injections in flow chart, including the different issues addressed in this work. Starting from the upper left part of the flowchart:

- The speed controller computes a current-amplitude instruction i_c^{**} from the error between the user speed-instruction ω_c^* and the estimated PM rotation speed $\hat{\omega}_q$;
- The current instruction is oriented following the estimated angle $\tilde{\varphi}_q$, corresponding to the torque-producing orientation related to the rotor-PM posi-

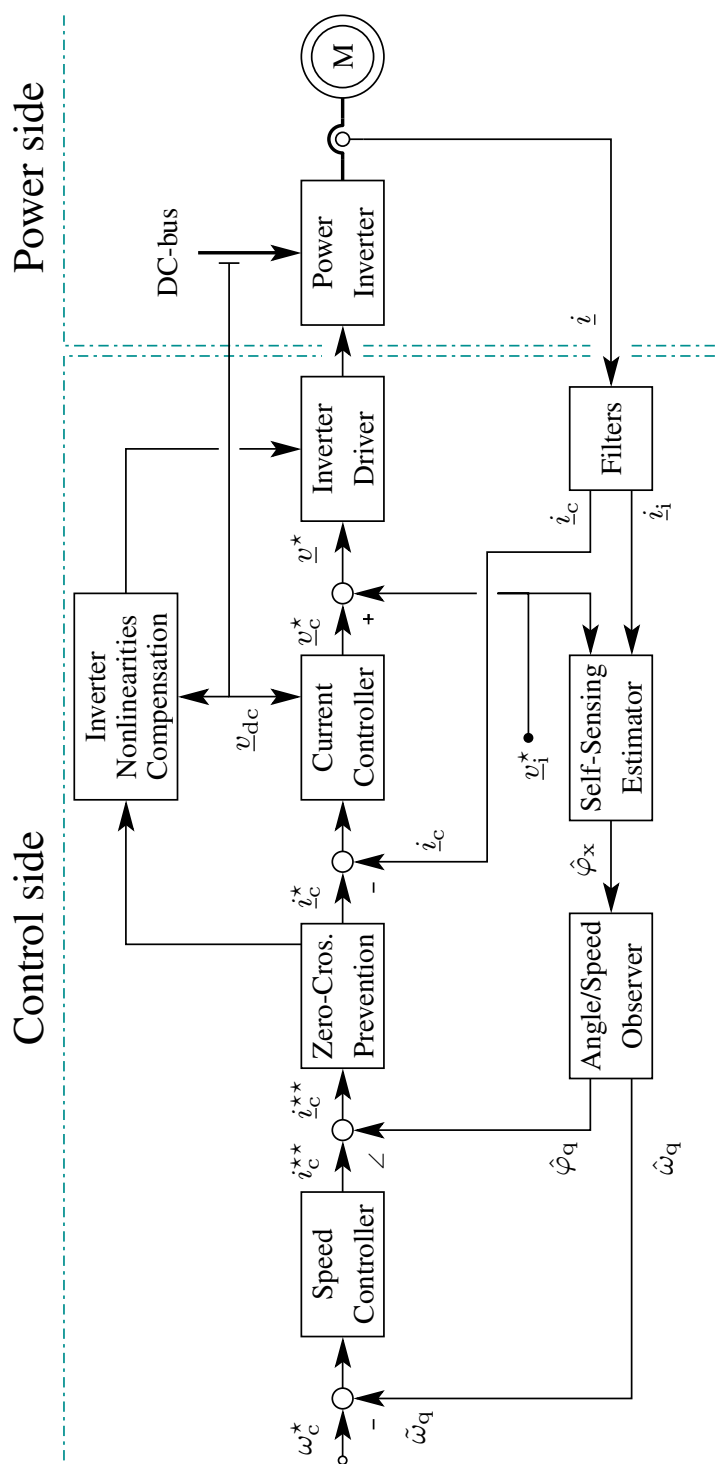


Figure 1.7: Global flow chart presenting the main blocs of the self-sensing control using signal-injections.

tion ;

- A zero-crossing prevention block computes a new current instruction i_c^* by adding an offset in order to prevent the zero-crossing nonlinearity of the power inverter ;
- The current controller computes the voltage command v_c^* from the error between the current instruction and the filtered current input \hat{i}_c ;
- A high-frequency voltage v_1^* is added to v_c^* , and the total voltage command v^* is sent to the block driving the power inverter ;
- If the voltage applied to the machine is not measured, the inverter nonlinearities should be compensated in order to improve the correspondence between the command voltage and the output voltage from the inverter ;
- The additional high-frequency voltage v_1^* produces a high-frequency current variation \hat{i}_1 in addition to the low-frequency current \hat{i}_c used for the rotation control. Both are separated by applying low-pass and high-pass filters ;
- The high-frequency current \hat{i}_1 is used to compute the estimation of the anisotropy angle $\hat{\varphi}_x$;
- An observer is used to provide an estimation of the rotor-PM speed $\tilde{\omega}_q$ and a filtered estimation of the angle $\tilde{\varphi}_q$, possibly taking the misalignment of the anisotropy into account.

1.3 Thesis Plan

This thesis is organized in four chapters, described hereafter. This organization does not correspond to the steps of the work progress, but to the sequence of concepts successively required to understand the issues met in the self-sensing implementation.

Chapter 2, entitled “Electromagnetic Model”, addresses the modelling of the electromagnetic phenomena in the case of cylindrical machines with nonlinear magnetic characteristics. Relations between the magnetic flux linked by one phase coil and the different magnetic contributions, that are the stator current and the permanent magnets for the PM machine, are developed. Special attention is given to linearized relations around working points, leading to the definition of incremental relations. These relations are extended to polyphase machines using the concept of space vectors to represent the phase values. This leads to the concept of anisotropy, represented by the anisotropic incremental self-inductance factor between the small current and their contribution to the linked flux. The relations are further simplified for the case of a three-phase machine without neutral connection. The incremental self-inductance therefore takes the form used in self-sensing operations. Through this chapter, we want to reintroduce the concept of space vectors and to illustrate

their potential for any number of phases. We want also to show the origin of the anisotropy, that is the basis of the considered self-sensing strategy. This allows to understand the causes of the anisotropy misalignment and to assess them in the case of the experimental BLDC motor.

Chapter 3, entitled “Electrical Circuit Model”, addresses the modelling of the relation between the currents and voltages at the machine terminals, firstly neglecting the eddy currents and secondly including them. Since the operations are performed by digital computation devices, the initial continuous-time model is substituted to a discrete-time model. Special attention is given to parameter distortions due to the discretization and due to the pulsewidth modulation of the voltage source, in particular for the case including eddy currents. The signal-injection methods mainly identify an impedance (or inversely an admittance, depending on the point of view), that can be modelled in equivalent apparent inductive and resistive effects. The theoretical variations of these apparent parameters as a function of the signal frequency are compared to measurements performed on the experimental BLDC motor, in order to validate the models. This chapter does not present any issue nor solution required for the self-sensing, but highlight the phenomenon of apparent parameter variations, that are experimentally observed. Through this chapter, we want to show that the discretization of the model in case of large eddy currents is not an obvious operation, and that its validity is not guaranteed. We propose therefore a tool allowing to assess the validity from the knowledge of the continuous-time model parameters.

Chapter 4, entitled “Voltage-Source Inverter”, addresses the working of the conventional two-level three-phase voltage-source inverter (VSI) based on IGBT commanded by conventional pulsewidth-modulated (PWM) signals with a fixed frequency. This is not the only type of power inverter nor the only type of command signals, but it is a proven and widespread industrial solution until now. Moreover, it is used in the experimental drive. The different nonlinearity issues met in that type of PWM-VSI are introduced. The most problematic is referred to as zero-clamping effect and occurs when a phase current crosses zero. By consequence, two methods to prevent zero-crossings are proposed and implemented for the experimental drive. Note that the presented issues are strongly related to the PWM-VSI type. They could possibly be removed using newer VSI types, or by the possible future manufactures of new and more efficient semiconductors.

Chapter 5, entitled “Signal Processing”, addresses firstly an overview of the vector controls and of different self-sensing methods. The case of the high-frequency signal-injected is secondly addressed in details. Concrete self-sensing operations are introduced depending on the type of injected signal. Different issues are addressed: the problem of the measurements noise, the separation between self-sensing and rotation-drive operations, the impact of the resistance, the sources of disturbances, the computation requirements, the robustness and the settling times. All these issues are analyzed regarding the case of the experimental drive for different types of signals (rotating, pulsating and alternating) at different frequencies. Through this chapter, we firstly want to justify the choice of the signal injection for

the experimental case. It is however not the only solution and we propose comparison tables, since others solutions could be more advised for other drive conditions. The quality of the position estimation is illustrated by experimental results.

Chapter 2

Electromagnetic Model

This chapter addresses the electromagnetic model of the permanent-magnet (PM) machine. This model describes the relation that exist between the different magnetic sources in the machine and the magnetic flux linked by the stator coils, named *phases*. In a permanent-magnet (PM) machine, the magnetic sources are the PM mounted in the rotor and the currents flowing in the stator coils. This relation may present nonlinear and anisotropic properties, that are defined in this chapter. The electrical torque due to the interaction between the magnetic field and the currents flowing in the coils is also introduced. This model provides essential mathematic tools to understand the behaviour of the machine in order to introduce control schemes and self-sensing methods in the last chapter.

2.1 Introduction

The concept of *space vectors* is widely used in machine control to describe the relations between the electromagnetic values [10, 11, 12, 13, 1]. This concept is also referred to as *two-dimensional equivalent values* or *space phasors* in some publications. It provides a significant simplification tool for the relations, especially for three-phase machines. This concept was initially addressed with the approximation of fundamental magnetomotive-force distributions by R. H. Park in 1929 [14, 15, 16, 17], and assuming synchronous operations, i.e. sinusoidal variations of the power signals. The first approximation is equivalent to assume that the magnetic field and the conductor distributions in the stator can be modelled by fundamental sinusoidal functions on the pole-pairs, as described by J. Holtz [18].

Many authors continue to maintain this approximation, even for recent variable speed drives and for machines where it could not be valid. In the early 20th century, this choice was only dictated by limitations of the analog control devices used at this time, and not to mathematical restrictions. The concept provides in fact very interesting relations also for machines presenting significant harmonics. The modelling in that case can be initiated by *Fourier series* developments of the different design characteristics and the different electromagnetic phenomenon occurring

all around the space separating the stator and the rotor, called the *air-gap*. These series provide results that can be easily related to the concept of *space vectors*, that is extended for the occasion. In a similar way, this methodology was proposed by G. Maggetto [19] in 1973 and by H. R. Fudeh [20, 21, 22] in 1983, in order to estimate the oscillations in the torque during synchronous operations. The consideration of the harmonics is of first important in some machines designs, such as in concentrated windings topologies or in recent brushless DC motors. They can significantly affect the behaviour of the machine and results in oscillating errors in the position estimated by self-sensing methods. This is addressed in this chapter.

Another widespread simplification in the machine modelling consist to neglect the nonlinear magnetic characteristics linking the magnetic sources to the produced magnetic B-field, and corresponding to magnetic saturations in the iron. This choice is only justified by the strong complexity to find simple models of the saturation. These nonlinear magnetic characteristics are however an important contribution to the anisotropic properties of the machines, that are expected for certain self-sensing methods. It can moreover be the only source of anisotropy in the case of surface-mounted PM. Many authors dealing with anisotropy-based self-sensing methods must assume the magnetic nonlinearities, but simplifies the model assuming that the magnetic state of the machine is mainly function of the PM field, neglecting the contribution of the stator currents. This contribution may however affect the magnetic state and result in a shift of the anisotropy orientation used to estimate the rotor position, as discussed in [23] with a model based on magnetic co-energy. This is also addressed in this chapter.

In the vast number of recent publications, the space vectors description are often very short using variable formalisms, and restricted to the fundamental model approximation. In this chapter, we propose therefore to clarify the description of the concept in a simple formalism. In a first time, the concept is generalized for an arbitrary n number of phases and taking the harmonics into account. It is reduced to three-phase machines only in a second time, leading to a more intuitive expression of the anisotropy. This anisotropy yields an orientation that can be used to estimate the rotor position. This orientation is affected by the two mentioned subjects: harmonics, leading to anisotropy oscillations, and nonlinearities, leading to anisotropy shifts. For convenience, both effects are referred to as anisotropy *misalignments* in this document.

~

This chapter is organized as follows: the section 2.2 introduces elementary descriptions of the design and the topologies of different electric machines, including the brushless DC (BLDC) motor ; Section 2.3 introduces some important assumptions for the modelling and describes several relations from the point of view of the stator coils, referred to as stator *phases*. Among them, we have the relation between the magnetic field and the magnetic flux linked by one coil, the nonlinear relation between the magnetomotive forces and the magnetic field, the

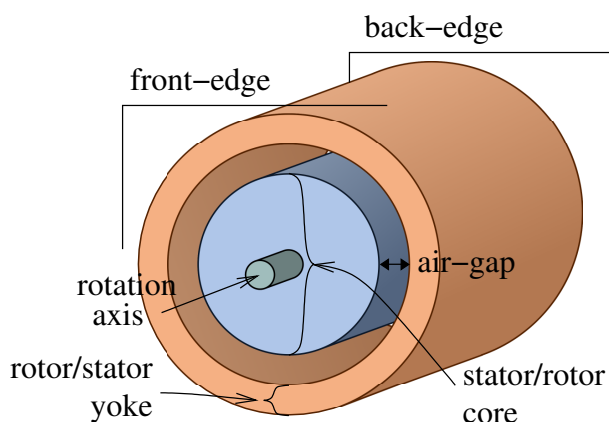


Figure 2.1: Illustration of a rotating electrical machine with cylindrical shaped parts.

corresponding incremental relation useful for anisotropy-based self-sensing theory, and the expression of the electrical torque ; Section 2.4 introduces the concept of space vectors for polyphase machines, assuming any number of phases and including harmonic aspects. The relations previously described are transposed in relations between the space vectors ; Section 2.5 specifically develops the relations for the widespread case of three-phase machines and introduces the mathematical expression of the anisotropic relation, as further used in this thesis ; Section 2.6 applies the modelling to the experimental BLDC motor and adjusts its characteristics by comparing experimental results to simulation results. This allows some draw some conclusions about the impact of harmonics and stator currents in anisotropy misalignment ; A summary of the important elements of this chapter is given in section 2.7.

2.2 Electric Machine Designs

As illustrated in Figure 2.1, a rotating electrical machine is made of two iron parts rotating with respect to each other. By convention, one part is called the *stator* and the other part is called the *rotor*. The stator is generally the part mounted on the same pedestal as the power electronic driving the machine. The space that separates the rotor and stator parts is called the *air-gap*. Most of the electrical machines present an *inner-rotor* design: the rotor is the core of the machine and is accessible through a rotation axis, while the stator is the yoke surrounding the core. The reverse *outer-rotor* design, with the rotor surrounding the stator, is less common. This is the design of our experimental in-wheel motor, intended for small car traction, where the rotation is assumed to be transmitted by a tire directly mounted on the rotor external surface, while the stator replaces the wheel rim and is fixed to the chassis of the car.

Most of the machines are formed by the assembly of cylindrical shaped parts.

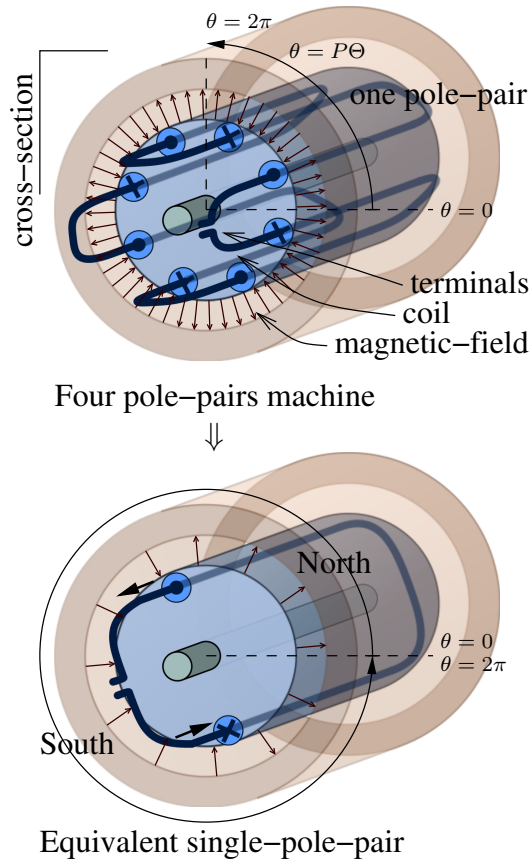


Figure 2.2: Illustration of a machine cross-section considering only one coil in the stator core (outer-rotor design), and the equivalent single-pole-pair representation. In a cross-section, \odot denotes a current flowing from back to front-edge and \otimes denotes an inverse flow.

In other words, the cross-section of the machine is the same at any axial position between front and back edges. This is the case of our experimental motor. In such a design, the conductors are laid in parallel to the rotation axis, in slots that are generally close to the air-gap surface, as illustrated in Figure 2.2 with one coil. Machines generally contain several interlaced coils, referred to as *phases*. And, it is assumed that the magnetic field crosses radially the air-gap and has no axial component. In less conventional designs (not illustrated), the magnetic field crosses axially the machine through disks. They are referred to as *axial-flux machines*. These less conventional designs are not specifically studied in this document, but most of the proposed theory could however be adapted and applied to them.

As illustrated in Figure 2.2, an electrical machine is often made by the juxtaposition of identical structure patterns along the physical angular position $\Theta \in \{0, 2\pi\}$, where identical electromagnetic phenomena are repeated. Such a pattern is referred to as *pole-pair* substructure since the magnetic field loops in that

place between two locations called *North* and *South* poles, crossing the air-gap. Thanks to the repetition property, the model of a multipole machine can be restricted to an equivalent single-pole-pair representation along an *electrical* angular position $\theta \in \{0, 2\pi\}$. If P is the number of pole-pairs the relation is: $\theta = P\Theta$. This property is however lost if the rotor and stator axes are misaligned (developments assuming misalignment are found in [24]), if small variations occur between substructures (such as differences in the aging of permanent magnets for instance) or if the machine is immersed in a significant external magnetic field. These special situations are not studied in this document and we assume therefore identical pole-pairs. Note some interesting designs where the number of identical structures are not the same at the stator and at the rotor. This is the case of the *modular* topologies of some BLDC motors as proposed by [25]. In that case, P is the common denominator between the stator and the rotor structures.

We distinct two main types of machines depending on the supply strategies at the stator side: the so-called DC and AC machines. An AC machine is a polyphase machine generally made of minimum three stator coils, whose windings are distributed over the circumference of the stator, and presenting at least one connectible output terminal. In so-called *star-connection* topologies, the others terminals of the coils can be connected in one point, often called the *neutral point*. In so-called *delta-connection* topologies, the terminals are connected by peers. The variations of the currents in the coils are either due to the alternating character of the supplying voltages, or they are controlled electronically by the modulation of an external DC-bus voltage. The torque in electrical machine is produced by the electromagnetic interactions between the stator and the rotor. The main part of the torque is due to the interaction of the stator current with the magnetic field produced from the rotor. This is produced either by the magnetic reaction in a closed coil located in the rotor (defining the *induction* machines, also called *asynchronous* machines), by a fixed current flow (DC) in one rotor coil (defining the *synchronous* machines) or by currents in polyphase rotor-coils (defining the *double-fed* asynchronous machines). The current flow in the rotor coils can be replaced by permanent-magnets (PM), leading to the so-called *PM synchronous* machines (PMSM). Variations of the reluctance in the machine, mainly due to salient pole designs at the rotor, also produce a torque (defining the *reluctance* motors). Only a small part of all the AC machines types are mentioned here. A larger overview is found in [26, 27, 2].

A DC machine is generally made of a multitude of windings distributed over the circumference of the rotor. The current flow in the different windings is commutated mechanically by brushes rubbing on rings, while the global value of the current flowing through two accessible terminals is controlled externally. In comparison to the AC machines, the drive of the DC machines is much simpler, but this type of machine is generally more expensive and requires a higher maintenance due to mechanical frictions. Note that the electric circuits of DC machines can be modeled assuming an equivalent high number of phases. This is made by [28]. The magnetic field from the stator can be produced by a fixed current flow (DC) in one coil or by permanent-magnets (PM). Note that some machines hold

additional compensation circuits for armature reactions and damping circuits, that are not discussed here.

The *Brushless-DC* (BLDC) machine reproduces the principle of the *DC* machine with PM, where the rotor and the stator topologies are inverted (the PM are in the rotor). The mechanical brushes are removed and replaced by electronic commutations. The design of the BLDC machine is however closer to an AC machine than a DC machine, and can be classified among the PM machines (non synchronous). In order to reproduce a behaviour similar to a DC machine, the conductors of each phases are generally concentrated in low number of slots. The reluctance variations due to the teeth separating the slots and the interaction with the PM may produce significant *cogging* torque. This effect have an important impact on the quality of the drive [29]. This is the case in the experimental BLDC motor of this study. The designs can be improved in order to reduce the cogging torque, such as the modular topology described in [25] or using skewing of the stator conductors [29].

As explained in the introduction, the PM machines have generally strong advantages compared to other types: they present high power densities (power with respect to the size and the weight), robustness and reliability. Their price is mainly related to the rare magnetic material cost, that decreased during last decades. By consequence, this work mainly focuses on that type of machine. To our opinion, it is however important to develop models and strategies that could be possibly applied to other machines types. This is not specifically mentioned in this work, but only small adaptations should be required to transpose the model to other designs.

2.3 Electromagnetic Relations

In this section, we develop the analytical relation between the magnetic flux ψ_p linked by the coil of one phase, numbered p , with the different magnetic contributions. In a permanent-magnet (PM) machine and neglecting the eddy currents, these contributions are the currents $i_{p'}$ flowing in the stator coils of the different phases p' , multiplied by stator inductance parameters $l_{pp'}$, and the permanent-magnets on the rotor written $\psi_{PM,p}$. Due to strong nonlinear properties of the magnetic materials, the relation between the flux variations $d\psi_p$ and small current variations $di_{p'}$ can be strongly dependent on the magnetic state of the machine. Local linearized values of the inductances $l_{t,pp'}$, denoted by the lower index t , are therefore required. They are called *incremental* inductances or *tangential* inductances [30, 31]. For convenience all the values and the relations related to small variations are called *incremental* in this work. The expression of the torque due to the interaction between the stator currents and the magnetic field is also introduced in this section.

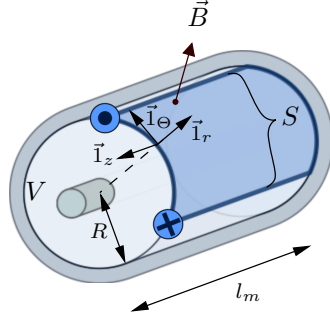


Figure 2.3: Illustration of a surface on the cylinder defined at radius R and on the machine length l_m ; and illustration of the magnetic field vector crossing this surface at one point.

2.3.1 Function of the radial air-gap magnetic-field

The definition of the magnetic flux flowing through a surface S is:

$$\phi(S) \triangleq \int_S \vec{B} \cdot d\vec{S} \quad (2.1)$$

The flux linked by a conductor winding is related to the magnetic field flowing through the surface defined by this winding. Assume a cylindrical shaped machine and assume that the different windings are located at the average radius R . The surface S is then located at this radius R , as illustrated in Figure 2.3. As a consequence, the normal vector $d\vec{S}$ is oriented along the radial unitary vector $\vec{1}_r$ such that only the radial component of \vec{B} remains: $B_r = \vec{B} \cdot \vec{1}_r$. Neglecting the axial component of the magnetic field, i.e. $\vec{B} \cdot \vec{1}_z = 0$, the magnetic field is constant along the axial axis z . The value of the magnetic B-field along S then only depends on the physical angle Θ . Since every pole-pair repeats the same electromagnetic phenomena, the magnetic B-field can be modelled as a function of the electrical angle θ as follows:

$$B(\theta) \triangleq B_r|_{S,(\theta)} \Rightarrow \frac{l_m R}{P} B(\theta) d\theta = \vec{B} \cdot d\vec{S} \quad (2.2)$$

where $B(\theta)$ is the radial magnetic B-field B_r crossing the surface S at the electrical angle θ . The flux (2.1) is computed along a physical angle Θ , thus replacing $d\Theta$ by $d\theta$ in (2.2) requires the division by P . This function is illustrated in Figure 2.4 assuming an ideal fundamental sinusoidal variation of the B-field along θ .

The Gauss's law, also called *flux conservation* law, states that the flux computed on the closed surface δV of a volume V is zero: $\phi(\delta V) = 0$. This implies that the flux flowing through the whole cylindrical surface at the radius R is zero. Since the same condition is observed along a single-pole-pair, it states:

$$\oint B(\theta) d\theta = 0 \quad (2.3)$$

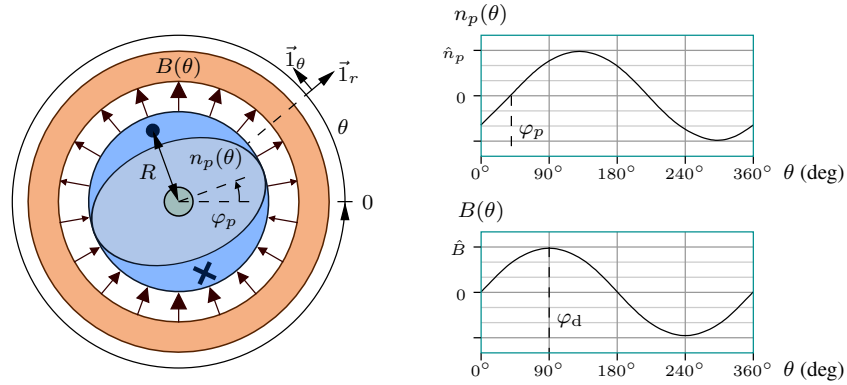


Figure 2.4: Illustration of the functions describing the conductor distribution of the coil p and the magnetic B -field in the equivalent single-pole-pair cross-section.

This is the first condition of the machine model, where it is assumed that the magnetic field has no axial component, thus no edge leakage. This assumption is made in many publications, such as [32, 33].

2.3.2 Function of the conductor distribution

The conductors of each stator coil numbered by p are approached by a distribution located at the mean radius R and described by the function $n_p(\theta)$. This is illustrated in Figure 2.4 assuming an ideal sinusoidal distribution (this is not a realistic distribution since the punctual location of the slots is not taken into account, but this is enough for the illustrations). The symbols \odot and \otimes denote the current flow signs in these conductors assuming a positive current flowing at the stator terminals of the phase, i.e. $i_p > 0$ (this is a convention). We assume that windings of each coil along the different P pole-pairs are connected in series, such as illustrated in Figure 2.2. In that case, $n_p(\theta)$ is defined as the number of conductors at every location θ along one single-pole-pair. The case where windings are connected in parallel requires some slight adaptations of the relations, adding a factor P . This is not done here.

In most of the machines, it can be assumed that the conductors are wound by pairs, such that the integral of $n_p(\theta)$ along the single-pole-pair is equal to zero:

$$\oint n_p(\theta) d\theta = 0 \quad \forall p \quad (2.4)$$

This is the second condition of the machine model. Note that the conditions (2.4) and (2.3) are not equivalent and both required for the modelling.

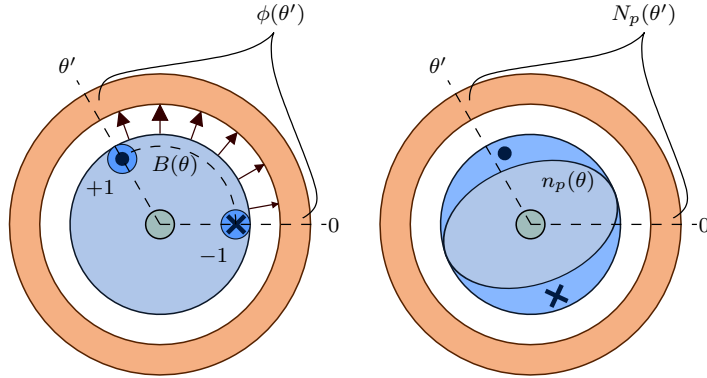


Figure 2.5: Illustration of the unitary magnetic flux and the linking distribution in the equivalent single-pole-pair cross-section.

2.3.3 Relation between the flux linked by a coil and the magnetic field

The magnetic flux linked by a coil is defined as the sum of the contribution of the magnetic fluxes linked by all the windings composing the coil. In order to propose a mathematical development of the magnetic flux, let us firstly introduce to the *unitary* magnetic flux. The unitary magnetic flux is defined as the flux linked by an *unitary* winding. As illustrated in Figure 2.5, the unitary winding is defined by one conductor located at a variable position θ' paired with a virtual return conductor located at the origin $\theta = 0$. This virtual conductor is not involved in the flux linked by the whole coil and its location is arbitrary (but fixed). This is justified as follows: summing the contributions of all unitary windings, thanks to (2.4), the total contribution of the virtual conductors on $n_p(\theta = 0)$ is zero. We define the unitary magnetic flux $\phi(\theta')$ as the flux linked by an unitary winding as follows:

$$\phi(\theta') \triangleq l_m \frac{R}{P} \int_0^{\theta'} B(\theta) d\theta \quad (2.5)$$

where l_m is the length of the machine, R is the radius of the winding locations. This definition is chosen such that the unitary flux is positive if the conductor of the unitary winding located at θ' is counted positive. Note again that (2.5) neglects the axial magnetic field flowing through the machine edges. The total magnetic flux ψ_p linked by the whole winding distribution of the coil p is then the integral of the elementary fluxes $\phi(\theta')$ multiplied by the number $n(\theta')$ at every location θ' , multiplied by the pole-pair number P :

$$\psi_p \triangleq P \oint n_p(\theta') \phi(\theta') d\theta' \quad (2.6)$$

Replacing the unitary winding by its expression (2.5), (2.6) yields:

$$\psi_p = l_m R \oint_{\theta'} \int_{\theta=0}^{\theta'} n_p(\theta') B(\theta) d\theta d\theta' \quad (2.7)$$

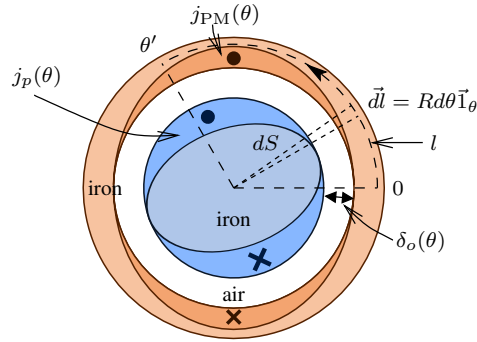


Figure 2.6: Illustration of the slice S in the equivalent single-pole-pair cross-section, where $j_p(\theta)$ is the contribution from the current flowing in the phase p and $j_{PM}(\theta)$ is the equivalent contribution from the permanent-magnets to the current density $j(\theta)$.

Inverting the successive order of integration yields:

$$\psi_p = l_m R \oint_{\theta} \left(- \int_{\theta'=0}^{\theta} n_p(\theta') d\theta' \right) B(\theta) d\theta \quad (2.8)$$

This expression can be shortened if we introduce the *linking distribution* $N_p(\theta)$ as the following integral of the distribution $n_p(\theta')$ between $\theta' = 0$ and θ :

$$N_p(\theta) - N_p(0) \triangleq - \int_0^{\theta} n_p(\theta') d\theta' \quad (2.9)$$

As illustrated in Figure 2.5. This distribution is defined within an arbitrary constant $N_p(0)$, but due to the property (2.3), this constant is removed in (2.8) and it yields:

$$\psi_p = l_m R \oint N_p(\theta) B(\theta) d\theta \quad (2.10)$$

We obtain here a quite simple expression linking the magnetic flux to the magnetic field multiplied by the linking distribution and integrated on a single-pole-pair revolution.

2.3.4 Relation between the magnetic field and the magnetomotive forces

The integral form of the Ampère's circuital law states that:

$$\oint_l \vec{H} \cdot d\vec{l} = \int_S \vec{j} \cdot d\vec{S} \quad (2.11)$$

where l is the contour of an arbitrary surface S , \vec{j} is the vector of the current density and \vec{H} is the vector of the magnetic H -field. These vectors should not be confused with the space vectors that are further used in this chapter. As illustrated

in Figure 2.6, we define the surface S in a slice between the angle $\theta = 0$ and θ' . Since the currents in the machine flow perpendicularly to the surface S and assuming that $j(\theta)$ models the current density included in an elementary slice $d\theta$, it yields:

$$\vec{j} \cdot d\vec{S} = j(\theta)d\theta \quad (2.12)$$

We introduce the magnetomotive force distribution $F(\theta')$, defined in this work from the right member integral of the Ampère's law (2.11) computed on the slice S :

$$F(\theta') - F(0) \triangleq - \int_0^{\theta'} j(\theta)d\theta \quad (2.13)$$

It is defined within an arbitrary constant.

Note that this definition of the magnetomotive force is not conventional: it is generally defined from the left member of the Ampère's law (2.11), i.e. as the integral of \vec{H} [19, 27]. This definition is however not convenient in our developments, justifying this small adaptation. For information, this value is called *current density distribution* by [34].

The left member of the Ampère's law is developed here below firstly in the case of an unsaturated iron (infinite permeability of the iron) and in the case of a saturated iron (local diminutions of the permeability).

Unsaturated case

The path l is partly located in the iron of the stator and the rotor, partly located in the air, crossing radially the air-gap by two angles $\theta = 0$ and $\theta = \theta'$. In the air, the magnetic B -field is linked to the magnetic H -field by a permeability constant $\mu_o = 4\pi 10^{-7} N/A^2$:

$$\vec{B} = \mu_o \vec{H} \quad (2.14)$$

In a ferromagnetic medium, such as the iron, the magnetic H -field interacts with the magnetic dipoles of the medium, producing an auxiliary magnetic field. It is said that the medium is *magnetized*. This magnetization can be modeled using a correction factor μ_r , called the *relative permeability*: $\vec{B} = \mu_r \mu_o \vec{H}$ [35]. The left member of the Ampère's law (2.11) can therefore be separated in two integrals, one path inside the air-gap and another path inside the iron:

$$\oint_l \vec{H} \cdot d\vec{l} = \int_{l_{\text{air}}} \frac{\vec{B}}{\mu_o} \cdot d\vec{l} + \int_{l_{\text{iron}}} \frac{\vec{B}}{\mu_r \mu_o} \cdot d\vec{l} \quad (2.15)$$

This relative permeability μ_r is very variable depending on the iron composition and on the magnetic H -field intensity, but it is generally be assumed to be much higher than the unity: $\mu_r \gg 1$ [36]. Assuming that the value of the magnetic B -field is not much increased in the iron compared to its value in the air (thank to the flux conservation principle), the integral in the iron of (2.15) can be neglected:

$$\oint_l \vec{H} \cdot d\vec{l} \approx \int_{l_{\text{air}}} \frac{\vec{B}}{\mu_o} \cdot d\vec{l} = \int_{\delta_o(0)} \frac{\vec{B}}{\mu_o} \cdot d\vec{l} - \int_{\delta_o(\theta)} \frac{\vec{B}}{\mu_o} \cdot d\vec{l} \quad (2.16)$$

where $\delta_o(\theta)$ is the radial air-gap length at the angle θ . If the rotor presents saliences or teeth, the air-gap length $\delta_o(\theta)$ then varies also with the rotor position oriented by φ_d (the exact location of this angle is further discussed), and we can mention it writing $\delta_o(\theta, \varphi_d)$. Let us define $\tilde{B}(\theta)$ as the mean of the radial component of the B -field crossing the air-gap:

$$\delta_o(\theta, \varphi_d) \tilde{B}(\theta) \triangleq \int_{\delta_o(\theta)} \vec{B} \cdot d\vec{l} \quad (2.17)$$

Combining these results (2.17) and (2.16) with the magnetomotive force (2.13) yields:

$$\tilde{B}(\theta) = \frac{\mu_o F(\theta)}{\delta_o(\theta, \varphi_d)} \quad (2.18)$$

The issue of the arbitrary constant $F(0)$ in (2.13) can be neglected in (2.18). This is justified in the next page.

The impact of the stator slots transposed in an equivalent enlarge air-gap length $\delta_o(\theta)$ is referred to as the *slotting effect* in the literature. This is largely addressed in many publications, such as [32, 33, 37, 38].

Saturated case

If a significant magnetic field is however flowing in the iron, the iron magnetization reaches its saturation level resulting in a reduction of its relative permeability. In that case, we proposed in [39] to transpose the saturation in an equivalent local increase of the air-gap length $\delta_1(\theta, F, \varphi_d)$ as a function of the global magnetomotive force F , referred to as the *magnetic state* of the machine. Note that “global” means here that the value of δ_1 at the position θ is related to the value of F everywhere, an not only at θ . The total length at the angle θ is then:

$$\delta(\theta, F, \varphi_d) \triangleq \delta_o(\theta, \varphi_d) + \delta_1(\theta, F, \varphi_d) \quad (2.19)$$

where we keep the mention to the rotor position φ_d , and it yields:

$$\tilde{B}(\theta) = \frac{\mu_o F(\theta)}{\delta(\theta, F, \varphi_d)} \quad (2.20)$$

The saturation does not occur equally everywhere in the iron. In some machines, this saturation mainly occurs around the stator teeth separating the winding slots, since these teeth concentrate the magnetic field in smaller sections, increasing locally the magnetic field density [40, 41]. In that case, we assumed in [39] that the saturation is a local phenomenon, such that it can be transposed as a local function of $F(\theta)$, i.e.: $\delta(\theta, F, \varphi_d) = \delta(\theta, F(\theta), \varphi_d)$. This does however not correctly models saturations occurring more deeply than the winding slots in the stator iron neither saturations occurring in the rotor iron.

Constant magnetomotive force

In order to satisfy the flux conservation law (2.3), it is required that $F(\theta)/\delta(\theta)$ does not have any constant component. Since $F(\theta)$ is defined within an arbitrary constant, this condition can simply be added to its definition. Let us write $F_0 + F'(\theta) := F(\theta)$, where F_0 is the constant component and $\oint F'(\theta)d\theta = 0$. It can be shown that the flux conservation law on (2.20) yields:

$$F_0 = - \oint \frac{F'(\theta)}{\delta(\theta, F, \varphi_d)} d\theta \bigg/ \oint \frac{1}{\delta(\theta, F, \varphi_d)} d\theta \quad (2.21)$$

More details can be found in [24]. In practice however, F_0 is not required since it is removed in the computation of the flux linked by the phase windings (2.10).

Leakage factor

If the stator conductor windings are close the air-gap surface (no deep slots), if the air-gap length is small compared to the radius and if the iron is not saturating, it can be assumed that the magnetic B -field in the air-gap is purely radial and of constant value crossing the air-gap path. As a consequence, the mean value of the field $\tilde{B}(\theta)$ is assumed equal to the field crossing radially the stator winding surface $B(\theta)$ [36]. It is however a strong approximation that neglects the azimuthal components of the magnetic field flowing in the air-gap and flowing around the conductors, between the stator teeth. These azimuthal components take part to the so-called *leakage* field. This leakage field is related to the air-gap length δ_o , thus it is a function of the rotor position φ_d in case of saliency, and it is a function of the saturation level linked to the magnetic state F . In order to take the leakage into account, some authors introduce a leakage factor $\kappa(\theta, F, \varphi_d)$ [36], whose inverse κ^{-1} is also referred to as the *Carter's factor* [19, 42, 37]:

$$\tilde{B}(\theta) = \kappa(\theta, F, \varphi_d)B(\theta) \quad (2.22)$$

Thus (2.20) yields:

$$B(\theta) = \frac{\mu_o F(\theta)}{\kappa(\theta, F, \varphi_d)\delta(\theta, F, \varphi_d)} \quad (2.23)$$

A detailed development of κ in the specific case of unsaturated machine with constant air-gap length and sinusoidal magnetic fields (no harmonics) can be found in chapter 4.7. of [36]. Note that κ can be very different regarding the permanent-magnet contribution, whose the major part of the field crosses the air-gap, and regarding the stator current contribution, whose part of the field jumps between the teeth. By definition, this factor κ models azimuthal phenomenons and cannot therefore be restricted to a local relationship occurring only at θ . Note also that they are other sources of leakage, due to rotor skewing effects and to the conductor loop at the edges of the machine for instance [26].

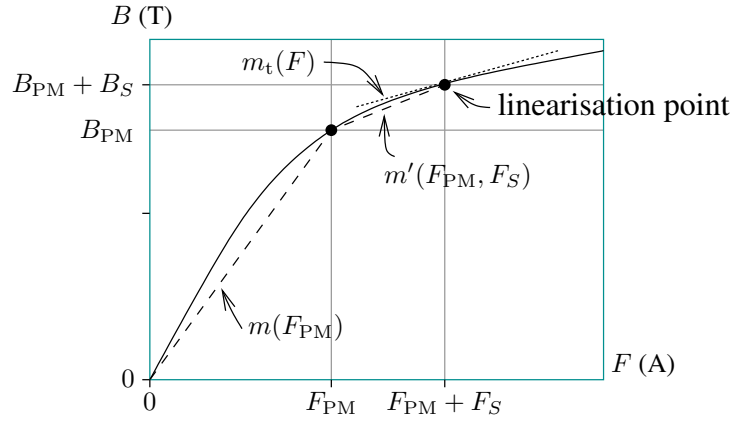


Figure 2.7: Illustration of the nonlinear relation between the magnetic B-field B and the magnetomotive force F .

Final relation

For convenience, let us shorten the relation (2.23) introducing a factor $m(\theta, F, \varphi_d)$ as follows:

$$m(\theta, F, \varphi_d) \triangleq \frac{\mu_0}{\kappa(\theta, F, \varphi_d)\delta(\theta, F, \varphi_d)} \Rightarrow \boxed{B(\theta) = m(\theta, F, \varphi_d)F(\theta)} \quad (2.24)$$

Note that this expression is very general and gives no indication about the modelling of κ nor δ included in m . This modelling requires further investigations and strongly depends on the machine design. The magnetic analysis of a surface-mounted PMSM design is proposed by [43]. It proposes a magnetic circuit model in order to compute the optimal torque design based on a finite-element analysis. Another analysis is proposed by [44]. The case of saturation occurring mainly in the teeth of a PM machine is modelled by [41]. It is however difficult to extract a simple model corresponding to (2.24) with these analysis. A strongly simplified model of m is further proposed for the experimental BLDC motor.

2.3.5 Contributions to the magnetomotive force

The magnetomotive force $F(\theta)$ can be developed as the sum of the different current density contributions. The contribution of the permanent magnets from the rotor side can be modelled by an equivalent magnetomotive force (MMF) $F_{PM}(\theta)$, as done in [38, 43, 44]. This model is very convenient for surface-mounted PM, but should be further analyzed for interior PM [6]. The contribution from the stator coils to the magnetomotive force distribution can be modeled using the conductor distributions: $j_p(\theta) = i_p n_p(\theta)$, where i_p is the current flowing at the phase terminal p . Using the embracing distributions (2.9), it yields: $F_p(\theta) = i_p N_p(\theta)$ [27]. The

sum of the stator coil contribution is written $F_S(\theta) \triangleq \sum_p F_p(\theta)$. Neglecting any other contribution, the total is: $F(\theta) = F_{\text{PM}}(\theta) + F_S(\theta)$. If required, the possible contribution of eddy current or any other additional circuit can be modeled using their equivalent current densities. It is not done here.

Transposing directly the different contributions to the magnetomotive force in (2.23) does not model the nonlinear behaviour in an intuitive way. It is preferred to model the different contributions such as if they could be successively superimposed. As illustrated in Figure 2.6, the contribution from the permanent magnets $B_{\text{PM}}(\theta)$ is modelled as if it was the only one, leading to a certain magnetic state, and the phase current contributions $B_S(\theta)$ are superimposed to this initial magnetic state. This can be written: $B(\theta) = B_{\text{PM}}(\theta) + B_S(\theta)$, where:

$$B_{\text{PM}}(\theta) = m(\theta, F_{\text{PM}}, \varphi_d) F_{\text{PM}}(\theta) \quad (2.25a)$$

$$B_S(\theta) = m'(\theta, F_{\text{PM}}, F_S, \varphi_d) F_S(\theta) \quad (2.25b)$$

where $m'(\theta, F_{\text{PM}}, F_S, \varphi_d)$ is the m factor of the magnetomotive force $F_S(\theta)$ with respect to an initial magnetomotive force $F_{\text{PM}}(\theta)$, as illustrated in Figure 2.7.

Incremental contribution

Control and self-sensing operations also requires to have a model of small signals. Due to the nonlinearity of m , the relation between the variations of the magnetic field $dB(\theta)$ related to small variations of the magnetomotive force $dF(\theta)$ must be linearized around the magnetic operating point F illustrated in Figure 2.7 [23]. This linearized relation can be written introducing an incremental factor m_t :

$$\boxed{dB(\theta) = m_t(\theta, F_{\text{PM}}, F_S, \varphi_d) dF_S(\theta)}$$

$$\text{where } m_t(\theta, F_{\text{PM}}, F_S, \varphi_d) \triangleq \frac{\partial(m(\theta, F_{\text{PM}}, F_S, \varphi_d) F_S(\theta))}{\partial F_S} \quad (2.26)$$

Note that only the variations due to dF are assumed here, while m_t is assumed constant. In a more general consideration however, variations of m_t may also contribute to dB . This is developed in the next chapter 3.

The concept of magnetic anisotropy is directly linked to the variations of m_t along θ , as developed in section 2.4. Observe here that m_t depends on three factors: the rotor position φ_d , the contribution from the permanent-magnets F_{PM} and from the stator currents F_S . At this point, the orientation of F_{PM} is still not defined. In permanent-magnet synchronous machines, the permanent-magnets (PM) are fixed to the rotor and φ_d can then be defined as the angle of the PM axis. The equivalent MMF distribution F_{PM} of the PM varies very slowly due to temperature variations or aging of the PM, but it can generally be assumed constant. The dependencies of m_t can be therefore restricted the PM-rotor angle φ_d and to F_S : $m_t(\theta, F_S, \varphi_d)$. If F_S is negligible regarding F_{PM} , the variations of m_t are mainly function of this angle φ_d : $m_t(\theta, \varphi_d)$. This property is used in motion-self-sensing methods based on the anisotropy in order to extract the rotor position φ_d .

2.3.6 Relations between the fluxes and the magnetic contributions

In practice, we generally do not have a direct access to the magnetic B-field and to the magnetomotive force, but we have an indirect access through the linked fluxes $\psi_p = \psi_{PM,p} + \psi_{S,p}$. The expression of the permanent-magnet contribution is found combining the expressions (2.25) and (2.24) in (2.10):

$$\psi_{PM,p} = l_m R \oint m(\theta, F_{PM}, \varphi_d) N_p(\theta) F_{PM}(\theta) d\theta \quad (2.27)$$

The expression of the stator current contribution is found to be:

$$\psi_{S,p} = \sum_{p'} l_{pp'} i_p' \quad (2.28)$$

where $l_{pp'}$ are called the stator inductances:

$$l_{pp'} \triangleq l_m R \oint m'(\theta, F_{PM}, F_S, \varphi_d) N_p(\theta) N_{p'}(\theta) d\theta \quad (2.29)$$

The expression of the incremental stator current contribution is found with (2.26):

$$d\psi_{S,p} = \sum_{p'} l_{t,pp'} di_p' \quad (2.30)$$

where $l_{t,pp'}$ are the incremental inductances:

$$l_{t,pp'} \triangleq l_m R \mu_o \oint m_t(\theta, F_{PM}, F_S, \varphi_d) N_p(\theta) N_{p'}(\theta) d\theta \quad (2.31)$$

The computation of these inductances are not directly required in self-sensing operations, but they allow to understand how the nonlinearity properties and the dependencies of m_t regarding the magnetomotive forces and the rotor position are inherited by these incremental inductances $l_{t,pp'}$. In particular, $l_{t,pp'}$ vary as a function of the rotor position φ_d . This property is strongly expected in anisotropy-based self-sensing strategies.

2.3.7 Electrical torque

In this part, we focus on the torque produced by the interactions between the stator windings and the magnetic B-field, called simply the *electrical torque*. The torque linked to the interaction between the permanent magnets and the stator teeth is called the *cogging torque*. It is often considered as disturbing and it can be very significant regarding the electrical torque in some machine designs such as our experimental machine. It is addressed by [25] and numerically computed by finite-element method in [38]. It seems however that finding a simple analytic expression of this cogging torque is rather complicated. This issue is however not studied here.

The Lorentz force law states that the force \vec{f} applied on a current density \vec{j} flowing in a conductor of length l_m immersed in a magnetic B -field \vec{B} is:

$$\vec{f} = l_m \vec{j} \times \vec{B} \quad (2.32)$$

where \times denotes the vector product. The torque produced by this force with respect to the rotation axis is:

$$\vec{\tau} = R \vec{1}_r \times \vec{f} \quad (2.33)$$

Transposed in the current density distributions, the total torque T_p applied on the phase p multiplied by the number of pole-pairs P yields:

$$T_p = i_p P l_m R \oint n_p(\theta) B(\theta) d\theta \quad (2.34)$$

The total torque applied on the stator is simply the sum of the different phase contributions:

$$T = \sum_p T_p = P l_m R \sum_p i_p \oint n_p(\theta) B(\theta) d\theta \quad (2.35)$$

Note that the torque applied on the rotor is simply $-T$.

2.4 Relations using Space Vectors

Strong simplifications in the machine modelling can be found using the concept of *space vectors* in two-dimensional frames, also referred to as *two-dimensional equivalent values* or *space phasors* [10, 11, 12, 13, 1]. This concept is a very powerful tool that we propose to clarify for an arbitrary n number of phases. The *space vectors* are written in this thesis with underlined symbols: \underline{x} . They are mathematical objects defined from the combination of a set of n phase values, x_p , related to electromagnetic phenomena occurring in the n different coils of the machine, numbered as follows: $p \in [0, n - 1]$. Note that “ n ” should not be confused with the conductor distribution $n(\theta)$. These phenomenons can be the voltage applied to the winding terminals v_p , the current flowing in the windings i_p , the magnetic flux linked by the windings ψ and the time-derivative of the flux $\underline{e} = d\psi/dt$. The relation between these space vectors are directly related to the magnetic phenomenons occurring along the air-gap, such as the magnetomotive force $F(\theta)$ and the magnetic B -field $B(\theta)$, and to spatial characteristics described as functions of θ , such as the conductor distribution $n_p(\theta)$ and the air-gap length $\delta(\theta)$. They are involved in the relation through the complex coefficients of their Fourier series, written by bold symbols: $\mathbf{f}_{(k)}$ being the k^{th} rank coefficient of the function $f(\theta)$ [19]. Often, the spatial phenomenons in the machines are approached by fundamental sinusoidal functions along a revolution of θ , so that only the fundamental coefficient $\mathbf{f}_{(1)}$ is nonzero. This approximation strongly simplifies the space vector relations, but this is sometimes not satisfying for the modelling of certain machine types, such as the

experimental BLDC motor. In this chapter, we propose thus to develop relations in a very general way, considering any coefficient spectrum.

Note that the number n used in the proposed model description may differ from the mentioned number of phases in the technical description of a polyphase machine. This is typically the case for machines whose mentioned number of phases is an even value. Modelling these machines with n equal to the even number of phases only makes sense if the pairs of opposite coils are related to measurements along different locations. In practice, many six-phase machines studied for faulty tolerance methods are three-phase machines whose windings of each phase have been divided in two independent coils, such as in [45]. By consequence, these pairs of coils are indistinctly measuring the same phenomena, and the contributions of their currents to the magnetic field are simply summed. These six-phase machines should therefore be modelled using $n = 3$. Note finally that the so-called equivalent two-phase machine representation, sometimes used to refer to the space vector transformation, corresponds in fact to a model with $n = 4$ where the windings are indistinct between opposite pairs.

2.4.1 Fourier transforms

Continuous function transform

Assume that $f(\theta)$ is a continuous 2π -periodical function that models an electromagnetic phenomenon, such as the magnetic field crossing the air-gap $B(\theta)$, or a physical characteristic such as the distribution of the conductors $n_p(\theta)$, as illustrated in Figure 2.4. The complex coefficients $\mathbf{f}_{(k)}$ of the continuous Fourier series transform of this function, normalized on π and computed with a rank numbering k that is opposite to the conventional way, are [46]:

$$\mathbf{f}_{(k)} \triangleq \frac{1}{\pi} \oint f(\theta') e^{jk\theta'} d\theta' \quad (2.36)$$

The function can then be developed as a Fourier series of its complex coefficients:

$$f(\theta) = \frac{1}{2} \sum_{k=-\infty}^{\infty} \mathbf{f}_{(k)} e^{-jk\theta} \quad (2.37)$$

If $f(\theta)$ is a real function of θ , the coefficients of opposite ranks are complex conjugates of each others, and the series component of rank $(-k)$ is equal to the complex conjugate of the series component of rank (k) :

$$\mathbf{f}_{(-k)} = \mathbf{f}_{(k)}^* \quad \Rightarrow \quad \mathbf{f}_{(-k)} e^{jk\theta} = \left(\mathbf{f}_{(k)} e^{-jk\theta} \right)^* \quad (2.38)$$

By consequence, the imaginary part of these complex components are simply canceled in the sum (2.37), while the real parts are cumulated. The Fourier series can

then be rearranged as a sum of real components $f_{(k)}(\theta)$ defined as follows:

$$f_{(k)}(\theta) \triangleq \Re \left(\mathbf{f}_{(k)} e^{-jk\theta} \right) \quad (2.39a)$$

$$\Rightarrow f(\theta) = \frac{f_{(0)}}{2} + \sum_{k=1}^{\infty} f_{(k)}(\theta) \quad (2.39b)$$

The real component $f_{(0)}/2$ and is called the *constant* component and $f_{(1)}(\theta)$ is called the *fundamental* component. The components of higher ranks are simply called *harmonics* of higher ranks.

Note that if $f(\theta)$ is an even-symmetric function around an angle φ , it can be shown that its coefficients have the following form:

$$\mathbf{f}_{(k)} = \hat{f}_{(k)} e^{jk\varphi} \quad (2.40)$$

where $\hat{f}_{(k)}$ are the peak values, that can be positive or negative scalars. This is typically the case for the magnetomotive force of the permanent-magnets (PM) fixed along an angle φ_d . If $f(\theta)$ is an odd-symmetric function around an angle φ , it can be shown that its coefficients have the following form:

$$\mathbf{f}_{(k)} = j \frac{k}{|k|} \hat{f}_{(k)} e^{jk\varphi} \quad (2.41)$$

This is typically the case for the conductor windings distribution of phase coils, assuming that the conductors are symmetrically wound around an axis located at φ_p . The factor $k/|k|$ is required in order to satisfy the property (2.38).

Discrete function transform

Assume that x_p is a set of n phase values, where $p \in \{0 \dots n-1\}$, that models an electromagnetic phenomenon linked to the n phases, such as the current flowing in the coils, the voltage applied to the terminals or the flux linked by the coils. The space vectors $\underline{x}_{(k)}$ are written with underline symbols and are defined as the complex coefficients of the discrete Fourier transform of the set of values x_p , normalized on $n/2$ and computed with a rank numbering p' that is opposite to the conventional way [46]:

$$\underline{x}_{(p')} \triangleq \frac{2}{n} \sum_{p=0}^{n-1} x_p e^{jp'\varphi_p} \quad (2.42)$$

where φ_p are phase angles starting at $\theta = 0$ and shifted by $2\pi/n$ between two consecutive phases:

$$\varphi_p \triangleq 2\pi p/n \quad (2.43)$$

Observe that: $\underline{x}_{(p'+n\xi)} = \underline{x}_{(p')} \forall \xi \in \mathbb{N}$. By consequence, there are no more than n distinct space vectors. The set is found back from these space vectors by the

following expression:

$$x_p = \frac{1}{2} \sum_{p'=0}^{n-1} \underline{x}_{(p')} e^{-jp' \varphi_p} \quad (2.44)$$

If x_p is a set of real values, the space vectors of opposite ranks are complex conjugates of each others, and the series component of rank $(n - p')$ is equal to the complex conjugate of the series component of rank (p') :

$$\underline{x}_{(n-p')} = \underline{x}_{(p')}^* \Rightarrow \underline{x}_{(n-p')} e^{jp' \varphi_p} = \left(\underline{x}_{(p')} e^{-jp' \varphi_p} \right)^* \quad (2.45)$$

By consequence, the imaginary part of these complex components are simply canceled in the sum (2.44), while the real parts are cumulated. If the number of phases n is odd, the Fourier series can then be rearranged as the following sum:

$$x_o \triangleq \frac{x(0)}{2} \Rightarrow x_p = x_o + \sum_{p'=0}^{(n-1)/2} \Re \left(\underline{x}_{(p')} e^{-jp' \varphi_p} \right) \quad \text{if } n \text{ odd} \quad (2.46)$$

The coefficient x_o is called the *homopolar*. The case n even is easily deduced, but it is not studied in this thesis and it is therefore not mentioned.

2.4.2 Relation between space vectors and coefficients of the flux

Assume that the coils of the n different phases p are identical and oriented by φ_p , as previously illustrated for one phase in Figure 2.4. This excludes cases of machines having misaligned coils. On the one hand, let us introduce a virtual magnetic flux function $\psi(\varphi)$ defined as the flux linked by one coil, identical to the phase coils, but oriented following a variable angle φ . Using (2.36), it is then possible to compute coefficients ψ of this function by substituting $\theta = \varphi$. The phase fluxes are then equal to the continuous flux function at angles φ_p :

$$\psi_p = \psi(\varphi = \varphi_p) \quad (2.47)$$

The continuous function $\psi(\varphi_p)$ can be developed using its series given in (2.37). Then separating the summation on $k \in \{-\infty, \infty\}$ by two summations on $p' \in \{0, n-1\}$ and $\xi' \in \{-\infty, \infty\}$, defined such that $p' + n\xi' := k$, yields:

$$\psi_p = \frac{1}{2} \sum_{p'=0}^{n-1} \underbrace{\left(\sum_{\xi'=-\infty}^{\infty} \psi_{(p'+n\xi')} \right)}_{\underline{\psi}_{(p')}} e^{-jp' \varphi_p} \quad (2.48)$$

On the other hand, the space vectors $\underline{\psi}_{(p')}$ corresponding to the linked magnetic fluxes $\underline{\psi}_p$ is computed following (2.42). Comparing (2.48) with the development given in (2.44) as a series of space vectors $\underline{\psi}_{(p')}$, we can see that the summation

content in brackets in (2.48) corresponds to these space vectors. It is therefore found that:

$$\boxed{\underline{\psi}_{(p')} = \sum_{\xi'=-\infty}^{\infty} \psi_{(p'+n\xi')}} \quad (2.49)$$

This relation between $\underline{\psi}$ and ψ is also referred to as the Poisson summation formula. It illustrates the importance of considering the harmonic content in the magnetic flux. All the harmonic ranks of ψ are however not included by $\underline{\psi}$, but only the multiple of the phase number n . By consequence, the higher n , the higher $p' + n\xi'$, reducing the harmonic pollution by lower harmonics in $\underline{\psi}$. This property can be an interesting consideration in the selection of the number of phases in electrical machines.

In many drives and for many synchronous machines, only the fundamental $\underline{\psi}_{(1)}$ is considered and the higher harmonics are neglected such that:

$$\underline{\psi}_{(p')} \approx \psi_{(p')} \quad \text{if} \quad |\psi_{(p')}| \gg |\psi_{(p'+n\xi')}| \quad \forall \xi' \neq 0 \quad (2.50)$$

It is however an approximation that must be validated by experiments performed for every machine that we want to study.

2.4.3 Relation between the flux and the B-field

Assume that the coils of the different phases p are symmetrically wound on either side of their location φ_p . This excludes cases of machines having asymmetrical coils. The functions $n_p(\theta)$ of their conduction distribution are therefore odd-symmetric with respect to their angle φ_p and their coefficients have the form (2.41) where $\varphi = \varphi_p$. The linked winding function $N_p(\theta)$ defined in (2.9) can then be developed replacing $n_p(\theta)$ by its series (2.37). Thus, computing the integral along the angle θ' yields:

$$\begin{aligned} N_p(\theta) - N_p(\varphi_p) &\triangleq - \int_{\varphi_p}^{\theta} n_p(\theta') d\theta' = - \int_{\varphi_p}^{\theta} \left(\frac{1}{2} \sum_{k=-\infty}^{\infty} \mathbf{n}_{p,(k)} e^{-jk\theta'} \right) d\theta' \\ &= - \int_{\varphi_p}^{\theta} \left(\frac{1}{2} \sum_{k=-\infty}^{\infty} \left(j \frac{k}{|k|} \hat{n}_{(k)} e^{jk\varphi_p} \right) e^{-jk\theta'} \right) d\theta' \\ &= \frac{1}{2} \sum_{k=-\infty}^{\infty} \frac{\hat{n}_{(k)}}{|k|} e^{jk\varphi_p} \left(\int_{\varphi_p}^{\theta} -jk e^{-jk\theta'} d\theta' \right) \\ &= \frac{1}{2} \sum_{k=-\infty}^{\infty} \frac{\hat{n}_{(k)}}{|k|} \left(e^{jk(\varphi_p-\theta)} - 1 \right) \quad (2.51) \end{aligned}$$

Note that according to (2.4), there is no constant coefficient $\hat{n}_{(0)} = 0$. Highlighting harmonics and the constant component yields:

$$N_p(\theta) = \frac{1}{2} \sum_{k=-\infty}^{\infty} \underbrace{\left(\frac{\hat{n}_{(k)}}{|k|} e^{jk\varphi_p} \right)}_{N_{p,(k)}} e^{-jk\theta} + \frac{1}{2} \underbrace{\left(2N_p(\varphi_p) - \sum_{k=-\infty}^{\infty} \frac{\hat{n}_{(k)}}{|k|} \right)}_{N_{p,(0)}} \quad (2.52)$$

Except for $k = 0$, the relation between the coefficients of the the coefficients of linking distribution and the conductor distribution is:

$$\boxed{N_{p,(k)} = \frac{\hat{n}_{(k)}}{|k|} e^{jk\varphi_p}} \quad \forall k \neq 0 \quad (2.53)$$

As shown in the following equations, the magnetic flux (2.10) can then be developed replacing $N_p(\theta)$ by (2.52), where the constant component $N_{p,(0)}$ is removed. Since $N_{p,(-k)} = N_{p,(k)}^*$, the sum on k can be substituted by a sum on $-k$ and it is possible to highlight the coefficients $B_{(k)}$ of $B(\theta)$ given in (2.36). Introducing $\psi_p = \psi(\varphi_p)$ given in (2.47) and considering φ_p as a variable, the result is the series of the coefficients $\psi_{(k)}$:

$$\begin{aligned} \psi(\varphi_p) &= l_m R \oint N_p(\theta) B(\theta) d\theta = l_m R \oint \left(\frac{1}{2} \sum_{k=-\infty}^{\infty} N_{p,(k)}^* e^{jk\theta} \right) B(\theta) d\theta \\ &= l_m R \oint \left(\frac{1}{2} \sum_{k=-\infty}^{\infty} \left(\frac{\hat{n}_{(k)}}{|k|} e^{-jk\varphi_p} \right) e^{jk\theta} \right) B(\theta) d\theta \\ &= \frac{1}{2} \sum_{k=-\infty}^{\infty} \underbrace{\frac{\pi l_m R \hat{n}_{(k)}}{|k|} \left(\frac{1}{\pi} \oint B(\theta) e^{jk\theta} d\theta \right)}_{\psi_{(k)}} e^{-jk\varphi_p} \quad (2.54) \end{aligned}$$

This yields to the relation between the coefficients of the magnetic field and the coefficients of the magnetic flux:

$$\boxed{\psi_{(k)} = \frac{\pi l_m R \hat{n}_{(k)}}{|k|} B_{(k)}} \quad \forall k \neq 0 \quad (2.55)$$

This relations (2.55) teaches us that the harmonic content of the magnetic B-field flux is filtered through the harmonics of the winding distribution. By consequence, it would be incomplete and abusive to speak about machines with *sinusoidal* PM-magnetic field, such as the synchronous machines for example, or with *trapezoidal* PM-magnetic field, such as BLDC machines for example. If the conductor distributions tend toward ideal fundamental sinusoidal functions, i.e. that

$\hat{n}_{(k)} \ll \hat{n}_{(1)}$, $\forall k > 1$, then the harmonics of the field are removed from the magnetic flux: $|\psi_{(k)}| \ll |\psi_{(1)}|$, $\forall k > 1$. It is therefore not specifically required that the magnetic B-field varies as a perfect sinusoidal function, but that the harmonic spectrum of the magnetic B-field and the harmonic spectrum of the conductor distributions concurs only at $k = 1$. In the second type of machines however, significant harmonic concordances must exist elsewhere than $k = 1$, otherwise the machine model would simply correspond to a synchronous machine. This is the reason why most of BLDC motors have conductors distributed punctually in low number of slots [29, 47]. Note that [29, 6, 2, 48] speak about sinusoidal and trapezoidal back-EMF (that is the time variation of the flux), what is more adequate.

2.4.4 Relation between the B-field and the magnetomotive forces

The electromagnetic values $B(\theta)$ and $F(\theta)$ are linked by a factor $m(\theta, F)$, as given by (2.24). All these values can be represented using their coefficients \mathbf{B} , \mathbf{F} and \mathbf{m} computed following (2.36). Using the Fourier series development of $B(\theta)$ given by (2.37), and replacing the sum on k'' by a sum on k defined as $k = k' + k''$, it is found:

$$\begin{aligned} B(\theta) &= m(\theta)F(\theta) \\ &= \frac{1}{4} \sum_{k''=-\infty}^{\infty} \sum_{k'=-\infty}^{\infty} \mathbf{m}_{(k'')} \mathbf{F}_{(k')} e^{-j(k'+k'')\theta} \\ &= \frac{1}{2} \sum_{k=-\infty}^{\infty} \underbrace{\left(\frac{1}{2} \sum_{k'=-\infty}^{\infty} \mathbf{m}_{(k-k')} \mathbf{F}_{(k')} \right)}_{\mathbf{B}_{(k)}} e^{-jk\theta} \quad (2.56) \end{aligned}$$

This yields the following relation, that is also referred to as *circular convolution* [46]:

$$\boxed{\mathbf{B}_{(k)} = \frac{1}{2} \sum_{k'=-\infty}^{\infty} \mathbf{m}_{(k-k')} \mathbf{F}_{(k')}} \quad \forall k \neq 0 \quad (2.57)$$

This convolution is valid for the permanent-magnets contribution, for the stator phase current contributions as described in (2.25), and for the incremental contributions (2.26):

$$\mathbf{B}_{\text{PM},(k)} = \frac{1}{2} \sum_{k'=-\infty}^{\infty} \mathbf{m}_{(k-k')} \mathbf{F}_{\text{PM},(k')} \quad (2.58a)$$

$$\mathbf{B}_{S,(k)} = \frac{1}{2} \sum_{k'=-\infty}^{\infty} \mathbf{m}'_{(k-k')} \mathbf{F}_{s,(k')} \quad (2.58b)$$

$$d\mathbf{B}_{(k)} = \frac{1}{2} \sum_{k'=-\infty}^{\infty} \mathbf{m}_{t,(k-k')} d\mathbf{F}_{(k')} \quad (2.58c)$$

Remember that $d\mathbf{B}_{(k)}$ only models here variations due to $d\mathbf{F}_{(k')}$, while $\mathbf{m}_{t,(k-k')}$ are assumed constant. We see here that the relations between the harmonic content of the magnetomotive forces and the magnetic B-fields are not straightforward. Since the \mathbf{m} factor can be strongly nonlinear, its harmonic spectrum may change with the magnetic state of the machine. In particular, the harmonic spectra of \mathbf{m} , \mathbf{m}' and \mathbf{m}_t can be very different.

2.4.5 Contribution of the currents to the magnetomotive force

The contribution of the currents to the magnetomotive force $F_p(\theta) = i_p N_p(\theta)$ can be developed replacing $N_p(\theta)$ by (2.52). Because all coils are identical but shifted along their respective angles, the condition $N_p(\varphi_p) = N_0(\varphi_0) \forall p \in \{1 \dots n-1\}$ can be added to the linking distributions (2.9). We can then highlight the space vectors \underline{i} of the currents. It yields:

$$\begin{aligned} F_S(\theta) &= \sum_{p=0}^{n-1} i_p N_p(\theta) = \sum_{p=0}^{n-1} i_p \left(\frac{1}{2} \sum_{k=-\infty}^{\infty} \mathbf{N}_{p,(k)} e^{-jk\theta} \right) \\ &= \frac{1}{2} \sum_{k=-\infty}^{\infty} \frac{\hat{n}_{(k)}}{|k|} \frac{n}{2} \underbrace{\left(\frac{2}{n} \sum_{p=0}^{n-1} i_p e^{jk\varphi_p} \right)}_{\underline{i}_{(k)}} e^{-jk\theta} + \frac{1}{2} \mathbf{N}_{p,(0)} \frac{n}{2} \underbrace{\left(\frac{2}{n} \sum_{p=0}^{n-1} i_p \right)}_{i_{(0)}} \end{aligned} \quad (2.59)$$

$\underbrace{\hspace{10em}}_{\mathbf{F}_{S,(k)}} \qquad \qquad \qquad \underbrace{\hspace{10em}}_{\mathbf{F}(S,(0))}$

Finally, the relation between the coefficients $\mathbf{F}_{S,(k)}$ of $F_S(\theta)$ and the space vectors of the currents is:

$$\boxed{\mathbf{F}_{S,(k)} = \frac{n}{2} \frac{\hat{n}_{(k)}}{|k|} \underline{i}_{(k)}} \quad \forall k \neq 0 \quad (2.60)$$

It is also valid for incremental contributions. Here also, the harmonic content of the magnetomotive force is related to the harmonics in the conductor distributions.

2.4.6 Relation between the flux space vectors and the magnetic sources

Except for the incremental relation, the following relations are given for information, since they are not used in the self-sensing theory. Combining (2.49) with (2.55) and with (2.58a), the relation between the permanent-magnet contribution to the flux and the contribution to the magnetomotive force yields:

$$\underline{\psi}_{\text{PM},(p')} = \sum_{k'=-\infty}^{\infty} \left(\sum_{\xi'=-\infty}^{\infty} \frac{\pi l_m R \hat{n}_{(p'+n\xi')}}{2|p'+n\xi'|} \mathbf{m}_{(p'+n\xi'-k')} \right) \mathbf{F}_{\text{PM},(k')} \quad (2.61)$$

where m are the coefficient of $m(\theta, F_{PM}, \varphi_d)$. Combining (2.58b) with (2.60), the relation between the current contribution to the flux and the contribution to the magnetomotive force yields:

$$\underline{\psi}_{S,(p')} = \sum_{k'=-\infty}^{\infty} \left(\sum_{\xi'=-\infty}^{\infty} \frac{\pi l_m R \hat{n}_{(p'+n\xi')}}{2|p'+n\xi'|} \mathbf{m}'_{(p'+n\xi'-k')} \right) \frac{n \hat{n}_{(k')}}{2 |k'|} \underline{i}_{(k')} \quad (2.62)$$

where m' are the coefficient of $m'(\theta, F_{PM}, F_S, \varphi_d)$. Note also that there is no more than n different ranks to $\underline{i}_{(k)}$. Therefore, the summation on $k' \in \{-\infty, \infty\}$ can be separated by two summations on $p \in \{0, n-1\}$ and $\xi \in \{-\infty, \infty\}$, defined such that $p + n\xi := k'$, and (2.62) yields:

$$\underline{\psi}_{S,(p')} = \sum_{p=0}^{n-1} \mathbf{l}_{(p,p')} \underline{i}_{(p)} \quad (2.63)$$

where the self-inductance $\mathbf{l}_{(p,p')}$ is:

$$\mathbf{l}_{(p,p')} \triangleq \frac{n\pi l_m R}{4} \sum_{\xi', \xi=-\infty}^{\infty} \frac{\hat{n}_{(p'+n\xi')}}{|p'+n\xi'|} \frac{\hat{n}_{(p+n\xi)}}{|p+n\xi|} \mathbf{m}'_{(p'-p+n(\xi'-\xi))} \quad (2.64)$$

In a similar way, the relation between the incremental current contribution to the flux and the contribution to the magnetomotive force can be found using (2.58c) and yields:

$$d\underline{\psi}_{S,(p')} = \sum_{p=0}^{n-1} \mathbf{l}_{t,(p,p')} d\underline{i}_{(p)} \quad (2.65)$$

incremental self-inductance $\mathbf{l}_{t,(p,p')}$ is:

$$\mathbf{l}_{t,(p,p')} \triangleq \frac{n\pi l_m R}{4} \sum_{\xi', \xi=-\infty}^{\infty} \frac{\hat{n}_{(p'+n\xi')}}{|p'+n\xi'|} \frac{\hat{n}_{(p+n\xi)}}{|p+n\xi|} \mathbf{m}_{t,(p'-p+n(\xi'-\xi))} \quad (2.66)$$

and where m_t are the coefficient of $m_t(\theta, F_{PM}, F_S, \varphi_d)$.

The factors m_t are complex values whose properties regarding the saturation are inherited by the incremental inductances $\mathbf{l}_{t,(p,p')}$. Their complex form result in an orientation shift between the incremental currents and the incremental fluxes. This shift defines the orientation of the anisotropy. This is developed specifically for three-phase machine in the next section.

2.4.7 Electrical torque

The expression of the total torque (2.34) applied on the stator can be developed replacing the conductor distribution $n_p(\theta)$ by its Fourier series (2.37) in (2.34),

where the coefficients are given by (2.41). Combined with (2.55), it yields:

$$\begin{aligned}
T &= Pl_m R \sum_{p=0}^{n-1} i_p \oint n_p(\theta) B(\theta) d\theta \\
&= Pl_m R \sum_{p=0}^{n-1} i_p \oint \left(\frac{1}{2} \sum_{k=-\infty}^{\infty} j \frac{k}{|k|} \hat{n}_{(k)} e^{jk(\varphi_p - \theta')} \right) B(\theta) d\theta \\
&= \frac{nP}{4} \sum_{k=-\infty}^{\infty} jk \underbrace{\left(\frac{2}{n} \sum_{p=0}^{n-1} i_p e^{jk\varphi_p} \right)}_{\underline{i}_{(k)}} \underbrace{\left(\frac{\pi l_m R \hat{n}_{(k)}}{|k|} \left(\frac{1}{\pi} \oint B(\theta) e^{-jk\theta'} d\theta \right) \right)}_{\psi_{(-k)}} \\
&= \frac{nP}{4} \sum_{k=-\infty}^{\infty} k \left(j \underline{i}_{(k)} \psi_{(-k)} \right) = \frac{nP}{2} \sum_{k=1}^{\infty} k \Im \left(\underline{i}_{(k)}^* \psi_{(k)} \right) \quad (2.67)
\end{aligned}$$

Note that $\underline{i}_{(k)}$ have no more than n distinct values on k , and the summation on $k \in \{1, \infty\}$ can be separated by two summations on $p \in \{0, n-1\}$ and $\xi \in \{0, \infty\}$, defined such that $p + n\xi := k$:

$$T = \frac{nP}{2} \sum_{p=0}^{n-1} \Im \left(\underline{i}_{(p)}^* \sum_{\xi=0}^{\infty} (p + n\xi) \psi_{(p+n\xi)} \right) \quad (2.68)$$

We see here that the torque can be affected by the harmonic content in the magnetic flux. If the higher harmonics are neglected, using (2.50), we obtain the traditional expression of the torque for the vector control:

$$T = \frac{nP}{2} \Im \left(\underline{i}_{(1)}^* \psi_{(1)} \right) \quad \text{if } |\psi_{(k)}| \ll |\psi_{(1)}| \quad \forall k \neq 1 \quad (2.69)$$

This approximation is largely assumed in the control of synchronous machines. It is found from experimental measurements that this approximation can be valid in the case of the experimental BLDC motor, even if the magnetic field contains a significant spectra of harmonics. This expression (2.69) introduces the importance of the rotor position φ_d : $\psi_{PM,(1)}$ is part of $\psi_{(1)}$ and its angle is related to φ_d . By consequence, a good knowledge of the rotor position is required in order to handle $\underline{i}_{(1)}$ to a value leading to an optimal torque production. Note that (2.69) also neglects the contribution of the interaction between the homopolar current and the third harmonic of the flux addressed by [49, 50], that are not necessarily null. This is exploited by [51] in order to increase the maximum torque.

Note that we addressed the torque applied on the stator. The torque applied on the rotor is $-T$.

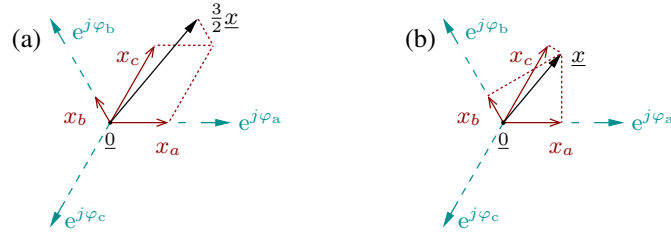


Figure 2.8: Illustration of (a) the geometrical construction of a space vector \underline{x} from the phase values x_a , x_b and x_c ; (b) and the recovering of the phase values from the space vector, assuming $x_o = 0$, corresponding to the projections of \underline{x} along the phase axes.

2.5 Three-Phase Machines

Most of the polyphase machines used in high power applications, such as vehicle traction or power productions, have three phases: $n = 3$. This choice is historical and linked to the connection with the three-phase network grid. It has benefits in the power transportation, minimizing the cost and the losses in cables and in power electronics compared to other number of phases. This number should however be reassess in the light of robust control aspects, but it is not done in this work.

2.5.1 Space vector computations

The phases are numbered $p \in \{a, b, c\}$ for the specific case of $n = 3$ in this document. Note that many other numbering are found in the literature and the technical documents. Using (2.42), the *homopolar* value $x_o \triangleq x_{(0)}/2$ is:

$$x_o \triangleq \frac{1}{3} \sum_{p=a,b,c} x_p \quad (2.70)$$

Since $\underline{x}_{(2)} = \underline{x}_{(1)}^*$, there is only one distinct space vector $\underline{x}_{(1)}$ in addition to the homopolar. It is simply referred to as *space vector* and is written \underline{x} :

$$\underline{x} \triangleq \frac{2}{3} \sum_{p=a,b,c} x_p e^{j\varphi_p} \quad (2.71)$$

Its geometrical construction is illustrated in Figure 2.8(a). The phase values are found back using (2.46):

$$x_p = x_o + \Re(\underline{x} e^{-j\varphi_p}) \quad (2.72)$$

It is illustrated in Figure 2.8(b).

These computations are valid for any type of connections between the coils, except the fact that the voltages or the currents at the machine terminals are not necessarily equal to v_p and i_p . In a star-connection, i_p is well the current flowing

through the terminals. The voltage at the machine terminals v'_p are however equal to the voltage v_p at the coil terminals plus the voltage of the neutral point v_n : $v'_p = v_p + v_n$. Since this v_n is equal for all the phases, it disappears in the space vector computation (2.71). This voltage v_n should however not be confused with the homopolar v_o , since v_o may also contain other internal voltages contributions in addition to v_n . This is specifically true in case of harmonics in the machine. Without neutral connection, the homopolar current is null: $i_o = 0$. Note that the voltage of the neutral point v_n is also sometimes called the *zero-sequence*. In a delta-connection, v_p is the difference between the voltage v'_p of two consecutive machine terminals: for example $v_a = v'_a - v'_b$. The current i'_p at the machine terminal is divided in the two connected phases: for example $i'_a = i'_a + i'_c$. This must be taken into account in the space vector transformation. Note that the homopolar voltage v_o is not necessarily null due to the back-EMF, whose mean on all the phases is not strictly null in case of harmonics. The homopolar current i_o is then the current flowing in the delta-loop, also sometimes called the *zero-sequence* current.

2.5.2 The incremental self-inductances

The restriction to the case of three-phase machine results in strong simplifications of the relation between the currents and the magnetic flux. Here, we focus on the incremental relation that is used in anisotropy-based self-sensing methods. The incremental relation (2.65) linking the fundamental space vectors $p' = 1$ yields:

$$d\underline{\psi}_S = 2\mathbf{l}_{t,(0,1)}d\underline{i}_o + \mathbf{l}_{t,(1,1)}d\underline{i} + \mathbf{l}_{t,(2,1)}d\underline{i}^* \quad (2.73)$$

where the different incremental self-inductances are:

$$\mathbf{l}_{t,(p,1)} = \frac{3\pi l_m R}{4} \sum_{\xi', \xi = -\infty}^{\infty} \frac{\hat{n}_{(1+3\xi')}}{|1+3\xi'|} \frac{\hat{n}_{(p+3\xi)}}{|p+3\xi|} \mathbf{m}_{t,(1-p+3(\xi'-\xi))} \quad (2.74)$$

In order to further simplify the relation, assume either that $\mathbf{l}_{t,(0,1)} = 0$ (i.e. $\hat{n}_{(3\xi')} \forall \xi'$), or that there is no homopolar connection $\underline{i}_o = 0$. Both conditions are met in the case of our experimental motor. By consequence, (2.74) becomes:

$$\boxed{d\underline{\psi}_S = \mathbf{l}_{t,(1,1)}d\underline{i} + \mathbf{l}_{t,(2,1)}d\underline{i}^*} \quad (2.75)$$

Remember that $d\underline{\psi}_S$ only models small variations due to $d\underline{i}$, while $\mathbf{l}_{t,(1,1)}$ and $\mathbf{l}_{t,(2,1)}$ are assumed constant.

Following the same steps, the relation (2.63) yields a similar result for the current contribution. Assuming either that $\mathbf{l}_{(0,1)} = 0$ or that $\underline{i}_o = 0$, it is found:

$$\underline{\psi}_S = \mathbf{l}_{(1,1)}\underline{i} + \mathbf{l}_{(2,1)}\underline{i}^* \quad (2.76)$$

This last relation is fundamental for the rotation-drive operations, controlling steady-state values \underline{i} , but it is not considered in anisotropy-based self-sensing operations.

2.5.3 The harmonic incremental self-inductances

The incremental self-inductances are affected by the harmonic spectrum of $m_t(\theta)$. In order to highlight the harmonic relation, let us define the following inductances linked to the k^{th} rank of $\mathbf{m}_{t,(k)}$:

$$\mathbf{l}_{t,(k)} \triangleq \frac{3\pi l_m R}{4} \sum_{\xi'=-\infty}^{\infty} \frac{\hat{n}_{(1+3\xi')}}{|1+3\xi'|} \frac{\hat{n}_{(1+3\xi'-k)}}{|1+3\xi'-k|} \mathbf{m}_{t,(k)} \quad (2.77)$$

Since $m_t(\theta)$ is a real function: $\mathbf{m}_{t,(-k)} = \mathbf{m}_{t,(k)}^*$. Applying a shift on ξ' , it can also be shown that the sum in (2.77) is symmetrical. By consequence, we have the following property:

$$\mathbf{l}_{t,(-k)} = \mathbf{l}_{t,(k)}^* \quad (2.78)$$

Introducing $\xi'' = \xi - \xi'$ and $k := 1 - p + 3\xi''$, (2.74) can be written as a developments of these harmonics:

$$\boxed{\mathbf{l}_{t,(p,1)} = \sum_{k=1-p+3\xi'', \forall \xi''} \mathbf{l}_{t,(k)}} \quad (2.79)$$

Using the property (2.78), it can be shown that $\mathbf{l}_{t,(1,1)}$ is strictly real. This property is important in the definition of the anisotropy.

2.5.4 The anisotropy definition

The concept of anisotropy is based on the shift between the space vectors of the currents and the fluxes. This shift is directly linked to the complex form of the incremental self-inductance $\mathbf{l}_{t,(2,1)}$, while $\mathbf{l}_{t,(1,1)}$ is strictly real. At this point, we propose to introduce some new parameters that correspond to the formalisms met in the literature in case of anisotropy. Let us therefore define the *positive* $l_{t,+}$ and *negative* $l_{t,-}$ incremental self-inductance, and the *anisotropy angle* φ_x respectively as follows:

$$\left\{ \begin{array}{l} l_{t+} \triangleq \mathbf{l}_{t,(1,1)} \in \Re \\ l_{t-} \triangleq \mathbf{l}_{t,(2,1)} \Rightarrow \left\{ \begin{array}{l} l_{t-} = |\mathbf{l}_{t-}| \\ \varphi_x \triangleq \angle(\mathbf{l}_{t-})/2 \end{array} \right. \end{array} \right. \quad (2.80)$$

where \angle denotes the complex argument. The positive and negative incremental self-inductances are sometimes referred to as average and difference inductances respectively [52], but this denomination is confusion with concepts further used in signal processing. Thus replacing the inductances in the relation (2.75) by (2.80), we have:

$$\boxed{d\underline{\psi}_S = l_{t+} d\underline{i} + \mathbf{l}_{t-} d\underline{i}^* = l_{t+} d\underline{i} + l_{t-} d\underline{i}^* e^{j2\varphi_x}} \quad (2.81)$$

This relation is illustrated in Figure 2.9. For convenience, (2.81) is also further written in short using a complex factor \mathbf{l}_t that is function of $d\underline{i}$ (that should not be confused with the coefficients of the Fourier series):

$$d\underline{\psi}_S = \mathbf{l}_t d\underline{i} \quad \text{where} \quad \boxed{\mathbf{l}_t \triangleq l_{t+} + l_{t-} e^{j2(\varphi_x - \angle d\underline{i})}} \quad (2.82)$$

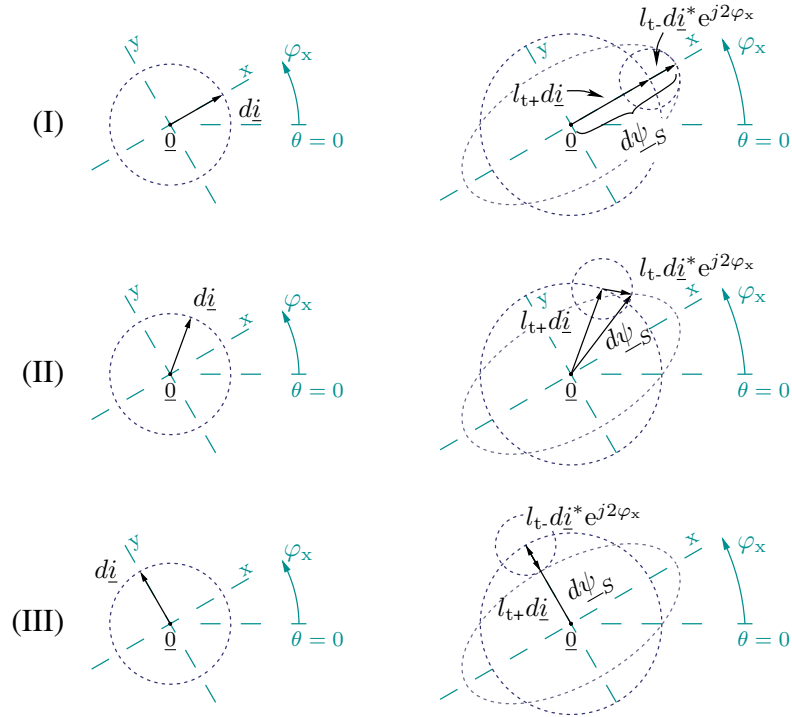


Figure 2.9: Illustration of $d\psi_S$ represented as the sum of the positive and the negative contributions, for different orientations of d_i (I), (II) and (III). The blue dashed lines represent the path drawn by the different contributions when d_i rotates.

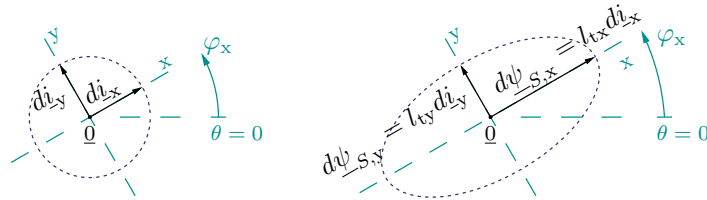


Figure 2.10: Illustration of the relation between $d\psi_S$ and d_i along the x-axis of the maximum self-inductance and along the y-axis of the minimum self-inductance.

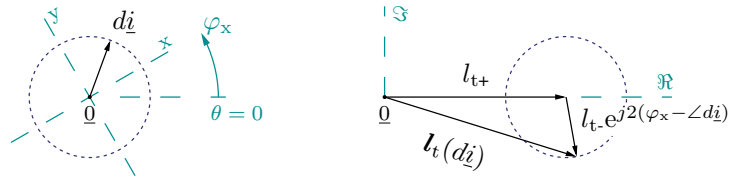


Figure 2.11: Illustration of $l_t(d_i)$ as defined in (2.82) in a complex frame, for an arbitrary orientation of d_i . The blue dashed lines represent the path drawn by the self-inductance when d_i rotates.

where $\angle d\underline{i}$ is the complex argument of $d\underline{i}$ and thus where $d\underline{i}^* = d\underline{i}e^{-j2\angle d\underline{i}}$. This new factor is illustrated in Figure 2.11.

It is possible to define an *anisotropy frame* made of two axes denoted x and y, illustrated in Figure 2.10, such that the x-axis is oriented by an angle φ_x with respect to $\theta = 0$. It is shown that the relation (2.81) is real along the axes of the anisotropy xy-frame and yields:

$$\begin{pmatrix} d\underline{\psi}_{S,x} \\ d\underline{\psi}_{S,y} \end{pmatrix} = \begin{pmatrix} l_{tx} & 0 \\ 0 & l_{ty} \end{pmatrix} \begin{pmatrix} d\underline{i}_x \\ d\underline{i}_y \end{pmatrix} \quad (2.83)$$

where the inductances l_{tx} and l_{ty} are:

$$l_{tx} = l_{t+} + l_{t-} \quad \& \quad l_{ty} = l_{t+} - l_{t-} \quad (2.84)$$

such that $l_{tx} > l_{ty}$. Note that the anisotropy xy-frame is here not defined by the rotor angle φ_d . The link with the rotor position is introduced after.

Following the same steps, the relation (2.76) yields a similar result for the current contribution. Transposing (2.80) with $\mathbf{l}_{(1,1)}$ and $\mathbf{l}_{(2,1)}$ yields:

$$\underline{\psi}_S = l_+ \underline{i} + \mathbf{l}_- \underline{i}^* = l_+ \underline{i} + l_- \underline{i}^* e^{j2\varphi_{x'}} \quad (2.85)$$

where the anisotropy angles may differ: $\varphi_{x'} \neq \varphi_x$. Again, this last relation is fundamental for the rotation-drive operations. It is not considered in anisotropy-based self-sensing operations, but we however introduce this relation since it appears in the electromagnetic relations, and it is required to discuss the fact that it can be neglected. This is done in chapter 5.

2.5.5 Impact of the harmonics on the anisotropy

We define the synchronous qd-frame made of two axes denoted q and d such that the d-axis is oriented along the permanent-magnets by an angle φ_d . The q-axis is defined here in back-quadrature with respect to the d-axis. From the perspective of anisotropy-based self-sensing, an ideal situation is met if the anisotropy xy-frame is aligned with the synchronous qd-frame. In that case, the estimation of the rotor position is directly obtained from the identification of the anisotropy orientation. Harmonics in the machine however lead to significant misalignments between these two frames, as explained here.

Assume that contribution of the stator currents F_S to the magnetic state is negligible regarding the contribution of the permanent-magnets, such that m_t is only function of F_{PM} oriented by φ_d . As a consequence, $m_t(\theta, F_{PM}, \varphi_d)$ is even symmetric along θ with respect to the angle φ_d and the coefficients $\mathbf{m}_{t,(k)}$ have the form (2.40). This form is inherited by $\mathbf{l}_{t,(k)}$ defined in (2.77):

$$\mathbf{m}_{t,(k)} = \hat{m}_{t,(k)} e^{jk\varphi_d} \quad \Rightarrow \quad \mathbf{l}_{t,(k)} = \hat{l}_{t,(k)} e^{jk\varphi_d} \quad (2.86)$$

Note that the peak values can be positive or negative. Combining (2.79) with the positive and negative incremental self-inductances defined in (2.80) yields:

$$l_{t+} = l_{t,(0)} + \sum_k 2\hat{l}_{t,(k)} \cos(k\varphi_d) \quad | \quad k = 3\xi \quad \forall \xi \in \mathbb{N} > 1 \quad (2.87a)$$

$$l_{t-} = l_{t-} e^{j2\varphi_x} = \sum_k \hat{l}_{t,(k)} e^{jk\varphi_d} \quad | \quad k = 2 + 3\xi \quad \forall \xi \in \mathbb{N} \quad (2.87b)$$

The positive inductance l_{t+} only contains harmonic ranks multiple of 3 and l_{t-} only contains harmonics of ranks 2 plus a multiple of 3. They are sometimes referred to as *multiple* saliencies [53, 23] and the rank $k = -2$ is sometimes referred to as *secondary* saliency [54, 55, 56]. If $l_{t,(k)} = 0$ except in $k \in \{0, 2\}$, then from (2.87b) it is shown that:

$$\varphi_x = \varphi_d \quad \text{if} \quad l_{t,(k)} = 0 \quad \forall k \notin \{0, 2\} \quad (2.88)$$

This situation corresponds to the ideal situation for self-sensing operations since the angle φ_x is directly equal to the rotor position. In qd values, it results generally that $l_{tx} = l_{tq}$ and $l_{ty} = l_{td}$, or inversely in some machine designs [57]. Otherwise, φ_x oscillate around φ_d during the rotation. This is clearly observed in our experimental motor.

2.5.6 Impact of the currents on the anisotropy

The value $m_t(\theta, F_{PM}, F_S, \varphi_d)$ is function of the PM contribution, but also to the stator current contribution $F_S(\theta)$. If the current increases, and if this increase mainly produce a significant contribution following a quadratic orientation with respect to φ_d , this may lead to a shift of m_t along θ , resulting in a shift of its harmonics $m_{t,(k)}$ inherited by the inductances and, especially, by l_{t-} . This shift increases the misalignments between the anisotropy xy-frame and the synchronous qd-frame, and it is not desired for position estimation. Generally, this shift can be assumed constant as a function of the component of stator current \underline{i} along the quadratic orientation. Note that this current can also be called *load current*. This is generally valid if the ideal condition (2.88) is met. The strategy proposed in many papers of the literature then consist to perform an initial estimation of that shift as a function of the load current, and to store it in look-up table in order to be used for position-estimation error compensation. This commissioning is however not easy. Different solutions are addressed in chapter 5. In the case of significant harmonics, the relation between the current and the shift in the different harmonic ranks must be assessed. This is done hereafter in case of our experimental machine.

The contribution of the stator current can also affect the inductance values and the anisotropy ratio l_{t-}/l_{t+} (sometimes defined by l_{tx}/l_{ty} [55]). Higher this ratio, more accurate the position estimation. Generally, the stator current tends to reduce this ratio. Therefore, some authors draw maps of feasibility regions for PM machines, considering the anisotropy ratio as a function of the stator current

Table 2.1: Design parameters of the experimental motor.

Machine length l_m	7.1 cm
Stator conductor radius R	12.1 cm
Air-gap length δ_o	5 mm
Pair-pole number P	14
PM angle extend ϑ	0.85π
Conductor turns \hat{n} per pole-pair	4

[58, 59, 60, 61]. They also address the issue of anisotropy misalignment, generally called *magnetic cross-saturation*. These maps are either estimated under commissioning, or by finite-element method (FEM) simulations. This is also analyzed in [62] for PM machines, drawing a graph of the anisotropy shift for various currents, or in [63] drawing graphs for a BLDC motor.

Special attention can be given to the machine design in order to increase their anisotropy ratio. A comparison between machines with buried magnets and surface-mounted magnets is discussed in [58, 59]. A comparison between conventional and “field-intensified” buried-magnet machines is discussed in [55]. Other “field-intensified” PM designs are studied by [64]. An analysis of the influence of the bridge between PM is given by [65]. Similar analysis are proposed in [66], comparing four types of IM, and in [67], comparing three geometric variations in the rotor of IM. Note that it is also possible to increase the some anisotropic properties of existing machines by adding a copper turn wound around the poles, as proposed by [68, 69]. The copper turn can be modelled in a similar way to the eddy current contributions, as done in the following chapter 3.

2.6 Experimental Brushless-DC Motor

The experimental BLDC motor is a three-phase machine with 14 pairs of surface-mounted permanent-magnets ($P = 14$) in an outer rotor and three coils at the stator, $n = 3$, that are connected in star: $i_o = 0$. A cross-section is shown in Figure 2.12 and an equivalent representation of a single-pole-pair is shown in Figure 2.13. The coils of each phase $p \in \{a, b, c\}$ are made of \hat{n} conductor turns per pole-pair located in single pairs of opposite slots a/a' , b/b' and c/c' on either side of their winding axes (in a single-pole-pair representation). The P windings of each phase are connected in series. The permanent-magnets (PM) are mounted on the rotor surface and centered along the angle φ_d . Each PM covers an angle extent ϑ . The values of the different design parameters are given in Table 2.1. More details on the design of similar machines can be found in [70].

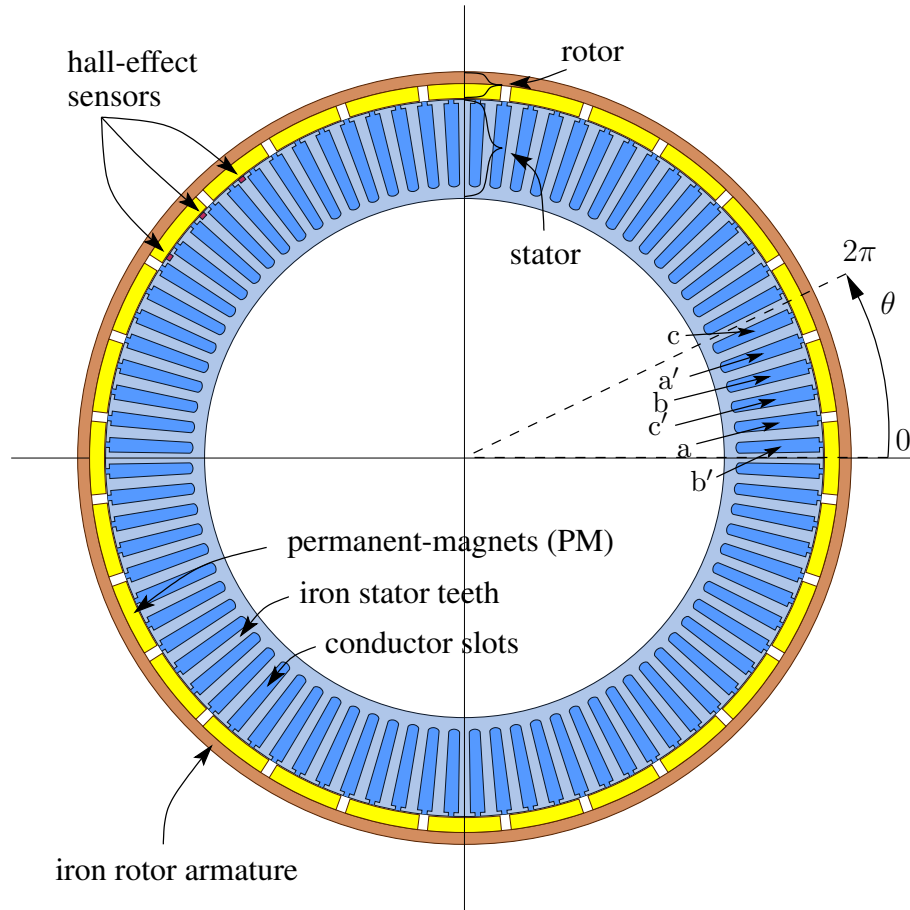


Figure 2.12: Cross-section of the experimental Brushless-DC (BLDC) motor.

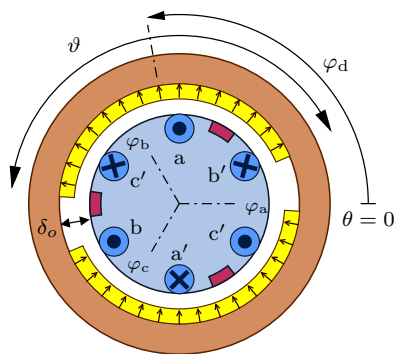


Figure 2.13: Representation of the experimental BLDC motor along a single-pole-pair.

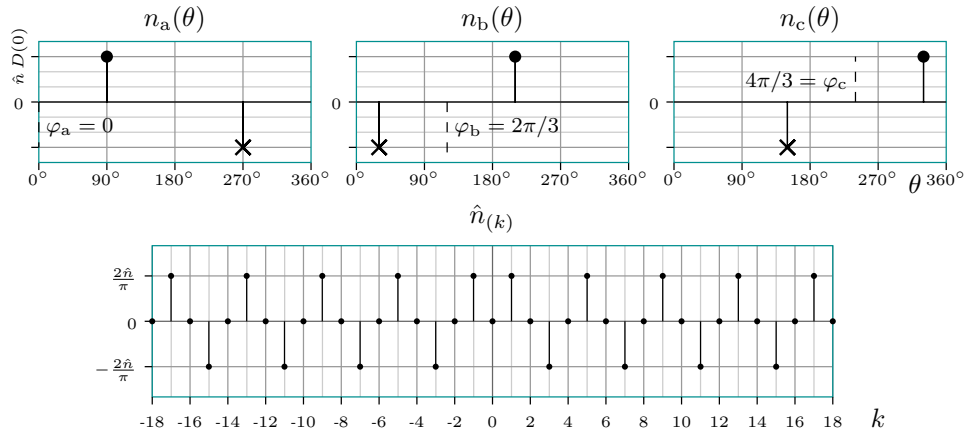


Figure 2.14: Conductor distributions $n_p(\theta)$ and their spectrum $\hat{n}_{(k)}$ (Fourier coefficients) in a simplified design model.

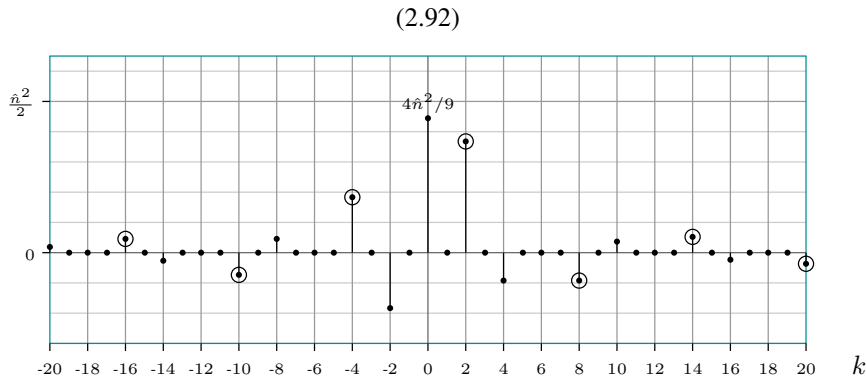


Figure 2.15: Values (2.91) as a function of k . The values involved in l_{t-} are mentioned by circles, in a simplified design model.

2.6.1 Simplified design model

In first approximation, the conductor distributions $n_p(\theta)$ can be modelled by punctual values using a delta Dirac function, written here D (it is traditionally written δ , but this notation is confusing with the air-gap length):

$$n_p(\theta) = \hat{n} (D(\theta - \varphi_p - \pi/2) - D(\theta - \varphi_p + \pi/2)) \quad (2.89)$$

It is illustrated in Figure 2.14. The Fourier coefficients (2.36) of this distribution are:

$$n_{p,(k)} = \frac{1}{\pi} \oint n_p(\theta') e^{jk\theta'} d\theta' = j \frac{2\hat{n}}{\pi} \sin(k\pi/2) e^{jk\varphi_p} \quad (2.90)$$

We have $\sin(k\pi/2) = 0$ if k is even, $\sin(k\pi/2) = 1$ if $k = 1 + 4\xi$ and $\sin(k\pi/2) = -1$ if $k = 3 + 4\xi$. Using the form (2.41), the peak values of the harmonics are:

$$\mathbf{n}_{p,(k)} = j\hat{n}_{(k)} \frac{k}{|k|} e^{jk\varphi_p} \Rightarrow \hat{n}_{(k)} = \begin{cases} 0 & \text{if } k \text{ even} \\ \frac{2\hat{n}}{\pi} (-1)^{\frac{|k|-1}{2}} & \text{if } k \text{ odd} \end{cases} \quad (2.91)$$

The spectrum is shown in Figure 2.14. Assuming (2.91), the value of the following expression, that is involved in the computation of the inductances $l_{t,(k)}$ (2.77), is given in Figure 2.15 as a function of k :

$$\sum_{\xi'=-\infty}^{\infty} \frac{\hat{n}_{(1+3\xi')} \hat{n}_{(1+3\xi'-k)}}{|1+3\xi'| |1+3\xi'-k|} \quad (2.92)$$

where $\hat{n}_{(1+3\xi')} = 0$ for ξ' odd. The sum can therefore be restricted to $\hat{n}_{(1+6\xi')}$, $\forall \xi'$. In particular, the case $k = 0$ yields:

$$\left(\frac{2\hat{n}}{\pi}\right)^2 \underbrace{\sum_{\xi'=-\infty}^{\infty} \frac{1}{(1+6\xi')^2}}_{(\pi/3)^2} = \frac{4}{9}\hat{n}^2 \quad (2.93)$$

while the cases $k = 3\xi$, $\forall \xi > 1$ yield 0. As a result, using (2.87a) and using this previous computation, it can be checked that the positive inductance l_{t+} is constant and yields:

$$l_{t+} = \frac{\hat{n}^2 \pi l_m R}{3} \hat{m}_{t,(0)} \quad (2.94)$$

The negative inductance $l_{t-} e^{j2\varphi_x}$ is not developed analytically, but the nonzero values of (2.92) involved in (2.87b) are shown by circles in Figure 2.15.

Traditionally, in a first approximation of the model of a BLDC motor, the permanent-magnet contribution to the magnetomotive force distribution $F_{PM}(\theta)$ is modelled by a trapezoidal function, as illustrated in Figure 2.16 with the corresponding spectrum $\hat{F}_{PM,(k)}$. This condition is assessed by [29, 6] from the back-EMF point of view. The incremental inductances are very sensitive to the magnetic state between the permanent magnets and this trapezoidal model does not well matches with the experimental measurements. We therefore propose to use a rectangular function, illustrated in Figure 2.17, as suggested by [44]. The real shape of the distribution is generally more complicated, as suggested by [71] that deeply studied the magnetic field distribution in BLDC motors.

The air-gap δ_o is assumed constant, neglecting the slot effects.

Simplified magnetic nonlinearity model

The variation of the factor $m(\theta)$ as a function of $F(\theta)$ in our experimental machine cannot directly be measured with the available sensors. By consequence, for the

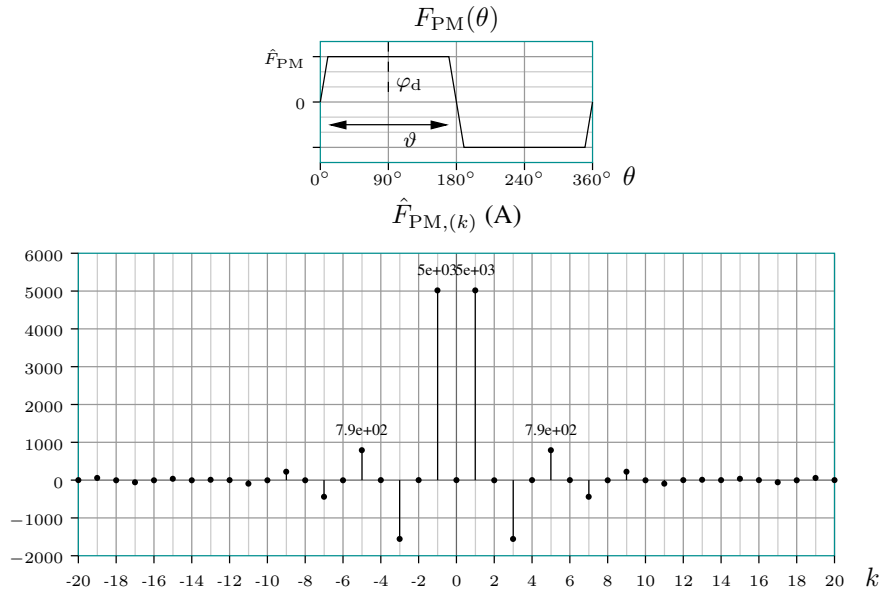


Figure 2.16: Traditional simplified model of the permanent-magnet contribution $F_{PM}(\theta)$ to the magnetomotive force, and the corresponding spectrum $\hat{F}_{PM,(k)}$.

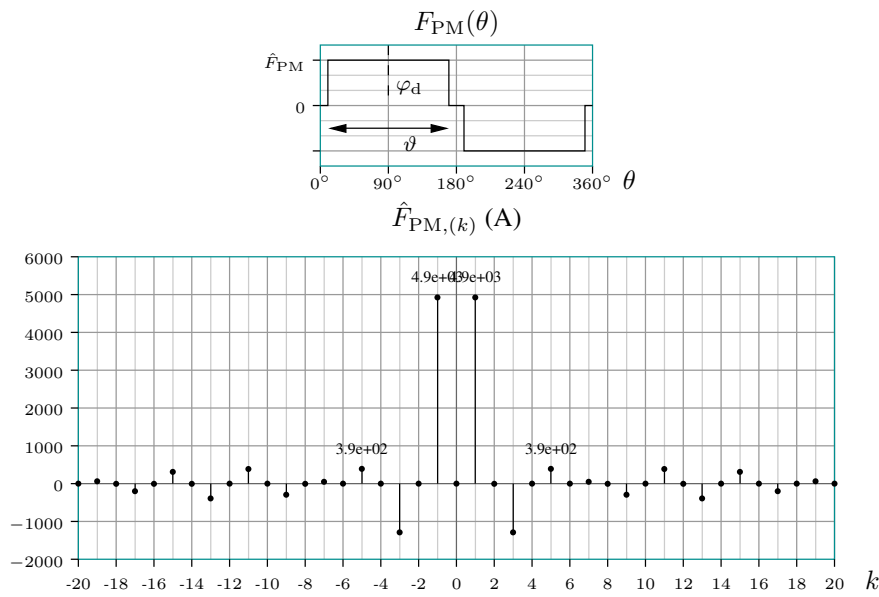


Figure 2.17: Proposed simplified model of the permanent-magnet contribution $F_{PM}(\theta)$ to the magnetomotive force, and the respective spectrum $\hat{F}_{PM,(k)}$.

simulations and the analysis, we propose the following simplified expression for

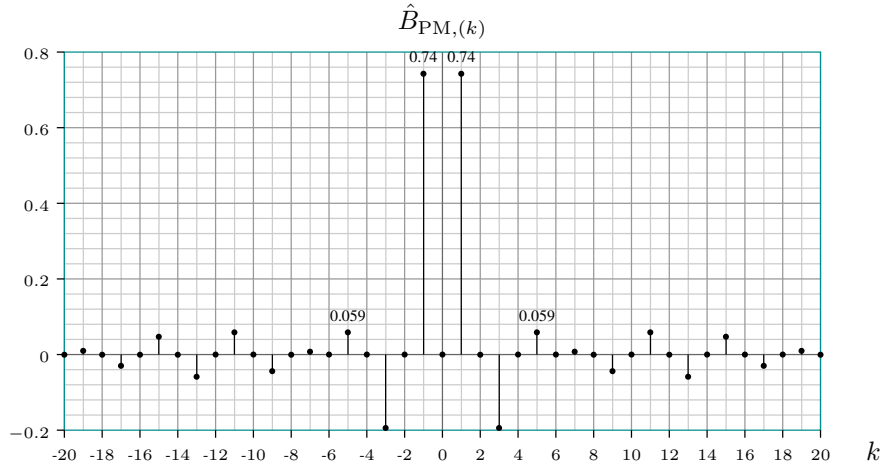


Figure 2.18: Spectrum of the permanent-magnet contribution to the magnetic field $\hat{B}_{PM,(k)}$ considering the simplified design model and the simplified magnetic nonlinearity model.

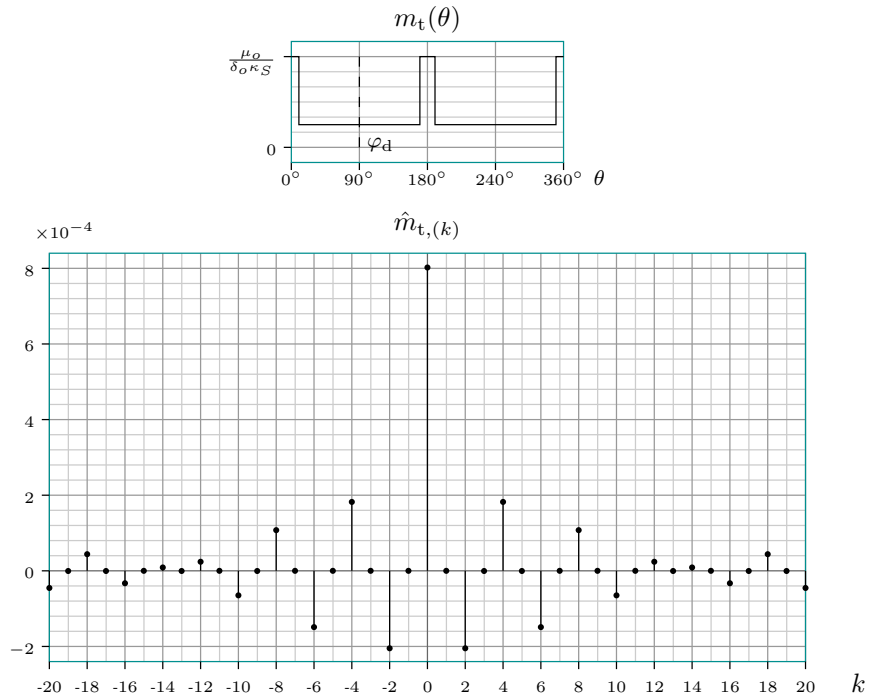


Figure 2.19: Illustration of the function $m_t(\theta)$ of the simplified magnetic nonlinearity model computed assuming $F(\theta) = F_{PM}(\theta)$ as given in Figure 2.17 and the corresponding spectrum $\hat{F}_{PM,(k)}$.

the local variation of the factor $m(\theta)$ as a function of $F(\theta)$, given in (2.24):

$$m(\theta) = \frac{\mu_o}{\delta_o} e^{-A|F(\theta)|} \Rightarrow B(\theta) = \frac{\mu_o}{\delta_o} e^{-A|F(\theta)|} F(\theta) \quad (2.95)$$

Table 2.2: Magnetic nonlinearity parameters.

Peak value of the PM contribution to the field \hat{B}_{PM}	0.6 T
Leakage factor regarding the PM contribution κ_{PM}	1
Leakage factor regarding the stator current contribution κ_S	0.25
Nonlinearity constant A	$1.28 \cdot 10^{-4} \text{ A}^{-1}$

The contribution of the permanent-magnets is approached without leakage, thus $\kappa_{\text{PM}} = 1$ regarding $F_{\text{PM}}(\theta)$. This model is purely intuitive, guided by characteristic curves found in the literature, but it is not sustained by any other study. Better model could certainly be used, such as the model proposed by [72].

The spectrum of corresponding magnetic field $\hat{B}_{\text{PM},(k)}$ is shown in Figure 2.18. For the stator current contribution of the magnetic field, it is necessary to consider significant leakages $\kappa_S = 0.25$ in order to obtain simulations results that match with the measurements. The selection of the leakage factor is empirical. Further investigations should be required in order to assess other possible sources of deviations between simulations and experiments. Transposed in the magnetomotive forces, it can be written:

$$F(\theta) = F_{\text{PM}}(\theta) + \kappa_S F_S(\theta) \quad (2.96)$$

The constant A is adjusted empirically so as to match to the best with the experimental measurements. Using (2.26), the incremental factor becomes:

$$m_t(\theta) = \frac{\mu_o}{\delta_o \kappa_S} (1 - A|F(\theta)|) e^{-A|F(\theta)|} \quad (2.97)$$

The results with this simplified model are compared with measurements. The value of $B_{\text{PM}}(\theta)$ is estimated by measurements (shown hereafter). The different parameters linked to the magnetic nonlinearity are summarized in Table 2.2.

2.6.2 Estimation of the PM field

The estimation of the permanent-magnet field is based on measurements performed on the experimental BLDC machine with open coil circuits (terminals disconnected to power source). The rotor is driven by an external motor at approximate constant electrical speed $\omega_d \approx 143 \text{ rad/s}$, measured by an external encoder. This rotation speed corresponds to a frequency of 22.76 Hz. Because we have no access to the neutral connection point, we measure the voltage difference between the terminals of two phases a and b: $v_{\text{ab}} = v_a - v_b$. We have 440 samples for the whole rotation (on one pole-pair $\theta = [0, 2\pi]$). Results are shown in Figure 2.20. The relation between the PM field and the measurements is developed hereafter.

The *Faraday's law of induction* states the induced back-electromotive force (back-emf) in a coil as follows:

$$e_p = -\frac{d\psi_p}{dt} = -\omega_d \frac{d\psi_p}{d\varphi_d} \quad (2.98)$$

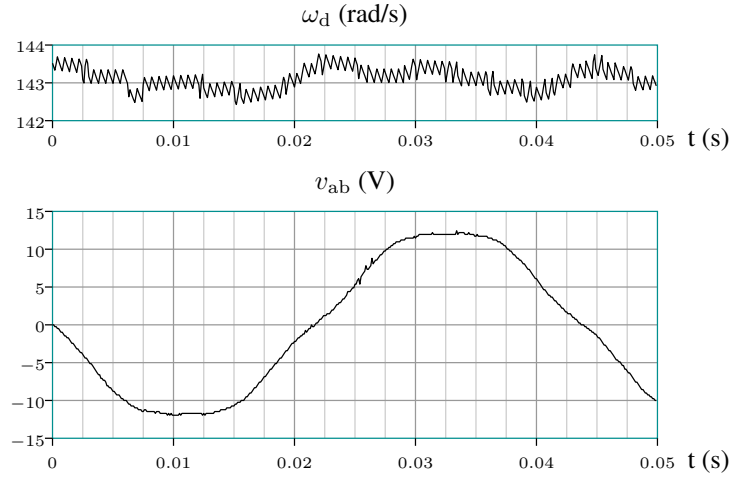


Figure 2.20: Experimental measurements of the voltage difference v_{ab} and the rotation speed ω_d .

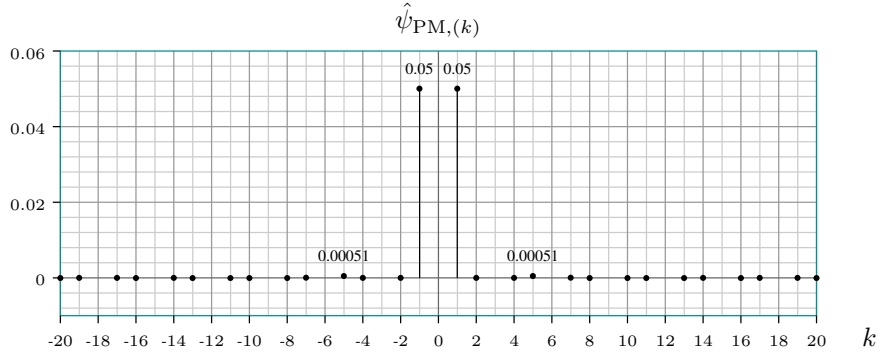


Figure 2.21: Spectrum of the permanent-magnet contribution to the flux, based on experimental measurements.

where $\omega_d = d\varphi_d/dt$ is the rotation speed in radian per second. Since no current is flowing in the coils (open circuits), the only contribution to the flux are the PM: $\psi_p = \psi(\varphi_p) = \psi_{PM}(\varphi_p)$. Without voltage drop due to stator currents, the voltage at coil terminals is equal to the back-emf: $v_p = e_{PM,p}$. Using (2.98), the ratio between the voltage difference v_{ab} and the rotation speed ω_d yields:

$$\frac{v_{ab}}{\omega_d} = - \frac{d(\psi_{PM}(\varphi_a) - \psi_{PM}(\varphi_b))}{d\varphi_d} \quad (2.99)$$

The Fourier series of this expression is given by (2.37). Using the property of symmetry of the flux along φ_d (2.40), inherited from the magnetic field $B(\theta)$,

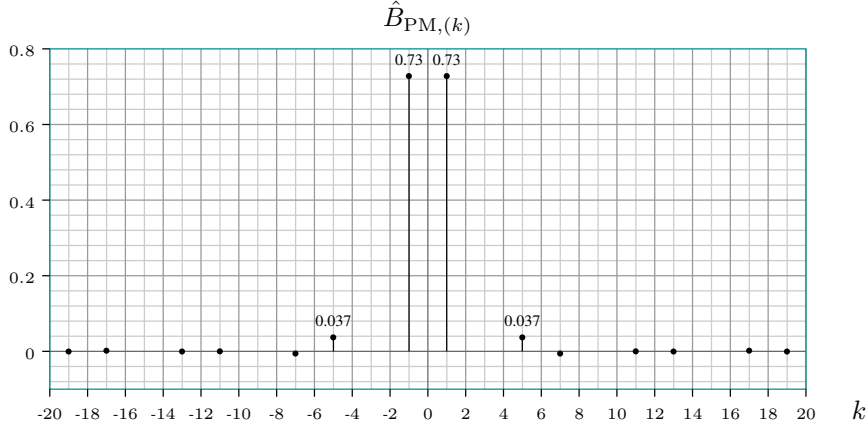


Figure 2.22: Spectrum of the permanent-magnet contribution to the magnetic field, based on experimental measurements.

(2.37) yields:

$$\begin{aligned} \psi_{PM}(\varphi_p) &= \frac{1}{2} \sum_{k=-\infty}^{\infty} \psi_{PM,(k)} e^{-jk\varphi_p} = \frac{1}{2} \sum_{k=-\infty}^{\infty} \left(\hat{\psi}_{PM,(k)} e^{jk\varphi_d} \right) e^{-jk\varphi_p} \\ &\Rightarrow \frac{d\psi_p(\varphi_p)}{d\varphi_d} = \frac{1}{2} \sum_{k=-\infty}^{\infty} jk \hat{\psi}_{PM,(k)} e^{jk(\varphi_d - \varphi_p)} \quad (2.100) \end{aligned}$$

Introducing this expression in (2.99) and using an opposite k order, it yields:

$$\begin{aligned} \frac{v_{ab}}{\omega_d} &= -\frac{1}{2} \sum_{k=-\infty}^{\infty} jk \hat{\psi}_{PM,(k)} \left(e^{-jk\varphi_a} - e^{-jk\varphi_b} \right) e^{jk\varphi_d} \\ &= \frac{1}{2} \sum_{k=-\infty}^{\infty} jk \underbrace{\left(1 - e^{j2k\pi/3} \right)}_{v_{ab}} \hat{\psi}_{PM,(k)} e^{-jk\varphi_d} \quad (2.101) \end{aligned}$$

where $\varphi_a = 0$ and $\varphi_b = 2\pi/3$. By consequence, computing the coefficients v_{ab} from the measurements, it is possible to compute $\hat{\psi}_{PM,(k)}$, except on $k = 3\xi$, $\forall \xi$, since $1 - e^{j2k\pi/3} = 0$, but these ranks are not involved in the computations:

$$\hat{\psi}_{PM,(k)} = \frac{v_{ab}}{jk \left(1 - e^{j2k\pi/3} \right)} \quad \forall k \neq 3\xi, \forall \xi \quad (2.102)$$

The results are shown in Figure 2.21. The main observation is that the fundamental $k = \pm 1$ is very dominant and that the harmonics of ranks $k = \pm 4$ are about only 1% of the fundamental. This suggests that the traditional synchronous vector control based on (2.50) and (2.69) could be an efficient solution, even if the magnetic field originally not sinusoidal. Note that part of the spectrum is unknown and

could be large also. Even if this part is not involved in the vector control, it affects the saturation and, by consequence, it affects the inductances. We cannot conclude about them without further experiments.

Assuming the simplified model of the conductor distribution given in (2.91), assuming no other contribution to the field than the permanent-magnets, and using the relation (2.55), we can compute the spectrum of the magnetic field for non-even k as follows:

$$\mathbf{B}_{(k)} = \frac{|k|}{\pi l_m R \hat{n}_{(k)}} \psi_{(k)} \quad \forall k \text{ odd} \neq 3\xi, \forall \xi \quad (2.103)$$

The results are shown in Figure 2.22. It seems not to be far from the model spectrum Figure 2.18.

2.6.3 Simulation Results

Simulation of the incremental self-inductance from the simplified models

The negative incremental inductance is computed using (2.87) assuming the simplified design model, the simplified magnetic nonlinearity model, and no other contribution to the field than the permanent-magnets. Using (2.94), the positive inductance yields:

$$l_{t+} = 115.5 \mu\text{H} \quad (2.104)$$

The negative inductance l_{t-} is computed using (2.87b).

Figures

The results shown in Figure 2.23 and Figure 2.24 are composed of:

- the value l_{t-} in the complex frame ;
- the amplitude $l_{t-} = |l_{t-}|$ as a function of the rotor position φ_d ;
- the anisotropy angle $\varphi_x = 0.5\angle(l_{t-})$ as a function of the rotor position φ_d ;
- the misalignment shift $\varphi_x - \varphi_q - 90^\circ$ as a function of the rotor position φ_d ;
- the harmonic spectrum of l_{t-} .

The 90° shift of φ_x with respect to φ_d is due to the fact that the peak value of $m_t(\theta)$, illustrated in Figure 2.19, is not along φ_d , but along $\varphi_d - 90^\circ$. As a consequence, the 2nd rank harmonic $\hat{l}_{t,(2)}$ is negative. These simulation results are compared to the results shown in Figure 2.23 assuming an ideal machine defined by (2.88).

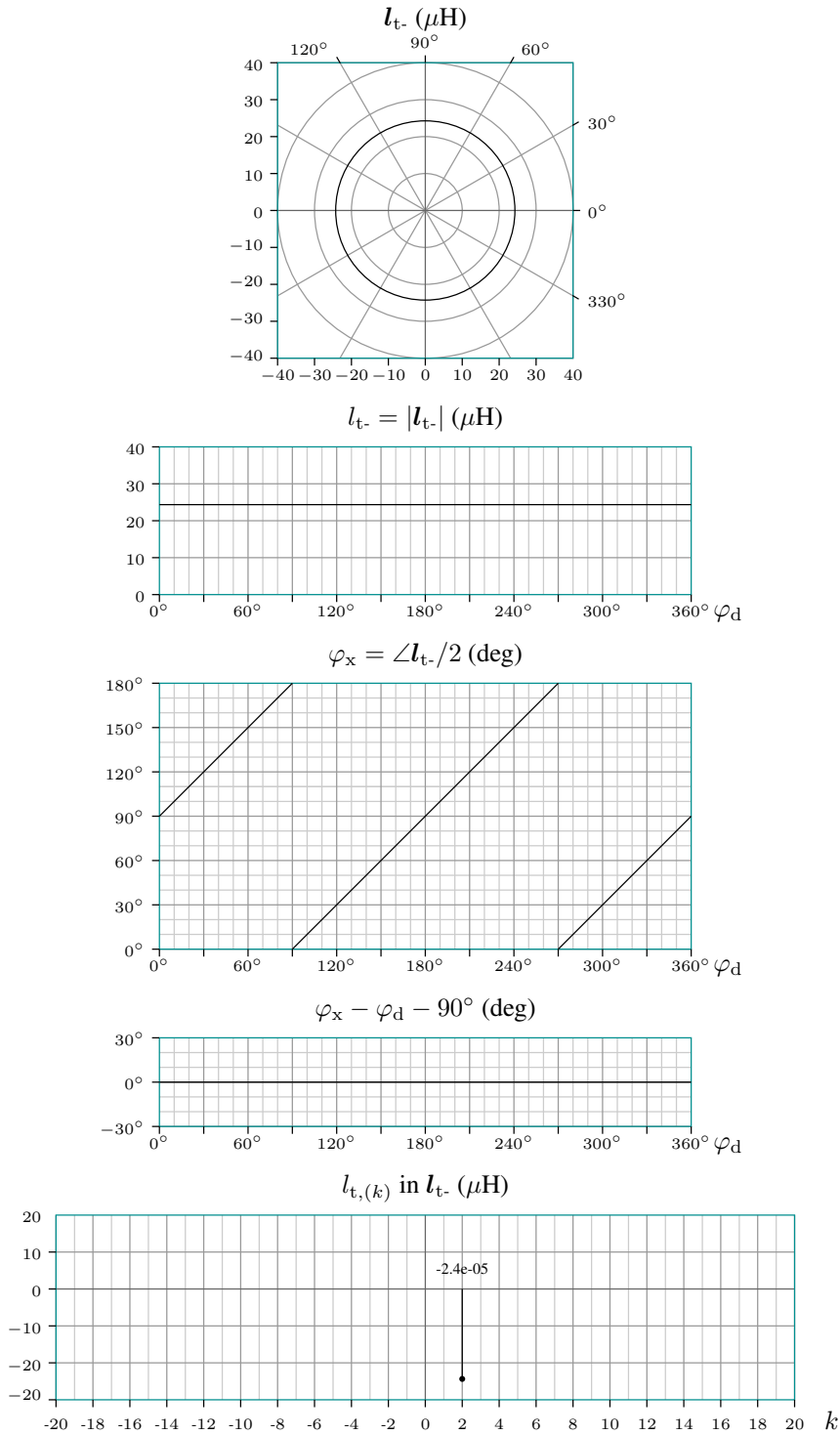


Figure 2.23: Virtual results of l_{t-} for $\varphi_d \in [0, 2\pi]$, assuming all harmonics are removed except $l_{t,(2)}$ (2.88), considering the simplified design model, the simplified magnetic non-linearity model and no other contribution to m_t than the permanent-magnets.

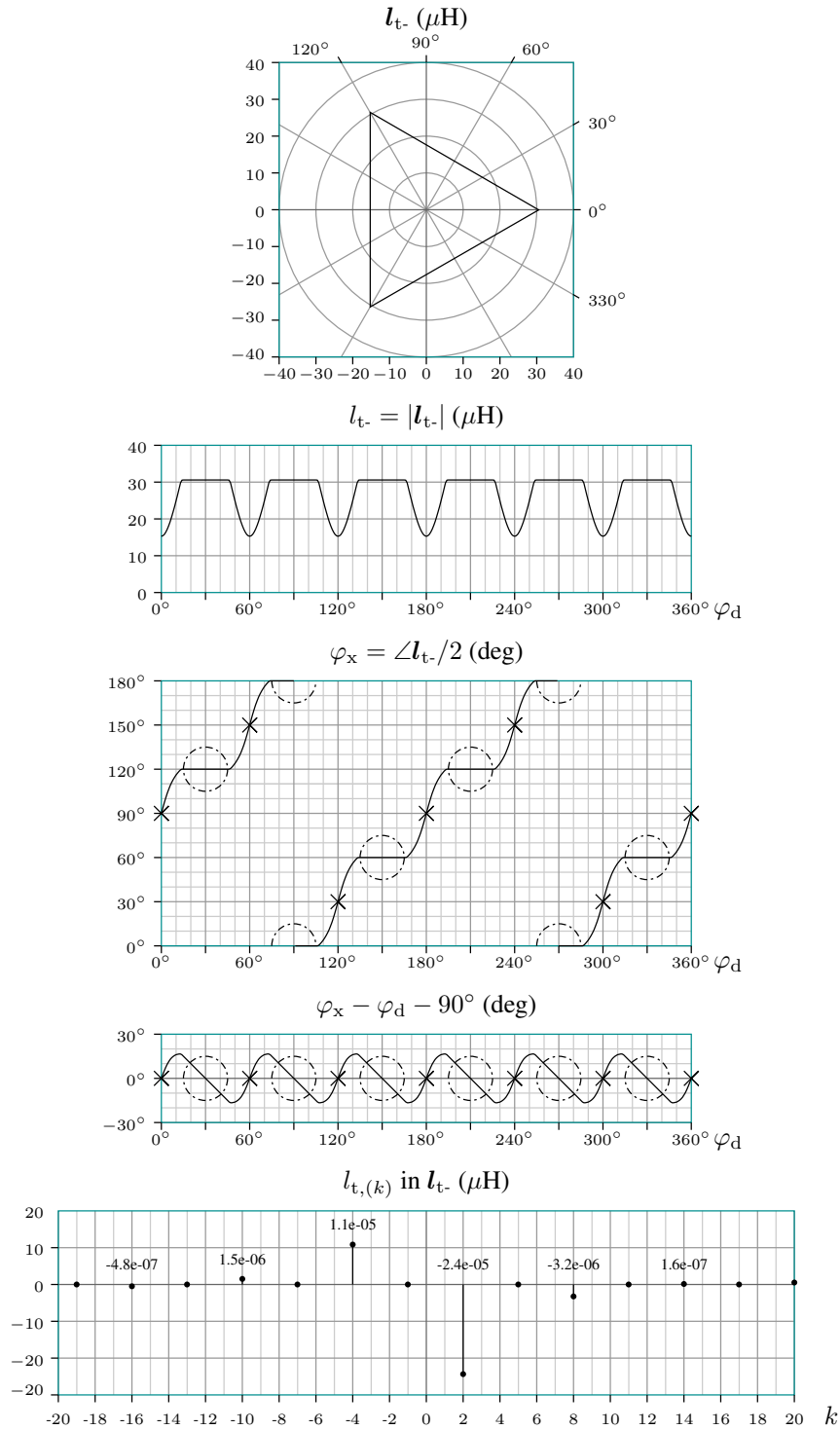


Figure 2.24: Values of l_{t-} for $\varphi_d \in [0, 2\pi]$ and spectrum of its harmonics, considering the simplified design model, the simplified magnetic nonlinearity model and no other contribution to m_t than the permanent-magnets.

Results

In Figure 2.23, the behaviour of l_{t-} is analyzed in the case of an ideal machine, by keeping only the second harmonic rank $l_{t(2)}$ and removing all other ranks. As a consequence, the shape drawn by l_{t-} during the rotation is a circle. This circle should not be confused with the circle drawn by $l_{t-}e^{j2(\varphi_x - \angle d\underline{i})}$ while $d\underline{i}$ is rotating, illustrated in Figure 2.11. As a consequence, the rotor angle is easily extracted as $\varphi_d = \varphi_x - 90^\circ$. In comparison, in the case of our nonideal machine shown in Figure 2.24, the relation between the anisotropy angle φ_x and the rotor angle φ_d is affected by significant harmonics. Due to these harmonics, the shape drawn by l_{t-} during the rotation becomes a triangle. An important consequence of the harmonics is the reduction of the accuracy of the rotor angle estimation based on φ_x . This estimation is reliable only around some particular angles $\xi 60^\circ$ illustrated by crosses in Figure 2.19, while the estimation is inaccurate around angles $30^\circ + \xi 60^\circ$, illustrated by dashed circles.

Simulations analyzing the impact of significant stator currents on the saturation is introduced in [39]. It is however not presented here because the model could not be validated at rated load. This would require further investigations and an improved test bench.

2.6.4 Experimental Results

Estimations of the incremental self-inductance from experiments

The experiments are performed on the standstill experimental BLDC motor, with the rotor blocked at 127 different positions between $\varphi_d = 0^\circ$ and 360° . At each rotor position, the incremental self-inductances are computed based on 2×100 samples taken with a voltage pulse instructions $d\underline{v}$ of 0.77 V amplitude injected during periods of $T_s = 0.1$ ms along two different directions, such that they produce flux variations $d\psi_S = d\underline{v}/T_s$ of 7700 Wb amplitude. The current variations $d\underline{i}$ related to these flux variations are between 0.7 A and 1.4 A, depending the orientation with respect to the anisotropy. They are measured by a current sensors with a 0.244 A resolution. This low resolution constitutes the main source of noise (digital noise) and the standard deviation of the current measurements is thus around half the sensor resolution. The noise issue is further addressed in section 5.3. Due to the low ratio of the current variations on the standard deviation, that is between 10 and 20, the standard deviation on the self-inductances is also quite large, between $5 \mu\text{H}$ and $13 \mu\text{H}$. The impact of this deviation is however reduced by 10 computing the mean of the results on 100 samples. Assuming a computation method based on these mean values, the error on self-inductances l_{t+} and l_{t-} should be around $2 \mu\text{H}$, and the error on the angle φ_d is around 2.5° . The resolution step of the encoder, measuring the rotor position, is 8192 on a whole rotation, thus $8192/P/360^\circ = 1.6^\circ$ on φ_d .

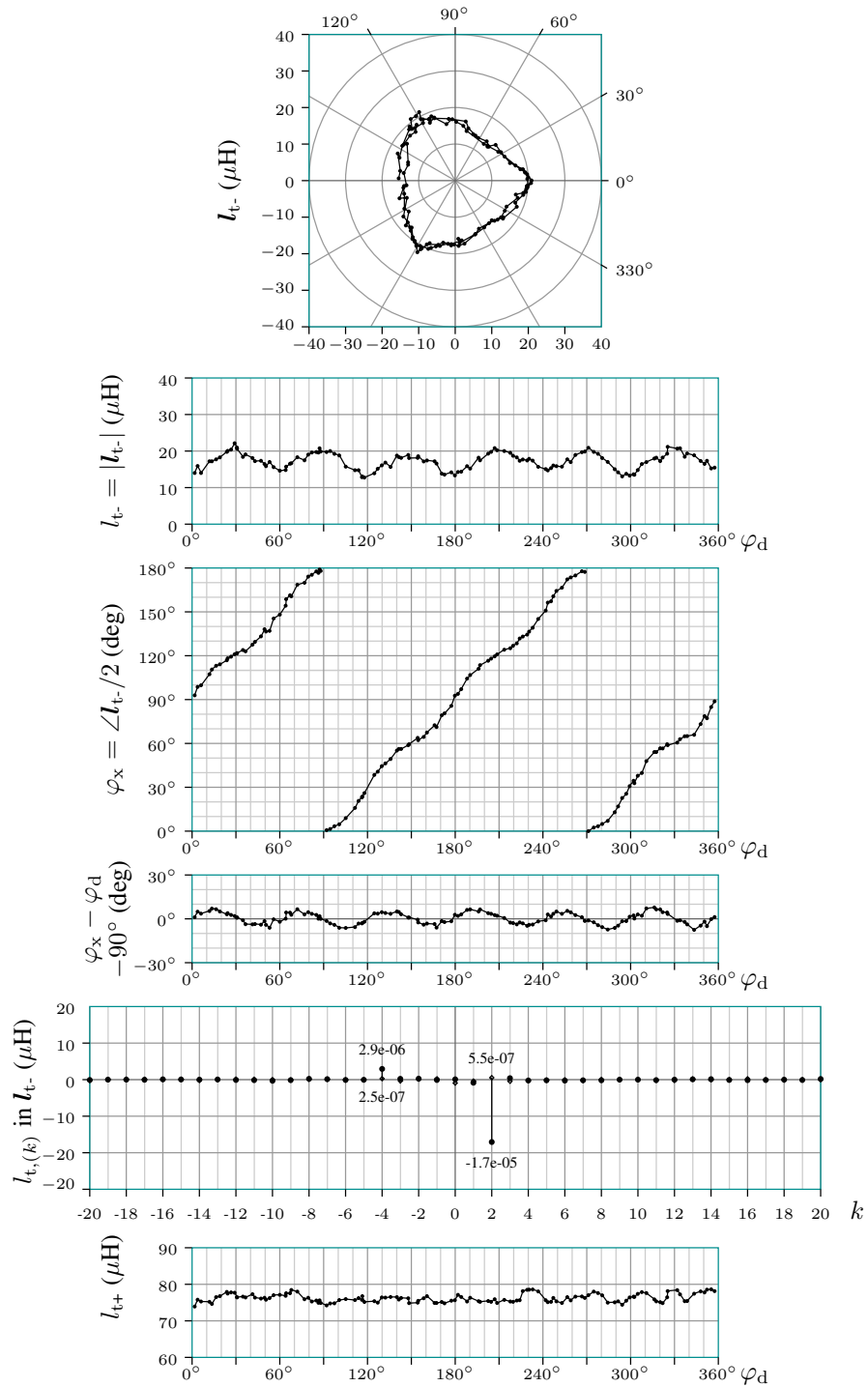


Figure 2.25: Experimental values of l_{t-} for $\varphi_d \in [0, 2\pi]$ and spectrum of its harmonics, with $\underline{i} = 0$ A.

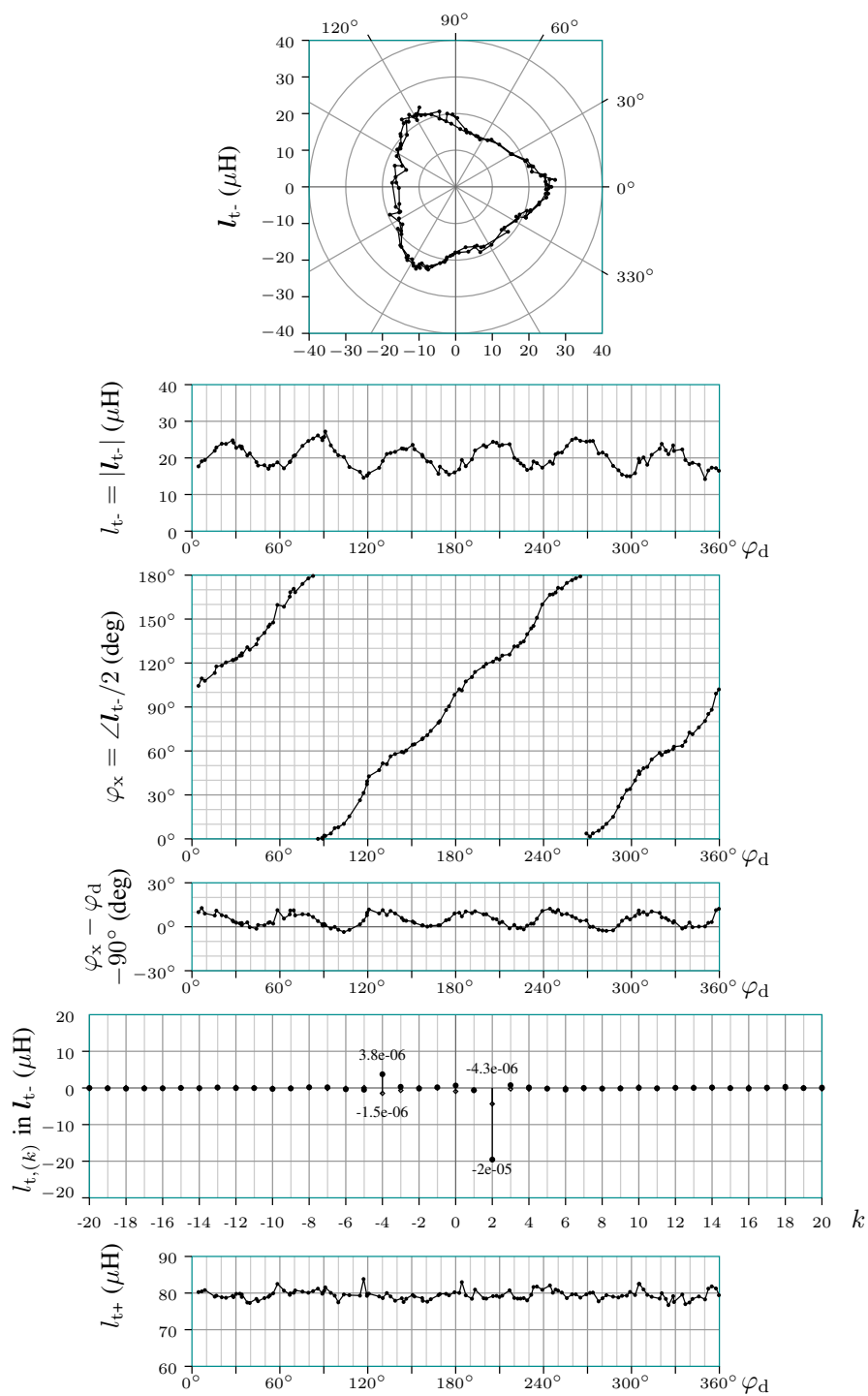


Figure 2.26: Experimental values of l_{t-} for $\varphi_d \in [0, 2\pi]$ and spectrum of its harmonics, with $\underline{i} = 36 \text{ A } e^{j\varphi_d}$.

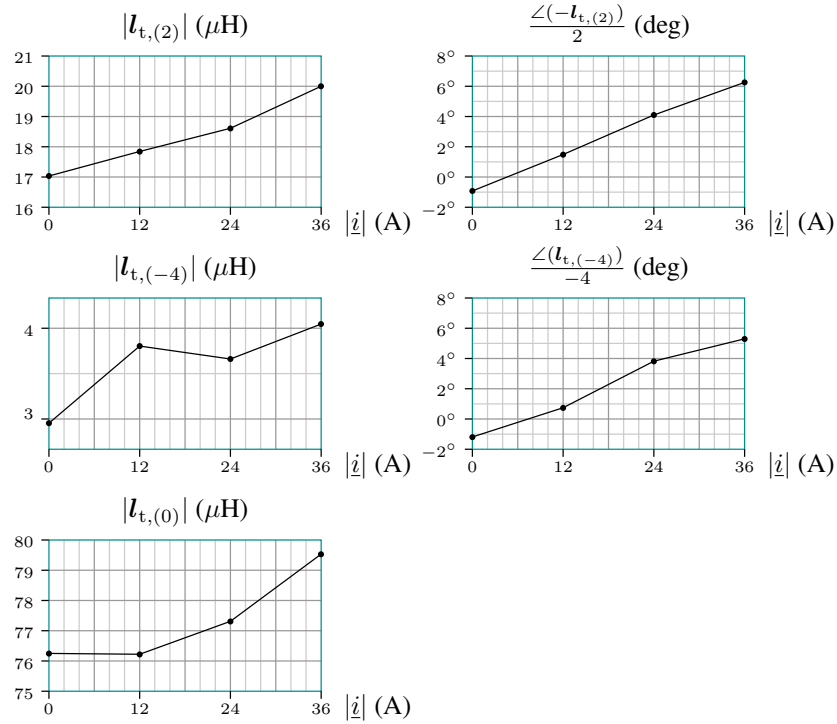


Figure 2.27: Experimental values of the load impact on the harmonic ranks $k = 2, -4$, involved in l_{t-} , and on the harmonic rank $k = 0$, involved in l_{t+} .

Figures

Results are shown in Figure 2.25 and Figure 2.26, respectively for a no-load situation ($\underline{i} = 0$) and for a loaded situation ($\underline{i} = 36$ A along the q-axis). They are composed as follows:

- the value l_{t-} in the complex frame ;
- the amplitude $l_{t-} = |l_{t-}|$ as a function of the rotor position φ_d ;
- the anisotropy angle $\varphi_x = 0.5\angle(l_{t-})$ as a function of the rotor position φ_d ;
- the misalignment shift $\varphi_x - \varphi_q - 90^\circ$ as a function of the rotor position φ_d ;
- the harmonic spectrum of l_{t-} , with real values shown by dots and imaginary values shown by small squares ;
- the value l_{t+} as a function of the rotor position φ_d .

Results

As we can see, Figure 2.25 is in good agreement with the simulation result Figure 2.24. The main difference concerns the harmonic spectrum where only the

ranks $k = 2$ and $k = -4$ present significant values. Concerning the self-sensing opportunities, compared to the previous conclusion based on simplified models, this experimental result suggests that it could be possible to increase the resolution of the rotor position estimation by taking only these second harmonics, of rank $k = -4$, into account. This is however not done in this thesis due to lack of time. As we can see in Figure 2.26, the increase of the load (stator current along the q-axis) produces a shift in the anisotropy angle. This is observed in the spectral content of l_{t-} , computed with respect to the angle φ_d given by the encoder. The positive inductance l_{t+} is also slightly increased.

Figure 2.27 shows the load impacts, measured for $|\dot{i}| = 0, 12, 24, 36$ A along the q-axis, on different harmonic ranks $k = 2, -4$, involved in l_{t-} , and on the harmonic rank $k = 0$, involved in l_{t+} . This impact is rather large and will certainly continuously increase up to the rated 134 A. If a linear behaviour is assumed, the anisotropy shift would reach 26° . Observe that the ranks 2 and -4 that are shifted by similar angles. This suggests that they are affected in a similar way by the load. Many papers propose to compensate for this load shift performing an offline commissioning. This commissioning however requires a specific test bench with a rotor position sensor and with a blocked rotor up to the maximum load. In the case of our experimental motor, the rated torque is 150 Nm. This is quite large and this experiment was not performed at this stage of the study. Different solutions are addressed in chapter 5.

2.7 Summary

In this chapter, we introduced the general electromagnetic model of the PM electric machine. Several assumptions were however required:

- machine made of cylindrical parts without magnetic field flowing through the edges, with as a consequence the exclusion of any axial component in the magnetic field ;
- symmetrically wounded coils on either side of their phase angles φ_p , plus the assumption of identical coils ;
- no homopolar current.

Large developments for any number of phases were proposed, offering tools for the study and the control of polyphase machines. We however focus on three-phase machine and the principal expressions to keep in mind for the rest of this thesis are:

- the computation of the fundamental complex space vector (2.71) for three-phase machines ;
- the expression of the torque (2.69) neglecting the harmonics ;

- the expression of the anisotropic incremental relation (2.81) in three-phase machines.

The experimental BLDC motor has been analyzed through simulations and experiments. The main experimental results are:

- Figure 2.21 shows that the magnetic flux contains harmonics of rank $k = 5$ that is only 1% the fundamental $k = 1$. We propose therefore to neglect these harmonics in the torque expression and to perform a field-oriented control generally applied on PMSM, as further described in chapter 5 ;
- Figure 2.25 and Figure 2.26 illustrate the oscillating error due to harmonics in the machine, and show that the negative self-inductance, used to obtain the anisotropy angle φ_x , contains harmonics of rank $k = -4$, referred to as second harmonics, while the other harmonics ranks are rather negligible. This would limit the complexity of the development of a compensation method (not done in this thesis) ;
- Figure 2.27 finally illustrated the significant impact of the stator currents.

Chapter 3

Electrical Circuit Model

This chapter addresses the model of the electrical circuit of the machine using space vectors. This model describes the relations linking the voltage and the current including the anisotropic properties described in the previous chapter 2. Since eddy currents can be significant in some types of machine, they are included for analysis in a second model for standstill machines. Because recent control operations are based on digital samples of the current, a transposition of the models in a discrete-time form is advised. The issues regarding parameters distortions are theoretically analyzed for the case of the model neglecting the eddy and for the model including the eddy currents. The study of the impact of eddy currents and the discretization on the model of the machine impedance is finally proposed.

3.1 Introduction

Since most of the recent drives are based on digital computations, it is advised to develop the control scheme and to adjust the operations based on a discrete-time model of the machine. All the publications found and dealing with digital control transpose the continuous-time model of the machine in an equivalent discrete-time model without taking care on any effect of the discretization on the apparent values of the machine parameters. In many drives, the transient time-constants of the electrical circuit of the machine are assumed large enough compared to the sampling period. In that case, the simple transposition to a discrete-time is valid, corresponding to a zero-order hold approach as done by [73, 74, 75]. In other cases however, the use of discrete-time operations may lead to significant distortions of the apparent parameters. Moreover, this distortion can be coupled with effects related to the presence of significant eddy currents.

The treatment of these issues are directly linked to problems faced on the experimental BLDC motor. Identification of the impedance using signal injections, as described in chapter 5, revealed variations of the parameter values as a function of the sampling frequency, and as a function of the signal frequency. In order to eliminate possible hardware errors or mistakes in the implemented methods, it was

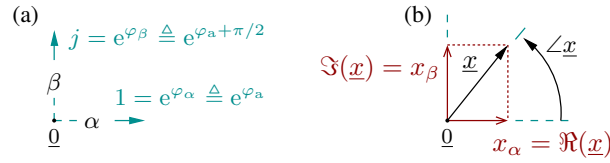


Figure 3.1: (a) Unitary space vectors of the stationary $\alpha\beta$ -frame ; and (b) illustration of a space vector \underline{x} and its axis components in the stationary $\alpha\beta$ -frame.

required to compare these results with simulations based on adequate models. It was firstly revealed that the simple modelling considering the discretization, but neglecting eddy currents gave unsatisfying results. Another model, much more complicated and including the eddy currents, was therefore developed. This new model offered very satisfying simulations results in adequacy with the experiments. For complexity reasons, the model was however restricted to standstill machines.

A significant part of this chapter addressed the mathematical development of the model discretization taking the eddy currents into account. This work allowed to conclude that the eddy current were the cause of the parameter distortion, excluding any cause from the hardware or the implementation.

~

This chapter is organized as follows: the section 3.2 introduces general relations with space vectors in different reference-frames ; Section 3.3 describes the electrical model in case of anisotropic relations firstly neglecting the eddy current, and secondly including the eddy currents ; Section 3.4 substitutes the continuous-time models by equivalent discrete-time models. The impact of the two-level three-phase pulse-width modulated voltage source inverter on this discretization is largely developed, assuming a standstill motor ; Section 3.5 introduces the model under the form of impedances, since the impedance is the value identified by the self-sensing method proposed in chapter 5. Comparisons between measurements on the experimental machines and model results confirm the validity of the models ; A summary of the important elements of this chapter is given in section 3.6.

3.2 Space Vectors in Different Frames

3.2.1 The Stationary Frame

Using complex space vectors

Assume a set of 3 phase values, written x_p where $p \in \{a, b, c\}$, related to an electromagnetic phenomenon occurring in the different stator phase-coils of the machine. This phenomenon can be the voltage applied to the coil terminals v_p , the current flowing in the phase coils i_p , the magnetic flux linked by the phase coils ψ_p . The complex space vector \underline{x} is defined in (2.71) of the chapter 2 as the phase

contributions x_p along the conductor orientations φ_p ; and the homopolar x_o is defined in (2.70) as the sum of the phase values x_p :

$$\underline{x} \triangleq \frac{2}{3} \sum_{p=a,b,c} x_p e^{j\varphi_p} \quad \text{and} \quad x_o \triangleq \frac{1}{3} \sum_{p=a,b,c} x_p \quad (3.1)$$

where $\varphi_a = 0$, $\varphi_b = 2\pi/3$ and $\varphi_c = 4\pi/3$. The phase values are found back using (2.46):

$$x_p = x_o + \Re(\underline{x} e^{-j\varphi_p}) \quad \forall p \in \{a, b, c\} \quad (3.2)$$

Being defined with respect to the stator phase-coils, it is said that this space vector \underline{x} is in the stationary frame. As illustrated in Figure 3.1, this stationary frame is generally identified by two orthogonal axes: one axis α is oriented along the first phase a, i.e. by an angle $\varphi_\alpha = \varphi_a$, and the other axis β is oriented in quadrature, i.e. by an angle $\varphi_\beta = \varphi_a + \pi/2$. Since $\varphi_a = 0$, the axis α is thus also the axis of the real values and β is the axis of the imaginary values, with the following unitary space vectors: $e^{j\varphi_\alpha} = 1$ and $e^{j\varphi_\beta} = j$. The real and imaginary components of \underline{x} are thus linked to the axes as follows:

$$x_\alpha \triangleq \Re\{\underline{x}\} \quad \text{and} \quad x_\beta \triangleq \Im\{\underline{x}\} \quad \Leftrightarrow \quad \underline{x} = x_\alpha + jx_\beta \quad (3.3)$$

The matrix relations

Combining (3.2) with (3.3) yields the matrix relation between the $\alpha\beta$ -components of the space vector, plus the homopolar, and the phase values as follows:

$$\begin{pmatrix} x_a \\ x_b \\ x_c \end{pmatrix} = \underbrace{\begin{pmatrix} \cos(\varphi_a) & \sin(\varphi_a) & 1 \\ \cos(\varphi_b) & \sin(\varphi_b) & 1 \\ \cos(\varphi_c) & \sin(\varphi_c) & 1 \end{pmatrix}}_C \begin{pmatrix} x_\alpha \\ x_\beta \\ x_o \end{pmatrix} \quad (3.4)$$

This computation is often referred to as the *Clark*-transformation. It can be reversed and yields:

$$\begin{pmatrix} x_\alpha \\ x_\beta \\ x_o \end{pmatrix} = \underbrace{\frac{2}{3} \begin{pmatrix} \cos(\varphi_a) & \cos(\varphi_b) & \cos(\varphi_c) \\ \sin(\varphi_a) & \sin(\varphi_b) & \sin(\varphi_c) \\ 0.5 & 0.5 & 0.5 \end{pmatrix}}_{C^{-1}} \begin{pmatrix} x_a \\ x_b \\ x_c \end{pmatrix} \quad (3.5)$$

The same result can be obtained combining (3.1) with (3.3).

Using matrix space vectors

In many papers of the literature, the term ‘‘space vector’’ refers to the matrix containing the components along the frame axes. To make the difference with the

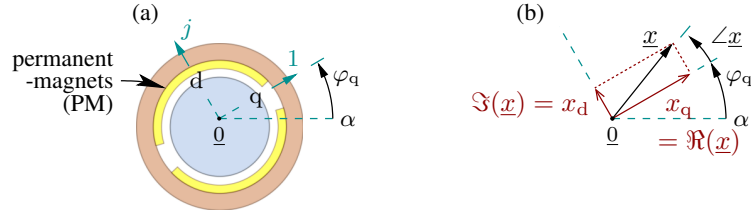


Figure 3.2: (a) Unitary space vectors of the synchronous qd-frame, with respect to the α -axis ; and (b) illustration of a space vector \underline{x} and its axis components in the synchronous qd-frame.

notation \underline{x} , this matrix is written here with an uppercase letter \underline{X} . Using (3.3), \underline{x} is related to \underline{x} by:

$$\underline{X} \triangleq \begin{pmatrix} x_\alpha \\ x_\beta \end{pmatrix} = \begin{pmatrix} \Re\{\underline{x}\} \\ \Im\{\underline{x}\} \end{pmatrix} \quad \text{and} \quad \underline{x} = \begin{pmatrix} 1 & j \end{pmatrix} \underline{X} \quad (3.6)$$

We propose here to simply refer to \underline{X} as *matrix space vector*, to be distinct from the *complex space vector* \underline{x} . Since conjugate values \underline{x}^* are involved in the anisotropic relations, in order to transpose these relations using matrix space vectors, we propose to define an equivalent conjugate \underline{X}^* as follows:

$$\underline{X}^* \triangleq \begin{pmatrix} x_\alpha \\ -x_\beta \end{pmatrix} \quad \text{and} \quad \underline{x}^* = \begin{pmatrix} 1 & j \end{pmatrix} \underline{X}^* \quad (3.7)$$

Both forms, complex and matrix space vectors, are equivalent. The choice to use one or the other depends on practical aspects in mathematical handling. For example, the self-sensing theory proposed in chapter 5 is easily based on the complex space vectors. While the matrix space vectors generally lead to more compact expressions. These last matrix space vectors are also more widespread in the literature.

3.2.2 The Synchronous Frame

Using complex space vectors

The machine model involves space vectors in different frames: stationary, synchronous or possibly others. Generally, one frame is chosen as the reference, namely we are observers in that frame. The reference-frame is indicated by the axis symbols adjoined to the space vectors, or in the text if it concerns the whole equation.

The *synchronous* frame is linked to the rotor in a single-pole-pair representation. As illustrated in Figure 3.2, it is identified by two orthogonal axes: the d-axis is centered along the permanent-magnet location ; and the q-axis is oriented in quadrature, or in back-quadrature, with respect to the d-axis. The back-quadrature is assumed in this document. The angle formed by the q-axis with respect to the

α -axis is written φ_q . As reference-frame, the q-axis becomes the axis of the real values and the d-axis becomes the axis of the imaginary values.

It is possible to switch the reference frame from the stationary $\alpha\beta$ -frame to the qd-frame, applying a negative rotation on the space vector by the angle φ_q of the q-axis with respect to the α -axis:

$$\underline{x}|_{qd} = e^{-j\varphi_q} \underline{x}|_{\alpha\beta} \quad (3.8)$$

Time derivatives of space vectors are involved in the model. It is therefore convenient to introduce the expression linking the time derivative of a space vector in different reference-frames. Using (3.8), in the qd reference-frame, it yields:

$$e^{-j\varphi_q} \frac{d\underline{x}|_{\alpha\beta}}{dt} = \frac{d\underline{x}|_{qd}}{dt} + j\omega_q \underline{x}|_{qd} \quad (3.9)$$

where $\omega_q = d\varphi_q/dt$. Observe that the change from the stationary $\alpha\beta$ reference-frame to the synchronous qd reference-frame introduce a term related to the speed between the reference-frames.

Using matrix space vectors

Handling the matrix space vectors (3.6) in the respective reference-frames, the relation (3.8) yields:

$$\underline{X}|_{qd} = \begin{pmatrix} \cos(\varphi_q) & \sin(\varphi_q) \\ -\sin(\varphi_q) & \cos(\varphi_q) \end{pmatrix} \underline{X}|_{\alpha\beta} \quad (3.10)$$

and the relation (3.9) yields:

$$\begin{pmatrix} \cos(\varphi_q) & \sin(\varphi_q) \\ -\sin(\varphi_q) & \cos(\varphi_q) \end{pmatrix} \frac{d\underline{X}|_{\alpha\beta}}{dt} = \frac{d\underline{X}|_{qd}}{dt} + \underbrace{\omega_q \begin{pmatrix} 0 & -1 \\ 1 & 0 \end{pmatrix}}_J \underline{X}|_{qd} \quad (3.11)$$

where we introduced the matrix J substituting the imaginary unity j .

The matrix relations including the homopolar

It is possible to link the axes components, plus the homopolar x_o , with the phase values directly by matrix referred to as *Park* transformations. This is found combining (3.4) and (3.5) with (3.10), and yields:

$$\begin{pmatrix} x_a \\ x_b \\ x_c \end{pmatrix} = C \begin{pmatrix} \cos(\varphi_q) & -\sin(\varphi_q) & 0 \\ \sin(\varphi_q) & \cos(\varphi_q) & 0 \\ 0 & 0 & 1 \end{pmatrix} \begin{pmatrix} x_q \\ x_d \\ x_o \end{pmatrix} \quad (3.12)$$

and

$$\begin{pmatrix} x_q \\ x_d \\ x_o \end{pmatrix} = \begin{pmatrix} \cos(\varphi_q) & \sin(\varphi_q) & 0 \\ -\sin(\varphi_q) & \cos(\varphi_q) & 0 \\ 0 & 0 & 1 \end{pmatrix} C^{-1} \begin{pmatrix} x_a \\ x_b \\ x_c \end{pmatrix} \quad (3.13)$$

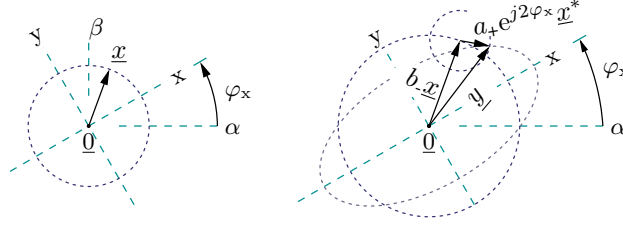


Figure 3.3: Illustration of the anisotropic relation between two space vectors \underline{x} and \underline{y} following (3.14), and the related anisotropy xy -frame.

These matrix transformations are given for information, but they will not be further used. We prefer to compute the space vectors using the initial definition (3.1) and then to handle them in the synchronous reference frame using complex space vectors (3.8) or matrix space vectors (3.10).

3.2.3 The Anisotropic Relation

Using complex space vectors

In a general way, an anisotropic relation between two space vectors \underline{x} and \underline{y} is defined in the stationary $\alpha\beta$ reference-frame by the following form:

$$\begin{aligned} \underline{y} &= a_+ \underline{x} + \mathbf{a}_- \underline{x}^* \\ &= a_+ \underline{x} + a_- e^{j2\varphi_x} \underline{x}^* \end{aligned} \quad \text{where } \begin{cases} a_+ \in \mathfrak{R} \\ \mathbf{a}_- \in \mathfrak{S} \Rightarrow \begin{cases} a_- = |\mathbf{a}_-| \in \mathfrak{R} \\ \varphi_x \triangleq \angle(\mathbf{a}_-)/2 \end{cases} \end{cases} \quad (3.14)$$

where a_+ and a_- are called the *positive* and *negative* parameters respectively, and φ_x is called the *anisotropy angle*. This angle gives the orientation of the related xy frame with respect to the reference-frame. This is illustrated in Figure 3.3. The relation between the linked flux and the current contributions (2.81) and (2.85), addressed in chapter 2, satisfy to this definition of the anisotropy.

Using (3.8), and since $\underline{x}^*|_{\text{qd}} = e^{j\varphi_q} \underline{x}^*|_{\alpha\beta}$, the anisotropic relation (3.14) transposed in the synchronous qd reference-frame yields:

$$\begin{aligned} \underline{y} &= a_+ \underline{x} + \mathbf{a}_- e^{-j2\varphi_q} \underline{x}^* \\ &= a_+ \underline{x} + a_- e^{j2(\varphi_x - \varphi_q)} \underline{x}^* \end{aligned} \quad (3.15)$$

If the synchronous qd frame is aligned with the anisotropy xy frame, we have $\varphi_x = \varphi_q$ and (3.15) yields:

$$\underline{y} = a_+ \underline{x} + a_- \underline{x}^* \quad (3.16)$$

We see hereafter how these relations appear using the matrix space vectors.

Using matrix space vectors

Handling matrix space vectors (3.6) and (3.7), the relation (3.14) in the stationary $\alpha\beta$ reference-frame yields:

$$\underline{Y} = a_+ \underline{X} + a_- \begin{pmatrix} \cos(2\varphi_x) & -\sin(2\varphi_x) \\ \sin(2\varphi_x) & \cos(2\varphi_x) \end{pmatrix} \underline{X}^* \quad (3.17)$$

This result can also be written as a matrix relation between \underline{X} and \underline{Y} :

$$\underline{Y} = \underbrace{\begin{pmatrix} a_{\alpha\alpha} & a_{\alpha\beta} \\ a_{\alpha\beta} & a_{\beta\beta} \end{pmatrix}}_A \underline{X} \Rightarrow \begin{cases} a_{\alpha\alpha} = a_+ + a_- \cos(2\varphi_x) \\ a_{\beta\beta} = a_+ - a_- \cos(2\varphi_x) \\ a_{\alpha\beta} = a_- \sin(2\varphi_x) \end{cases} \quad (3.18)$$

For information, reversing it, yields:

$$a_+ = \frac{a_{\alpha\alpha} + a_{\beta\beta}}{2} \quad \text{and} \quad a_- = a_- e^{j2\varphi_x} = \frac{a_{\alpha\alpha} - a_{\beta\beta}}{2} + ja_{\alpha\beta} \quad (3.19)$$

This relation can be used to compute the parameters of the space vector relation from the knowledge of the matrix A .

The relation (3.15) in the synchronous qd reference-frame yields:

$$\underline{Y} = \begin{pmatrix} a_{qq} & a_{qd} \\ a_{qd} & a_{dd} \end{pmatrix} \underline{X} \Rightarrow \begin{cases} a_{\alpha\alpha} = a_+ + a_- \cos(2(\varphi_x - \varphi_q)) \\ a_{\beta\beta} = a_+ - a_- \cos(2(\varphi_x - \varphi_q)) \\ a_{\alpha\beta} = a_- \sin(2(\varphi_x - \varphi_q)) \end{cases} \quad (3.20)$$

If the synchronous qd frame is aligned with the anisotropy xy frame, we have $\varphi_x = \varphi_q$ and (3.20) yields:

$$\underline{Y} = \begin{pmatrix} a_+ + a_- & 0 \\ 0 & a_+ - a_- \end{pmatrix} \underline{X} \quad (3.21)$$

where $a_x = a_+ + a_-$ and $a_y = a_+ - a_-$ are respectively the maximum and minimum values of the parameter.

Since the matrix (3.21) is diagonal, it is said that the relation along the x and the y axes is uncoupled. A contrario, the matrix (3.20) is not diagonal if the synchronous and anisotropy frames are misaligned. In that case, it is said that the q and the d axes cross-coupled. These terms of “saturation cross-coupling” [76, 63, 59, 55] or “cross-saturation” [54, 77, 60] or “cross-magnetization” [78] are often addressed in literature concerning the position self-sensing strategies. We see however that these coupling effects are only a point of view depending on the considered reference-frame. Generally, the coupling is assessed with respect to the qd frame and, thus, simply qualifies the fact that the synchronous qd frame is misaligned with the anisotropy.

3.3 Continuous-time models

3.3.1 Induced Voltages

The *Faraday's law of induction* states that the time derivative of the flux $\underline{\psi}$ linked by the phase coils induces a voltage \underline{e} in the machine circuits. This relation is stated in the reference-frame of the linking coils, that is the stationary $\alpha\beta$ -frame. In that frame, the relation can be written:

$$\underline{e} = \frac{d\underline{\psi}}{dt} \quad (3.22)$$

In a permanent-magnet machine, the flux $\underline{\psi}$ can be separate in three main contributions:

$$\underline{\psi} = \underline{\psi}_S + \underline{\psi}_{PM} + \underline{\psi}_E \quad (3.23)$$

1. a self-contribution from the stator currents \underline{i} , written $\underline{\psi}_S$, that is possibly nonlinear (since the relation depends on the magnetic state of the machine and therefore varies as a function of the different magnetic sources) and possibly anisotropic (due to rotor geometry variations or to magnetic saturation effects) ;
2. the contribution from the permanent magnets (PM), written $\underline{\psi}_{PM}$, that by definition only depends on the PM contribution to the magnetic state of the machine. Since the magnetomotive force (mmf) of the PM is assumed constant along the rotor-side, $\underline{\psi}_{PM}$ has a constant amplitude and is oriented as a function of the PM position φ_d ;
3. the contribution from eddy currents \underline{i}_E appearing in the iron of the machine, written $\underline{\psi}_E$, that is further discussed.

The respective induced voltages are \underline{e}_S , \underline{e}_{PM} and \underline{e}_E , such that: $\underline{e} = \underline{e}_S + \underline{e}_{PM} + \underline{e}_E$. In addition, the *Ohm's law* states that the electrical current \underline{i} flowing through the phase coils produce a voltage drop \underline{v}_r by a factor of resistance, introduced hereafter. The supply voltage \underline{v} applied to the coil terminals is then equal to the induced voltage \underline{e} plus the voltage drop \underline{v}_r :

$$\underline{v} = \underline{v}_r + \underline{e} = \underline{v}_r + \underline{e}_S + \underline{e}_{PM} + \underline{e}_E \quad (3.24)$$

These different voltages are developed hereafter. Note that we often switch between complex and matrix space vectors, since both are useful.

3.3.2 The Resistive Voltage Drop

The relation between the voltage drop \underline{v}_r and the current \underline{i} can reveal an anisotropic property, as defined by (3.14), due to unbalancing between the resistances of the

different stator coils. This is shown as follows. The resistive voltage drop $v_{r,p}$ of the different phases p can be written in a matrix form as:

$$\begin{pmatrix} v_{r,a} \\ v_{r,b} \\ v_{r,c} \end{pmatrix} = \underbrace{\begin{pmatrix} r_a & 0 & 0 \\ 0 & r_b & 0 \\ 0 & 0 & r_c \end{pmatrix}}_{R_{abc}} \begin{pmatrix} i_a \\ i_b \\ i_c \end{pmatrix} \quad (3.25)$$

Using the Clack matrices (3.4) and (3.5), it is possible to compute the equivalent relation between the space vector components in the stationary frame, plus the homopolar, as follows:

$$\begin{pmatrix} v_{r,\alpha} \\ v_{r,\beta} \\ v_{r,o} \end{pmatrix} = \underbrace{\begin{pmatrix} r_{\alpha\alpha} & r_{\alpha\beta} & r_{\alpha o} \\ r_{\beta\alpha} & r_{\beta\beta} & r_{\beta o} \\ r_{o\alpha} & r_{o\beta} & r_{oo} \end{pmatrix}}_{R_{\alpha\beta o}} \begin{pmatrix} i_\alpha \\ i_\beta \\ i_o \end{pmatrix} \quad (3.26)$$

where $R_{\alpha\beta o} = C^{-1}R_{abc}C$

$$= \frac{2}{3} \begin{pmatrix} r_a + \frac{1}{2}(r_b + r_c) & \frac{\sqrt{3}}{4}(r_c - r_b) & r_a - \frac{1}{2}(r_b + r_c) \\ \frac{\sqrt{3}}{4}(r_c - r_b) & \frac{3}{4}(r_c + r_b) & \frac{\sqrt{3}}{2}(r_b - r_c) \\ \frac{1}{2}r_a - \frac{1}{4}(r_b + r_c) & \frac{\sqrt{3}}{4}(r_b - r_c) & \frac{1}{2}(r_a + r_b + r_c) \end{pmatrix} \quad (3.27)$$

We firstly observe that there is an interaction between the homopolar current i_o and the voltage drops $v_{r,\alpha}$ and $v_{r,\beta}$ in the stationary frame through $r_{\alpha o}$ and $r_{\beta o}$ that are possibly not null. Since there are no neutral connection in our experimental machine, we propose to assumed the case $i_o = 0$ and to ignore this interaction. Thus using matrix space vectors (3.6), the relation (3.26) yields:

$$\underline{V}_r = \underbrace{\begin{pmatrix} r_{\alpha\alpha} & r_{\alpha\beta} \\ r_{\beta\alpha} & r_{\beta\beta} \end{pmatrix}}_R \underline{I} \quad (3.28)$$

We secondly observe that the interaction between the two axes is reciprocal: $r_{\alpha\beta} = r_{\beta\alpha}$. Thanks to this reciprocity, (3.28) has the form of an anisotropic relation in its matrix form (3.18). Computing r_+ and r_- as given in (3.19), (3.28) can be written with complex space vectors as given in (3.14) in the stationary reference-frame:

$$\underline{v}_r = r_+ \underline{i} + r_- \underline{i}^* \quad (3.29)$$

It is important to note that the orientation of this resistive anisotropy, i.e. $\angle(r_-)/2$, is only function of the phase resistances, but does not contain any rotor position information.

3.3.3 Back-electromagnetic force

Approximations for a synchronous machine

The back-electromagnetic force (back-emf) is the contribution from the PM to the induce voltage, written $\underline{e}_{\text{PM}}$. Assume that the the contribution from the PM is only function of the PM angle φ_d . Thus we can write in the stationary $\alpha\beta$ -frame:

$$\underline{e}_{\text{PM}} = \frac{d\underline{\psi}_{\text{PM}}}{dt} = \omega_d \frac{\partial \underline{\psi}_{\text{PM}}}{\partial \varphi_d} \quad (3.30)$$

where $\omega_d = d\varphi_d/dt$. The expression (3.30) in the synchronous qd reference-frame is found using (3.9) and yields:

$$\underline{e}_{\text{PM}} = \frac{d\underline{\psi}_{\text{PM}}}{dt} + j\omega_d \underline{\psi}_{\text{PM}} = \omega_d \left(\frac{\partial \underline{\psi}_{\text{PM}}}{\partial \varphi_d} + j\underline{\psi}_{\text{PM}} \right) \quad (3.31)$$

where $\omega_q = \omega_d$.

Assume that $\underline{\psi}_{\text{PM}}$ can be approached as a space vector oriented along the d-axis. In the stationary reference-frame, (3.30) yields:

$$\underline{\psi}_{\text{PM}} = |\underline{\psi}_{\text{PM}}| e^{j\varphi_d} \Rightarrow \frac{\partial \underline{\psi}_{\text{PM}}}{\partial \varphi_d} = j\underline{\psi}_{\text{PM}} \Rightarrow \underline{e}_{\text{PM}} = j\omega_d \underline{\psi}_{\text{PM}} \quad (3.32)$$

In the synchronous reference-frame, we have:

$$\underline{\psi}_{\text{PM}} = |\underline{\psi}_{\text{PM}}| e^{j\varphi_d} e^{-j\varphi_q} = |\underline{\psi}_{\text{PM}}| e^{j\pi/2} \Rightarrow \frac{\partial \underline{\psi}_{\text{PM}}}{\partial \varphi_d} = 0 \quad (3.33)$$

And thus, (3.30) yields the same expression as (3.32).

3.3.4 Current Contribution To The Induced Voltage

Assume that the contribution from the stator current is function not only of the stator currents \underline{i} , but also of the PM angle φ_d . Thus, using $\varphi_q = \varphi_d - \pi/2$, we can develop the induced voltage in the stationary $\alpha\beta$ reference-frame as follows:

$$\underline{e}_S = \frac{d\underline{\psi}_S}{dt} = \frac{\partial \underline{\psi}_S}{\partial \underline{i}} \frac{d\underline{i}}{dt} + \omega_q \frac{\partial \underline{\psi}_S}{\partial \varphi_q} \quad (3.34)$$

Note that $\omega_q = \omega_d$. The partial derivative on the angle φ_q is found assuming a constant current, i.e. it is found around the linearization point given by (2.85):

$$\underline{\psi}_S = l_+ \underline{i} + l_- \underline{i}^* \Rightarrow \frac{\partial \underline{\psi}_S}{\partial \varphi_q} = \frac{\partial l_+}{\partial \varphi_q} \underline{i} + \frac{\partial l_-}{\partial \varphi_q} \underline{i}^* \quad (3.35)$$

It is not demonstrated here, but it can be shown that the derivative of the positive and negative inductances still yields an anisotropic relation, i.e. the anisotropy is

not lost in (3.35). The partial derivative on the current \underline{i} is addressed in the previous chapter 2 and corresponds to the incremental contribution (2.81):

$$\frac{\partial \psi_S}{\partial \underline{i}} \frac{d\underline{i}}{dt} = l_{t+} \frac{d\underline{i}}{dt} + l_{t-} \frac{d\underline{i}^*}{dt} \quad (3.36)$$

Replacing the partial derivatives (3.35) and (3.36) in (3.34) yields:

$$\underline{e}_S = l_{t+} \frac{d\underline{i}}{dt} + l_{t-} \frac{d\underline{i}^*}{dt} + \omega_q \left(\frac{\partial l_{t+}}{\partial \varphi_q} \underline{i} + \frac{\partial l_{t-}}{\partial \varphi_q} \underline{i}^* \right) \quad (3.37)$$

The expression in the synchronous qd reference-frame is found using (3.9) and yields:

$$\underline{e}_S = \frac{d\underline{\psi}_S}{dt} + j\omega_q \underline{\psi}_S \quad (3.38)$$

Since $\underline{x}^*|_{qd} = e^{j\varphi_q} \underline{x}^*|_{\alpha\beta}$ and hence in the qd reference-frame:

$$\underline{\psi}_S = l_{t+} \underline{i} + l_{t-} e^{-2j\varphi_q} \underline{i}^* \quad \Rightarrow \quad \frac{\partial \underline{\psi}_S}{\partial \varphi_q} = \frac{\partial l_{t+}}{\partial \varphi_q} \underline{i} + \frac{\partial l_{t-} e^{-2j\varphi_q}}{\partial \varphi_q} \underline{i}^* \quad (3.39)$$

Then (3.38) in the qd reference-frame yields:

$$\underline{e}_S = l_{t+} \frac{d\underline{i}}{dt} + l_{t-} e^{-2j\varphi_q} \frac{d\underline{i}^*}{dt} + \omega_q \left(\frac{\partial l_{t+}}{\partial \varphi_q} \underline{i} + \frac{\partial l_{t-} e^{-2j\varphi_q}}{\partial \varphi_q} \underline{i}^* + j(l_{t+} \underline{i} + l_{t-} e^{-2j\varphi_q} \underline{i}^*) \right) \quad (3.40)$$

This expression may look more complicated than (3.37), but let us see hereafter how it looks like assuming a synchronous machine.

Relation using matrix space vectors

Using matrix space vectors, where the relation is given by (3.18), (3.37) yields in the stationary $\alpha\beta$ reference-frame:

$$\underline{E}_S = L_t \frac{d\underline{I}}{dt} + \omega_q \frac{\partial L}{\partial \varphi_q} \underline{I} \quad (3.41)$$

In the synchronous qd-reference-frame, the relation is given by (3.20) and (3.40) yields:

$$\underline{E}_S = L_t \frac{d\underline{I}}{dt} + \omega_q \left(\frac{\partial L}{\partial \varphi_q} + JL \right) \underline{I} \quad (3.42)$$

As we can see, these expressions are more compact than their equivalent complex relations. But their anisotropic properties are not highlighted in these matrix relations.

Approximations for a synchronous machine

Assume that the anisotropy frame related to the self-inductances is aligned with the synchronous frame, i.e. $\varphi_x = \varphi_q$ as introduced in (2.88), such that $\underline{l}_- = l_- e^{j2\varphi_q}$. Assume moreover that l_+ and l_- are constant. Hence:

$$\frac{\partial l_+}{\partial \varphi_q} = 0 \quad \text{and} \quad \frac{\partial \underline{l}_-}{\partial \varphi_q} = j2l_- e^{j2\varphi_q} \quad (3.43)$$

Idem, assume that the anisotropy frame related to the incremental self-inductances is aligned with the synchronous frame, hence: $\underline{l}_{t-} = l_{t-} e^{j2\varphi_q}$. Therefore, (3.37) in the stationary $\alpha\beta$ reference-frame yields:

$$\underline{e}_S = l_{t+} \frac{d\underline{i}}{dt} + l_{t-} \frac{d\underline{i}^*}{dt} e^{j2\varphi_q} + j\omega_q 2l_- \underline{i}^* e^{j2\varphi_q} \quad (3.44)$$

We can see that, even in a synchronous machine, a contribution related to l_- remains. This specific contribution is not easily transposable in a matrix form, such as (3.41).

In the synchronous qd reference-frame, we have:

$$\frac{\partial l_+}{\partial \varphi_q} = 0 \quad \text{and} \quad \underline{l}_- e^{-2j\varphi_q} = l_- \quad \Rightarrow \quad \frac{\partial \underline{l}_- e^{-2j\varphi_q}}{\partial \varphi_q} = 0 \quad (3.45)$$

Therefore, (3.40) in the synchronous qd reference-frame is:

$$\underline{e}_S = l_{t+} \frac{d\underline{i}}{dt} + l_{t-} \frac{d\underline{i}^*}{dt} + j\omega_q (l_+ \underline{i} + l_- \underline{i}^*) \quad (3.46)$$

This last expression is often found in the literature under a matrix relation between the axis components:

$$\underline{E}_S = L_t \frac{d\underline{I}}{dt} + \omega_q J L \underline{I} \quad (3.47)$$

Impact of the harmonics

The upper conditions of the synchronous machines are not met in the case of the experimental BLDC motor. Since the inductances l_+ and l_- content harmonics of φ_q , then $\partial l_+ / \partial \varphi_q$ and $\partial \underline{l}_- / \partial \varphi_q$ oscillate at frequencies multiple of ω_q , as explained in chapter 2.

Selection of the reference-frame

Assuming an ideal synchronous machine, the incremental part $L_t d\underline{I}/dt$ of (3.46) in the qd reference-frame yields a diagonal matrix relation (3.21). The relation is qualified as “magnetically decoupled”. A contrario, the matrix relation in the stationary reference-frame leads to a magnetic cross-coupling (3.18). Many anisotropy-based self-sensing methods found in the literature are thus developed in the qd-frame exclusively, such as in [79]. This frame is however not necessarily aligned

with the anisotropy xy -frame if the machine is not ideally synchronous, due to the stator current contribution to the anisotropy and due to the anisotropy harmonics as discussed in the previous chapter 2.

Some papers propose a strategy, referred to as cross-saturation compensation, that consists to perform the self-sensing operations in an hypothetical qd -frame taking the cross-saturation into account. This is equivalent to take the misalignment $\varphi_x - \varphi_q$ into account. Unfortunately, neither φ_q nor φ_x are apriori known, since they are the value to be estimated in self-sensing operations. As a consequence, it seems to us that this strategy is rather complicated and estimations of φ_q and φ_x could interfere. In the stationary-reference-frame however, only φ_x appears in the relation (3.36). In a first step, φ_x can be estimated using, for example, signal injection methods. In second step only, it is possible to estimate φ_q assuming a good model of the current contribution and the anisotropic harmonics, or assuming a compensation commissioning. Both step are therefore well separated. Both φ_x and φ_q are then consecutive and the estimation of φ_q is not interfering back in the estimation of φ_x .

Note that the term “cross-coupling” may also refer to JLI in (3.47) [79].

3.3.5 Electrical Circuit Model Without Eddy Currents

Combining the previous expression of this section, we can write the continuous-time model of the machine neglecting the contribution of eddy currents. In the stationary $\alpha\beta$ reference-frame, introducing the resistive voltage drop (3.29), the back-emf (3.30) and the self-induced voltage (3.37), the relation with the supply voltage (3.24) assuming $e_E = 0$ yields:

$$\underline{v} = l_{t+} \frac{d\underline{i}}{dt} + l_{t-} \frac{d\underline{i}^*}{dt} + \left(r_+ + \omega_q \frac{\partial l_+}{\partial \varphi_q} \right) \underline{i} + \left(r_- + \omega_q \frac{\partial l_-}{\partial \varphi_q} \right) \underline{i}^* + \underline{e}_{PM} \quad (3.48)$$

This expression can also be written using matrix space vectors (3.6) and (3.7), and the matrix of the factors are computed by (3.18). It yields:

$$\underline{V} = L_t \frac{d\underline{I}}{dt} + \left(R + \omega_q \frac{\partial L}{\partial \varphi_q} \right) \underline{I} + \underline{E}_{PM} \quad (3.49)$$

3.3.6 Electrical Circuit Model Including Eddy Currents

The eddy currents occur in the stator iron and in the rotor iron, but also in the permanent-magnets [80, 81, 82]. All the eddy currents must be modelled in the reference-frame related to the location where they appear, and then be transposed in one reference-frame. By consequence, a model including all the possibilities combining the different eddy currents, while moreover the machine is rotating, is very complicated. The goal is here however not to study all these possibilities, but to have a slight idea of some possible impacts. We propose therefore here a first

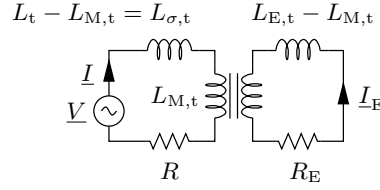


Figure 3.4: Model of the electrical circuit including the eddy currents.

analysis with a simplified model assuming a standstill rotor: $\omega_q = 0$. As consequence, the back-emf is null and the eddy currents from the rotor-side can be mixed with the eddy currents from the stator-side, all being developed in the stationary reference-frame. For convenience, the relations are given between matrix space vectors only, since they are more compact. As illustrated in Figure 3.4, the contribution of the eddy currents is modelled by an equivalent current \underline{I}_E flowing in a closed circuit presenting a resistance R_E [83, 59, 84, 85]. The mutual inductances between the two circuits are denoted by the lower index M. It yields:

$$\begin{aligned} \underline{V} &= L_t \frac{d\underline{I}}{dt} + L_{M,t} \frac{d\underline{I}_E}{dt} + R\underline{I} \\ \underline{0} &= L_{E,t} \frac{d\underline{I}_E}{dt} + L_{M,t} \frac{d\underline{I}}{dt} + R_E \underline{I}_E \end{aligned} \quad (3.50)$$

where all the inductances are possibly nonlinear and anisotropic. Note that eventual homopolar component in the eddy currents is neglected here. The difference between the mutual inductance and the self-inductances is related to flux leakages phenomena. Let us define the incremental stator leakage inductance as follows: $L_{\sigma,t} \triangleq L_t - L_{M,t}$; and the mutual current: $\underline{I}_M \triangleq \underline{I}_E + \underline{I}$. It can be shown that an equivalent system, presenting the same behaviour, is found assuming $L_{M,t} = L_{E,t}$. This transformation is demonstrated in [11]. As a result, (3.50) yields:

$$\begin{aligned} \underline{V} &= L_{\sigma,t} \frac{d\underline{I}}{dt} + L_{E,t} \frac{d\underline{I}_M}{dt} + R\underline{I} \\ \underline{0} &= L_{E,t} \frac{d\underline{I}_M}{dt} + R_E \underline{I}_E \end{aligned} \quad (3.51)$$

One-line expression

Let us define the transient time-constant of the eddy current circuit:

$$T_{E,t} = R_E^{-1} L_{E,t} \quad (3.52)$$

It is possible to combine the relations of both circuits of (3.51) to obtain the differential equation of second order linking $\underline{V}_{S,t}$ to \underline{I} . Introducing (3.52) yields:

$$\underline{V} + T_{E,t} \frac{d\underline{V}}{dt} = T_{E,t} L_{\sigma,t} \frac{d^2 \underline{I}}{dt^2} + (L_t + T_{E,t} R) \frac{d\underline{I}}{dt} + R\underline{I} \quad (3.53)$$

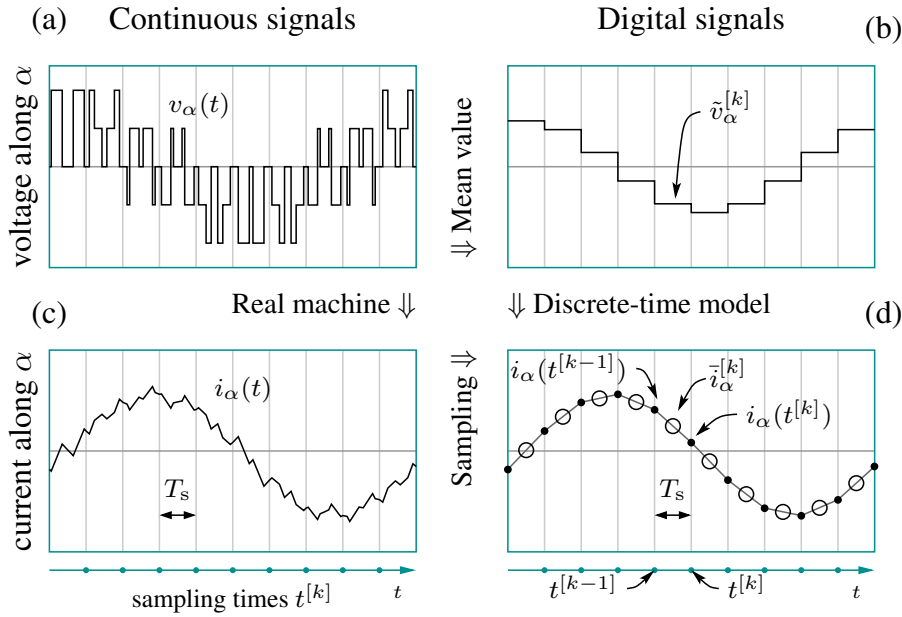


Figure 3.5: Illustration of typical signals along the α -axis: (a) the supply voltage $v_\alpha(t)$ synthesized by a two-level three-phase PWM-VSI ; (b) the related mean values $\tilde{v}_\alpha^{[k]}$ during the PWM periods ; (c) Stator current response $i_\alpha(t)$; (d) the current samples $i_\alpha(t^{[k]})$ (●) and the sampling averages $\bar{i}_\alpha^{[k]}$ (○).

If I models a small signal (small amplitude) and assuming a small period of time, the parameters can be assumed constant.

3.4 Discrete-Time Models

The drive operations are often described assuming a continuous-time model of the electrical machine. In practice however, most of the machines are driven by digital controllers and a digital model of the machine is therefore advised. Figure 3.5 illustrates typical signals, along the α -axis, that could appear in an electrical machine supplied by a pulse-width-modulated (PWM) voltage-source inverter (VSI). At every period of time T_s , the PWM-VSI generates a voltage signal switching between fixed step values, as shown in (a). The mean value $\tilde{v}_\alpha^{[k]}$ of the voltage during every period numbered k is shown in (b). As explained in chapter 4, ideally, this mean value should be equal to the instruction voltage. Due to the PWM voltage, the current response $i_\alpha(t)$ exhibits ripples, as shown in (c). The current measurements are periodically samples, as shown in (d). We assume that the sampling times of the currents are synchronized with the PWM signal driving the VSI. The currents are therefore sampled with a frequency ν_s at instants $t^{[k]} = kT_s$, where $T_s = 1/\nu_s$ is also the sampling period.

It is generally assumed that the mean of the current during a period is equal to

the average between two samples. This assumption strongly simplifies the discrete-time expressions. This should however be validated. In this section, we firstly propose the discrete-time machine model that we wish to substitute to the continuous-time model for digital operations. Their validity is then verified for standstill machines. The upper index $[k]$ placed on a value refers to the related sampling period k . For convenience however, this index will not be mentioned on the symbols in the text if it is not confusing. For convenience also, the subscript t indicating incremental parameters is removed, but all the parameters in the discrete-time modeling are necessarily incremental.

3.4.1 Electrical Circuit Model Without Eddy Currents

Using matrix space vectors and removing the indication t , the continuous-time model of the electrical circuit model neglecting the contribution of the eddy currents is:

$$\underline{V} = L \frac{d\underline{I}}{dt} + R\underline{I} \quad (3.54)$$

Assume that the influence of the so-called PWM-VSI nonlinearities are compensated, as addressed in chapter 4. The discrete-time operations can therefore be handled by the mean value $\tilde{\underline{V}}$ of the voltage supplied by the VSI between two sampling times:

$$\tilde{\underline{V}}^{[k]} \triangleq \frac{1}{T_s} \int_{t^{[k-1]}}^{t^{[k]}} \underline{V}(t) dt \quad (3.55)$$

Applying this mean on (3.54) and assuming constant parameters, it yields:

$$\tilde{\underline{V}}^{[k]} = L \frac{\delta \underline{I}^{[k]}}{T_s} + R \tilde{\underline{I}}^{[k]} \quad (3.56)$$

where $\tilde{\underline{I}}$ is the mean value of the current between two sampling times and $\delta \underline{I}$ is the sampling backward-difference of the current defined as the difference between two samples:

$$\delta \underline{I}^{[k]} \triangleq \underline{I}(t^{[k]}) - \underline{I}(t^{[k-1]}) = \int_{t^{[k-1]}}^{t^{[k]}} d\underline{I}(t) dt \quad (3.57)$$

Except if dedicated sensors are added, $\tilde{\underline{I}}$ is not measured and the expression (3.56) is not convenient for digital operations. We propose therefore to substitute $\tilde{\underline{I}}$ with the sampling average of the current $\bar{\underline{I}}$, defined as the average between two consecutive samples:

$$\bar{\underline{I}}^{[k]} \triangleq \frac{\underline{I}(t^{[k]}) + \underline{I}(t^{[k-1]})}{2} \quad (3.58)$$

The model (3.56) is then substituted by the following discrete-time model:

$$\tilde{\underline{V}}^{[k]} = \bar{L} \frac{\delta \underline{I}^{[k]}}{T_s} + \bar{R} \bar{\underline{I}}^{[k]} \quad (3.59)$$

where \bar{L} and \bar{R} are the discrete-time parameters substituting the continuous-time parameters. Note that these new parameters can significantly differ with respect to the continuous-time parameters if $\bar{I} \neq \tilde{I}$. This is shown hereafter. The steps leading to (3.59) from the continuous-time model (3.54) is proposed hereafter for the case of a standstill machine and separating the relations along uncoupled x and y-axes. Note that other discrete-time formulations can be found in the literature [74, 75], mainly using directly the samples $\underline{I}(t^{[k-1]})$ or $\underline{I}(t^{[k]})$ instead of \bar{I} . But comparatively (3.59) as significant advantages in the digital signal-injection processing. This is further explained in chapter 5.

Development of the proposed model

The proposed development is performed assuming a standstill machine, i.e. $\omega_q = 0$, and assuming that both incremental self-inductance and resistance present the same anisotropy orientation. In that case, the relations can be separated along the x and y-axes (entirely uncoupled). This is an approximation since, as we showed previously, the resistance may present an anisotropy due to unbalancing that is independent to the rotor position, while the incremental self-inductance presents an anisotropy that is function of that rotor position. By consequence, both are not necessarily aligned. A more general development can probably be obtained without these assumptions, but this is not done here. For convenience, we do not mentioned the axes symbols x and y, but they must be considered. For any of the two axes, the components are linked by the following first-order derivative expression:

$$\frac{v(t)}{l} = \frac{di(t)}{dt} + \frac{1}{\tau}i(t) \quad (3.60)$$

where the transient time-constant is $\tau = l/r$. Note the time-constant can be different along the x-axis and along the y-axis. The solution of this expression between two sampling times is [86]:

$$i(t^{[k]}) = e^{-\frac{T_s}{\tau}} i(t^{[k-1]}) + \int_{t^{[k-1]}}^{t^{[k]}} e^{-\frac{t-t^{[k]}}{\tau}} \frac{v(t)}{l} dt \quad (3.61)$$

We propose to compare the integral of the real PWM voltages with the ideal case of constant step voltages equal to \tilde{v} . If the voltage is constant during the period, it can be taken out the integral, and thus the integral yields:

$$\int_{t^{[k-1]}}^{t^{[k]}} e^{-\frac{t-t^{[k]}}{\tau}} \frac{\tilde{v}^{[k]}}{\tau} dt = \tilde{v}^{[k]} \left(1 - e^{-\frac{T_s}{\tau}}\right) \quad (3.62)$$

The *PWM distortion factor* k_{pwm} is then defined as the ratio between the real PWM voltage integral and the constant step voltage integral (3.62):

$$k_{\text{pwm}} \triangleq \int_{t^{[k-1]}}^{t^{[k]}} e^{-\frac{t-t^{[k]}}{\tau}} \frac{v(t)}{\tau} dt \Big/ \left(\tilde{v}^{[k]} \left(1 - e^{-\frac{T_s}{\tau}}\right) \right) \quad (3.63)$$

This factor is an indicator of the distortion due to the PWM pattern compared to a step voltage input. Note that k_{pwm} should vary at each PWM period. Introducing (3.63) in (3.61) yields:

$$\left(1 - e^{-\frac{T_s}{\tau}}\right) k_{\text{pwm}} \frac{\tilde{v}^{[k]}}{r} = i(t^{[k]}) - e^{-\frac{T_s}{\tau}} i(t^{[k-1]}) \quad (3.64)$$

The relation between the samples $i(t^{[k]})$, $i(t^{[k-1]})$ and δi , \bar{i} is found using (3.57) and (3.58), and it yields:

$$i(t^{[k]}) - e^{-\frac{T_s}{\tau}} i(t^{[k-1]}) = \frac{1 + e^{-\frac{T_s}{\tau}}}{2} \delta i^{[k]} + (1 - e^{-\frac{T_s}{\tau}}) \bar{i}^{[k]} \quad (3.65)$$

Rearranging (3.64) where the left member was replaced by (3.65) yields:

$$k_{\text{pwm}} \tilde{v}^{[k]} = \left(\frac{T_s}{2\tau} \frac{1 + e^{-\frac{T_s}{\tau}}}{1 - e^{-\frac{T_s}{\tau}}} \right) l \frac{\delta i^{[k]}}{T_s} + r \bar{i}^{[k]} \quad (3.66)$$

The *discretization distortion factor* K_{c2d} is defined as follows:

$$K_{c2d} \triangleq \frac{T_s}{2\tau} \frac{1 + e^{-\frac{T_s}{\tau}}}{1 - e^{-\frac{T_s}{\tau}}} \quad (3.67)$$

This factor K_{c2d} only depends on the ratio T_s/τ , but not on the PWM pattern. Introducing (3.67) in (3.66) yields:

$$k_{\text{pwm}} \tilde{v}^{[k]} = K_{c2d} l \frac{\delta i^{[k]}}{T_s} + r \bar{i}^{[k]} \quad (3.68)$$

Let us define the discrete-time parameters as follows:

$$\bar{l} = l K_{c2d} / k_{\text{pwm}} \quad \text{and} \quad \bar{r} = r / k_{\text{pwm}} \quad (3.69)$$

Introducing these parameters (3.69) in (3.68) yields the substituting discrete-time model expression (3.59):

$$\tilde{v}^{[k]} = \bar{l} \frac{\delta i^{[k]}}{T_s} + \bar{r} \bar{i}^{[k]} \quad (3.70)$$

The condition to have $\bar{i} \approx \tilde{i}$ is therefore that $K_{c2d} \approx 1$ and $k_{\text{pwm}} \approx 1$. Note that the transient time constant of the discrete-time model is $\bar{\tau} \triangleq \bar{r} / \bar{l}$.

Analysis of the parameter distortions

As shown by (3.69), the discretization distorts the substituting discrete-time value of the self-inductance \bar{l} with respect to the continuous-time value l through the discretization distortion factor K_{c2d} . It does however not affect the substituting discrete-time resistance \bar{r} . The distortion error $K_{c2d} - 1$ is drawn in Figure 3.6(a) as a function of τ/T_s . The 10% error is chosen as reference for the analysis and it

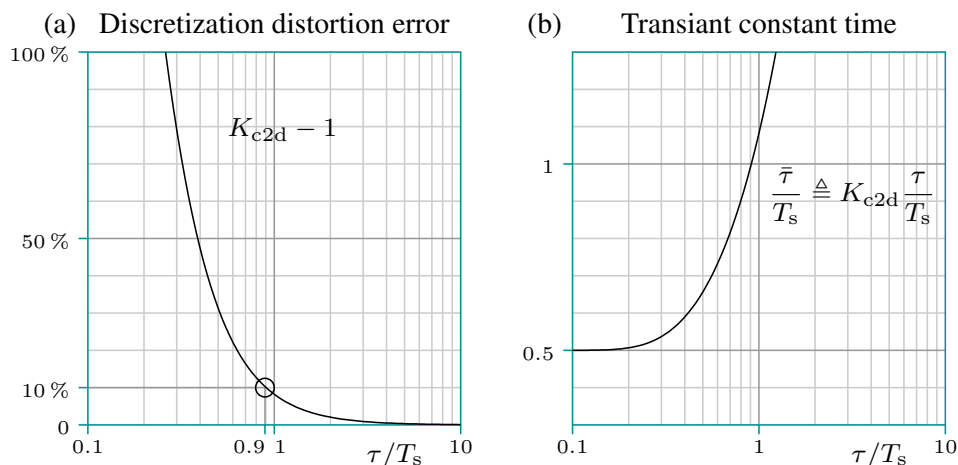


Figure 3.6: Graph of (a) the distortion error $K_{c2d} - 1$ due to the discretization and the 10% error point (\circ); Graph of (b) the transient time constant of the discrete-time model $\bar{\tau}$ in ratio with the sampling period T_s , as a function of τ/T_s .

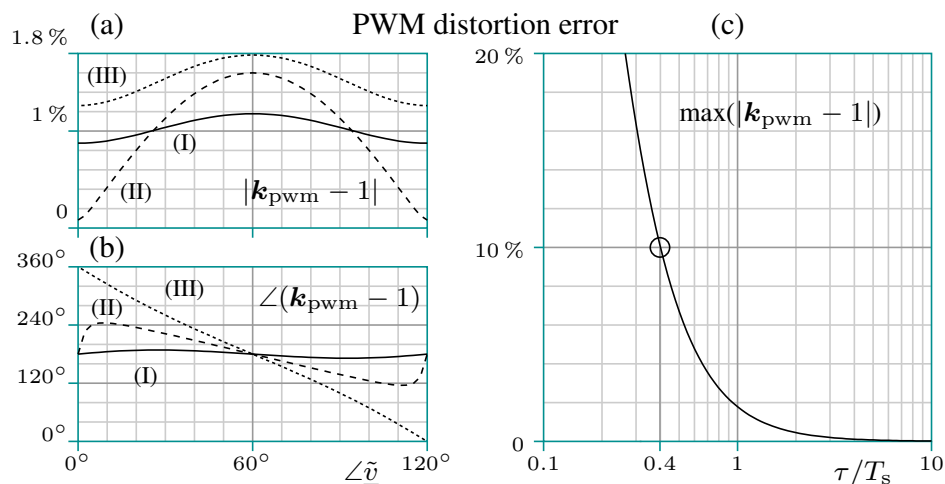


Figure 3.7: PWM distortion error $k_{pwm} - 1$ in case of a two-level three-phase VSI commanded by a conventional symmetrical PWM. Graph of (a) the complex amplitude $|\cdot|$ and (b) the complex angle $\angle(\cdot)$ of the error $k_{pwm} - 1$ as a function of the voltage angle $\angle\tilde{v}$ for the cases $|\tilde{v}| = \frac{v_{dc}}{20}$ (—), $\frac{v_{dc}}{4}$ (- -), $\frac{v_{dc}}{2}$ (\cdots), assuming $\tau/T_s = 1$; Graph of (c) the maximum amplitude $|k_{pwm} - 1|$ as a function of τ/T_s and the 10% error point (\circ).

is found around $\tau/T_s = 0.9$. Figure 3.6(b) shows the variation of the discrete-time transient time constant $\bar{\tau}$ as a function of τ . We can see that $\bar{\tau}$ tends to 0.5 while τ tends to zero. A first consequence for anisotropy-based self-sensing is that the difference between maximum and minimum values of \bar{l} , required for the position estimation, decreases strongly for ranges under $\tau/T_s \ll 1$.

In a first approximation, the PWM distortion factor is presented in (3.63) separately along the x and y-axes. By performing simulations with the case of a two-level three-phase VSI commanded by a conventional symmetrical PWM, some interactions between the two axes however appeared. These interactions strongly vary as a function of the voltages. As a consequence, we propose to redefine a PWM distortion factor, written k_{pmw} , using complex space vectors of the voltage \underline{v} . The PWM distortion error $k_{\text{pmw}} - 1$ is drawn in Figure 3.7. Assuming $\tau/T_s = 1$ equal for both axes, Figure 3.7(a) shows the complex amplitude of the error and Figure 3.7(b) shows the complex angle of the error as a function of the angle of the mean voltage $\angle \tilde{v}$ and for three different voltage amplitudes $|\tilde{v}|$. The complex angle of the error denotes a shift with respect to the orientation of \tilde{v} . We observe in (a) and (b) that the error amplitude and angle are very sensitive to the mean voltage. The effect of this error would therefore be very difficult to predict. The graph of the maximum amplitude of the error is shown in Figure 3.7(c). The main observation is that the 10% error is reached at $\tau/T_s = 0.4$. This limit is lower than the limit of 10% error for the discretization distortion error. We suggest therefore to focus only on the discretization distortion factor to validate the discrete-time model of an electrical machine.

Note that $\tau/T_s \gg 1$ in many drives. If not, a solution consists to increase the sampling frequency. But nonlinearities of the voltage-source inverter (VSI) and the switching losses tends however to increase with the frequency [87]. Moreover, the time for the control operations tends to decrease when the frequency increase. It is therefore not always advised to remove the discretization issues by this way.

3.4.2 Electrical Circuit Model Including Eddy Currents

Using matrix space vectors and removing the indication t, the continuous-time model of the electrical circuit model including the contribution of the eddy currents and assuming a standstill machine is:

$$\underline{V} + T_E \frac{d\underline{V}}{dt} = T_E L_\sigma \frac{d^2 \underline{I}}{dt^2} + (L + T_E R) \frac{d\underline{I}}{dt} + R \underline{I} \quad (3.71)$$

Except if dedicated sensors are added and if noise problems are considered, neither the mean current nor the current-derivative, nor the voltage derivative are measured. We propose therefore a discrete-time expression by substituting the continuous-time current \underline{I} , its derivative $d\underline{I}/dt$ and its second-derivative $d^2 \underline{I}/dt^2$ using samples only. For this, the backward-second-difference $\delta \delta \underline{I}$ is defined as:

$$\delta \delta \underline{I}^{[k]} \triangleq \delta \underline{I}^{[k]} - \delta \underline{I}^{[k-1]} = \underline{I}(t^{[k]}) - 2\underline{I}(t^{[k-1]}) + \underline{I}(t^{[k-2]}) \quad (3.72)$$

The current sampling backward-difference after two sampling periods $\Delta \underline{I}$ is defined as:

$$\Delta \underline{I}^{[k]} \triangleq \delta \underline{I}^{[k]} + \delta \underline{I}^{[k-1]} = \underline{I}(t^{[k]}) - \underline{I}(t^{[k-2]}) \quad (3.73)$$

And the sampling average of the current after two sampling periods $\bar{\bar{I}}$ is defined as:

$$\bar{\bar{I}}^{[k]} \triangleq \frac{\underline{I}^{[k]} + \underline{I}^{[k-1]}}{2} = \frac{\underline{I}(t^{[k]}) + 2\underline{I}(t^{[k-1]}) + \underline{I}(t^{[k-2]})}{4} \quad (3.74)$$

Concerning the voltages, we define the mean of the voltage during two sampling periods $\tilde{\underline{V}}$ as:

$$\tilde{\underline{V}}^{[k]} = \frac{\tilde{\underline{V}}^{[k]} + \tilde{\underline{V}}^{[k-1]}}{2} \quad (3.75)$$

and the voltage backward-difference $\delta \tilde{\underline{V}}$ as:

$$\delta \tilde{\underline{V}}^{[k]} = \tilde{\underline{V}}^{[k]} - \tilde{\underline{V}}^{[k-1]} \quad (3.76)$$

Using $\delta \delta \underline{I}/T_s^2$ defined in (3.72) to substitute $d^2 \underline{I}/dt^2$, using $\delta \bar{\bar{I}}/T_s$ defined in (3.73) to substitute $d\underline{I}/dt$, using $\bar{\bar{I}}$ defined in (3.74) to substitute \underline{I} , using $\delta \tilde{\underline{V}}^{[k]}/T_s$ defined in (3.76) to substitute $d\underline{V}/dt$ and using $\tilde{\underline{V}}$ defined in (3.75) to substitute \underline{V} , we propose the following discrete-time model expression at standstill:

$$\tilde{\underline{V}}^{[k]} + \bar{T}_E \frac{\delta \tilde{\underline{V}}^{[k]}}{T_s} = \bar{T}_E L_\sigma \frac{\delta \delta \underline{I}^{[k]}}{T_s^2} + (\bar{L} + \bar{T}_E \bar{R}) \frac{\Delta \bar{\bar{I}}^{[k]}}{2T_s} + \bar{R} \bar{\bar{I}}^{[k]} \quad (3.77)$$

where \bar{L}_σ and \bar{T}_E are respectively the equivalent discrete-time leakage inductance and eddy circuit transient time-constant. The eddy circuit discrete-time self-inductance and resistance of the eddy circuit are then:

$$\bar{L}_E \triangleq \bar{L} - \bar{L}_\sigma \quad \text{and} \quad \bar{R}_E \triangleq \bar{L}_E / \bar{T}_E \quad (3.78)$$

These new parameters can significantly differ with respect to the continuous-time parameters. The steps leading to (3.77) from the continuous-time model (3.71) is proposed hereafter for the case of a standstill machine and separating the relations along uncoupled x and y-axes.

Development of the proposed model

The proposed development is performed assuming a standstill machine, i.e. $\omega_q = 0$, and assuming that the anisotropic relations present the same anisotropy orientation. In that case, the relations can be separated along the x and y-axes (entirely uncoupled). Again, a more general development can probably be obtained without these assumptions, but this is not done here. Note that the following development is quite long since all the details are given. If the reader is not interested in this

long development, we can propose to go to the end of this subsection to read the analysis.

For convenience, we do not mentioned the axes symbols x and y , but they must be considered. For any of the two axes, the components are linked by the following first-order derivative expression:

$$v(t) + \tau_E \frac{dv(t)}{dt} = \tau_E l_\sigma \frac{d^2 i(t)}{dt^2} + (l + \tau_E r) \frac{di(t)}{dt} + ri(t) \quad (3.79)$$

where the transient time-constant of the eddy-current circuit is $\tau_E = l_E/r_E$. The global behaviour of this model is characterized by two other transient time-constants τ_1 and τ_2 than are computed as the inverse and opposite values of the roots x_1 and x_2 of the following second-order homogeneous equation [86]:

$$\begin{aligned} \tau_E l_\sigma x^2 + (l + \tau_E r) x + r = 0 &\Rightarrow (x - x_1)(x - x_2) = 0 \\ \Rightarrow \tau_1 = -1/x_1 \quad \text{and} \quad \tau_2 = -1/x_2 \end{aligned} \quad (3.80)$$

Note the time-constants can be different along the x -axis and along the y -axis. If τ_1 and τ_2 are distinct, the solution of this second-order derivative expression between two arbitrary times t_o and t_f is [86]:

$$\begin{aligned} i(t_f) = e^{-\frac{t_f-t_o}{\tau_1}} i_1(t_o) + e^{-\frac{t_f-t_o}{\tau_2}} i_2(t_o) \\ + \int_{t_o}^{t_f} \left(\frac{v(t)}{\tau_E} + \frac{dv(t)}{dt} \right) \left(e^{\frac{t-t_f}{\tau_1}} - e^{\frac{t-t_f}{\tau_2}} \right) dt / \left(\frac{l_\sigma}{\tau_2} - \frac{l_\sigma}{\tau_1} \right) \end{aligned} \quad (3.81)$$

The initial condition is given by:

$$i(t_o) = i_1(t_o) + i_2(t_o) \quad (3.82)$$

The integral right member of (3.81), including the voltage v plus it derivative dv/dt , can be strongly simplified if we assume that the PWM is such that the voltage is switched to zero at sampling times: $v(t^{[k-1]}) = v(t^{[k]}) = 0$. This is largely the case in many PWM strategies, such as in the illustration Figure 3.5. Therefore, we can write:

$$\begin{aligned} \frac{dv(t) e^{t/\tau}}{dt} = \frac{dv(t)}{dt} e^{t/\tau} + \frac{v(t)}{\tau} e^{t/\tau} \quad \forall \tau \\ \text{Since: } \int_{t^{[k-1]}}^{t^{[k]}} d \left(v(t) e^{t/\tau} \right) = \left(v(t) e^{t/\tau} \right)_{t^{[k-1]}}^{t^{[k]}} = 0 \\ \Rightarrow \int_{t^{[k-1]}}^{t^{[k]}} \frac{dv(t)}{dt} e^{t/\tau} dt = - \int_{t^{[k-1]}}^{t^{[k]}} \frac{v(t)}{\tau} e^{t/\tau} dt \end{aligned} \quad (3.83)$$

Introducing (3.83) in (3.81), the integral right member becomes:

$$\int_{t_o}^{t_f} v(t) \left(\left(\frac{e^{\frac{t-t_f}{\tau_1}}}{\tau_E} - \frac{e^{\frac{t-t_f}{\tau_2}}}{\tau_E} \right) - \left(\frac{e^{\frac{t-t_f}{\tau_1}}}{\tau_1} - \frac{e^{\frac{t-t_f}{\tau_2}}}{\tau_2} \right) \right) dt / \left(\frac{l_\sigma}{\tau_2} - \frac{l_\sigma}{\tau_1} \right) \quad (3.84)$$

This can be further simplified considering the following developments. In one hand, the numerator of (3.84) yields:

$$\begin{aligned} & \left(\frac{e^{-\frac{t-t_f}{\tau_1}}}{\tau_E} - \frac{e^{-\frac{t-t_f}{\tau_2}}}{\tau_E} \right) - \left(\frac{e^{-\frac{t-t_f}{\tau_1}}}{\tau_1} - \frac{e^{-\frac{t-t_f}{\tau_2}}}{\tau_2} \right) \\ &= \left(\frac{1}{\tau_E} - \frac{1}{\tau_1} \right) e^{-\frac{t-t_f}{\tau_1}} - \left(\frac{1}{\tau_E} - \frac{1}{\tau_2} \right) e^{-\frac{t-t_f}{\tau_2}} \\ &= (\tau_1 - \tau_E) \frac{e^{-\frac{t-t_f}{\tau_1}}}{\tau_E \tau_1} - (\tau_2 - \tau_E) \frac{e^{-\frac{t-t_f}{\tau_2}}}{\tau_E \tau_2} \end{aligned} \quad (3.85)$$

And in the other hand, the denominator of (3.84) yields:

$$\left(\frac{l_\sigma}{\tau_2} - \frac{l_\sigma}{\tau_1} \right) = l_\sigma \frac{\tau_1 - \tau_2}{\tau_1 \tau_2} \quad (3.86)$$

From these results, we define two new time-constants:

$$\tau'_1 = \frac{l_\sigma \tau_E}{r \tau_2} \left(\frac{\tau_1 - \tau_2}{\tau_1 - \tau_E} \right) \quad \text{and} \quad \tau'_2 = \frac{l_\sigma \tau_E}{r \tau_1} \left(\frac{\tau_2 - \tau_1}{\tau_2 - \tau_E} \right) \quad (3.87)$$

Introducing (3.87) in (3.84), (3.81) finally yields:

$$i(t_f) = e^{-\frac{t_f-t_o}{\tau_1}} i_1(t_o) + e^{-\frac{t_f-t_o}{\tau_2}} i_2(t_o) - \frac{1}{r} \int_{t_o}^{t_f} v \left(\frac{e^{-\frac{t-t_f}{\tau_1}}}{\tau'_1} + \frac{e^{-\frac{t-t_f}{\tau_2}}}{\tau'_2} \right) dt \quad (3.88)$$

In order to obtain a discrete-time model expression, it is required to solve the differential expression (3.88) during two different periods. As detailed hereafter, we propose to solve it between:

1. $t^{[k-2]}$ and $t^{[k-1]}$. It is then possible to remove $i_1(t^{[k-2]})$ and $i_2(t^{[k-2]})$;
2. $t^{[k-2]}$ and $t^{[k]}$. It yields then an expression linking $i(t^{[k]})$, $i(t^{[k-1]})$ and $i(t^{[k-2]})$.

We temporary write the integral right member of (3.88): w_1/r between $t^{[k-2]}$ and $t^{[k-1]}$; and: w_2/r between $t^{[k-2]}$ and $t^{[k]}$. These integrals are further solved. In a matrix form, the initial condition and the solution 1) gathered yield:

$$\begin{pmatrix} i(t^{[k-1]}) - w_1/r \\ i(t^{[k-2]}) \end{pmatrix} = \begin{pmatrix} e^{-\frac{T_s}{\tau_1}} & e^{-\frac{T_s}{\tau_2}} \\ 1 & 1 \end{pmatrix} \begin{pmatrix} i_1(t^{[k-2]}) \\ i_2(t^{[k-2]}) \end{pmatrix} \quad (3.89)$$

By inverting it, it yields:

$$\begin{pmatrix} i_1(t^{[k-2]}) \\ i_2(t^{[k-2]}) \end{pmatrix} = \frac{\begin{pmatrix} 1 & -e^{-\frac{T_s}{\tau_2}} \\ -1 & e^{-\frac{T_s}{\tau_1}} \end{pmatrix}}{e^{-\frac{T_s}{\tau_1}} - e^{-\frac{T_s}{\tau_2}}} \begin{pmatrix} i(t^{[k-1]}) - w_1/r \\ i(t^{[k-2]}) \end{pmatrix} \quad (3.90)$$

We have here the relation between $i_1(t^{[k-2]})$ and $i_2(t^{[k-2]})$ and the samples $i(t^{[k-1]})$ and $i(t^{[k-2]})$. This result can be replaced in the following solution of 2):

$$i(t^{[k]}) - \begin{pmatrix} e^{-\frac{2T_s}{\tau_1}} & e^{-\frac{2T_s}{\tau_2}} \end{pmatrix} \begin{pmatrix} i_1(t^{[k-2]}) \\ i_2(t^{[k-2]}) \end{pmatrix} = w_2/r \quad (3.91)$$

The resulting matrix yields:

$$\begin{aligned} & \begin{pmatrix} e^{-\frac{2T_s}{\tau_1}} & e^{-\frac{2T_s}{\tau_2}} \end{pmatrix} \frac{\begin{pmatrix} 1 & -e^{-\frac{T_s}{\tau_2}} \\ -1 & e^{-\frac{T_s}{\tau_1}} \end{pmatrix}}{e^{-\frac{T_s}{\tau_1}} - e^{-\frac{T_s}{\tau_2}}} \\ &= \frac{\begin{pmatrix} \left(e^{-\frac{2T_s}{\tau_1}} - e^{-\frac{2T_s}{\tau_2}} \right) \\ \left(e^{-\frac{2T_s}{\tau_2} - \frac{T_s}{\tau_1}} - e^{-\frac{2T_s}{\tau_1} - \frac{T_s}{\tau_2}} \right) \end{pmatrix}^t}{e^{-\frac{T_s}{\tau_1}} - e^{-\frac{T_s}{\tau_2}}} = \begin{pmatrix} \left(e^{-\frac{T_s}{\tau_1}} + e^{-\frac{T_s}{\tau_2}} \right) \\ -e^{-\left(\frac{T_s}{\tau_2} + \frac{T_s}{\tau_1}\right)} \end{pmatrix}^t \end{aligned} \quad (3.92)$$

Combining these results, it yields in a matrix form:

$$\begin{aligned} & \begin{pmatrix} 1 \\ -\left(e^{-\frac{T_s}{\tau_1}} + e^{-\frac{T_s}{\tau_2}} \right) \\ e^{-\left(\frac{T_s}{\tau_2} + \frac{T_s}{\tau_1}\right)} \end{pmatrix}^t \begin{pmatrix} i(t^{[k]}) \\ i(t^{[k-1]}) \\ i(t^{[k-2]}) \end{pmatrix} \\ &= w_2/r - \left(e^{-\frac{T_s}{\tau_1}} + e^{-\frac{T_s}{\tau_2}} \right) w_1/r \end{aligned} \quad (3.93)$$

The result in an one-line relation is:

$$\begin{aligned} & i(t^{[k]}) - \left(e^{-\frac{T_s}{\tau_1}} + e^{-\frac{T_s}{\tau_2}} \right) i(t^{[k-1]}) \\ &+ e^{-\left(\frac{T_s}{\tau_2} + \frac{T_s}{\tau_1}\right)} i(t^{[k-2]}) = w_2/r - \left(e^{-\frac{T_s}{\tau_1}} + e^{-\frac{T_s}{\tau_2}} \right) w_1/r \end{aligned} \quad (3.94)$$

We should replace the current samples by the substitution values $\delta\delta i$, Δi and \bar{i} using their definitions (3.72), (3.73) and (3.74). In a matrix form, the definitions yield:

$$\begin{pmatrix} \delta\delta i^{[k]} \\ \Delta i^{[k]} \\ \bar{i}^{[k]} \end{pmatrix} = \begin{pmatrix} 1 & -2 & 1 \\ 1 & 0 & -1 \\ 0.25 & 0.5 & 0.25 \end{pmatrix} \begin{pmatrix} i(t^{[k]}) \\ i(t^{[k-1]}) \\ i(t^{[k-2]}) \end{pmatrix} \quad (3.95)$$

By inverting it, it yields:

$$\begin{pmatrix} i(t^{[k]}) \\ i(t^{[k-1]}) \\ i(t^{[k-2]}) \end{pmatrix} = \begin{pmatrix} 0.25 & 0.5 & 1 \\ -0.25 & 0 & 1 \\ 0.25 & -0.5 & 1 \end{pmatrix} \begin{pmatrix} \delta\delta i^{[k]} \\ \Delta i^{[k]} \\ \bar{i}^{[k]} \end{pmatrix} \quad (3.96)$$

We have here the relation between the samples and the substitution values. This result can be replaced in the solution (3.93). The resulting matrix yields:

$$\begin{aligned} & \begin{pmatrix} 1 \\ -\left(e^{-\frac{T_s}{\tau_1}} + e^{-\frac{T_s}{\tau_2}}\right) \\ e^{-\left(\frac{T_s}{\tau_2} + \frac{T_s}{\tau_1}\right)} \end{pmatrix}^t \begin{pmatrix} 0.25 & 0.5 & 1 \\ -0.25 & 0 & 1 \\ 0.25 & -0.5 & 1 \end{pmatrix} \\ &= \begin{pmatrix} \left(1 + \left(e^{-\frac{T_s}{\tau_1}} + e^{-\frac{T_s}{\tau_2}}\right) + e^{-\left(\frac{T_s}{\tau_2} + \frac{T_s}{\tau_1}\right)}\right) / 4 \\ \left(1 - e^{-\left(\frac{T_s}{\tau_2} + \frac{T_s}{\tau_1}\right)}\right) / 2 \\ 1 - \left(e^{-\frac{T_s}{\tau_1}} + e^{-\frac{T_s}{\tau_2}}\right) + e^{-\left(\frac{T_s}{\tau_2} + \frac{T_s}{\tau_1}\right)} \end{pmatrix}^t \\ &= \begin{pmatrix} \left(1 + e^{-\frac{T_s}{\tau_1}}\right) \left(1 + e^{-\frac{T_s}{\tau_2}}\right) / 4 \\ \left(1 - e^{-\left(\frac{T_s}{\tau_2} + \frac{T_s}{\tau_1}\right)}\right) / 2 \\ \left(1 - e^{-\frac{T_s}{\tau_1}}\right) \left(1 - e^{-\frac{T_s}{\tau_2}}\right) \end{pmatrix}^t \end{aligned} \quad (3.97)$$

Dividing the result by $\left(1 - e^{-\frac{T_s}{\tau_1}}\right) \left(1 - e^{-\frac{T_s}{\tau_2}}\right)$, it yields in an one-line relation:

$$\begin{aligned} & \frac{\left(1 + e^{-\frac{T_s}{\tau_1}}\right) \left(1 + e^{-\frac{T_s}{\tau_2}}\right)}{\left(1 - e^{-\frac{T_s}{\tau_1}}\right) \left(1 - e^{-\frac{T_s}{\tau_2}}\right)} \delta\delta i^{[k]} + \frac{\left(1 - e^{-\left(\frac{T_s}{\tau_2} + \frac{T_s}{\tau_1}\right)}\right)}{\left(1 - e^{-\frac{T_s}{\tau_1}}\right) \left(1 - e^{-\frac{T_s}{\tau_2}}\right)} \frac{\Delta i^{[k]}}{\bar{i}^{[k]}} \\ &= \frac{w_2/r - \left(e^{-\frac{T_s}{\tau_1}} + e^{-\frac{T_s}{\tau_2}}\right) w_1/r}{\left(1 - e^{-\frac{T_s}{\tau_1}}\right) \left(1 - e^{-\frac{T_s}{\tau_2}}\right)} \end{aligned} \quad (3.98)$$

We define here the following discretization distortion factors:

$$K_{c2d}^{\delta\delta} \triangleq \frac{T_s^2}{4\tau_1\tau_2} \frac{\left(1 + e^{-\frac{T_s}{\tau_1}}\right) \left(1 + e^{-\frac{T_s}{\tau_2}}\right)}{\left(1 - e^{-\frac{T_s}{\tau_1}}\right) \left(1 - e^{-\frac{T_s}{\tau_2}}\right)} \quad (3.99)$$

and

$$K_{c2d}^{\Delta} \triangleq \frac{T_s}{\tau_1 + \tau_2} \frac{1 - e^{-\frac{T_s}{\tau_1} - \frac{T_s}{\tau_2}}}{\left(1 - e^{-\frac{T_s}{\tau_1}}\right) \left(1 - e^{-\frac{T_s}{\tau_2}}\right)} \quad (3.100)$$

It can be checked that $\tau_1 \tau_2 = \tau_E l_\sigma / r$ and $\tau_1 + \tau_2 = \tau + \tau_E$. Therefore, introducing (3.99) and (3.100) in (3.98) yields:

$$\begin{aligned} K_{c2d}^{\delta\delta} \tau_E l_\sigma \frac{\delta\delta i^{[k]}}{T_s^2} + K_{c2d}^{\Delta} (l + \tau_E r) \frac{\Delta i^{[k]}}{2T_s} + r \bar{i}^{[k]} \\ = \frac{w_2 - \left(e^{-\frac{T_s}{\tau_1}} + e^{-\frac{T_s}{\tau_2}}\right) w_1}{\left(1 - e^{-\frac{T_s}{\tau_1}}\right) \left(1 - e^{-\frac{T_s}{\tau_2}}\right)} \end{aligned} \quad (3.101)$$

For the development of the integral right member of (3.101), we separate the integral of w_2 between the two sampling periods:

$$\begin{aligned} w_2 &= \int_{t^{[k-2]}}^{t^{[k]}} v(t) \left(\frac{e^{-\frac{t-t^{[k]}}{\tau_1}}}{\tau_1'} + \frac{e^{-\frac{t-t^{[k]}}{\tau_2}}}{\tau_2'} \right) dt \\ &= \int_{t^{[k-1]}}^{t^{[k]}} v(t) \left(\frac{e^{-\frac{t-t^{[k]}}{\tau_1}}}{\tau_1'} + \frac{e^{-\frac{t-t^{[k]}}{\tau_2}}}{\tau_2'} \right) dt \\ &\quad + \int_{t^{[k-2]}}^{t^{[k-1]}} v(t) \left(\frac{e^{-\frac{t-t^{[k-1]}}{\tau_1}} e^{-\frac{-T_s}{\tau_1}}}{\tau_1'} + \frac{e^{-\frac{t-t^{[k-1]}}{\tau_2}} e^{-\frac{-T_s}{\tau_2}}}{\tau_2'} \right) dt \end{aligned} \quad (3.102)$$

Gathering the common sampling periods of the integrals, it yields:

$$\begin{aligned} w_2 - \left(e^{-\frac{T_s}{\tau_1}} + e^{-\frac{T_s}{\tau_2}}\right) w_1 &= \int_{t^{[k-1]}}^{t^{[k]}} v(t) \left(\frac{e^{-\frac{t-t^{[k]}}{\tau_1}}}{\tau_1'} + \frac{e^{-\frac{t-t^{[k]}}{\tau_2}}}{\tau_2'} \right) dt \\ &\quad + \int_{t^{[k-2]}}^{t^{[k-1]}} v(t) \left(\frac{e^{-\frac{t-t^{[k-1]}}{\tau_1}} e^{-\frac{-T_s}{\tau_1}}}{\tau_1'} + \frac{e^{-\frac{t-t^{[k-1]}}{\tau_2}} e^{-\frac{-T_s}{\tau_2}}}{\tau_2'} \right) dt \\ &\quad - \left(e^{-\frac{T_s}{\tau_1}} + e^{-\frac{T_s}{\tau_2}}\right) \int_{t^{[k-2]}}^{t^{[k-1]}} v(t) \left(\frac{e^{-\frac{t-t^{[k-1]}}{\tau_1}}}{\tau_1'} + \frac{e^{-\frac{t-t^{[k-1]}}{\tau_2}}}{\tau_2'} \right) dt \end{aligned} \quad (3.103)$$

$$\begin{aligned} &= \int_{t^{[k-1]}}^{t^{[k]}} v(t) \left(\frac{e^{-\frac{t-t^{[k]}}{\tau_1}}}{\tau_1'} + \frac{e^{-\frac{t-t^{[k]}}{\tau_2}}}{\tau_2'} \right) dt \\ &\quad - \int_{t^{[k-2]}}^{t^{[k-1]}} v(t) \left(\frac{e^{-\frac{t-t^{[k-1]}}{\tau_1}} e^{-\frac{-T_s}{\tau_1}}}{\tau_1'} + \frac{e^{-\frac{t-t^{[k-1]}}{\tau_2}} e^{-\frac{-T_s}{\tau_2}}}{\tau_2'} \right) dt \end{aligned} \quad (3.104)$$

$$\begin{aligned}
&= \frac{1}{\tau_1'} \left(\int_{t^{[k-1]}}^{t^{[k]}} v(t) e^{\frac{t-t^{[k]}}{\tau_1}} dt - \int_{t^{[k-2]}}^{t^{[k-1]}} v(t) e^{\frac{t-t^{[k]}}{\tau_1}} e^{-\frac{T_s}{\tau_2}} dt \right) \\
&\quad + \frac{1}{\tau_2'} \left(\int_{t^{[k-1]}}^{t^{[k]}} v(t) e^{\frac{t-t^{[k]}}{\tau_2}} dt - \int_{t^{[k-2]}}^{t^{[k-1]}} v(t) e^{\frac{t-t^{[k]}}{\tau_2}} e^{-\frac{T_s}{\tau_1}} dt \right) \quad (3.105)
\end{aligned}$$

We use here the following PWM distortion factors similarly to (3.63) :

$$k_{\text{pwm}}^1 [k] \triangleq \int_{t^{[k-1]}}^{t^{[k]}} \frac{v(t)}{\tau_1} e^{\frac{t-t^{[k]}}{\tau_1}} dt / \left(\tilde{v}^{[k]} \left(1 - e^{-\frac{T_s}{\tau_1}} \right) \right) \quad (3.106)$$

$$k_{\text{pwm}}^2 [k] \triangleq \int_{t^{[k-1]}}^{t^{[k]}} \frac{v(t)}{\tau_2} e^{\frac{t-t^{[k]}}{\tau_2}} dt / \left(\tilde{v}^{[k]} \left(1 - e^{-\frac{T_s}{\tau_2}} \right) \right) \quad (3.107)$$

Using these factors, it yields:

$$\begin{aligned}
&w_2 - \left(e^{-\frac{T_s}{\tau_1}} + e^{-\frac{T_s}{\tau_2}} \right) w_1 \\
&= \frac{\tau_1}{\tau_1'} \left(1 - e^{-\frac{T_s}{\tau_1}} \right) \left(k_{\text{pwm}}^1 [k] \tilde{v}^{[k]} - k_{\text{pwm}}^1 [k-1] \tilde{v}^{[k-1]} e^{-\frac{T_s}{\tau_2}} \right) \\
&\quad + \frac{\tau_2}{\tau_2'} \left(1 - e^{-\frac{T_s}{\tau_2}} \right) \left(k_{\text{pwm}}^2 [k] \tilde{v}^{[k]} - k_{\text{pwm}}^2 [k-1] \tilde{v}^{[k-1]} e^{-\frac{T_s}{\tau_1}} \right) \quad (3.108)
\end{aligned}$$

Or, in a matrix form:

$$= \begin{pmatrix} \frac{\tau_1}{\tau_1'} \left(1 - e^{-\frac{T_s}{\tau_1}} \right) k_{\text{pwm}}^1 [k] \\ + \frac{\tau_2}{\tau_2'} \left(1 - e^{-\frac{T_s}{\tau_2}} \right) k_{\text{pwm}}^2 [k] \\ - \frac{\tau_1}{\tau_1'} \left(1 - e^{-\frac{T_s}{\tau_1}} \right) k_{\text{pwm}}^1 [k-1] e^{-\frac{T_s}{\tau_2}} \\ - \frac{\tau_2}{\tau_2'} \left(1 - e^{-\frac{T_s}{\tau_2}} \right) k_{\text{pwm}}^2 [k-1] e^{-\frac{T_s}{\tau_1}} \end{pmatrix}^t \begin{pmatrix} v^{[k]} \\ v^{[k-1]} \end{pmatrix} \quad (3.109)$$

We can replace the voltages by the substitution values \tilde{v} and $\delta\tilde{v}$ using the definitions (3.75) and (3.76). In matrix form, the definitions are:

$$\begin{pmatrix} \tilde{v}^{[k]} \\ \delta\tilde{v}^{[k]} \end{pmatrix} = \begin{pmatrix} 0.5 & 0.5 \\ 1 & -1 \end{pmatrix} \begin{pmatrix} v^{[k]} \\ v^{[k-1]} \end{pmatrix} \quad (3.110)$$

By inverting it, it yields:

$$\begin{pmatrix} v^{[k]} \\ v^{[k-1]} \end{pmatrix} = \begin{pmatrix} 1 & 0.5 \\ 1 & -0.5 \end{pmatrix} \begin{pmatrix} \tilde{v}^{[k]} \\ \delta\tilde{v}^{[k]} \end{pmatrix} \quad (3.111)$$

This result can be replaced in the solution (3.109). The resulting matrix yields:

$$\begin{aligned}
 & \begin{pmatrix} \frac{\tau_1}{\tau_1} \left(1 - e^{-\frac{T_s}{\tau_1}}\right) k_{\text{pwm}}^1 [k] \\ + \frac{\tau_2}{\tau_2} \left(1 - e^{-\frac{T_s}{\tau_2}}\right) k_{\text{pwm}}^2 [k] \\ - \frac{\tau_1}{\tau_1} \left(1 - e^{-\frac{T_s}{\tau_1}}\right) k_{\text{pwm}}^1 [k-1] e^{-\frac{T_s}{\tau_2}} \\ - \frac{\tau_2}{\tau_2} \left(1 - e^{-\frac{T_s}{\tau_2}}\right) k_{\text{pwm}}^2 [k-1] e^{-\frac{T_s}{\tau_1}} \end{pmatrix}^t \begin{pmatrix} 1 & 0.5 \\ 1 & -0.5 \end{pmatrix} \\
 &= \begin{pmatrix} \frac{\tau_1}{\tau_1} \left(1 - e^{-\frac{T_s}{\tau_1}}\right) \left(k_{\text{pwm}}^1 [k] - k_{\text{pwm}}^1 [k-1] e^{-\frac{T_s}{\tau_2}}\right) \\ + \frac{\tau_2}{\tau_2} \left(1 - e^{-\frac{T_s}{\tau_2}}\right) \left(k_{\text{pwm}}^2 [k] - k_{\text{pwm}}^2 [k-1] e^{-\frac{T_s}{\tau_1}}\right) \\ \frac{\tau_1}{\tau_1} \left(1 - e^{-\frac{T_s}{\tau_1}}\right) \left(k_{\text{pwm}}^1 [k] + k_{\text{pwm}}^1 [k-1] e^{-\frac{T_s}{\tau_2}}\right) / 2 \\ + \frac{\tau_2}{\tau_2} \left(1 - e^{-\frac{T_s}{\tau_2}}\right) \left(k_{\text{pwm}}^2 [k] + k_{\text{pwm}}^2 [k-1] e^{-\frac{T_s}{\tau_1}}\right) / 2 \end{pmatrix}^t \quad (3.112)
 \end{aligned}$$

Note that:

$$\frac{\tau_1}{\tau_1'} = \underbrace{\frac{r\tau_1\tau_2}{l_\sigma\tau_E}}_{=1} \left(\frac{\tau_1 - \tau_E}{\tau_1 - \tau_2}\right) \quad \text{and} \quad \frac{\tau_2}{\tau_2'} = \underbrace{\frac{r\tau_1\tau_2}{l_\sigma\tau_E}}_{=1} \left(\frac{\tau_2 - \tau_E}{\tau_2 - \tau_1}\right) \quad (3.113)$$

Introducing these results, (3.109) yields:

$$\begin{aligned}
 & \frac{v_2 - \left(e^{-\frac{T_s}{\tau_1}} + e^{-\frac{T_s}{\tau_2}}\right) v_1}{\left(1 - e^{-\frac{T_s}{\tau_1}}\right) \left(1 - e^{-\frac{T_s}{\tau_2}}\right)} \\
 &= \begin{pmatrix} \left(\frac{\tau_1 - \tau_E}{\tau_1 - \tau_2}\right) \frac{k_{\text{pwm}}^1 [k] - k_{\text{pwm}}^1 [k-1] e^{-\frac{T_s}{\tau_2}}}{1 - e^{-\frac{T_s}{\tau_2}}} \\ + \left(\frac{\tau_2 - \tau_E}{\tau_2 - \tau_1}\right) \frac{k_{\text{pwm}}^2 [k] - k_{\text{pwm}}^2 [k-1] e^{-\frac{T_s}{\tau_1}}}{1 - e^{-\frac{T_s}{\tau_1}}} \\ \left(\frac{\tau_1 - \tau_E}{\tau_1 - \tau_2}\right) \frac{k_{\text{pwm}}^1 [k] + k_{\text{pwm}}^1 [k-1] e^{-\frac{T_s}{\tau_2}}}{1 - e^{-\frac{T_s}{\tau_2}}} / 2 \\ + \left(\frac{\tau_2 - \tau_E}{\tau_2 - \tau_1}\right) \frac{k_{\text{pwm}}^2 [k] + k_{\text{pwm}}^2 [k-1] e^{-\frac{T_s}{\tau_1}}}{1 - e^{-\frac{T_s}{\tau_1}}} / 2 \end{pmatrix}^t \begin{pmatrix} \tilde{v} [k] \\ \delta \tilde{v} [k] \end{pmatrix} \quad (3.114)
 \end{aligned}$$

We define here one new discretization distortion factor and two new PWM distortion factors as follows:

$$k_{\text{pwm}}^{\sim [k]} \triangleq \left(\frac{\tau_1 - \tau_E}{\tau_1 - \tau_2} \right) \frac{k_{\text{pwm}}^{1 [k]} - k_{\text{pwm}}^{1 [k-1]} e^{-\frac{T_s}{\tau_2}}}{1 - e^{-\frac{T_s}{\tau_2}}} + \left(\frac{\tau_2 - \tau_E}{\tau_2 - \tau_1} \right) \frac{k_{\text{pwm}}^{2 [k]} - k_{\text{pwm}}^{2 [k-1]} e^{-\frac{T_s}{\tau_1}}}{1 - e^{-\frac{T_s}{\tau_1}}} \quad (3.115)$$

$$K_{c2d}^{\delta} \triangleq \frac{T_s}{2\tau_E} \left(\left(\frac{\tau_1 - \tau_E}{\tau_1 - \tau_2} \right) \frac{1 + e^{-\frac{T_s}{\tau_2}}}{1 - e^{-\frac{T_s}{\tau_2}}} + \left(\frac{\tau_2 - \tau_E}{\tau_2 - \tau_1} \right) \frac{1 + e^{-\frac{T_s}{\tau_1}}}{1 - e^{-\frac{T_s}{\tau_1}}} \right) \quad (3.116)$$

$$k_{\text{pwm}}^{\delta [k]} \triangleq \frac{T_s}{2\tau_E} \left(\left(\frac{\tau_1 - \tau_E}{\tau_1 - \tau_2} \right) \frac{k_{\text{pwm}}^{1 [k]} + k_{\text{pwm}}^{1 [k-1]} e^{-\frac{T_s}{\tau_2}}}{1 - e^{-\frac{T_s}{\tau_2}}} + \left(\frac{\tau_2 - \tau_E}{\tau_2 - \tau_1} \right) \frac{k_{\text{pwm}}^{2 [k]} + k_{\text{pwm}}^{2 [k-1]} e^{-\frac{T_s}{\tau_1}}}{1 - e^{-\frac{T_s}{\tau_1}}} \right) / K_{c2d}^{\delta} \quad (3.117)$$

Introducing these factors in (3.109) and replacing the integral right member of (3.101) by the result, it yields the discrete-time model expression:

$$K_{c2d}^{\delta\delta} \tau_E l_{\sigma} \frac{\delta\delta i^{[k]}}{T_s^2} + K_{c2d}^{\Delta} (l + \tau_E r) \frac{\Delta i^{[k]}}{2T_s} + r \bar{i}^{[k]} = k_{\text{pwm}}^{\sim [k]} \tilde{v}^{[k]} + K_{c2d}^{\delta} k_{\text{pwm}}^{\delta [k]} \tau_E \frac{\delta\tilde{v}^{[k]}}{T_s} \quad (3.118)$$

Let us define the equivalent discrete-time parameters as follows:

$$\left\{ \begin{array}{l} \bar{\tau}_E^{[k]} \triangleq \tau_E K_{c2d}^{\delta} k_{\text{pwm}}^{\delta [k]} / k_{\text{pwm}}^{\sim [k]} \\ \bar{r}^{[k]} \triangleq r / k_{\text{pwm}}^{\sim [k]} \\ \bar{l}_{\sigma}^{[k]} \triangleq l_{\sigma} K_{c2d}^{\delta\delta} / K_{c2d}^{\delta} / k_{\text{pwm}}^{\delta [k]} \\ \bar{l}^{[k]} \triangleq (l + \tau_E r) K_{c2d}^{\Delta} / k_{\text{pwm}}^{\sim [k]} - \bar{\tau}_E^{[k]} \bar{r}^{[k]} \end{array} \right. \quad (3.119)$$

Assume that the PWM distortion error is small, i.e. $k_{\text{pwm}}^{\delta} \approx 1$ and $k_{\text{pwm}}^{\sim} \approx 1$, $\forall k$. By consequence, the discrete-time parameters (3.119) are assumed constant and the index $[k]$ can be removed. Introducing them in (3.118) yields the following discrete-time model:

$$\tilde{v}^{[k]} + \bar{\tau}_E \frac{\delta\tilde{v}^{[k]}}{T_s} = \bar{\tau}_E \bar{l}_{\sigma} \frac{\delta\delta i^{[k]}}{T_s^2} + (\bar{l} + \bar{\tau}_E \bar{r}) \frac{\Delta i^{[k]}}{2T_s} + \bar{r} \bar{i}^{[k]} \quad (3.120)$$

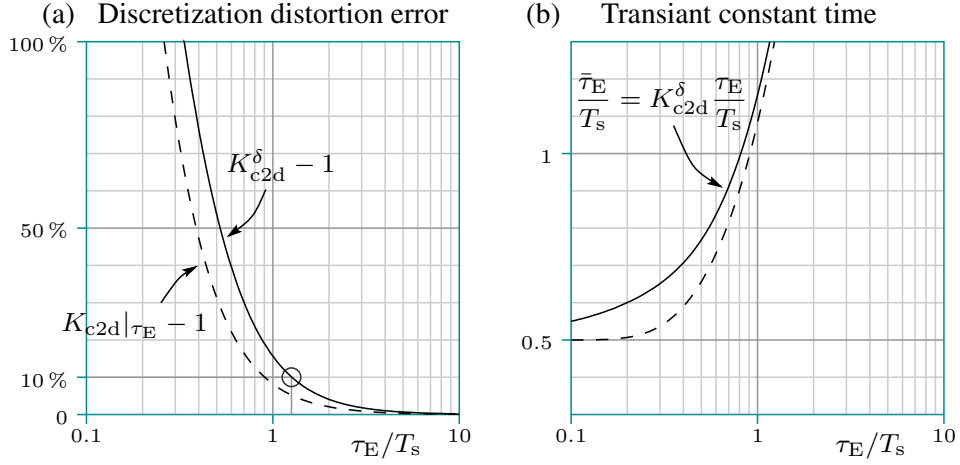


Figure 3.8: Graph of (a) the discretization distortion error $K_{c2d}^\delta - 1$ (plain line) as a function of τ_E/T_s and the 10% error point (\circ), for the case $l_\sigma/l = 0.5$. Illustration of the shift with respect to the graph of $K_{c2d}|_{\tau_E} - 1$ (dashed line) shown in Figure 3.6(a), as the ratio $l_\sigma/l < 1$ decreases ; Graph of (b) $\bar{\tau}_E$ in ratio with the sampling period T_s (plain line). Illustration of the shift with respect to the graph Figure 3.6(b) (dashed line), as the ratio $l_\sigma/l < 1$ decreases.

Analysis of the parameter distortions

As shown by (3.119), the discretization distorts all the substituting discrete-time parameters $\bar{\tau}_E$, \bar{l}_σ and \bar{l} with respect to their continuous-time parameters, except the resistance \bar{r} . In order to limit the length of this analysis, we propose here to assume that the stator resistance is negligible: $r \approx 0$; and therefore that the stator transient time-constant is much larger than the PWM period: $\tau = r/l \gg T_s$. The discretization distortions are therefore only related to the presence of the eddy currents, that vary as a function of the transient time-constant of the eddy-current circuit: τ_E . With this assumption, using (3.100) it can be shown that $K_{c2d}^\Delta \rightarrow 1$. Using (3.99) it can be shown that $K_{c2d}^{\delta\delta} \rightarrow K_{c2d}|_{\tau_E}$, where $K_{c2d}|_{\tau_E}$ is the discretization distortion factor (3.67) computed with τ_E instead of τ . The conclusions on this factor of distortion are therefore similar to the conclusions proposed in the previous subsection, related to the Figure 3.6. As illustrated in Figure 3.8(a), the factor K_{c2d}^δ computed in (3.116) deviates from $K_{c2d}|_{\tau_E}$ as the ratio $l_\sigma/l < 1$ decreases. The 10% error limit tends to shift to higher values of τ_E while l_σ/l decreases. Figure 3.8(b) shows the variation of the discrete-time transient time constant $\bar{\tau}$ as a function of τ . We can see that lower l_σ/l , higher the distortion due to the discretization. Concerning the PWM distortion factors, their graphs are not shown here. We assume that the conclusion on these factors are similar to the previous conclusions concerning the case of a model without eddy current.

As a first conclusion, we see that even if the stator circuit model presents an adequate transient time-constant $\tau \gg T_s$, this does not prevent from an impact of

eddy currents on the discretization. This impact is analyzed hereafter, focusing on signal-injection-based self-sensing methods. Note also that many models including the eddy currents assume a large value of r_E . This assumption however lead to high values of τ_E and the discretization impact is therefore augmented. This is not necessarily a big issue, but this should however be considered to validate the model.

3.5 Machine Impedance

Many anisotropy-based self-sensing methods using high-frequency signal-injections are based on the identification of the high-frequency *admittance* linking the high-frequency test voltage to the high-frequency current response, and written $y(\omega)$. If the admittance contains an anisotropy linked to the rotor, it can be used to track the rotor position. In a machine model where the eddy currents are neglected, the *impedance* $z(\omega)$, that is the inverse of the admittance $y(\omega) = 1/z(\omega)$, is easily handled as the sum of the stator resistance, r , and the incremental self-inductance multiplied by the frequency of the signals, $j\omega l$. In case of significant eddy currents, this model is not valid anymore. Nevertheless, many authors propose to keep that model and to transpose the impact of the eddy currents on variations of r and l . These parameters becomes then frequency-dependent. They are sometimes referred to as “*frequency-dependent*”, “*apparent*”, “*eddy-currents-reflected*” or simply “*high-frequency*” [88, 89, 90, 82, 91, 85]. We chose to keep the denomination “*apparent*” parameters. Signal-injection based self-sensing methods generally rely on the apparent incremental self-inductance.

In this section, we propose the expression of these apparent parameters considering the impact of the eddy-currents, but also the impact of the discretization. For this, we use the discretized models (3.120) and (3.70) that were developed in the previous assuming a standstill machine and assuming anisotropic relations presenting equal anisotropy orientations, such that the relations can be separated along the x and y -axes (entirely uncoupled). A more general model can probably be proposed without these assumptions, but this is not done here. The different distortion on these apparent parameters are analyzed. Finally, comparisons between simulations and experiments validate the models.

For convenience, the upper index $[k]$ referring to the PWM/sampling period will not be mentioned on the symbols in the text if it is not confusing. We assume that the current variations related to the signal injection are small enough in order to use the incremental models. For convenience also, the subscript t indicating incremental parameters is removed, but all the parameters are necessarily incremental.

3.5.1 Continuous-time parameters

In order to allow a comparison, we propose here to introduce the apparent parameters for the continuous-time case. The model of the standstill machine, along any of the xy -axes, neglecting the eddy currents is:

$$v(t) = l \frac{di(t)}{dt} + ri(t) \quad (3.121)$$

The impedance $z(\omega)$ is defined as the frequency response of the circuit, computed as the transmittance linking the *Fourier-transform* of the current $\mathcal{F}\{i\}$ to the Fourier-transform of the voltage $\mathcal{F}\{v\}$ [46]. It is found using the following property:

$$\mathcal{F}\{dx/dt\} = j\omega\mathcal{F}\{x\} \quad x \in \{v, i\} \quad (3.122)$$

And yields:

$$z(\omega) \triangleq \mathcal{F}\{v\}/\mathcal{F}\{i\} = j\omega l + r \quad (3.123)$$

where ω is the considered signal frequency. Including the eddy currents, the model is:

$$v(t) + \tau_E \frac{dv(t)}{dt} = \tau_E l_\sigma \frac{d^2 i(t)}{dt^2} + (l + \tau_E r) \frac{di(t)}{dt} + ri(t) \quad (3.124)$$

The impedance $z(\omega)$ then yields:

$$z(\omega) = \frac{j\omega(l + \tau_E r) + r - \omega^2 \tau_E l_\sigma}{1 + j\omega \tau_E} \quad (3.125)$$

Using $l_\sigma = l - l_E$, this impedance can be rearranged as follows:

$$\begin{aligned} z(\omega) &= \frac{j\omega(l + \tau_E r) + r - \omega^2 \tau_E l_\sigma}{1 + \omega^2 \tau_E^2} (1 - j\omega \tau_E) \\ &= \frac{j\omega(l + \tau_E r) + r - \omega^2 \tau_E l_\sigma + \omega^2 \tau_E (l + \tau_E r) - j\omega \tau_E (r - \omega^2 \tau_E l_\sigma)}{1 + \omega^2 \tau_E^2} \\ &= \frac{j\omega(l + \omega^2 \tau_E^2 l_\sigma)}{1 + \omega^2 \tau_E^2} + \frac{(1 + \omega^2 \tau_E^2)r + \omega^2 \tau_E (l - l_\sigma)}{1 + \omega^2 \tau_E^2} \\ &= j\omega \underbrace{\left(l - l_E \frac{\omega^2 \tau_E^2}{1 + \omega^2 \tau_E^2} \right)}_{\hat{l}(\omega)} + \underbrace{\left(r + r_E \frac{\omega^2 \tau_E^2}{1 + \omega^2 \tau_E^2} \right)}_{\hat{r}(\omega)} \quad (3.126) \end{aligned}$$

We highlighted here the apparent resistance $\hat{r}(\omega)$ and the apparent incremental self-inductance $\hat{l}(\omega)$. As we can see, they are frequency-dependent.

Analysis of the apparent values

Including eddy currents, the apparent resistance and incremental self-inductance of the continuous-time operations are illustrated in Figure 3.9. We see that \hat{r} varies

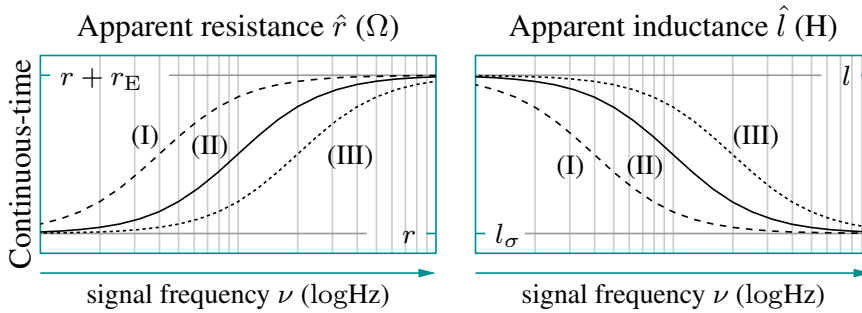


Figure 3.9: Illustration of the apparent parameter values of the continuous-time model including eddy currents, as a function of the frequency $\nu = \omega/(2\pi)$. Graphs for cases: $\tau_{E,(I)} > \tau_{E,(II)} > \tau_{E,(III)}$.

between r at low frequencies and $r + r_E$ at higher frequencies ; and that \hat{l} varies between l at low frequencies and $l_\sigma = l - l_E$ at higher frequencies. The frequency range where the apparent parameters shift between the two extrema values depends on the eddy circuit transient time-constant τ_E . Higher τ_E , lower is the frequency of the shift. This is illustrated with cases (I), (II) and (III). This property is used in some self-sensing strategies where a dedicated closed coil is added at the rotor side [68, 68]. This coil can be handled using the same model as the eddy current circuit. It is added along the d or the q-axis in order to modify the anisotropy at higher frequency without affecting the lower-frequency behaviour of the model.

3.5.2 Discrete-time parameters

The discrete-time model of the standstill machine, along any of the xy-axes, neglecting the eddy currents is:

$$\hat{v}^{[k]} = \bar{l} \frac{\delta i^{[k]}}{T_s} + \bar{r} i^{[k]} \quad (3.127)$$

The transmittance linking the *Discrete-time Fourier-transform* (DTFT) of two values is found using the following property [46]:

$$\mathcal{F}\{x^{[k+1]}\} = e^{j\omega T_s} \mathcal{F}\{x^{[k]}\} \quad \text{for } x^{[k]} \in \{v^{[k]}, i(t^{[k]}), \bar{i}^{[k]}, \delta i^{[k]}, \dots\} \quad (3.128)$$

Thanks to this property, we can compute the relation between the DTFT of the average current \bar{i} and the sampling backward-difference δi :

$$\mathcal{F}\{i(t^{[k]})\} = e^{j\omega T_s} \mathcal{F}\{i(t^{[k-1]})\} \Rightarrow \mathcal{F}\{\delta i\} = \frac{2(1 - e^{-j\omega T_s})}{1 + e^{-j\omega T_s}} \mathcal{F}\{\bar{i}\} \quad (3.129)$$

This relation can be rearranged in order to define the discrete-time frequency $\bar{\omega}$:

$$\frac{2(1 - e^{-j\omega T_s})}{1 + e^{-j\omega T_s}} = \frac{2(e^{j\omega T_s/2} - e^{-j\omega T_s/2})}{e^{j\omega T_s/2} + e^{-j\omega T_s/2}} = j \underbrace{\frac{2}{T_s} \tan(\omega \frac{T_s}{2})}_{\bar{\omega}} T_s \quad (3.130)$$

Such that $\delta i/T_s = j\bar{\omega}\bar{i}$. Let us define $\omega_s = 2\pi/T_s$. Note that $\bar{\omega} \rightarrow \omega$ when $\omega \ll \omega_s$. Using this result in (3.127) yields the impedance $\bar{z}(\omega)$:

$$\bar{z}(\omega) \triangleq \mathcal{F}\{\tilde{v}\}/\mathcal{F}\{\bar{i}\} = j\bar{\omega}\bar{l} + \bar{r} \quad (3.131)$$

This expression is quite similar to the continuous-time impedance (3.125). Including the eddy currents, the model is:

$$\tilde{v}^{[k]} + \bar{r}_E \frac{\delta \tilde{v}^{[k]}}{T_s} = \bar{r}_E \bar{l}_\sigma \frac{\delta \delta i^{[k]}}{T_s^2} + (\bar{l} + \bar{r}_E \bar{r}) \frac{\Delta i^{[k]}}{2T_s} + \bar{r} \bar{i}^{[k]} \quad (3.132)$$

Thanks to the property (3.128), we can compute the relation between the DTFT of the average current on two periods \bar{i} , the backward-difference after two periods Δi and the backward-second-difference $\delta \delta i$:

$$\mathcal{F}\{\Delta i\} = \frac{4(1 - e^{-2j\omega T_s})}{1 + 2e^{-j\omega T_s} + e^{-2j\omega T_s}} \mathcal{F}\{\bar{i}\} = 2j\bar{\omega}T_s \mathcal{F}\{\bar{i}\} \quad (3.133)$$

and

$$\mathcal{F}\{\delta \delta i\} = \frac{4(1 - 2e^{-j\omega T_s} + e^{-2j\omega T_s})}{1 + 2e^{-j\omega T_s} + e^{-2j\omega T_s}} \mathcal{F}\{\bar{i}\} = -\bar{\omega}^2 T_s^2 \mathcal{F}\{\bar{i}\} \quad (3.134)$$

We have also the following relation:

$$\mathcal{F}\{\delta \tilde{v}\} = j\bar{\omega}T_s \mathcal{F}\{\tilde{v}\} \quad (3.135)$$

Using these relations, the impedance $z(\omega)$ then yields an expression similar to the continuous-time impedance (3.126):

$$\bar{z}(\omega) = j\bar{\omega} \underbrace{\left(\bar{l} - \bar{l}_E \frac{\bar{\omega}^2 \bar{\tau}_E^2}{1 + \bar{\omega}^2 \bar{\tau}_E^2} \right)}_{\hat{l}(\omega)} + \underbrace{\left(\bar{r} + \bar{r}_E \frac{\bar{\omega}^2 \bar{\tau}_E^2}{1 + \bar{\omega}^2 \bar{\tau}_E^2} \right)}_{\hat{r}(\omega)} \quad (3.136)$$

where $\hat{r}(\omega)$ and $\hat{l}(\omega)$ are the apparent resistance and incremental self-inductance of the discrete-time model.

Analysis of the distortions

Consider firstly the case where we neglect the PWM and discretization distortions. The apparent resistance and inductance of the discrete-time operations are illustrated in Figure 3.10. From (3.130), we deduced that $\bar{\omega} \rightarrow \omega$ when the sampling frequency is much higher than the signal frequency, i.e. $\omega T_s \ll \pi$. In that case, illustrated by (I) by the plain line, the discrete-time behaviour of the machine is similar to the continuous-time case Figure 3.9(II). When the sampling frequency is decreasing however, i.e. $\omega T_s \rightarrow \pi$, then $\bar{\omega} \rightarrow \infty$. Note that $\omega T_s \not\ll \pi$ since it is not possible to produce an oscillating signal with a frequency higher than half

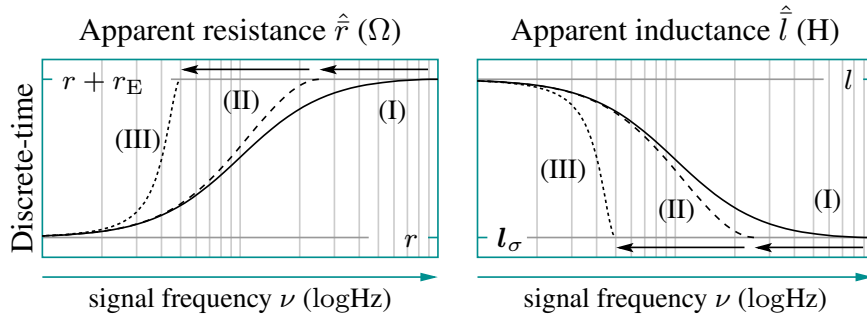


Figure 3.10: Illustration of the apparent parameter values of the discrete-time model including eddy currents but neglecting discretization distortions. Graphs for cases: $\nu_{s,(I)} > \nu_{s,(II)} > \nu_{s,(III)}$, τ_E constant.

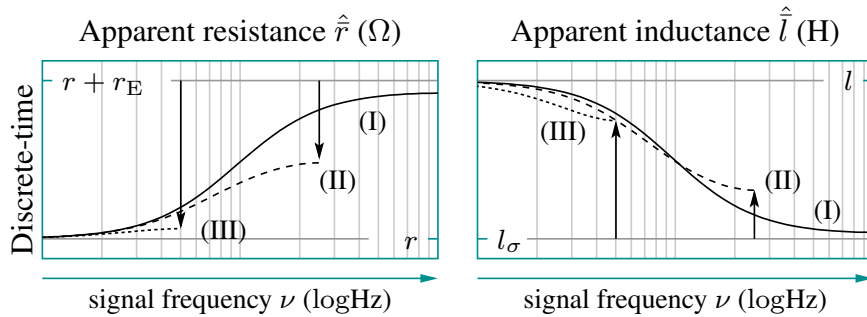


Figure 3.11: Illustration of the apparent parameter values of the discrete-time model including eddy currents and taking distortions into account. Graphs for cases: $\nu_{s,(I)} > \nu_{s,(II)} > \nu_{s,(III)}$, τ_E constant.

the sampling frequency $\nu \neq \nu_s/2$. The shift of $\bar{\omega}$ regarding ω distorts the graph of the apparent parameters of the discrete-time compared to the continuous-time: the values are shifted up to the maximum frequency $\nu_s/2$. This is illustrated with different sampling frequency cases Figure 3.10(II) and (III).

Taking the discretization distortions into account (assuming $\tau_E \ll \tau$), the apparent resistance and inductance of the discrete-time operations are illustrated in Figure 3.11. The distortions result in vertical shift of the graphs compared to the case neglecting the distortions. This is illustrated with different sampling frequency cases (I)-(III). Compared to the continuous-time case Figure 3.9(II), the deviations and distortions of the discrete-time impact like an homothetic contraction of the curves. Even with very small τ_E , the eddy current would therefore still be observed on the graphs. But while the sampling frequency decreases, the eddy current impact decreases in amplitude and could not be measurable anymore.

In order to reduce the eddy currents, one can use specific designs, such as the modular topology [25].

3.5.3 Experiments and Simulations

Experimental set-up

The experiments are performed on the standstill uncoupled experimental BLDC machine with PM oriented following $\varphi_d = 120^\circ$, equivalent to $\varphi_q = 30^\circ$ as illustrated in Figure 3.1(a). The PM flux is positive in the negative d-axis direction. The operating stator current \hat{i}_o has an amplitude of 25 A and is oriented along the negative d-axis, i.e. $\angle \hat{i}_o = -60^\circ$. This operating stator current is chosen in order to prevent some effects of the inverter nonlinearities and in order to keep the rotor fixed in the desired position. As introduced in chapter 2, with these rotor and current conditions, we have an alignment of the qd frame and the xy frame [92]. Therefore: $x \approx q$ and $y \approx d$.

The apparent discrete-time parameters of the experimental machine are identified by the injection of pulsating high-frequency voltages, once along the d-axis and once along the q-axis. More details about the signal injection methods are found in chapter 5. In order to validate the characteristic curves illustrated in Figure 3.11, the identifications are performed with series of 20 different frequencies ν , that are integer fractions of the PWM frequency: between half the PWM frequency $\nu = \nu_s/2$ down to a fourth of the PWM frequency $\nu = \nu_s/40$. Each series are performed for three different PWM frequencies ν_s at 13 kHz, 10 kHz and 6 kHz. It was not possible to reach higher frequencies due to measurement constrains from the DSP. In order to assess the standard deviation due to the measurement noise, the computation of each point of the curves is based on 201 samples.

Along the axis	$\nu_s = 13$ kHz	10 kHz	6 kHz
$x \approx q$	9.6 A	6.0 A	4.8 A
$y \approx d$	14.1 A	9.0 A	7.0 A

Table 3.1: Amplitudes of the high-frequency current response $|\hat{i}|$.

In order to produce equal high-frequency current amplitudes during every series, the amplitude of the high-frequency voltage is adapted at each frequency ν , from 11.5 V at $\nu = \nu_s/2$ down to 1.8 V at $\nu = \nu_s/40$. Since the results for every series were not predictable, the voltage amplitude were not adapted along the two axes and for the different PWM frequencies. This choice leads to very different high-frequency current amplitudes, given in Table 3.1. The order of amplitudes (between 3.6 % and 10.5 % of the rated current) was chosen to obtain a satisfying signal-to-noise response, especially for the resistance identification.

Measurements compared to simulations

The machine parameters for the simulation have been empirically adjusted in order to correspond, as good as possible, to the experimental results. By consequence, experiments precede simulations. Parameter estimations are shown in Table 3.2.

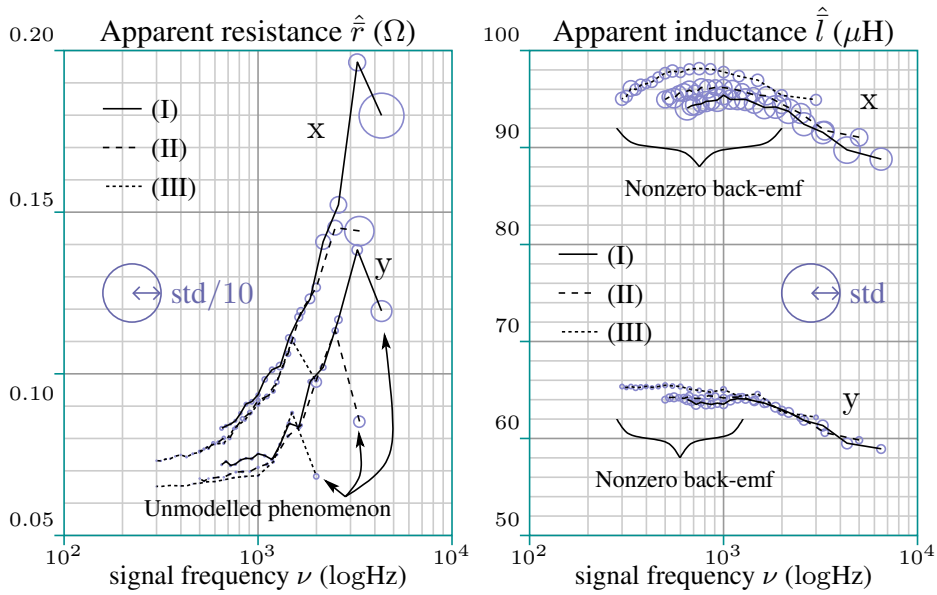


Figure 3.12: Experimental results of the apparent discrete-time parameter values along the x-axis and y-axis. Graphs for cases: $\nu_{s,(I)} = 13$ kHz (—), $\nu_{s,(II)} = 10$ kHz (---), $\nu_{s,(III)} = 6$ kHz (⋯). The radius of the circles indicate the standard deviation of each point (tenth of it for \hat{r}).

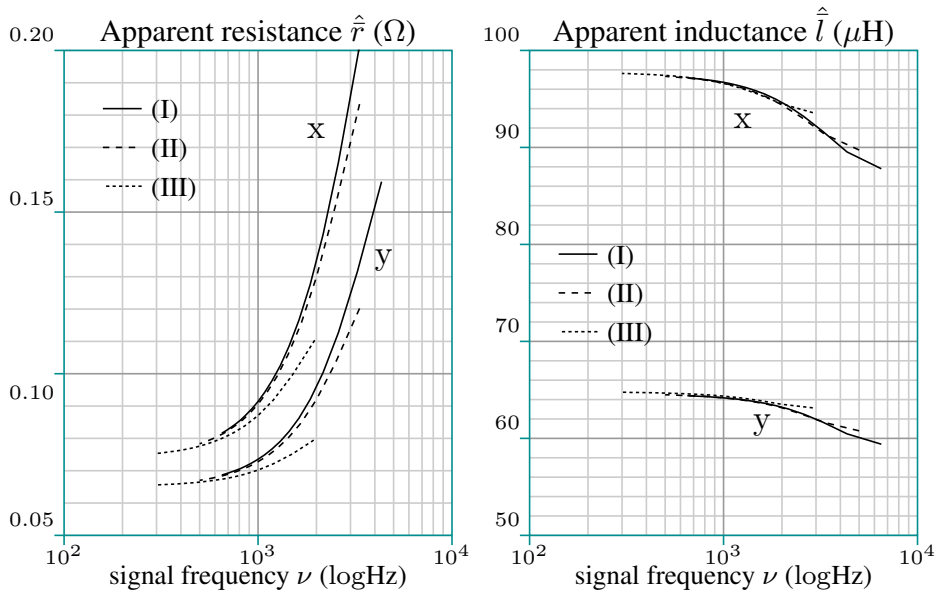


Figure 3.13: Simulation of the apparent discrete-time parameter values along the x-axis and y-axis assuming continuous-time values given in Table 3.2. Graphs for cases: $\nu_{s,(I)} = 13$ kHz (—), $\nu_{s,(II)} = 10$ kHz (---), $\nu_{s,(III)} = 6$ kHz (⋯).

Along the axis	r (Ω)	l (μH)	τ (μs)	r_E (Ω)	l_σ (μH)	τ_E (μs)
$x \approx q$	0.068	95.5	1404	0.5	80	31
$y \approx d$	0.059	62.5	1059	0.5	51.5	22

Table 3.2: Continuous-time parameters used for the simulations.

Figure 3.12 shows the experimental results with series of identification tests performed along the x-axis and the y-axis for three different sampling frequencies. Each estimation is computed from 201 samples. The standard deviation (std) is indicated by circles on the graphs. The std is notably larger for \hat{r} compared to \hat{l} . Thus the circle radius indicates tenth of the std for \hat{r} . This difference is explained by the relative smaller impact of the resistance compared to the inductance, leading to important noise estimations.

Figure 3.13 shows the simulation results to be compared with Figure 3.12. The first difference concerns the last estimation of \hat{r} that suddenly deflects downwardly. This is possibly due to missing phenomenon in the modelling such as multiple eddy current sources, skin effects or simply VSI-PWM nonlinearities. The second difference concerns the deflection of the estimation of \hat{l} for lower frequencies. This is possibly due to the emergence of undamped high-frequency oscillations and thus to nonzero back-emf. This explanation is evidenced by the higher impact along the x-axis, that is aligned with the torque producing q-axis. Besides these differences, the simulations are consistent with the experiments.

As a conclusion for this experimental machine, the eddy currents produce significant distortions of the discrete-time parameters, mainly on the apparent resistance \hat{r} that is very sensitive to the signal frequency and to the PWM frequency. These effects should be increased with the rotation speed $\omega_q \neq 0$, since angular variations of the inductance appear in the relation (3.59), and that these variations should a fortiori be involved also in the model that includes the eddy currents (3.59). The incremental self-inductance \hat{l} is also distorted. A large difference of the incremental self-inductance between the two qd axes is however maintained. As consequence, this value is still a very good candidate for digital anisotropy-based self-sensing operations.

3.6 Summary

In this chapter, we introduced the electrical model of the machine using complex and matrix space vectors. The issue of cross-saturation, corresponding to anisotropy misalignment, is discussed. The model in the stationary reference-frame, without eddy current, is given in (3.48). This expression involves many terms:

- the anisotropic incremental relation, that contains the rotor position information to extract ;

- the stator resistance that can present anisotropic properties independent to the rotor position, as shown in shown in (3.29) ;
- terms related to the variation of the inductance ;
- the back-EMF.

Because the control and the self-sensing operations are based on digital measurements, a discrete-time model expression is advised. The distortion of the discrete-time parameters with respect to the continuous-time parameters is mathematically studied under the following hypothesis:

- the PWM of the VSI operates on fixed period lengths T_s ;
- the sampling of the measurements is synchronized at the beginning of the PWM periods ;
- we assume a standstill motor for reasons of simplicity in the mathematical developments ;
- we assume that the model relations can be uncoupled along x and y-axes.

It was possible to distinct two factors of distortion on the parameters:

1. one related to the discretization operation, modelled by the *discretization distortion factor* ;
2. another related to the voltage commutations caused by the PWM, and modelled by the *PWM distortion factor*.

It is firstly shown that the discretization distortion is larger that the PWM distortion factor, such that we may focus on the discretization distortion only. In case of negligible eddy currents, the distortion is function of τ/T_s , where $\tau = l/r$ is the transient time-constant of the stator circuit. Lower this transient time-constant, higher the distortion. It is shown that the discretization distortion reaches 10 % at $\tau/T_s = 0.9$. Fortunately, the stator resistance in many machine is very small and this condition is satisfied. This is the case of the experimental BLDC motor, where $\tau_y/T_s = 6.35$ for the worst studied case at $\nu_s = 6$ kHz. Noticeable distortions are however experimentally observed and denotes the presence of significant eddy currents.

A second mathematical study is thus performed based on an initial continuous-time model including the eddy currents at standstill. Assuming that the transient time-constant of the stator circuit is much higher than the sampling period $\tau \gg T_s$, the distortion is mainly function of τ_E/T_s , where τ_E is the transient time-constant of the eddy-current circuit. Lower this transient time-constant, higher the distortion. In the case of the experimental BLDC motor, $\tau_{E,x}/T_s = 0.31$ for the best studied case at $\nu_s = 10$ kHz. This is very small and it explains why the eddy currents have a significant impact on the parameter distortions.

In practice, self-sensing operations identify the machine impedance. This impedance is generally divided in resistive and inductive contributions. If the eddy currents are negligible, the resistive contribution is directly related to the stator resistance and the inductive contribution is related to the incremental self-inductance. If the eddy currents are significant however, many publications on self-sensing methods still model the contributions by apparent parameters. These parameters become frequency-dependent and are sometimes referred to as eddy-current-reflected.

The strange behaviour of the discretization distortion and the eddy currents are mathematically analyzed. Comparing with simulations, experimental results performed on the BLDC motor allow to estimate the motor parameters, including the inaccessible inductance and resistance of the eddy current circuit. These results do not lead to any self-sensing method improvement, but it gives important information on the machine in order to select the self-sensing method that is the more adequate.

Note finally that identification methods based on the injection of multi-sine [93] could have been implemented in order to observe the importance of the eddy currents. However, this type of identification requires additional offset, which we did not have.

Chapter 4

Voltage-Source Inverter

This chapter addresses the issues of nonlinearities in widespread two-level three-phase voltage source inverters (VSI) commanded by conventional pulsewidth modulated (PWM) signals. Some characteristics of the PWM-VSI leads to nonlinear relations between the command voltage send to the PWM signal generator and the expected output voltage. They are mainly due to voltage drops at the semiconductors and to commutation delays resulting in so-called *dead times*. Related to these nonlinearities, when a phase current crosses zero during the dead times, it is clamped to zero for the rest of that dead time. This phenomenon is referred to as the *zero-clamping* and has important consequences on the control and on the self-sensing operations. Solutions to this zero-clamping consist to prevent for zero-crossings, as largely proposed in this chapter.

4.1 Introduction

Many traditional control methods use the command voltage in their models [94], since the nonlinearities generally have limited impacts on the current controller, that compensates for these effects. The self-sensing methods however require an accurate knowledge of the voltages applied at the machine terminals [95, 96], and the voltage distortions due to the nonlinearities may have a significant impacts on the rotor position estimations.

One solution to overcome the nonlinearities consist to introduce voltage sensors measuring the mean value of the output voltage during a PWM period, using dedicated analog [84] or digital integrators [97]. The voltage sensors however reduce the reliability of the drive (these sensors are additional sources of failure), require data-acquisition hardware [98], result in additional costs and are additional source of noise to consider. Another solution consists in the compensation of the nonlinearities. An overview of these nonlinearities and a state-of-the-art of some solutions to compensate for them are proposed in the first half of the chapter. We also introduce the problem of the *zero-clamping effect* occurring when a phase current crosses zero.

This zero-clamping effect is noticeable on the experimental BLDC motor. Its impact was so large that the self-sensing methods initially implemented in the machine were inefficient and the position was quickly lost during the rotation. It was therefore absolutely required to find a method to overcome that problem. Since the solutions found in the existing literature were irrelevant for the experimental conditions, the only solution found was to prevent the zero-crossings of the current adding an offset to the instruction, with a reduced impact on the torque. This solution is addressed in the second half of this chapter

~

This chapter is organized as follows: the section 4.2 introduces elementary descriptions of the two-level voltage-source inverter design, the modulation techniques and the different nonlinearities, including the zero-clamping phenomenon occurring when a phase crosses zero ; Section 4.3 describes the zero-crossing issue for the point of view of space vectors, and proposes a model of the current ripples that result from the modulation. It also introduces two methods for the estimation of the minimum margin required between the current samples and the zero-crossing lines in order to prevent zero-crossings by the ripples. Finally, it introduces the operations of the zero-crossing prevention based on the estimated margins ; Section 4.4 analyzes the margin estimations for the case of the experimental BLDC motor ; A summary of the important elements of this chapter is given in section 4.5.

4.2 Pulse-Width Modulated Voltage

This section describes the design of the *voltage source inverter* (VSI) and its mathematical model. A VSI provides several outputs with commanded voltages. The number of outputs is related to the number of machine terminals to be connected. The denomination of *phase* may also refer to the circuits of the VSI for the different outputs, but they should not be confused with the machine phases.

We consider a *two-level* VSI, as it is the most simple and the most widespread topology used in industrial power drive applications [99, 18]. In this topology, each output is switched between two voltages, called high or low level voltages, by commanding the conductivity of two half-bridges. The design of one phase is described in section 4.2.1. We consider that the half-bridges of every phase are commanded by *carrier-based pulsewidth modulated* signals [18], also simply called *pulsewidth modulated* (PWM) signals, based on cyclical sequences of commutations. A review of the state-of-the-art about carrier-based PWM and others such as carrierless PWM and PWM-control schemes at the year of 1994 is given in [18]. Section 4.2.2 addresses the PWM principle, the concept of symmetric and asymmetric modulation techniques, and the PWM computation assuming an ideal PWM-VSI. Non-ideal effects of the real VSI (non-ideal) are explained in section 4.2.3, section 4.2.4 and section 4.2.4.

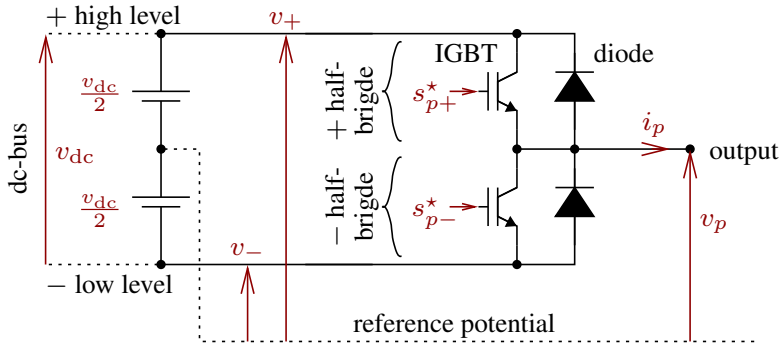


Figure 4.1: Design of one phase p of a two-level VSI: a dc-bus with a dc voltage v_{dc} between a high level (+) and a low level (-); two half-bridges (+) and (-) with freewheeling devices (diode) and switching devices (IGBT) driven by two switching signals s_{p+}^* and s_{p-}^* ; an output that presents a voltage v_p and delivers a current i_p .

4.2.1 The Two-Level Design

The circuit of one phase p of the VSI is shown in Figure 4.1. It is made of two *half-bridges*, one connected to the *high level* and the other to the *low level* of the dc-bus, respectively denoted + and -. If the point of the middle voltage of the dc-bus is connected to the ground potential, taken as reference potential, the high and low level voltages are $v_+ = v_{dc}/2$ and $v_- = -v_{dc}/2$ respectively, where v_{dc} is the dc-bus voltage.

Each half-bridge is composed of two semiconductor devices: one *switching device* and one *freewheeling device* (diode). The switching devices are generally IGBT for medium power applications, and can be MOFSET [100] for lower power applications. No snubber circuit coupled to the half-bridges is assumed. A *switching signal* is sent to the driver of each switching device. The switching signals are noted s_{p+}^* and s_{p-}^* respectively for the high level and low levels of the phase p . The signals can take two values 0 or 1. The value 0 denotes a signal that commands the device to be in a blocking state and 1 denotes a signal that commands the device to be in a conducting state. We say that a signal turns on when it commutates from blocking 0 to conducting state command 1, and that it turns off when it commutates from conducting 1 to blocking state command 0. The corresponding real *switching states* of the switching devices are noted s_{p+} and s_{p-} , for which the value 0 denotes a infinite device impedance and 1 denotes a null device impedance. Note that $s_{p+} = s_{p-} = 1$ corresponds to a dc-bus short-circuit and results in a failure. The effective *level connection* is given by S_p that is 1 if the phase terminal output is connected to the high level or 0 if it is connected to the low level.

We say that the VSI is *ideal* if the semiconductor devices are ideal, i.e., they cause no voltage drop and the switching devices commutate instantly between perfect conducting states and perfect blocking states. In that ideal situation, the output

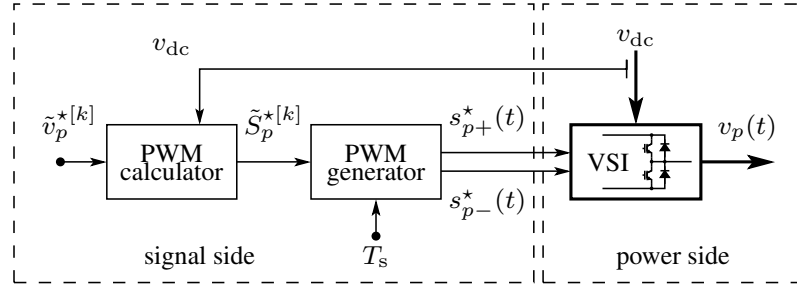


Figure 4.2: Flowchart of the PWM principle: reference voltage v_p^* sent to the PWM calculator; reference duty-cycles \tilde{S}_p^* sent to the PWM generator; switching signals s_{p+}^* and s_{p-}^* sent to the drivers of the VSI that outputs v_p .

voltage is modelled by:

$$v_p = \frac{v_{dc}}{2} (2S_p - 1) \quad (4.1)$$

If the states of the switching devices are complementary $s_{p+} = 1 - s_{p-}$, we simply have $S_p = s_{p+}$ [100]. If both switching devices are blocking $s_{p+} = s_{p-} = 0$, either the current is positive $i_p > 0$ and flows through the low level freewheeling device, making the connection to the low level $S_p = 0$. Or the current is negative $i_p < 0$ and flows through the high level freewheeling device, making the connection to the high level $S_p = 1$. Note that the case $s_{p+} = s_{p-} = 0$ and $i_p = 0$ is undetermined in an ideal VSI. This is further addressed in section 4.2.4.

We say that the PWM is *ideal* if there is no delay between the command of the switching signals and the commutation of the state of the switching devices:

$$s_{p+} = s_{p+}^* \text{ and } s_{p-} = s_{p-}^* \quad (4.2)$$

The nonideal VSI, considering voltage drops and commutation delays, is addressed in section 4.2.3 and section 4.2.4.

4.2.2 Modulation techniques

The PWM principle is based on *carrier cycles*, also sometimes simply called *cycles* [18], of constant periods T_s called *carrier cycle* periods or more generally simply *PWM* period. Both denominations are mixed in this chapter, but this last one, “PWM period“, is more widespread. The PWM operations are based on mean values during PWM periods [101, 102] defined by:

$$\tilde{x}^{[k]} = \frac{1}{T_s} \int_{t^{[k-1]}}^{t^{[k]}} x(t) dt \quad (4.3)$$

where x can be the output voltages, the switching signals, switching states or the level connections. The value \tilde{x} at the period k is computed between the instants $t^{[k-1]}$ and $t^{[k]}$ that correspond to the beginning and the end of the PWM period,

such that $T_s = t^{[k]} - t^{[k-1]}$. We assume that these instants are synchronized with the sampling times of the current measurements sampling, as described in section 3.5. The mean \tilde{S}_p of S_p is the *duty-cycle* corresponding to the relative duration of the high level connection, assuming a low level connection the rest of the PWM period. Note that $0 \leq \tilde{S}_p \leq 1$. For convenience and in order to shorten the expressions, the upper index $[k]$ mentioning the period is sometimes not mentioned if it is not confusing.

As explained by a flowchart in Figure 4.2 for one phase p , before each cycle, a *reference voltage* \tilde{v}_p^* is sent to a *PWM calculator*. This calculator computes a *reference duty-cycle* \tilde{S}_p^* . This reference duty-cycle is sent to a *PWM generator* that synthesizes the two switching signals s_{p+}^* and s_{p-}^* [103]. The switching signals are sent to the drivers of the switching devices of the VSI. Note that no signal corresponding to S_p^* is ever computed, as \tilde{S}_p^* is directly used as a reference value to synthesize the switching signals s_{p+}^* and s_{p-}^* .

The reference duty-cycle \tilde{S}_p^* is generally computed by the PWM calculator so that the mean of the output voltage \tilde{v}_p is equal to the reference voltage [104, 94]:

$$\tilde{v}_p = \tilde{v}_p^* \quad (4.4)$$

If this condition is actually satisfied, the reference voltage \tilde{v}_p^* can be used instead of the output voltage in rotation-drive operations, self-sensing operations and any other operations based on the discrete-time model of the machine, as explained in section 3.5 of chapter 3. The computation leading to (4.4) is explained here below.

Duty-Cycle Computation

Assume that the VSI is ideal (4.1) and that the PWM is also ideal (4.2). If the PWM generator synthesizes complementary switching signals $s_{p+}^* = 1 - s_{p-}^*$ such that $\tilde{s}_{p+}^* = \tilde{S}_p^*$, the mean output voltage defined by (4.3) during every cycle k yields:

$$\tilde{v}_p = \frac{v_{dc}}{2} \left(2\tilde{S}_p^* - 1 \right) \quad (4.5)$$

By consequence, in order to have $\tilde{v}_p = v_p^*$, as given in (4.4), the PWM calculator should compute its output using the following expression:

$$\tilde{S}_p^* := \frac{\tilde{v}_p^*}{v_{dc}} + 0.5 \quad (4.6)$$

The nonideal VSI introduce a nonlinear relation between \tilde{s}_{p+}^* and \tilde{v}_p . The expression (4.6) must therefore be adapted in order to take the nonlinearity into account, as further explained.

Symmetric and asymmetric modulations

Before introducing the VSI nonlinearities, it is required to shortly explain the principle of the PWM. The *conventional modulation techniques* are based on two *car-*

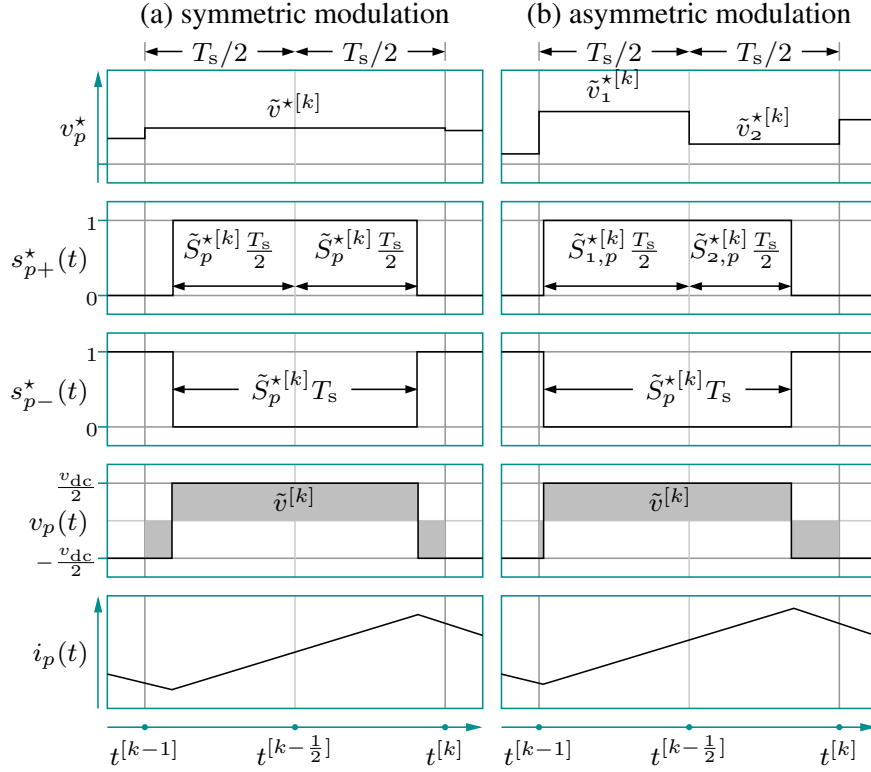


Figure 4.3: Switching signals $s_{p\pm}^*$ synthesized by the PWM generator, assuming complementary signals: illustration by two carrier half-cycles in case of (a) symmetric modulation and (b) asymmetric modulation, assuming $(\tilde{S}_{1,p}^* + \tilde{S}_{2,p}^*)/2 = \tilde{S}_p^*$.

rier half-cycles of equal durations $T_s/2$ (PWM half-periods) [18]. The values corresponding to the first and the second carrier half-cycles will be denoted respectively by the lower index 1 and 2. Let us therefore define the mean values \tilde{x}_1 and \tilde{x}_2 of the variable x respectively during the first and the second half-cycle periods as follow:

$$\tilde{x}_1^{[k]} = \frac{1}{T_s/2} \int_{t^{[k-1]}}^{t^{[k-1/2]}} x(t) dt \quad \text{and} \quad \tilde{x}_2^{[k]} = \frac{1}{T_s/2} \int_{t^{[k-1/2]}}^{t^{[k]}} x(t) dt \quad (4.7)$$

where $t^{[k-1/2]}$ is conventionally the middle instant of the PWM period: $t^{[k-1/2]} = (t^{[k]} + t^{[k-1]})/2$. Using (4.7), we can define two distinct reference half-duty-cycles $\tilde{S}_{1,p}^*$ and $\tilde{S}_{2,p}^*$. In the *continuous modulation techniques*, every switching signal $s_{p\pm}^*$ turns “on” or “off” once during the first half-cycle and turns reversely “off” or “on” once during the second half-cycle. Two continuous modulation techniques are illustrated in Figure 4.3 [18]:

- (a) either $\tilde{S}_{1,p}^*$ and $\tilde{S}_{2,p}^*$ are equal to \tilde{S}_p^* and the modulation is said *symmetric*. The reference duty-cycle \tilde{S}_p^* is calculated from one reference voltage \tilde{v}_p^* using (4.6) ;

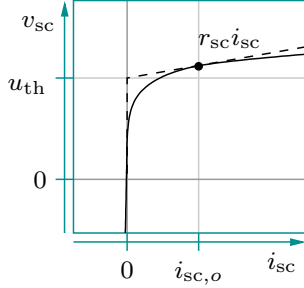


Figure 4.4: Typical voltage/current characteristic of a diode and linearized model.

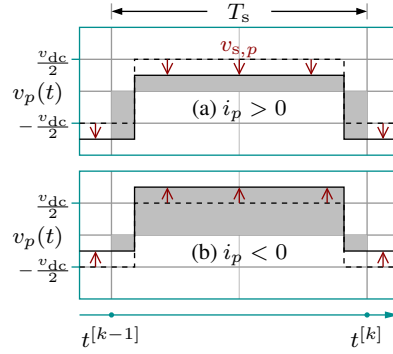


Figure 4.5: PWM-VSI considering the semiconductor voltage drops: effect on the output voltage v_p if (a) $i_p > 0$ (b) $i_p < 0$.

(b) or $\tilde{S}_{1,p}^*$ and $\tilde{S}_{2,p}^*$ are different and the modulation is said *asymmetric* [105], or *unsymmetrical* [106]. Hence, both $\tilde{S}_{1,p}^*$ and $\tilde{S}_{2,p}^*$ can be computed from two different reference voltages $\tilde{v}_{1,p}^*$ and $\tilde{v}_{2,p}^*$ using (4.6).

All the PWM generator does not offer the possibility to work in an asymmetric modulation mode. This is the case of the PWM generator of our test bench that only allows symmetric modulations. In practice however, due to inherent delays of the commutations of the nonideal VSI, the actual half-duty-cycles are always slightly different [107]. This slight difference is considered in the VSI nonlinearities addressed hereafter.

Note that many other modulation techniques exist. Among the conventional modulation techniques, the *discontinuous modulation techniques* are characterized by the saturation of the reference duty-cycle of one phase or more [99, 100]: $\tilde{S}_p^* = 1$ or $\tilde{S}_p^* = 0$. In that case, no switching may occur in the phase p . Some newer non conventional modulation techniques such as [108] are characterized by switching signals turning on or off more than once during the carrier half-cycles. Intuitively, the method we propose could be extended to these cases, but this document only focuses on the conventional modulation techniques.

4.2.3 Semiconductor Voltage Drop

The first nonlinearity introduced by the real VSI comes from the voltage drops that exist across the semiconductor devices. For illustration, a typical static voltage/current characteristic of a diode is presented Figure 4.4. Note that the characteristics are generally different between the switching and freewheeling device types and vary with the temperature [5]. Let define $v_{sc,p}$ that models an equivalent voltage drop at the phase output p . The output voltage is

$$v_{p|\text{real}} = v_{p|\text{ideal}} - v_{sc,p}(i_p, s_{p+}, s_{p-}, \mathbf{T}^\circ) \quad (4.8)$$

where $v_{p|\text{ideal}}$ is given by (4.1). The output voltage drop mainly depends on the current i_p , the states of the two switching devices s_{p+} , s_{p-} that determines which half-bridge is active (if both switching devices are blocking, the current flows in one of the freewheeling devices) and the temperature T° .

In many machine drives, the voltage drops are small compared to the reference voltages \tilde{v}_p^* and no compensation is necessary. For drives using lower controlled voltages, the impact of the voltage drops can be more significant. They are naturally compensated by many controllers. However, the control efficiency can be improved compensating them. Besides the issue of the zero-crossings, addressed in section 4.2.4, the voltage drops have no impact on self-sensing operations using additional high-frequency signals. In order to compensate for them, one may approach their effects neglecting the influence of the temperature and assuming an approximate characteristic. Hence, the output voltage drop can be linearized using a threshold voltage u_{th} and a resistor r_{sc} [5]:

$$v_{\text{sc},p}(i_p) = \text{sign}(i_p) u_{\text{th}} + r_{\text{sc}} i_p \quad (4.9)$$

Generally, the resistor r_{sc} is mixed up with the stator circuit resistors and it is not required to compensate for it. Only the threshold voltage multiplied by the current sign remains to compensate:

$$v_{\text{sc},p}(i_p) \approx \text{sign}(i_p) u_{\text{th}} \quad (4.10)$$

The current sign is generally approached by the sign of the sampled measurements of the currents or by the sign of the instruction value of the current i_p^* sent to the controller. This last solution is more stable although it may differ from the sign of the current samples while reaching values close to zero. Assuming that no zero-crossing occurs, applying (4.3) and using (4.10), (4.8) during every cycle k yields:

$$\tilde{v}_{p|\text{real}} \approx \tilde{v}_{p|\text{ideal}} - \text{sign}(i_p^*) u_{\text{th}} \quad (4.11)$$

Assume that there is no switching delay (4.2). If the PWM generator synthesizes complementary switching signals $s_{p+}^* = 1 - s_{p-}^*$ such that $\tilde{s}_{p+}^* = \tilde{S}_p^*$, the ideal mean output voltage $\tilde{v}_{p|\text{ideal}}$ is given by (4.5). In order to have $\tilde{v}_{p|\text{real}} \approx \tilde{v}_p^*$, the PWM calculator computes its output using (4.6) and using (4.11) at every cycle k :

$$\tilde{S}_p^* := \frac{\tilde{v}_p^* + \text{sign}(i_p^*) u_{\text{th}}}{v_{\text{dc}}} + 0.5 \quad (4.12)$$

This compensation is also valid for each carrier half-cycle separately. Note that the computation (4.12) is not valid when the current i_p crosses zero as it creates a nonlinearity during the carrier cycle. The specific question of the zero-crossing is further addressed in section 4.2.4.

Compensation method based on (4.12) are proposed in [87, 18, 5]. More accurate compensation methods exist that makes the distinction between both device types, but they are not addressed in this paper. More information can be found in [104, 109].

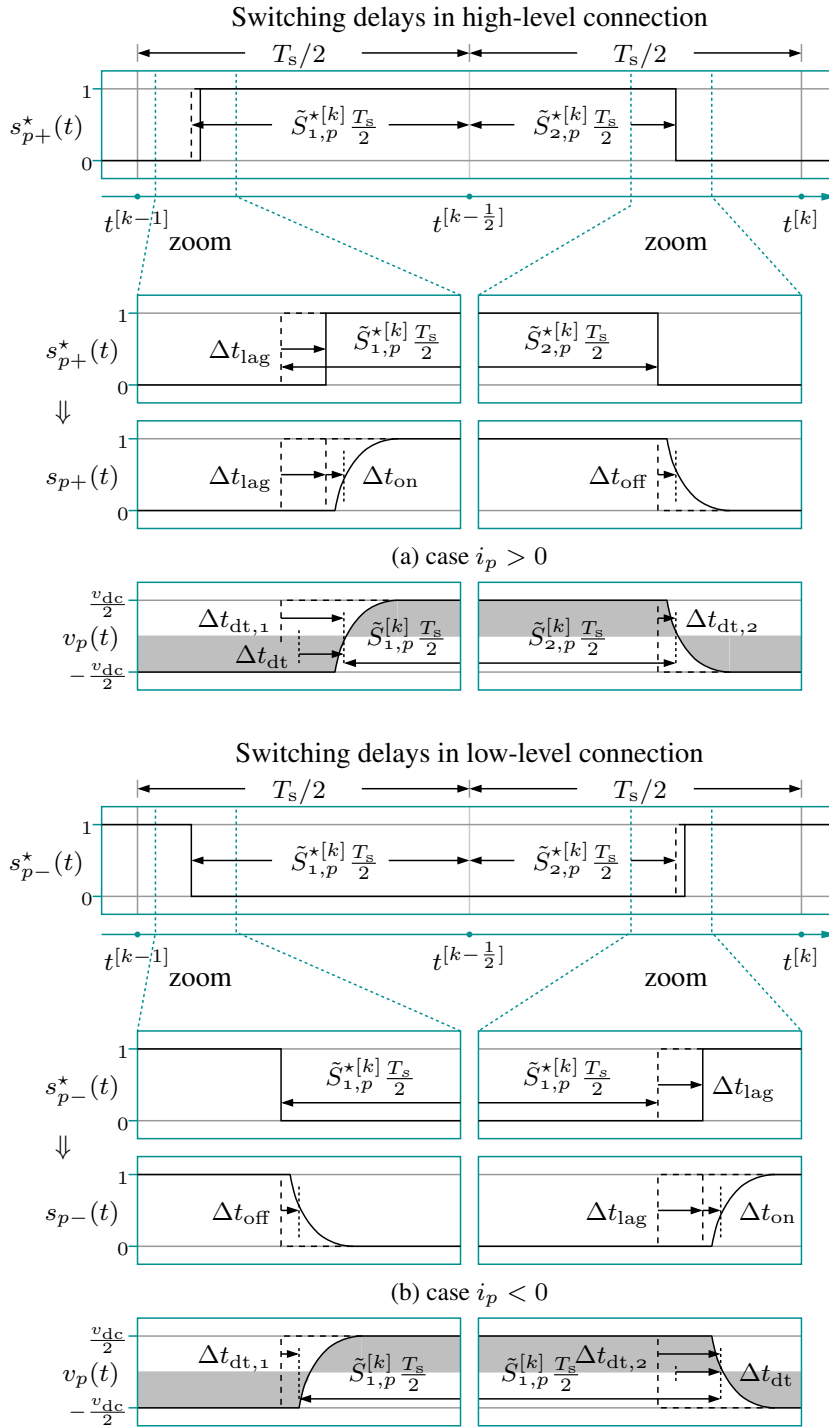


Figure 4.6: Zoom in two half-cycles of the PWM-VSI showing the switching delays: expected switching signals (---) and synthesized switching signals s_{p+}^* and s_{p-}^* (—), switching states s_{p+} and s_{p-} with their commutation delays. Output voltage v_p in case (a) i_p is positive and in case (b) i_p is negative.

4.2.4 Switching Dead Time

The second nonlinearity introduced by the real VSI comes from the inherent commutation times of the switching devices to turn “on” and to turn “off”. Note that the commutation times are generally different between the turn “on” and turn “off”, and vary with the temperature and the current [18]. In order to avoid that the switching devices of the two half-bridges are simultaneously conducting, and so to prevent dc-bus short-circuit, it is indispensable to add a delay to the turn on moments of the signals. This delay is called *lag time* [103], or sometimes *blanking time* [110, 104], and we write it Δt_{lag} . The usual lag time is around 1-20 μs [103, 111, 106, 110, 112], depending on the device technology. As a result of the lag time and the commutation times, during a short period of time, both switching devices remain blocking. This short period is called *dead time*.

In some machine drives, dead times are small compared to the cycle periods and no compensation is necessary. For many other drives however, their impacts are more significant. This is especially the case when the frequency of the PWM is increased. The dead times are naturally compensated by many controllers. However, the control efficiency can be improved compensating them. Besides the issue of the zero-crossings, addressed in section 4.2.4, the dead times have no impact on self-sensing operations using additional high-frequency signals. In order to compensate them, one may approach the commutation times by average commutation delays, neglecting the influence of the temperature and the variations with the current. We define Δt_{on} and Δt_{off} as the commutation delays respectively for the on and the off transitions (assuming they are the same for both half-bridges). Using these average commutation delays, the VSI is idealized and we may use the equations (4.5). The goal is now to determine the impact of the delays on S_p .

The situation of both carrier half-cycles are illustrated in Figure 4.6. Assume the output is initially connected to the low level at the beginning of the first carrier half-cycle: $S_p = s_{p+} = 0$ and $s_{p-} = 1$. (a) If the current i_p is positive, the switching “off” of the low level switching device s_{p-} does not affect the connection to the low level, as the current continues to flow through the freewheeling device. The commutation to the high level $S_p = 1$ occurs when the high level switching device s_{p+} turns on after a total delay $\Delta t_{\text{on}} + \Delta t_{\text{lag}}$ compared to the signal s_{p+}^* . (b) If the current i_p is negative, the commutation to the high level $S_p = 1$ occurs when the low level switching device s_{p-} turns off after a delay Δt_{off} . The turn on of the high level switching device s_{p+} does not affect the connection to the high level. By consequence, depending on the sign of the current, the real duty-cycle \tilde{S}_p is shortened by one of these delays. Using mean values (4.7), all this is summarized by:

$$\tilde{S}_{1,p} = \begin{cases} \tilde{S}_{1,p}^* - (\Delta t_{\text{on}} + \Delta t_{\text{lag}})/(T_s/2) & \text{if } i_p > 0 \\ \tilde{S}_{1,p}^* - \Delta t_{\text{off}}/(T_s/2) & \text{if } i_p < 0 \end{cases} \quad (4.13)$$

The reasoning for the second carrier half-cycle (b) is similar assuming the output is initially connected to the high level: $S_p = s_{p+} = 1$ and $s_{p-} = 0$. It can be shown

that the result is:

$$\tilde{S}_{2,p} = \begin{cases} \tilde{S}_{2,p}^* + \Delta t_{\text{off}}/(T_s/2) & \text{if } i_p > 0 \\ \tilde{S}_{2,p}^* + (\Delta t_{\text{on}} + \Delta t_{\text{lag}})/(T_s/2) & \text{if } i_p < 0 \end{cases} \quad (4.14)$$

If we use a symmetric modulation, remember that we have $\tilde{S}_{1,p}^* = \tilde{S}_{2,p}^* = \tilde{S}_p^*$. The resulting duty-cycle during T_s is given by:

$$\tilde{S}_p = \frac{\tilde{S}_{1,p} + \tilde{S}_{2,p}}{2} = \tilde{S}_p^* - \text{sign}(i_p) \frac{\Delta t_{\text{dt}}}{T_s} \quad (4.15)$$

where:

$$\Delta t_{\text{dt}} = \Delta t_{\text{on}} - \Delta t_{\text{off}} + \Delta t_{\text{lag}} \quad (4.16)$$

This expression is found in many publications, such as [113, 104]. Remark: the relations (4.13) and (4.14) do not model situations where $\tilde{S}_{1,p}$ or $\tilde{S}_{2,p}$ is smaller than 0 or larger than 1, since it would correspond to commutations occurring outside the half-cycle.

Assuming that no zero-crossing occurs, the sign of the current is generally approached by the sign of the sampled measurements of the currents or by the sign of the instruction value of the current i_p^* sent to the controller. In that last case, (4.15) yields:

$$\tilde{S}_p \approx \tilde{S}_p^* - \text{sign}(i_p^*) \frac{\Delta t_{\text{dt}}}{T_s} \quad (4.17)$$

Assume that the VSI is ideal (4.1), i.e. no voltage drop. In order to have $\tilde{v}_p \approx v_p^*$, the computation of the PWM calculator is found using (4.17) and yields:

$$\tilde{S}_p^* := \frac{\tilde{v}_p^*}{v_{\text{dc}}} + \text{sign}(i_p^*) \frac{\Delta t_{\text{dt}}}{T_s} + 0.5 \quad (4.18)$$

This compensation is no valid for each carrier half-cycle separately. For this, the distinct expressions (4.13) and (4.14) must be used. Note also that this solution is not valid when the current i_p crosses zero. The specific question of the zero-crossing is addressed hereafter.

Some methods are included in the control operations, such as in [113, 111, 5, 112]. The benefit is that the PWM generator is not modified and no additional setup is required. Such a method is integrated in an self-sensing control using high-frequency signal injection by [114]. It is also possible to take benefit of asymmetric modulations in order to specifically compensate the dead times during every half-cycles, as done in [106, 107, 115]. This has the advantage to improve the shape of the PWM compared to the first methods, an asymmetric PWM generator is required. The solution proposed by [110] is based on the fact that when the current of a phase is flowing in the diode of a half-bridge, it is not necessary to turn on the switching device of this half-bridge. By consequence, no lag time delay is required. Older methods use additional analogical delayers, such as [116, 117, 118]. They are not much used to our knowledge. All the mentioned methods are based on

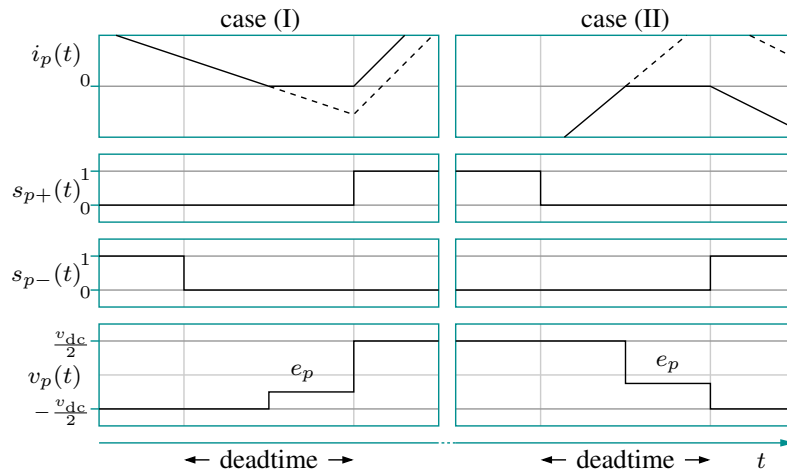


Figure 4.7: Zoom in two half-cycles of the PWM-VSI showing the zero-clamping phenomenon during dead times.

constant delays. More accurate methods exist that detects the real commutations using extra detection circuits. That solution was initially proposed by [103] using photocoupled devices in order to detect the voltage commutations. Another extra current-polarity detection-circuit is used by [94] and applies a solution based on an asymmetrical modulation similar to [110]. It also gives a very good state-of-the-art about dead time issues. A estimation method of the dead time without additional setup is proposed by [109] for permanent-magnet synchronous motor (PMSM) in steady-state operations. It is based on the observation of the currents along the d-axis, maintained to zero during a whole rotation. Another estimation method for steady-state operations is proposed in [112]. It is based on integration of a steady-state error related to the dead time. A dead time compensation is proposed by [104] for open-loop drives, where the dead time is given by a look-up table from manufacturer specifications or semiconductor models. Most of the proposed methods do not compensate for nonlinearities occurring when a phase current crosses zero.

Zero-Crossing Problems

Finding a compensation solution valid also when a phase current crosses zero poses some problems [94, 120, 121, 41]. First of all, assuming that the problem only consists in determining the accurate moment when the current crosses zero: either additional measurements should be used, but this is not advised for low cost solutions; or accurate estimation of the current variations during the carrier cycles should be used, but this is not a robust solution as it is very sensitive to errors and to approximations in the model of the machine.

Another problem comes from the *zero-current clamping effect* illustrated in Figure 4.7: if the current reaches zero during the dead time, it is clamped to zero for the rest of the dead time [122, 107]. This is explained as follows: remember that

the current flows in one of the freewheeling devices while the switching devices are blocking. To overpass the voltage drop across the freewheeling device, the output voltage v_p must necessarily be higher than the high level voltage v_+ : $v_p = v_+ + v_{\text{diode}}$ if $i_p < 0$; or lower than the low level voltage v_- : $v_p = v_- - v_{\text{diode}}$ if $i_p > 0$. Note that this is possible because the machine is an inductive circuit. The fact that i_p slides to zero is related to a decrease of v_{diode} , as shown in Figure 4.4. The freewheeling device becomes blocking when the current reaches zero. At this moment, both freewheeling devices are blocking and all the half-bridges are completely blocking. As a consequence, the output voltage freely varies between the low level and the high level voltages: $v_- < v_p < v_+$. This phenomenon is not easy modelled since it is strongly nonlinear, the zero-clamping instant is very sensitive to very small variations of the current, and the topology of the machine is changed with one disconnected phase during the zero-clamping.

The solutions proposed by [122, 123] consist in a compensation method based on the repetitive nature of the zero-crossing in steady-state operations. The solution is integrated by [96] in back-EMF-based self-sensing methods. In [107], a feedback term in a predictive current controllers is used in order to reduce the zero-current clamping effect. This effect is however not completely compensated. All these solutions are not operating correctly during transient operations and are not efficient for many anisotropy-based self-sensing methods due to the large approximation of the correction. An improved method integrated in self-sensing operations is proposed by [124]. The duration of the zero-crossing, to be compensated, is predicted using a first-order approximation of the circuit model. This solution however assume only small ripple amplitudes and the accuracy should be further analyzed with machine presenting significant resistive voltage drops.

If we want to keep a simple hardware solution and a low computation time, one solution is therefore to find a method that maintains i_p far enough from zero most of the time, for example adding an offset in the current reference. When a zero-crossing is required, it must occur as quick as possible, for example during one carrier cycle, in order to reduce its impact. Ideally, the offset is selected in order to minimize its impact on the torque and the performances of the machine. This is addressed in the next section 4.3.

4.3 Zero-Crossing Issues and Prevention

We restrict the analysis to the case of a three-phase VSI supplying a three-phase machine without neutral connection, i.e. without homopolar current $i_o = 0$. The VSI phases are numbered by $p \in \{a, b, c\}$. The proposed solution is based on space vectors handled in the stationary $\alpha\beta$ reference-frame.

Due to the pulsewidth modulation (PWM) principle of the voltage source inverters, described in section 4.2.2, the space vector of the output voltage switches between fixed values, called *switching-state voltage space-vectors*, during the carrier cycle. These voltages are addressed in section 4.3.1. These switches result in

small variations of the currents between two samples used by the current controller. These variations are called *current ripples* and are addressed in section 4.3.2. In section 4.3.3, different methods are addressed to estimate the margin required between the current samples and the zero-crossing lines in order to prevent zero-crossings. The strategy used to prevent zero-crossing from this margin is then proposed in section 4.3.4.

For convenience, the index $[k]$ of the period is not mentioned if not confusion, but it should be considered.

4.3.1 Space Vector of Switching State Voltages

The Switching States

Assuming an ideal VSI, each level connection can take two values: 0 or 1. Therefore, in a three-phase VSI, there are 2^3 possible combinations for the three level connections S_a , S_b and S_c . A level connection combination $\mathbf{S} = \{S_a, S_b, S_c\}$ is often called *switching state* [108, 114] and should not be confused with the switching state of the switching devices $s_{p\pm}$. The sequence of the different switching states $\{\mathbf{S}_1, \mathbf{S}_2, \dots\}$ during the carrier cycle is called a *switching sequence* [108], or *switching pattern* [101]. The number of distinct switching states in a switching sequence depends on the modulation technique and is further addressed. On one hand, let us define \mathcal{S}_ξ of the ξ^{th} switching state of the sequence such that $\mathcal{S}_\xi = 1$ when $\mathbf{S} = \mathbf{S}_\xi$, and $\mathcal{S}_\xi = 0$ otherwise. We may therefore write:

$$\mathbf{S}(t) = \sum_{\xi} \mathbf{S}_\xi \mathcal{S}_\xi(t) \quad (4.19)$$

Using (4.7) in (4.19), the three-phase duty-cycles $\tilde{\mathbf{S}} = \{\tilde{S}_a, \tilde{S}_b, \tilde{S}_c\}$ are:

$$\tilde{\mathbf{S}} = \sum_{\xi} \mathbf{S}_\xi \tilde{\mathcal{S}}_\xi \quad (4.20)$$

where $\tilde{\mathcal{S}}_\xi$ is given by (4.7) and corresponds to the relative duration of the switching state number ξ . The time duration of this state, called switching state subperiod, is equal to $\tilde{\mathcal{S}}_\xi T_s$. On the other hand, let us define the sorted duty-cycles, in a decreasing order, as follows:

$$\tilde{\mathbf{S}}' \triangleq \text{sort}(\tilde{\mathbf{S}}) \quad (4.21)$$

where $\tilde{\mathbf{S}}' = \{\tilde{S}_{a'}, \tilde{S}_{b'}, \tilde{S}_{c'}\}$ such that $\{a, b, c\} \rightarrow \{a', b', c'\}$ are the phase numbers of the sorted set of duty-cycles. It can also be written:

$$\tilde{S}_{a'} \triangleq \max(\tilde{\mathbf{S}}) \quad \text{and} \quad \tilde{S}_{b'} \triangleq \text{med}(\tilde{\mathbf{S}}) \quad \text{and} \quad \tilde{S}_{c'} \triangleq \min(\tilde{\mathbf{S}}) \quad (4.22)$$

Using (4.21), then (4.19) yields:

$$\tilde{\mathbf{S}}' = \sum_{\xi} \mathbf{S}'_{\xi} \tilde{\mathcal{S}}_{\xi} \quad (4.23)$$

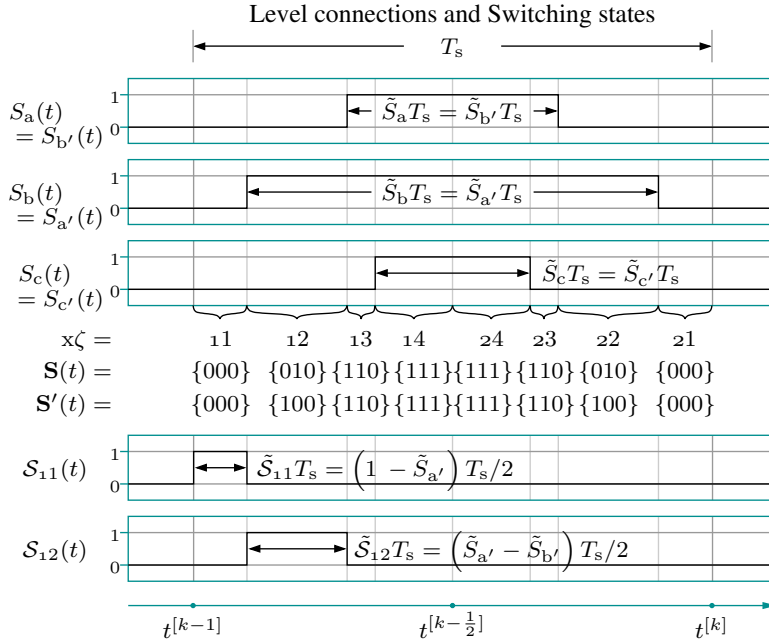


Figure 4.8: Illustration of the level connections S_p and their sorted numbering $S_{p'}$ in an ideal conventional symmetrical modulation technique commanding an ideal two-level three-phase VSI. In this example: $a' = b$, $b' = c$ and $c' = c$. Corresponding switching states $\mathbf{S}_{x\zeta}$ and ordered switching states $\mathbf{S}'_{x\zeta}$ numbered from $x\zeta = 11$ to 14 for the first half-period and from $x\zeta = 24$ to 21 for the second half-period. Illustration of $S_{11}(t)$ and $S_{12}(t)$ (the next $S_{x\zeta}(t)$ follow the same principle).

where $\mathbf{S}'_{\xi} = \{S_{a'}, S_{b'}, S_{c'}\}_{\xi}$. Note that \tilde{S}_{ξ} is not affected by the sorting. These relations (4.19)-(4.23) are also valid for carrier half-cycles using (4.7).

As illustrated in Figure 4.8 for a continuous modulation technique, during every carrier half-cycle, each VSI phase output switches once between the high and low levels. Therefore, in a three-phase VSI, there are four different switching states in one switching half-sequence. By consequence, instead of numbering the switching states by 1, 2, ..., let us number them by an index made of the half-cycle number $x \in \{1, 2\}$ followed by their order of occurrence from $\xi = 1$ to 4 in the first switching half-sequence: $\{\mathbf{S}_{11}, \mathbf{S}_{12}, \mathbf{S}_{13}, \mathbf{S}_{14}\}$; and reversely from $\xi = 4$ to 1 in the second switching half-sequence: $\{\mathbf{S}_{24}, \mathbf{S}_{23}, \mathbf{S}_{22}, \mathbf{S}_{21}\}$. Using this numbering, it is possible to write expressions that cover indiscriminately each carrier half-cycle. Note that if the modulation is perfectly symmetric: $\mathbf{S}_{1\xi} = \mathbf{S}_{2\xi}$, $\forall \xi \in \{1, 2, 3, 4\}$.

Assume a continuous modulation technique with $\mathbf{S}_{x1} = \{000\}$ and $\mathbf{S}_{x4} = \{111\}$. Using the sorting of the duty-cycles as defined in (4.21) or (4.22), it can be

shown that the respective consecutive switching states are:

$$\begin{aligned} \mathbf{S}'_{x1} &= \{000\} \\ \mathbf{S}'_{x2} &= \{100\} \\ \mathbf{S}'_{x3} &= \{110\} \\ \mathbf{S}'_{x4} &= \{111\} \end{aligned} \quad (4.24)$$

In other words, the different level connections switch “on” successively in the order of their sorted duty-cycles. Assuming a symmetric modulation, it can also be demonstrated that the successive switching state durations are:

$$\begin{aligned} \tilde{\mathcal{S}}_{x1} &= \left(1 - \tilde{\mathcal{S}}_{a'}\right) / 2 \\ \tilde{\mathcal{S}}_{x2} &= \left(\tilde{\mathcal{S}}_{a'} - \tilde{\mathcal{S}}_{b'}\right) / 2 \\ \tilde{\mathcal{S}}_{x3} &= \left(\tilde{\mathcal{S}}_{b'} - \tilde{\mathcal{S}}_{c'}\right) / 2 \\ \tilde{\mathcal{S}}_{x4} &= \left(\tilde{\mathcal{S}}_{c'}\right) / 2 \end{aligned} \quad (4.25)$$

where $\{a', b', c'\}$ are the sorted phase numbers. The same computation is also valid for each carrier half-cycles in case of an asymmetric modulation, considering distinct half-duty-cycles. Note that, in that asymmetric modulation case, the order $\{a', b', c'\}$ is not necessarily the same for the first and the second carrier half-cycles. As a conclusion, the duration of the different switching states are easily computed from the sorted phase duty-cycles. In case of nonideal three-phase VSI, the same computation (4.25) is valid, but the dead times should be cut off the duty-cycle computations, as explained in section 4.2.4.

The Switching-State Voltage Space-Vectors

The space vector \underline{v} of the output voltage is defined by (2.71) in chapter 2 as the phase contributions v_p counted along the conductor orientations φ_p :

$$\underline{v} \triangleq \frac{2}{3} \left(v_a e^{j\varphi_a} + v_b e^{j\varphi_b} + v_c e^{j\varphi_c} \right) \quad (4.26)$$

where $\varphi_a = 0$, $\varphi_b = 2\pi/3$ and $\varphi_c = 4\pi/3$. Assuming an ideal three-phase VSI, v_p can be replaced by the expression (4.1). Since $e^{j\varphi_a} + e^{j\varphi_b} + e^{j\varphi_c} = 0$, (4.26) yields [100]:

$$\underline{v}_{[S]} = \frac{2v_{dc}}{3} \left(S_a e^{j\varphi_a} + S_b e^{j\varphi_b} + S_c e^{j\varphi_c} \right) \quad (4.27)$$

As illustrated in Figure 4.9, the space vector of the output voltages \underline{v} can thus take 2^3 positions called *switching-state voltage space-vectors* $\underline{v}_{[S]}$ that correspond to the different possible switching states $\mathbf{S} = \{S_a, S_b, S_c\}$ [108, 101, 18]. There are two equal *zero switching-state voltage space-vectors* $\underline{v}_{[000]} = \underline{v}_{[111]} = \underline{0}$ and six different *active switching-state voltage space-vectors* of amplitude $\frac{2}{3}v_{dc}$ and oriented in one phase direction φ_a , φ_b or φ_c [101, 100, 18].

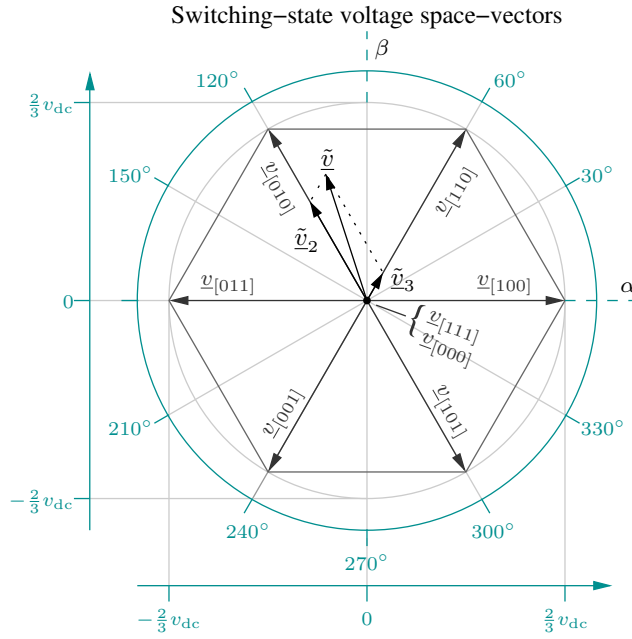


Figure 4.9: Illustration of the different switching-state voltage space-vectors $\underline{v}_{[S]}$ in an ideal two-level three-phase VSI. Example of the mean active space-vectors $\tilde{\underline{v}}_2$ and $\tilde{\underline{v}}_3$ corresponding to the illustrated mean voltage $\tilde{\underline{v}}$.

For convenience, the switching-state voltage space-vectors $\underline{v}_{[S_\xi]}$ corresponding to the ξ^{th} switching state S_ξ is written in short \underline{v}_ξ . The sequence of the different switching-state voltage space-vectors $\{\underline{v}_1, \underline{v}_2, \dots\}$ during the carrier cycle is also called a *switching sequence*. Using S_ξ as previously defined, we can write:

$$\underline{v}(t) = \sum_{\xi} \underline{v}_\xi \mathcal{S}_\xi(t) \quad (4.28)$$

Using (4.3) in (4.28), the mean space vector of the three-phase voltages $\tilde{\underline{v}}$ is:

$$\tilde{\underline{v}} = \sum_{\xi} \underline{v}_\xi \tilde{\mathcal{S}}_\xi \quad (4.29)$$

For convenience, we define the relative contribution of the ξ^{th} switching-state voltage space-vectors by:

$$\tilde{\underline{v}}_\xi = \underline{v}_\xi \tilde{\mathcal{S}}_\xi \Rightarrow \tilde{\underline{v}} = \sum_{\xi} \tilde{\underline{v}}_\xi \quad (4.30)$$

These relations (4.29)-(4.30) are also valid for carrier half-cycles using (4.7).

As illustrated in Figure 4.10 for the conventional continuous modulation technique, during every carrier half-cycle, the output voltage switching between the

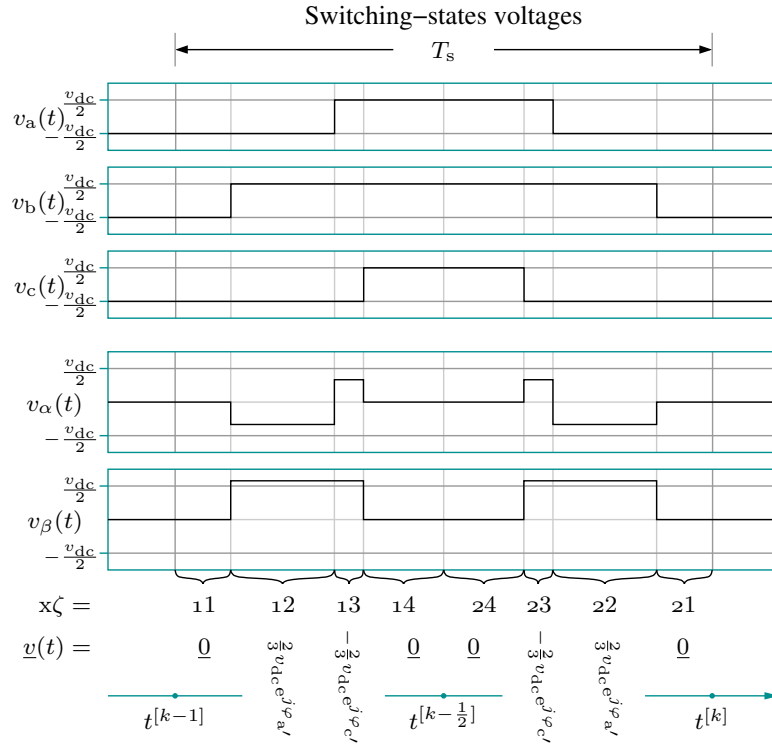


Figure 4.10: Illustration of the switching-states voltages along the phase and along the $\alpha\beta$ -axes, in an ideal conventional symmetrical modulation technique commanding an ideal two-level three-phase VSI.

zero switching-state voltage space-vectors and two active switching-state voltage space-vectors [18]. Such as with the switching states, let us write the first and second switching half-sequences with the following numbering: $\{v_{11}, v_{12}, v_{13}, v_{14}\}$ and $\{v_{24}, v_{23}, v_{22}, v_{21}\}$, respectively. Assume also that $\mathbf{S}_{x1} = [000]$ and $\mathbf{S}_{x4} = [111]$. Hence $v_{x1} = v_{x4} = 0$, and v_{x2} and v_{x3} are active switching-state voltage space-vectors. Using the sorted phase numbers $\{a', b', c'\}$, the sequence (4.24) yields [87, 99, 100]:

$$\begin{aligned} v_{x1} &= \underline{0} \\ v_{x2} &= \frac{2}{3}v_{dc} e^{j\varphi_{a'}} \\ v_{x3} &= -\frac{2}{3}v_{dc} e^{j\varphi_{c'}} \\ v_{x4} &= \underline{0} \end{aligned} \quad (4.31)$$

And using (4.25) and (4.31), (4.30) yields:

$$\begin{aligned} \tilde{v}_{x1} &= \underline{0} \\ \tilde{v}_{x2} &= \frac{1}{3}v_{dc} \left(\tilde{S}_{a'} - \tilde{S}_{b'} \right) e^{j\varphi_{a'}} \\ \tilde{v}_{x3} &= \frac{1}{3}v_{dc} \left(\tilde{S}_{c'} - \tilde{S}_{b'} \right) e^{j\varphi_{c'}} \\ \tilde{v}_{x4} &= \underline{0} \end{aligned} \quad (4.32)$$

These results are easily computed from the apriori knowledge of the duty-cycle and the measurement of v_{dc} . The mean active space vectors $\tilde{v}_2 \triangleq \tilde{v}_{12} + \tilde{v}_{22}$ and $\tilde{v}_3 \triangleq \tilde{v}_{13} + \tilde{v}_{23}$ corresponding to an example of \underline{v} are illustrated in Figure 4.9.

PWM strategies

Using (2.72) with the supply voltages, it yields:

$$\tilde{v}_p = \tilde{v}_o + \Re(\tilde{v} e^{-j\varphi_p}) \quad (4.33)$$

where \tilde{v}_o is sometimes called the *zero-sequence* voltage. Introduced this in (4.6)

$$\tilde{S}_p^* := \frac{\tilde{v}_o^* + \Re(\tilde{v}^* e^{-j\varphi_p})}{v_{dc}} + 0.5 \quad (4.34)$$

By the difference in (4.32), this value \tilde{v}_o^* is simply removed in the active vector expression. This value gives therefore a degree of freedom in the selection of the phase duty-cycles [18], and defines the different PWM strategies.

A review of the state-of-the-art about the conventional modulation techniques at the year of 1999 is given in [99]. It compares the switching loss and harmonic contents of the waveforms. Different strategies for continuous modulation technique are compared by [101] regarding the minimization of root mean square (RMS) of the current ripples in induction motors. They are compared regarding the total harmonic distortion (TDH) in [102]. Discontinuous modulation techniques are addressed by [100] regarding the RMS reduction of the current ripples at the DC-bus. Less conventional hybrid modulation techniques are proposed by [108] regarding the current ripples at phase outputs and DC-bus. The maximum voltage in the space-vector frame supplied by the VSI is addressed by [101] for different strategies. All of these papers give interesting state-of-the-arts concerning the modulation techniques, but they all neglect the nonlinearities of the VSI.

The voltage drops

The voltage drop at the semiconductors of the real VSI can be transposed in the machine model as a constant offset space vector \underline{v}_{sc} computed using (4.26) from $v_{sc,p}$ given in (4.10). Details are found in [87, 18, 5, 114].

4.3.2 The Current Ripples

Zero-crossing lines

Assuming no neutral connection, i.e. $i_o = 0$, the relation between the space vector of the currents \underline{i} and the phase values i_p is given by (2.72) in chapter 2 and yields:

$$i_p = \Re(\underline{i} e^{-j\varphi_p}) \quad \forall p \in \{a, b, c\} \quad (4.35)$$

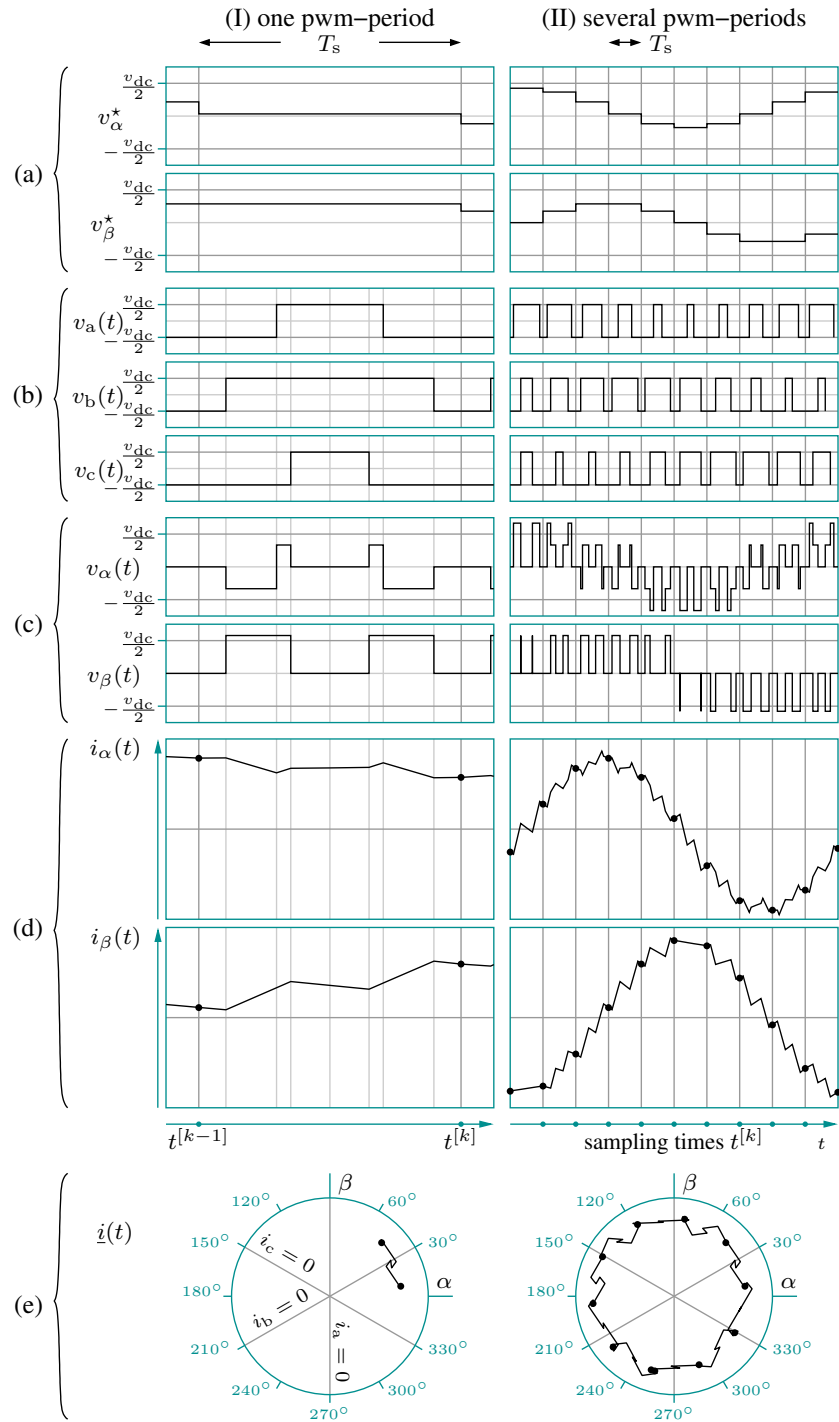


Figure 4.11: Illustration of the current ripples due to the PWM during (I) one PWM period and (II) several PWM periods, assuming an ideal PWM-VSI. From top to bottom: (a) $\alpha\beta$ -components of the instruction \underline{v}^* ; (b) phase output voltages ; (c) output voltage along the $\alpha\beta$ -axes ; (d) current response along the $\alpha\beta$ -axes ; (e) current response \underline{i} in the space vector $\alpha\beta$ -frame, with indication of the zero-crossing lines.

where $\varphi_a = 0$, $\varphi_b = 2\pi/3$ and $\varphi_c = 4\pi/3$. It can be deduced that the location of \underline{i} corresponding to a zero-crossing are along angles $e^{j(\varphi_p + \pi/2)}$. They are represented by gray lines in Figure 4.11(e) and Figure 4.12(c). These zero-crossings should be prevented since they lead to inverter nonlinearities that are not compensated.

Due to the pulsewidth modulation (PWM) principle of the voltage source inverters, described in section 4.2.2, there are small variations of the currents between two samples used by the current controller. These variations are called *current ripples* [102, 99, 108, 101, 100] and are illustrated in Figure 4.11. In the example of the illustration, the signals vary with a high frequency close to the PWM frequency and a large amplitude regarding the amplitude of the ripples. This could give the illusion that computation of the zero-crossing check could be restricted to the samples. In practice however, the signals controlled by the normal rotation-drive operations (fundamental signals) vary at a much lower frequencies related to the rotation speed. As a consequence, the current ripples can be much larger than the variations between two samples. In signal-injection-based self-sensing methods, the injected signals have high-frequencies close to the PWM frequency, but their amplitudes should be as small as possible in order to reduce the impact on the torque (the goal is also to prevent the emergence of a high-frequency back-emf and to limit the production of noise). As a consequence, the current ripples can be much larger than the injected signals. In both case, the current ripples may cross a zero-crossing line even if the samples $\underline{i}(t^{[k]})$ and $\underline{i}(t^{[k-1]})$ do not. This is the main problem met with the current ripples that requires to keep a minimum distance between \underline{i} and the zero-crossing lines. This is illustrated in Figure 4.12 where we assumed much larger ripples regarding the sampling variations.

The first step hereafter is thus to propose an expression of these current ripples in order to find the minimum margin required between the current samples and the zero-crossing lines such that, $\forall p \in \{a, b, c\}$:

$$\text{sign}(i_p(t)) = \text{sign}(i_p(t^{[k]})) = \text{sign}(i_p(t^{[k-1]})) \quad \forall t \in [t^{[k-1]}, t^{[k]}] \quad (4.36)$$

The expression of this margin should be as simple as possible to allow quick and robust operations.

Model of the ripples

The current ripples are described in this section using matrix space vectors instead of complex space vectors. We assume that the current ripples can be modelled by the relation (3.49) addressed in chapter 3, neglecting the eddy currents. Using (4.8), we can link the real and ideal supply voltages by: $\underline{V}_{\text{ideal}} = \underline{V}_{\text{real}} + \underline{V}_{\text{sc}}$. Removing the subscript “ideal” of \underline{V} for convenience, we can thus write:

$$\underline{V} = L_t \frac{d\underline{I}}{dt} + \underline{E} \quad \text{where} \quad \underline{E} = \left(R + \omega_q \frac{\partial L}{\partial \varphi_q} \right) \underline{I} + \underline{E}_{\text{PM}} + \underline{V}_{\text{sc}} \quad (4.37)$$

where $\underline{E}_{\text{PM}}$ is the back-emf related to the permanent-magnets. Since we only focus on the current variations $d\underline{I}$, that describe the current ripples, we gather all

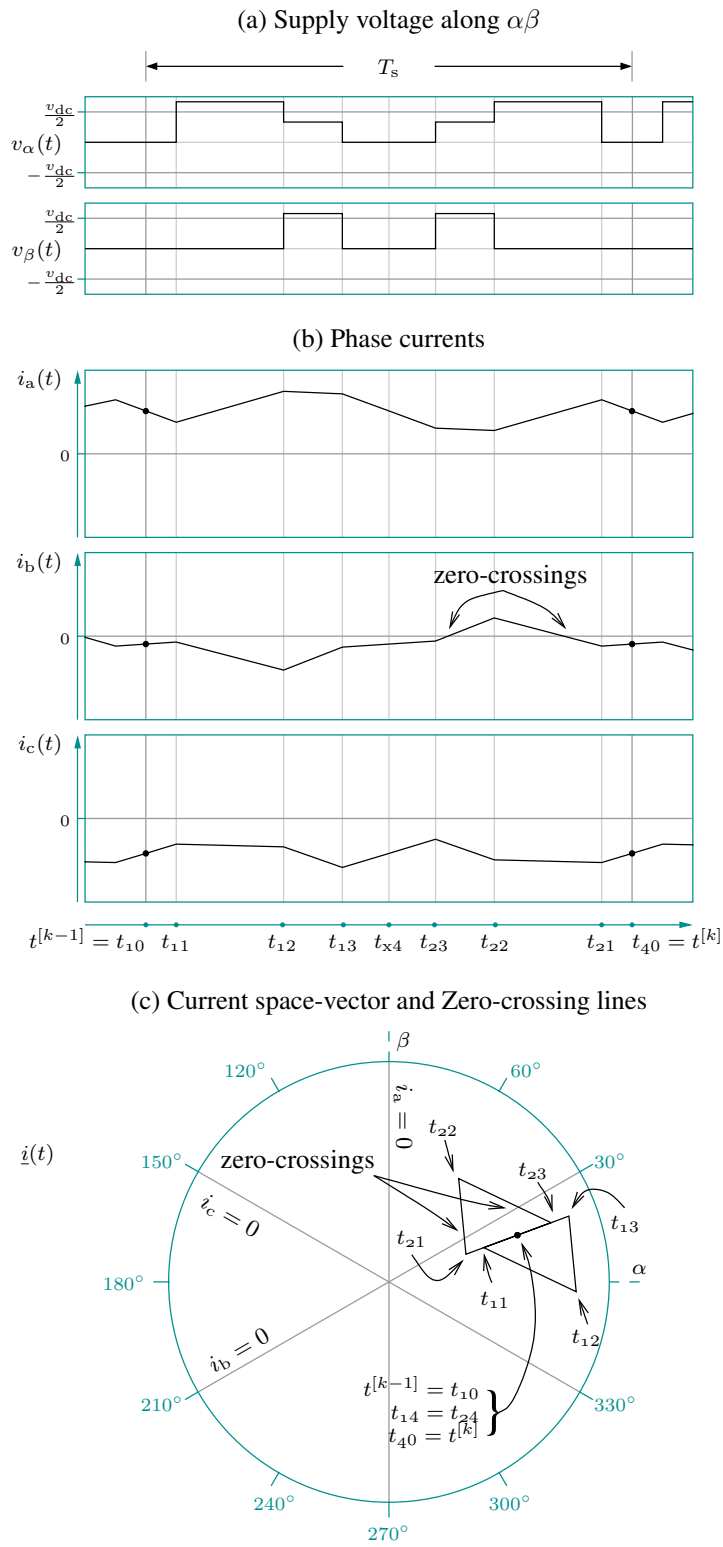


Figure 4.12: Assuming an ideal PWM-VSI, illustration of the (b) phase current response to (a) PWM voltage and (c) corresponding space vector of the currents \underline{i} crossing the zero-crossing line $i_b = 0$ in the space vector $\alpha\beta$ -frame.

the other components in a temporary value \underline{E} . This expression (4.37) neglects the eddy current contribution. As it was shown in chapter 3 however, they are not negligible in the experimental BLDC motor. Moreover, the value of the discrete-time parameters may differs from the continuous-time expression. In first approximation however, we assume that the model (4.37) is valid by approaching L_t with the apparent discrete-time high-frequency inductance. The resistive voltage drop should be separated in two contributions: one related to the operating current, using the low-frequency continuous-time resistance ; another related to the current ripples, that could be approached by the apparent discrete-time high-frequency resistance. This is further addressed. In order to compute the current ripples, (4.37) is therefore rewritten:

$$d\underline{I} = L_t^{-1} (\underline{V} - \underline{E}) dt \quad (4.38)$$

At every carrier cycle period of the PWM, for each switching subperiod ξ , the time integral of (4.38) yields:

$$\delta\underline{I}_\xi = L_t^{-1} \left(\int_{\tilde{\mathcal{S}}_\xi T_s} \underline{V} dt - \int_{\tilde{\mathcal{S}}_\xi T_s} \underline{E} dt \right) \quad (4.39)$$

where $\delta\underline{I}_\xi = \underline{I}(t_\xi) - \underline{I}(t_{\xi-1})$ defines the current back-difference between the end t_ξ and the beginning $t_{\xi-1}$ of the subperiod. Since the voltage \underline{V} is constant during every subperiod, its integration can be replaced by $\underline{V}_\xi \tilde{\mathcal{S}}_\xi T_s$ that is equal to $\tilde{\underline{V}}_\xi T_s$ using the definition (4.32). Keeping a similar notation, we propose to define $\tilde{\underline{E}}_\xi T_s$ as the integration result of \underline{E} during the subperiod. Therefore, (4.39) yields:

$$\delta\underline{I}_\xi = \underbrace{L_t^{-1} \tilde{\underline{V}}_\xi T_s}_{\delta\underline{I}_{V,\xi}} - \underbrace{L_t^{-1} \tilde{\underline{E}}_\xi T_s}_{\delta\underline{I}_{E,\xi}} \quad (4.40)$$

where we defined $\delta\underline{I}_{V,\xi}$ and $\delta\underline{I}_{E,\xi}$ as virtual current variations due to the contributions of \underline{V} and \underline{E} respectively. The points reached by the current ripples during every subcycle are found at the instants t_ξ . The sign of their phase values define the zero-crossing check: $\forall p \in \{a, b, c\}$

$$\text{sign}(i_p(t_\xi)) = \text{sign}(i_p(t_0)) \quad \forall \xi \in \{1..n\} \quad (4.41)$$

However their computations are not straightforward. The value $\delta\underline{I}_{V,\xi}$ can be computed from the PWM calculator during every subcycle. But $\delta\underline{I}_{E,\xi}$ are unknown and may change at every subcycle. Moreover, since only the initial and final current values of the carrier cycle are sampled, the computation of the current after every subcycle would cumulate any error from previous subcycles. A zero-crossing check would therefore be inaccurate. We propose therefore another checking method that consist to determine a margin around the current samples, that can be larger than the real ripples. While the margins between the current samples and the zero-crossing lines are satisfied, no zero-crossing should occurs. The main difficulty

consists to fix these margins without two criteria: 1) a quick and reliable computation method regarding all the possible distortions, error and noise sources ; 2) the smallest possible margin.

Two methods are proposed hereafter. The first one comes from [125]. It is described for information only since it was not retained for several annoying drawbacks: the margins are largely overestimated, they change at every subcycle and require to be continuously recomputed. The second one is more approximate, but offers a smaller margin that is fixed for a constant amplitude of the instruction current and a constant speed.

4.3.3 The Margin Estimation - previous method

This method was published in [125]. Using complex space vectors, the principle consists to use the virtual currents defined in (4.40), as boundary points to the current ripples. Using the numbering $x\zeta$ as introduced in section 4.3.1 and summing all the $\delta \underline{i}_{x\zeta}$ during the different subperiods of one PWM carrier half-cycle x and using (4.40) yields:

$$\delta \underline{i}_x = \sum_{\zeta=1}^4 \delta \underline{i}_{x\zeta} = \sum_{\zeta=1}^4 \delta \underline{i}_{v,x\zeta} - \sum_{\zeta=1}^4 \delta \underline{i}_{e,x\zeta} \quad (4.42)$$

Using (4.32) with (4.40), we have $\delta \underline{i}_{v,x1} = \delta \underline{i}_{v,x4} = 0$. Let us also define the virtual current variation due to \underline{e} during the half-cycle:

$$\delta \underline{i}_{e,x} \triangleq \sum_{\zeta=1}^4 \delta \underline{i}_{e,x\zeta} \quad (4.43)$$

We therefore can write (4.42) as follows:

$$\underline{i}(t_{x4}) - \underline{i}(t_{x0}) = \delta \underline{i}_x = \delta \underline{i}_{v,x2} + \delta \underline{i}_{v,x3} - \delta \underline{i}_{e,x} \quad (4.44)$$

The virtual currents $\delta \underline{i}_{v,x2}$ and $\delta \underline{i}_{v,x3}$ are computed using (4.40) with the VSI active voltages \tilde{v}_{x2} and \tilde{v}_{x3} respectively, that are themselves computed using (4.32). The virtual current $\delta \underline{i}_{e,x}$ can be deduced from (4.44) assuming that $\underline{i}(t_{x0})$ and $\underline{i}(t_{x4})$ are known. The currents are sampled at $t_{10} = t^{[k-1]}$ and $t_{20} = t^{[k]}$, but generally no sampling occurs at the half-cycle time $t_{14} = t_{24}$. By approximation however, we assume that the modulation is symmetric. Thus both half-cycles are symmetrical and we can assume that $t_{x4} = (t_{10} + t_{20})/2$.

Assume that the virtual currents $\delta \underline{i}_{e,x\zeta}$ contribute all to the total $\delta \underline{i}_{e,x}$ in the same directions along the different phases. It means that there is no inversion of the virtual currents during the carrier cycle. This condition can be written as follows:

$$\begin{aligned} \text{sign}(\delta i_{p,e,x}) &= \text{sign}(\delta i_{p,e,x\zeta}) \\ |\delta i_{p,e,x}| &\geq |\delta i_{p,e,x\zeta}| \end{aligned} \quad (4.45)$$

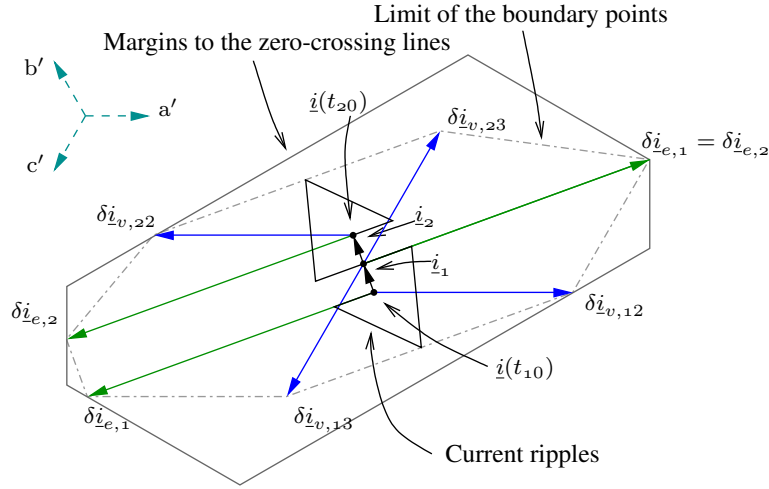


Figure 4.13: Illustration of the boundary points and the margins around the current samples in the space vector $\alpha\beta$ -frame. In that example: $a' = a$, $b' = b$ and $c' = c$.

This condition is satisfying if the different components of \underline{e} introduced in (4.37) can be assumed approximately constant during the carrier cycle. In that case, it is demonstrated hereafter that, during the first half-cycle $x = 1$, the following six current space vectors are:

$$\left\{ \begin{array}{l} \underline{i}(t_{10}), \underline{i}(t_{14}), \underline{i}(t_{10}) - \delta i_{e,1}, \underline{i}(t_{14}) + \delta i_{e,1}, \\ \underline{i}(t_{10}) + \delta i_{v,12}, \underline{i}(t_{14}) - \delta i_{v,13} \end{array} \right\} \quad (4.46)$$

During the second half-cycle $x = 2$, they are:

$$\left\{ \begin{array}{l} \underline{i}(t_{20}), \underline{i}(t_{24}), \underline{i}(t_{20}) + \delta i_{e,2}, \underline{i}(t_{24}) - \delta i_{e,2}, \\ \underline{i}(t_{20}) - \delta i_{v,22}, \underline{i}(t_{24}) + \delta i_{v,23} \end{array} \right\} \quad (4.47)$$

They are illustrated in Figure 4.13. The sign of these boundary points along the different phases should be the same in order to guarantee no zero-crossing.

The computation can be reduced along the different phases if we can assume moreover that, using the sorted phase numbers $\{a', b', c'\}$, the two virtual currents $\delta i_{v,x2}$ and $\delta i_{v,x3}$ are such that:

$$\begin{aligned} \text{sign}(\delta i_{a',v,x2}) &= \text{sign}(\delta i_{a',v,x3}) \\ \text{sign}(\delta i_{b',v,x2}) &\neq \text{sign}(\delta i_{b',v,x3}) \\ \text{sign}(\delta i_{c',v,x2}) &= \text{sign}(\delta i_{c',v,x3}) \end{aligned} \quad (4.48)$$

This condition is met if the incremental self-inductance anisotropy do not exceed a certain ratio:

$$\text{atan} \left(\frac{l_{t-}}{l_{t+}} \right) = \text{atan} \left(\frac{l_{tx} - l_{ty}}{l_{tx} + l_{ty}} \right) \leq 30^\circ \quad \Rightarrow \quad \frac{l_{ty}}{l_{tx}} \geq \frac{1 - \tan(30^\circ)}{1 + \tan(30^\circ)} = 0.2679 \quad (4.49)$$

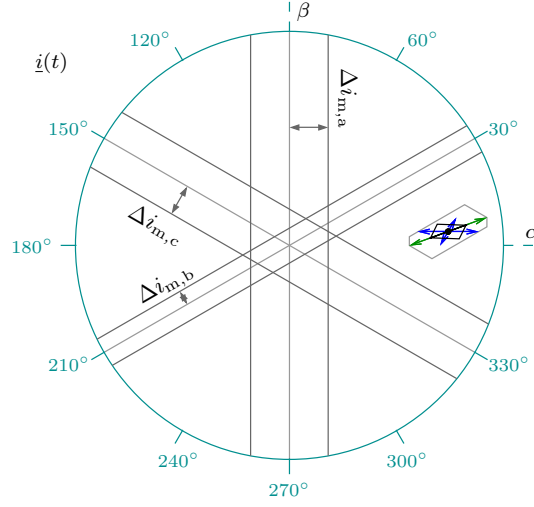


Figure 4.14: Illustration of the margins transposed around the zero-crossing lines in the space vector $\alpha\beta$ -frame.

The experimental BLDC motor satisfies this conditions with anisotropic ratio around 0.66. If the conditions (4.45) and (4.48) are satisfied, it is demonstrated that the boundary points whose sign must be checked are reduced to:

$$\begin{aligned}
 \text{along } p = a' : & \left\{ i_{a'}(t_{10}), i_{a'}(t_{10}) - \delta i_{a',e,1}, i_{a'}(t_{14}) + \delta i_{a',e,1}, i_{a'}(t_{14}) \right\} \\
 \text{along } p = b' : & \left\{ \begin{array}{l} i_{b'}(t_{10}) + \delta i_{b',v,12}, i_{b'}(t_{10}) + \delta i_{b',v,13}, \\ i_{b'}(t_{14}) - \delta i_{b',v,12}, i_{b'}(t_{14}) - \delta i_{b',v,13} \end{array} \right\} \\
 \text{along } p = c' : & \left\{ i_{c'}(t_{10}), i_{c'}(t_{10}) - \delta i_{c',e,1}, i_{c'}(t_{14}) + \delta i_{c',e,1}, i_{c'}(t_{14}) \right\}
 \end{aligned} \tag{4.50}$$

and for the second half-cycle:

$$\begin{aligned}
 \text{along } p = a' : & \left\{ i_{a'}(t_{20}), i_{a'}(t_{20}) + \delta i_{a',e,2}, i_{a'}(t_{24}) - \delta i_{a',e,2}, i_{a'}(t_{24}) \right\} \\
 \text{along } p = b' : & \left\{ \begin{array}{l} i_{b'}(t_{20}) - \delta i_{b',v,22}, i_{b'}(t_{20}) - \delta i_{b',v,23}, \\ i_{b'}(t_{24}) + \delta i_{b',v,22}, i_{b'}(t_{24}) + \delta i_{b',v,23} \end{array} \right\} \\
 \text{along } p = c' : & \left\{ i_{c'}(t_{20}), i_{c'}(t_{20}) + \delta i_{c',e,2}, i_{c'}(t_{24}) - \delta i_{c',e,2}, i_{c'}(t_{24}) \right\}
 \end{aligned} \tag{4.51}$$

These points can be checked geometrically by the projection of the boundary points, illustrated in Figure 4.13, along the phase axes.

The zero-crossing margins are computed from these points and correspond to the distance between the current samples $i_p(t_{x0}), i_p(t_{x4})$ and the boundary points. For convenience, they can be transposed along the zero-crossing lines, as illustrated in Figure 4.14. In order to simplify the computation of the margin, we assume that the ripples are much large than the variation between two consecutive current

samples. It can be written: $i_p(t_{x0}) = i_p(t_{x4})$. The margins are therefore:

$$\begin{aligned} \text{along } p = a' : \quad \Delta i_{m,a'} &:= |\delta i_{p,e,a'}| \\ \text{along } p = b' : \quad \Delta i_{m,b'} &:= \max(|\delta i_{b',v,x2}|, \delta i_{b',v,x3}) \\ \text{along } p = c' : \quad \Delta i_{m,c'} &:= |\delta i_{p,e,c'}| \end{aligned} \quad (4.52)$$

Benefits of this method: no need to estimate the values contained in \underline{e} , such as the back-emf and the voltage drops. Drawbacks: the margins are overestimated, they must be recomputed after every carrier cycle and they are sensitive to VSI time delays and to the dc-bus voltage measurement. Moreover, the margins computed using (4.52) do not take into account the oscillations due to the high-frequency signal than can be injected for the self-sensing in addition to the low-frequency signal used for the rotation-drive.

Demonstrations

It is demonstrated here that the points (4.46) are bounding the current ripples reached after every subcycle of the first half-cycle $x = 1$. The demonstration for the second half-cycle follows exactly the same principle. During the subcycle $\zeta = 1$, since $\delta i_{p,v,x1} = 0$ and using (4.45), it is shown that $i_p(t_{11})$ along the phase p is limited by the following boundaries:

$$\begin{aligned} i_p(t_{11}) &= i_p(t_{10}) - \delta i_{p,e,11} \\ \Rightarrow \quad i_p(t_{11}) &\in [i_p(t_{10}), i_p(t_{10}) - \delta i_{p,e,11}] \end{aligned} \quad (4.53)$$

During the subcycle $\zeta = 4$, since $\delta i_{p,v,14} = 0$ and using (4.45), it is shown that $i_p(t_{13})$ is in:

$$\begin{aligned} i_p(t_{13}) &= i_p(t_{14}) + \delta i_{p,e,14} \\ \Rightarrow \quad i_p(t_{13}) &\in [i_p(t_{14}), i_p(t_{14}) + \delta i_{p,e,14}] \end{aligned} \quad (4.54)$$

For the middle point $i_p(t_{12})$, the result is:

$$\begin{aligned} \left. \begin{aligned} i_p(t_{12}) &= i_p(t_{10}) + \delta i_{p,v,12} - \delta i_{p,e,11} - \delta i_{p,e,12} \\ i_p(t_{12}) &= i_p(t_{14}) - \delta i_{p,v,13} + \delta i_{p,e,14} + \delta i_{p,e,13} \end{aligned} \right\} \\ \Rightarrow \quad i_p(t_{12}) &\in [i_p(t_{10}) + \delta i_{p,v,12}, i_p(t_{14}) - \delta i_{p,v,13}] \end{aligned} \quad (4.55)$$

These points form the boundaries of the ripples given (4.46).

Using (4.48), the number of boundary points can be further reduced. For this, we start with the relation (4.44) along the phase p :

$$i_p(t_{14}) - i_p(t_{10}) = \delta i_{p,v,12} + \delta i_{p,v,13} - \delta i_{p,e,1} \quad (4.56)$$

Along $p = a'$ or c' , the boundary point $i_p(t_{10}) + \delta i_{p,v,12}$ is limited by two other boundary points:

$$\begin{aligned} i_p(t_{10}) + \delta i_{p,v,12} &= i_p(t_{14}) + \delta i_{p,e,1} - \delta i_{p,v,13} \\ \Rightarrow \quad i_p(t_{10}) + \delta i_{p,v,12} &\in [i_p(t_{10}), i_p(t_{14}) + \delta i_{p,e,1}] \end{aligned} \quad (4.57)$$

and the boundary point $i_p(t_{14}) - \delta i_{p,v,13}$ is in:

$$\begin{aligned} i_p(t_{14}) - \delta i_{p,v,13} &= i_p(t_{10}) - \delta i_{p,e,1} + \delta i_{p,v,12} \\ \Rightarrow i_p(t_{14}) - \delta i_{p,v,13} &\in [i_p(t_{14}), i_p(t_{10}) - \delta i_{p,e,1}] \end{aligned} \quad (4.58)$$

It is therefore not required to check these points along a' and c' . Along $p = b'$, it yields:

$$i_p(t_{10}) \in [i_p(t_{10}) + \delta i_{p,v,12}, i_p(t_{10}) + \delta i_{p,v,13}] \quad (4.59)$$

and

$$i_p(t_{14}) \in [i_p(t_{14}) - \delta i_{p,v,12}, i_p(t_{14}) - \delta i_{p,v,13}] \quad (4.60)$$

Moreover:

$$i_p(t_{10}) - \delta i_{p,e,1} \in [i_p(t_{14}) - \delta i_{p,v,12}, i_p(t_{14}) - \delta i_{p,v,13}] \quad (4.61)$$

and

$$i_p(t_{14}) + \delta i_{p,e,1} \in [i_p(t_{10}) + \delta i_{p,v,12}, i_p(t_{10}) + \delta i_{p,v,13}] \quad (4.62)$$

It is therefore not required to check these points along b' . This leads to the boundaries mentioned in (4.50).

4.3.4 The Margin Estimation - simplified method

In this simplified method, the issue of the high-frequency and low-frequency components of the current signal are analyzed separately. We assume that their corresponding margins required to prevent the zero-crossing can be summed in order to provide the total margin.

Low-frequency margin

For the low-frequency components, we assume that the current variations are much smaller than the ripples, as in the previous method: $\underline{i}(t_{x0}) = \underline{i}(t_{x4})$. The margins are however not computed for any position of the current space vector, but only around the zero-crossing lines. The computation is based on the value \underline{e} only, and not on the supply voltage anymore. The benefit is that the computation of the switching voltages at every carrier cycle is not required anymore, but the drawback is that an estimation of \underline{e} is needed. The contributions of $r\underline{i}$, e_{PM} and v_{sc} in \underline{e} are analyzed, but $\omega_q \frac{\partial L}{\partial \varphi_q}$ is neglected. Note that we make the approximation of an ideal symmetrical modulation. For reason of uniformity in the notations, we maintain the index of the half-cycle (with the index $x = 1$ hereafter), but the results are independent on this index.

The margins that should be kept between the current samples and the zero-crossing lines vary as a function of the current values. In order to give a simple solution, we make the assumption that the largest margin would be found for current samples located on a zero-crossing line, assuming not inverter nonlinearity. The

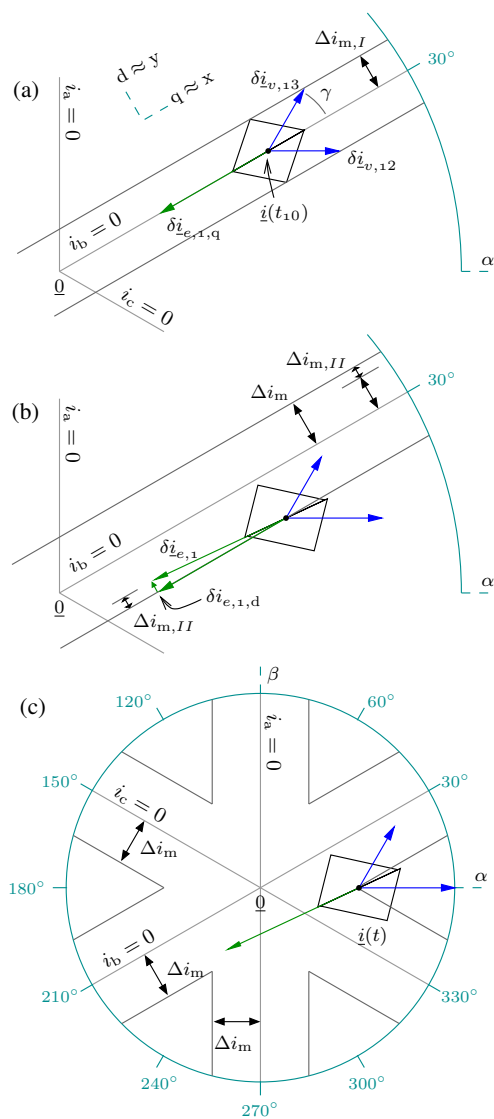


Figure 4.15: Illustration of the margin $\Delta i_m := \Delta i_{m,I} + \Delta i_{m,II}$ transposed around the zero-crossing line $i_b = 0$ in the space vector $\alpha\beta$ -frame. Geometrical construction of (a) $\Delta i_{m,I}$ alone and (b) with $\Delta i_{m,II}$. (c) Illustration of a current space-vector close to $\underline{0}$, where the zero-crossing margin seems to be valid with respect to multiple zero-crossing lines.

margin is therefore computed for current virtually located at these positions, even if the current should be kept outside this margin in practice. In that location and neglecting any anisotropy on the resistance r , the resistive voltage drop $r\dot{i}$, computed with the sample $\dot{i}(t_{10})$, is parallel to the zero-crossing line and directed toward zero $\underline{0}$. We neglect here the current ripple contribution to the resistive voltage drop. Assume also that the current is controlled along the quadratic q-axis and that the back-emf $\underline{e}_{\text{PM}} = j\omega_d \underline{\psi}_{\text{PM}}$ is along the q-axis oriented toward zero $\underline{0}$, i.e. the shift between the PM magnetic flux $\underline{\psi}_{\text{PM}}$ and the d-axis is neglected. As a consequence, $\underline{e}_{\text{PM}}$ and $r\dot{i}$ both act in the same direction along the q-axis. While no zero-crossing occurs, the semiconductor voltage drop $\underline{v}_{\text{sc}}$ is a constant space vector oriented by an angle of 30° with respect to the zero-crossing line and towards this line. Its contribution along the q-axis is therefore equal to $|\underline{v}_{\text{sc}}| \cos(30^\circ) = |\underline{v}_{\text{sc}}| \sqrt{3}/2$. Adding this contribution of the $\underline{v}_{\text{sc}}$, the virtual current variation along the q-axis is:

$$\delta i_{e,1,q} := \frac{1}{l_{\text{tq}}} \left(r|\dot{i}(t_o)| + \omega_d |\underline{\psi}_{\text{PM}}| + \frac{\sqrt{3}}{2} |\underline{v}_{\text{sc}}| \right) \frac{T_s}{2} \quad (4.63)$$

where $T_s/2$ is the period of the carrier half-cycle and where l_{tq} is the value of the incremental self-inductance along the q-axis. This virtual current is illustrated in Figure 4.15(a) with the current samples located on the line $i_b = 0$ (the result is the same along any zero-crossing line) and neglecting the contribution of the $\underline{v}_{\text{sc}}$ along the d-axis: $\delta \underline{i}_{e,1} = \delta i_{e,1,q} e^{j\varphi_q}$. This contribution along the d-axis is introduced hereafter. Assuming that the samples are fixed, this virtual current variation $\delta \underline{i}_{e,1}$ is compensated by the virtual current variations $\delta \underline{i}_{v,12}$ and $\delta \underline{i}_{v,13}$ related to the active switching voltages. These virtual currents are oriented by an angle γ symmetrically one either side of the zero-crossing line. If the incremental self-inductance has no anisotropy, this angle is $\gamma = 30^\circ$. In case of anisotropy, this angle should be slightly smaller. We propose therefore to use the overestimated angle $\gamma = 30^\circ$ for the margin computation:

$$|\delta \underline{i}_{v,12}| \cos(30^\circ) = |\delta \underline{i}_{v,13}| \cos(30^\circ) = \frac{\delta i_{e,1,q}}{2} \quad (4.64)$$

The margin to keep is equal to the component of $\delta \underline{i}_{v,12}$ or $\delta \underline{i}_{v,11}$ perpendicular to the zero-crossing line:

$$\Delta i_{m,I} := |\delta \underline{i}_{v,12}| \sin(30^\circ) = \frac{\delta i_{e,1,q}}{2} \tan(30^\circ) = \frac{1}{\sqrt{3}} \delta i_{e,1,q} \quad (4.65)$$

It is illustrated in Figure 4.15(a). Consider the semiconductor voltage drop along the d-axis: $|\underline{v}_{\text{sc}}| \sin(30^\circ) = |\underline{v}_{\text{sc}}|/2$. Since there is not other contribution, the virtual current variation along the d-axis is thus:

$$\delta i_{e,1,d} := \frac{1}{l_{\text{td}}} \left(\frac{1}{2} |\underline{v}_{\text{sc}}| \right) \frac{T_s}{2} \quad (4.66)$$

It is illustrated in Figure 4.15(b) with the current samples located at the limit with the margin. An margin additional margin is approached by this virtual current:

$$\Delta i_{m,II} := \delta i_{e,1,d} \quad (4.67)$$

The total margin is then the sum of the two proposed margins:

$$\begin{aligned} \Delta i_m &:= \Delta i_{m,I} + \Delta i_{m,II} \\ &= \frac{T_s}{2\sqrt{3} l_{tq}} \left(r |\dot{i}(t_o)| + \omega_d |\psi_{PM}| \right) + \frac{T_s}{4} \left(\frac{1}{l_{tq}} + \frac{1}{l_{td}} \right) |v_{sc}| \quad (4.68) \end{aligned}$$

This is illustrated in Figure 4.15(b). This margin is proposed with respect to one zero-crossing line, in the illustration it is $i_b = 0$. For very small operating current however, the possibility of zero-crossing with respect to another zero-crossing line should also be analyzed. From simulations, it seemed however that the proposed margin prevent from multiple zero-crossing. It is illustrated in Figure 4.15(c).

Remember that these computation are performed for a current that is virtually located along a zero-crossing line, but it is independent to the real position of the current. The only values that are required for this computation are those used in (4.68). Note that overestimated parameters r , ω_d , l_{tq}^{-1} and l_{td}^{-1} are valid. Note that issues regarding the resolution and the measurement noise must be considered if the resistive voltage drop is computed using current samples. To remove that problem, we propose to simply use the current instruction instead of the samples.

High-frequency margin

The additional margin linked to the high-frequency digital signal $\Delta i_{m,hf}$ is simply approached as the biggest magnitude of the high-frequency digital current-response \dot{i}_{hf} :

$$\Delta i_{m,hf} = |\dot{i}_{hf}| \quad (4.69)$$

This is a strong approximation, but this solution was satisfying during experiments with our experimental machine. The total margin is then the low-frequency margin $\Delta i_{m,lf}$ given in (4.68) plus $\Delta i_{m,hf}$:

$$\begin{aligned} \Delta i_m &:= \Delta i_{m,lf} + \Delta i_{m,hf} \\ &= \frac{T_s}{2\sqrt{3} l_{tq}} \left(r |\dot{i}(t_o)| + \omega_d |\psi_{PM}| \right) + \frac{T_s}{4} \left(\frac{1}{l_{tq}} + \frac{1}{l_{td}} \right) |v_{sc}| + |\dot{i}_{hf}| \quad (4.70) \end{aligned}$$

Restrictions of the methods

The method is restricted to vector control where the current is controlled along the q-axis. The proposed zero-crossing prevention, introduced hereafter, add an offset to the current instruction that is partly oriented along the d-axis. So we deviate

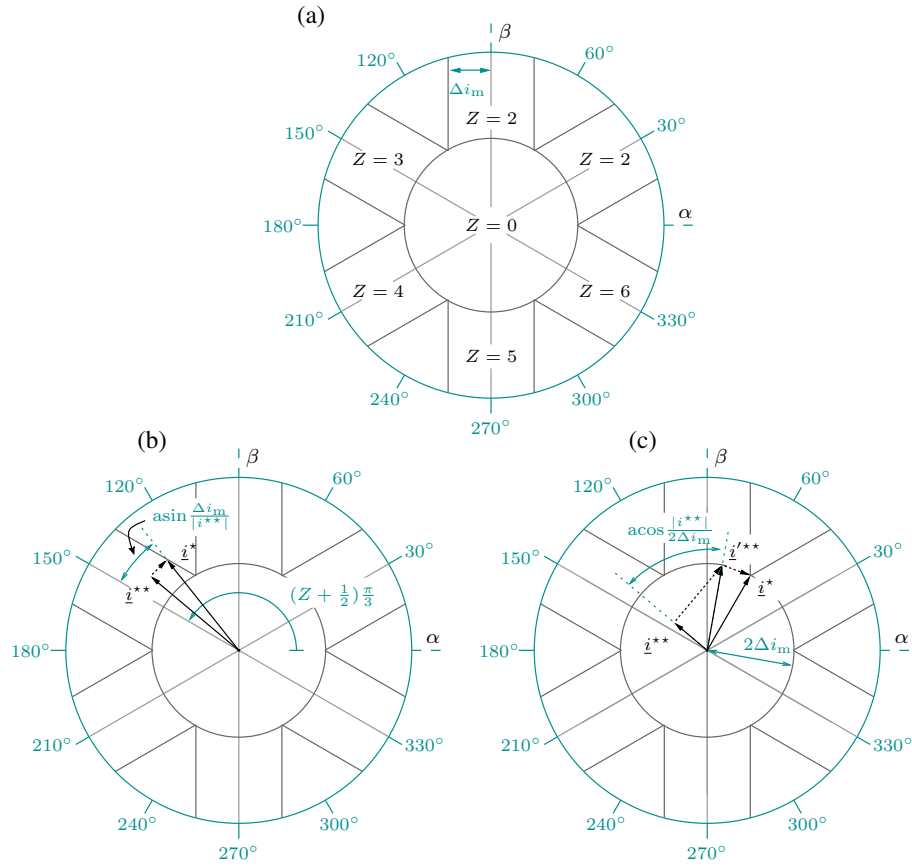


Figure 4.16: Illustration of (a) the different margin zones $Z = 1 \dots 6$; (b) Case of an instruction \underline{i}^{**} inside the zone $Z = 3$; (c) Case of an instruction inside the the central zone $Z = 0$.

slightly from the hypothesis. Moreover, it is assumed that the synchronous qd-frame is aligned with the anisotropy xy-frame, but this condition is not always met in our experimental motor. This method is therefore rather approximate and further improvements could certainly be introduced.

4.3.5 Zero-Crossing Prevention

Computation of the Offset

The strategy consist in adding an offset to the initial current instruction \underline{i}^{**} such that the new current instruction \underline{i}^* is outside the zero-crossing margins. In order to minimize the torque impact, the offset should be oriented as much as possible in a direction that minimize the torque production. It is assumed here that this direction is along the direction d-axis. A first method was proposed in [125] and a slightly improved method was proposed in [126]. We introduce this last method hereafter.

Assume that \underline{i}^{**} is along the q-axis. The possible locations of the instruction \underline{i}^{**}

inside the margins are divided in zones Z , as illustrated in Figure 4.16(a). They are numbered from 1 to 6 in an anticlockwise order, and the central zone of the margin intersections is numbered $Z = 0$. The first step consist to compute the zone Z where \underline{i}^{**} is located. If it is in $Z \in \{1 \dots 6\}$ as illustrated in Figure 4.16(b), we propose to compute the new instruction \underline{i}^* with the same amplitude but with an angle rotated outside the margin as follows:

$$\begin{cases} |\underline{i}^*| := |\underline{i}^{**}| \\ \angle \underline{i}^* := (Z + \frac{1}{2})\frac{\pi}{3} + \text{sign}(\angle \underline{i}^{**} - (Z + \frac{1}{2})\frac{\pi}{3}) \text{asin} \frac{\Delta i_m}{|\underline{i}^{**}|} \end{cases} \quad (4.71)$$

If the margin size is small compared to the amplitude of the current instruction, the offset should be along the d-axis in order to keep the impact on the torque small. If $Z = 0$, as illustrated in Figure 4.16(c), we add a first instruction offset along the d-axis, such that a temporary new instruction \underline{i}'^{**} is:

$$\begin{cases} |\underline{i}'^{**}| := 2\Delta i_m \\ \angle \underline{i}'^{**} := \angle \underline{i}^{**} + \text{acos} \frac{|\underline{i}^{**}|}{2\Delta i_m} \end{cases} \quad (4.72)$$

and then (4.71) is used with \underline{i}'^{**} instead of \underline{i}^{**} to compute the second offset. This second offset is not necessarily along the d-axis, resulting in some torque ripples during the rotation [125].

Impact of the Offset

There is a discontinuity in the proposed method introduced by the “sign” function in (4.71). Due to this discontinuity, the new current instruction \underline{i}^* jumps across the margins during the rotation. Assuming a good controller, the jumps should be small (a few PWM-periods). For the case when the initial instruction is remaining close to a zero-crossing line, it is strongly advised to compute the “sign” using an hysteresis in order to avoid uncontrollable and repetitive jumps.

In order to reduce as much as possible the current jumps and in order to reduce the torque impact, the margin Δi_m should be as small as possible. This is satisfied as low speed and small controlled currents. When the torque requirements or when the speed increase however, the margins can be quite larges. This is the case with our experimental motor.

4.4 Experimental Analysis

4.4.1 Estimation of the Margins

We propose to assess the margin corresponding to the method section 4.3.4 for the case of the experimental drive. For this, it is required to estimate different values and parameters of the test-bench VSI and the experimental machine.

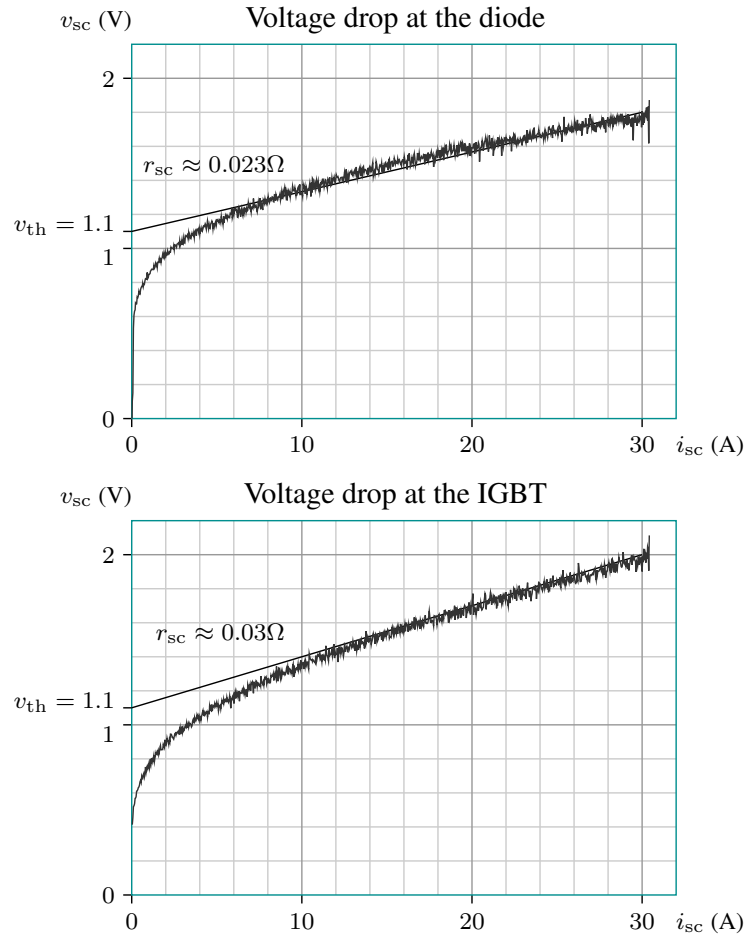


Figure 4.17: Graph of the voltage drop at the semiconductors v_{sc} as a function of the current i_{sc} , for the diode and for the IGBT. Linear approximations (plain lines). Standard deviation of the voltage measurements: 0.17 V.

Dead-time and Voltage drops

The semiconductor voltage drops have been sampled at the beginning of the PWM cycle for 2×941 different values of the currents between -30 A and 30 A. For each current value, the voltage drop is averaged on about 100 samples. Referring to Figure 4.1, for positive values, the current is flowing through the diode while, for negative values, it is flowing through the IGBT. Results are shown in Figure 4.17. We see that the voltage threshold is about the same for the diode and the IGBT, $v_{th} \approx 1.1$ V, but that the resistance is slightly different. Note that these resistances represent about half the machine resistance mentioned in Table 3.2. For information, the dead-time is approximately $\Delta t_{dt} \approx 4.2 \mu s$ (4.2% of the PWM-period $T_s = 10^{-4} s^{-1}$). For the margin computations, we neglect the dead-time and we approach the semiconductor voltage drop by the voltage threshold. Using the space

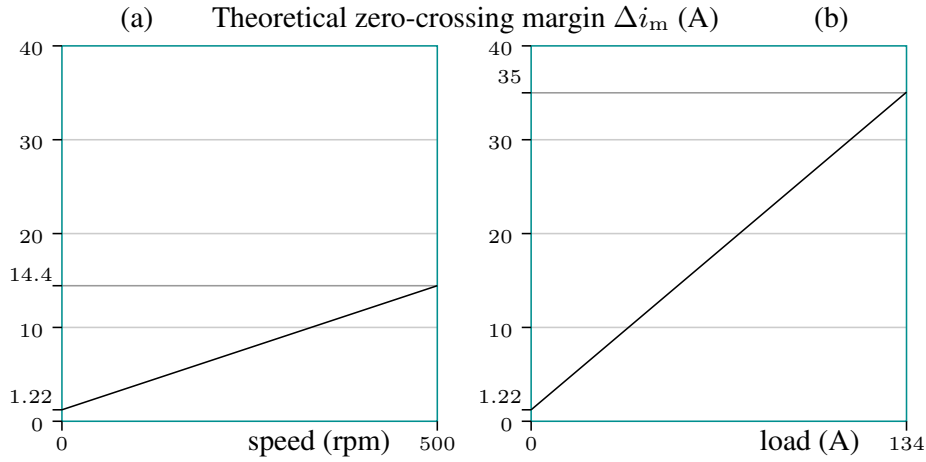


Figure 4.18: Graph of the theoretical margin, computed using (4.68), as a function of the speed and as a function of the load.

vector definition (4.26), we have $|\underline{v}_{sc}| = 4/3 u_{th} \approx 1.5$ V.

Machine Parameters

For the machine circuit parameters, we propose to base them on the estimations performed at the previous chapter 3. We take a slightly overestimation of the low-frequency resistance $r \approx 0.7 \Omega$, and underestimations of the discrete-time apparent incremental self-inductances $\hat{l}_{tx} = 80 \mu\text{H}$ and $\hat{l}_{ty} = 50 \mu\text{H}$. Neglecting the harmonics, the PM flux was estimated in chapter 2 around: $\hat{\psi}_{PM} \approx 0.05$ Wb.

T_s (μs)	$ \underline{v}_{sc} $ (V)	r (Ω)	\hat{l}_{tx} (μH)	\hat{l}_{ty} (μH)	$\hat{\psi}_{PM}$ (Wb)
100	1.5	0.7	80	50	0.05

Table 4.1: Parameters required for the computation of the zero-crossing margin.

Results

The different parameters are gathered in Table 4.1. Based on these parameters, the margin computed using (4.68), as a function of the speed, assuming no load 0 A and no high-frequency signal injection, is shown in Figure 4.18(a). It starts at 1.22 A up to 14 A for an unloaded machine rotating at the rated 500 rpm. This represents about 10% of the rated current, that is significant. The margin as a function of the load in current, assuming standstill machine and no high-frequency signal injection, is shown in Figure 4.18(b). It reaches 34.7 A for a standstill machine loaded at the rated current 134 A, that is about 25% of the rated current. This margin would lead to huge cogging torque and it is not advised. As a consequence, for that type

machine and if any method that needs an accurate knowledge of the voltage is operating (such as signal-injection-based self-sensing methods), it is therefore required to reduce the maximum eligible load. This illustrates how annoying is the problem of zero-crossings. The margin related to the high-frequency signal-injection should be added using (4.70). Experimental results with signal injections used for the position self-sensing and performing the zero-crossing prevention method explained in section 4.3.5 are shown in the next chapter 5. Empirical observations on an oscilloscope for experiments at standstill, without load and with a signal-injection of 1 A amplitude showed us that the minimum margin required to prevent zero-crossings was found around 2.1 A. Subtracting the injected-signal amplitude, it corresponds to a low-frequency margin of 1.1 A. This matches well with the theoretical margin computed with the new method (4.68) and shown in Figure 4.18. At this stage of the study however, further experiments would be required to measure the experimental margin under load and at higher speeds.

Experiments

For illustration, Figure 4.19 shows previous experimental results without signal injection and with a machine rotating at $\omega_d \approx 10$ Hz (43 rpm). The rotor position is given by an encoder. The zero-crossing prevention is based on the previous method to compute the margin (4.52). We can see the effect of the offset on the currents in (a) that produce jumps of the current across the zero. The margins are not represented in (b) because, in this previous method, the margins were changing all around the rotation. An approximation of the electrical torque, computed with $T \approx 1.5P \Im(\underline{i}^* \underline{\psi}_{PM})$, is shown in (c). We see the oscillating impact of the offset on the torque, that must be compared to the rated torque of 150 Nm. Figure 4.20 shows the measurements performed through an oscilloscope for the same experiment (not at the same instant). We see by these measurements that the current ripples are between 1 A and 2 A amplitude. This matches with the estimated ripple amplitude using (4.68). We see also that the margins of the method (4.52) are rather larger than the ripples.

4.5 Summary

In this chapter, we described the topology and the nonlinear characteristics of the two-level voltage-source inverter (VSI) with switching devices commanded by carrier-based pulsewidth modulated (PWM) signals. They mainly are:

1. the voltage drops at the semiconductor devices ;
2. the lag-time in the switching signals plus the commutation delays of the semiconductor devices, that result in so-called dead times.

The voltage drop can be linearized by a fixed voltage threshold in opposition to the current flow and a semiconductor resistance. The dead times can be linearized by

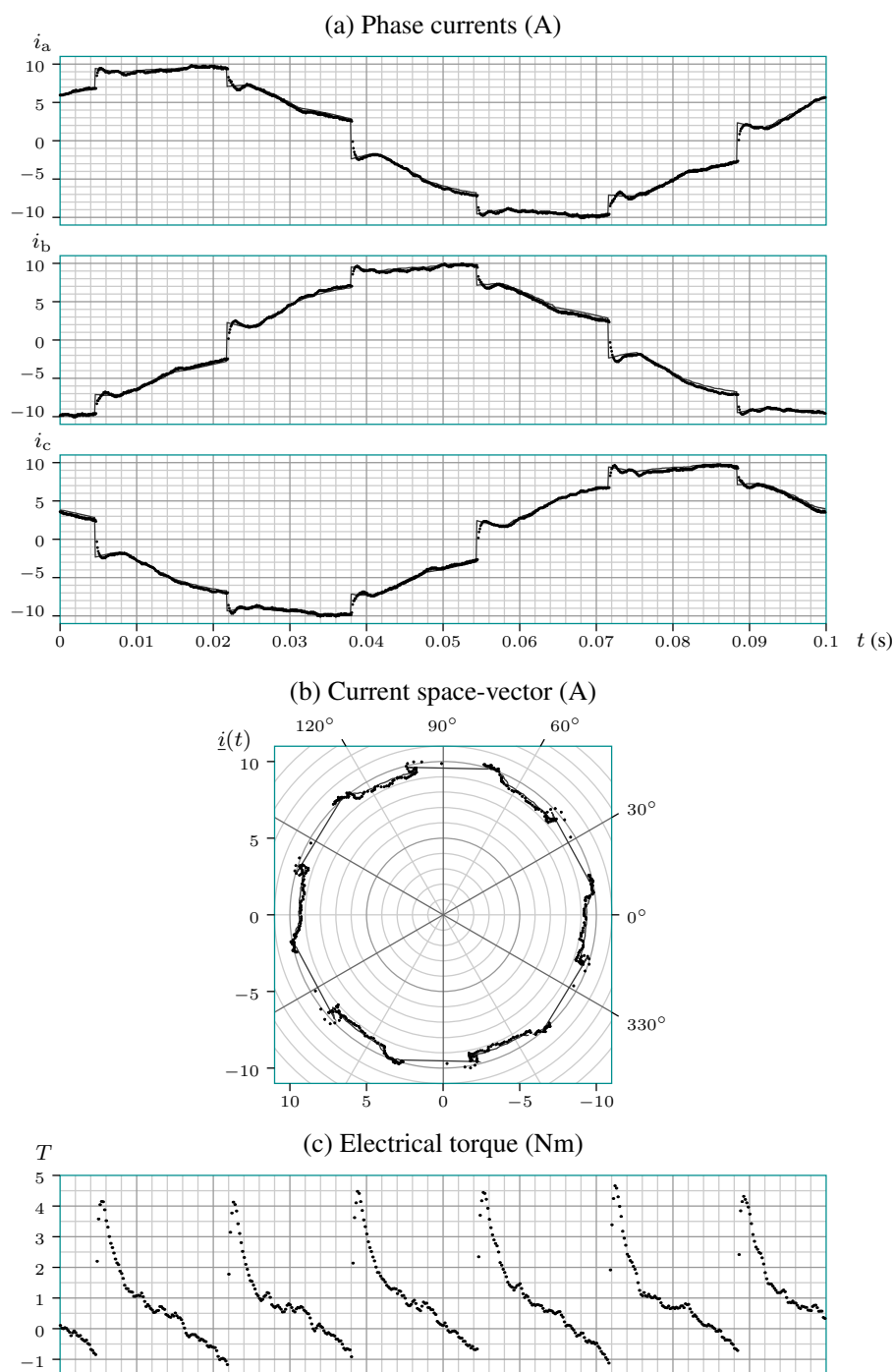


Figure 4.19: Experimental results of the zero-crossing prevention method based on the margin (4.52), for a initial current instruction around 1 A along the q-axis. No high-frequency signal is injected. The rotor orientation is given by an encoder. (a) New current instruction with the offset (plain lines) and measurements samples of the phase currents (dots) ; (b) Representation of the currents in the space-vector frame ; (c) Electrical torque approached using the fundamental space-vector of the PM flux.

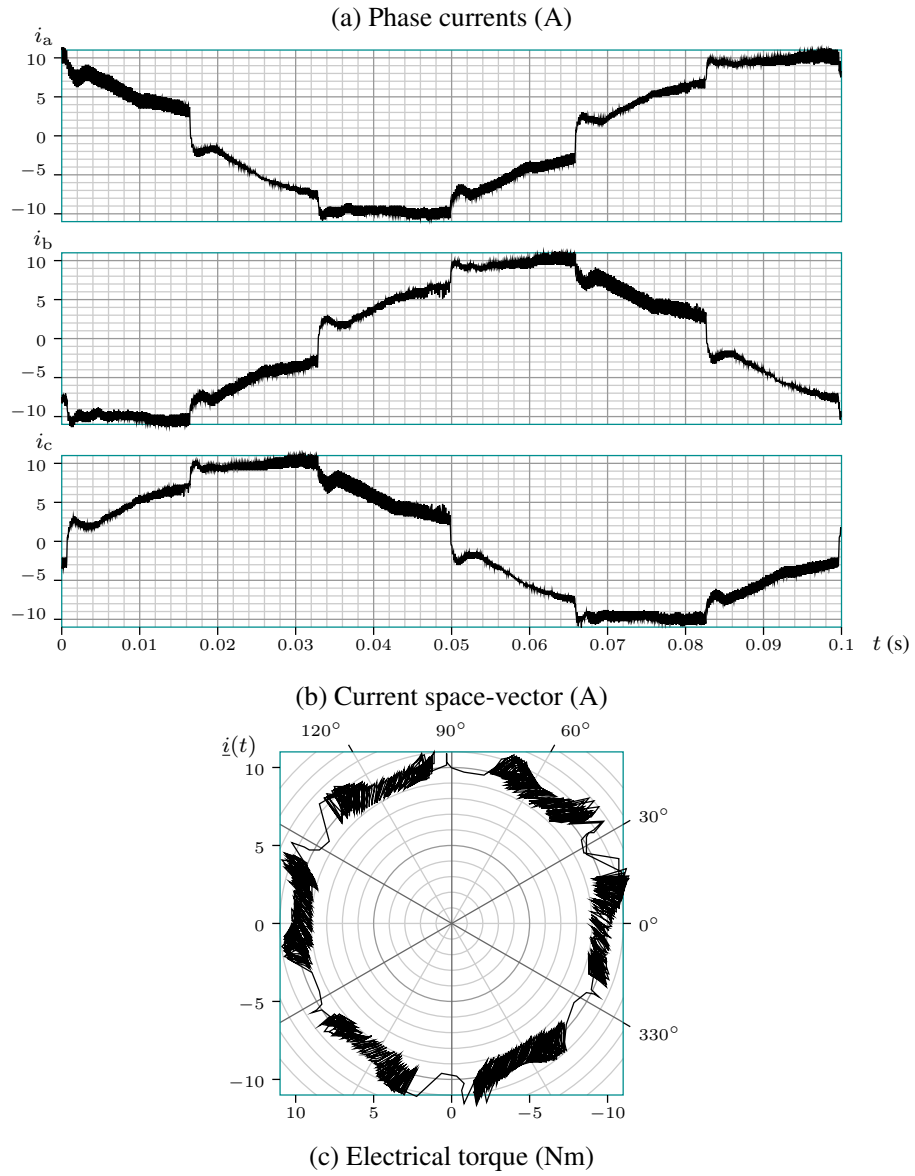


Figure 4.20: Oscilloscope measurements related to the experiment shown in Figure 4.19.

fixed values with a sign depending on the current flow. The compensation methods are therefore closely related to the current flow in the different phases. Note however that these nonlinearities, when no phase current crosses zero, are not involved in the self-sensing operations.

When a phase current crosses zero however, a phenomenon called zero-clamping tends to maintain the current at zero during the dead time. This phenomenon has a dramatic impact on the self-sensing operations based on signal injection, and leads to faulty estimations. No simple and efficient compensation method was found to compensate this zero-crossing nonlinearity. The solution is even more complicated than the current ripples may cross zero even if the current samples do not. It is therefore proposed to maintain the current instruction far enough from the zero-crossing lines and to jump through these lines when required. This solution limits the number of zero-crossings and the impact of the nonlinearity.

The first step consist to estimate the required margins. Two methods were proposed:

1. the first method computes confident margins after every sampling period. The margins are however overestimated and vary during the control operations ;
2. the second method proposes approximate margins, as a function of the stator current amplitude and the speed. This method requires an initial estimation of the stator resistance and an estimation of the PM magnetic flux. The margin is however smaller and fixed for stead-state operations.

The second step is the implementation of the zero-crossing prevention method. This method adds an offset to the initial current instruction in order to keep the current outside the margins. The offset is selected in order to have a reduced impact on the control operations, but it inevitably produces a small torque. It was shown that the required margin for the experiment BLDC motor at rated conditions are rather large. This zero-crossing prevention solution requires therefore a reduction of the maximum torque in order to limit the margin amplitude.

Chapter 5

Signal Processing

This chapter addresses the control of the machines and the position-self-sensing solutions. It details the numerous self-sensing strategies and gives the concrete operations for the studied case of high-frequency signal-injections used by the anisotropy-based self-sensing method. It is the outcome of the developments initiated from the first chapter of this thesis.

5.1 Introduction

The optimal control of PM machines requires the knowledge of the rotor position, that can be measured by external dedicated sensors. However, more and more, these sensors are removed for all the reasons mentioned in the introduction chapter 1, leading to so-called *self-sensing* methods. The principle is to use electromechanical phenomenons in the machine itself, that vary with the rotor position, to estimate the rotor position. These phenomenons can be observed and tracked from measurable electrical variables, such as currents and voltages.

At high speeds, the back-emf is a reliable source to estimate the rotor position without much effort. Its signal-to-noise quality however decreases with the rotation speed. At low rotation speed and standstill, an estimation of the rotor position can be obtained from anisotropic properties linked to the rotor position. As addressed in chapter 2, these anisotropies can be due to variations in the rotor geometry or to magnetic saturation effects in the iron and are revealed through parameters, such as the incremental self-inductance. Anisotropy misalignment may appear due to significant stator currents and to harmonics in the machines related to harmonics in the conductor distributions and to nonsinusoidal magnetic-fields.

In the vast majority of anisotropy-based strategies without extra sensors, the anisotropy is tracked performing high-frequency signal injection in addition to the rotation-drive operating signals. Many different types of signal injection can be used: test-pulse trains, PWM modifications, carrier-based pulsating and rotating-signals injection. Mathematical developments and comparisons between different signal injections are proposed in this chapter.

Except in some publications, the resistance impact is often neglected in signal-injection operations, assuming an ideal inductive machine. The eddy currents however increase with the frequency and may significantly affect the apparent resistance value, as describe in chapter 3, leading to position-estimation errors. This issue is closely related to the frequency of the injected signals. This frequency is often selected between 400 Hz and 2 kHz [127, 128] and many papers introduce self-sensing using continuous-time operations. We propose here to study discrete-time operations up to one third of the sampling frequency used by the current controller, which is the maximum possible frequency defining rotating signals. The benefits of the proposed method are analyzed regarding disturbing interactions between the rotation-drive and the self-sensing operations, regarding the filtering and the computational requirement, the robustness and the impact of the apparent resistance.

~

This chapter is organized as follows: the section 5.2 introduces elementary descriptions of the field-orient control. It is attempted to give a large overview of the many different self-sensing, to categorize them and to compared their advantages and drawbacks ; Section 5.3 addresses the model specially for the high-frequency signal-injection methods using digital measurements of the terminal currents. The principle, the assumptions and the filtering operations of the signal-injection are introduced. The position estimations operations are developed for rotating and pulsating signal injections. A last case of alternating signal injection is also addressed ; Section 5.4 shows experiment results of the self-sensing operations applied on the experimental BLDC motor ; A summary of the important elements of this chapter is given in section 5.5.

5.2 Self-Sensing Field-Oriented Vector-Control

5.2.1 The Vector-Control Principle

The term *vector controls* gather all variable-speed control-schemes intended for polyphase machines and using tools based on the space-vector concept. The current and voltage values are therefore handled using their transpositions in space vector frames, either by their complex or their matrix forms. Note that the classification of a control method in the category of “vector controls” is sometime only a question of point of view: a same processing can be equivalently deduced from phase relations or space-vector relations. In the case of a three-phase machine without neutral connection however, the space-vector relations offer generally more intuitive and shorter expressions than the phase relations.

Among the vector controls, we mainly have two strategies:

- the *Field-Oriented Control* (FOC), described hereafter and assumed in this work ;

- the *Direct Torque Controls* (DTC) and the more recent *Predictive Torque Controls* (PTC).

Comparisons between FOC and PTC for induction machines (IM) are proposed by [130, 131]. Comparisons between different PTC, called *Optimal Switching Time* PTC, *hysteresis based* PTC and more basic PTC are addressed in [132]. They are however not addressed in the frame of self-sensing controls. Review of the adjustable-speed drives, including open-loop scalar controls, are found in [5, 2, 1, 7]. Note that the choice of FOC in this work is not due to any performance consideration, but simply to the experimental equipment that does not allow to perform PTC.

5.2.2 The Field-Oriented Control

The *Field-Oriented Control* (FOC) is a vector control generally intended to three-phase synchronous machines, i.e. machines where the harmonics are small compared to the fundamental of the flux. In that case, the fundamental space vector of the flux $\underline{\psi}$ yields a good approximation of the fundamental coefficient $\psi_{(1)}$, as shown in chapter 2 by (2.50). Combining this approximation with the expression of the torque applied on the stator (2.69) yields:

$$T = \frac{3P}{2} \Im(\underline{i}^* \underline{\psi}) \quad (5.1)$$

where n is the number of phases and P is the number of pole-pair in the machine. Note that the torque applied on the rotor is $-T$. This expression (5.1) is valid with space vectors in any reference-frame. This is demonstrated here with the transposition in the synchronous qd-reference-frame using (3.8), as described in chapter 3:

$$(\underline{i}^* \underline{\psi})|_{\text{qd}} = (\underline{i}^* e^{j\varphi_q} \underline{\psi} e^{-j\varphi_q})|_{\alpha\beta} = (\underline{i}^* \underline{\psi})|_{\alpha\beta} \quad (5.2)$$

In the case of a permanent-magnet (PM) machine, the flux $\underline{\psi}$ is made of two contributions: one from the stator currents and one from the rotor PM:

$$\underline{\psi} = \underline{\psi}_S + \underline{\psi}_{\text{PM}} \quad (5.3)$$

On the other hand, the assumption of synchronous machines yields that the PM flux $\underline{\psi}_{\text{PM}}$ is oriented along the d-axis of the permanent magnet locations (by convention in a negative direction along this axis). In the synchronous qd-reference-frame, this yields:

$$\underline{\psi}_{\text{PM}}|_{\text{qd}} = -j\hat{\psi}_{\text{PM}} \quad (5.4)$$

On the other hand, for convenience, it is generally assumed that the synchronous qd-frame is aligned with the anisotropy frame related to the relation linking \underline{i} to $\underline{\psi}_S$. In the synchronous qd-reference-frame, this yields:

$$\underline{\psi}_S = l_q i_q + j l_d i_d \quad (5.5)$$

Combining these results with $\underline{i}^*|_{\text{qd}} = i_q - j\hat{i}_d$, (5.1) yields:

$$\begin{aligned} T &= \frac{3P}{2} \Im \left((i_q - j\hat{i}_d) (l_q i_q + j(l_d \hat{i}_d - \hat{\psi}_{\text{PM}})) \right) \\ &\Rightarrow T = -\frac{3P}{2} \underbrace{\left((l_q - l_d) \hat{i}_d + \hat{\psi}_{\text{PM}} \right)}_{\text{Magnetization}} i_q \end{aligned} \quad (5.6)$$

A similar expression is found in [1, 114]. A matrix form is found in [133]. Assuming that the magnetization part, made of $\hat{\psi}_{\text{PM}}$ and $(l_q - l_d)\hat{i}_d$, is constant, this expression shows that the torque T_{PM} is only function of i_q . The q-axis can therefore also be referred to as the torque axis. Note that some publications in the field of PM-machine sensorless control neglect the contribution of the anisotropy to the torque, such as [79] for the PM-machines and [131] in the case of an inductance machine. The FOC schemes are illustrated in [79, 1] with flowcharts.

The current i_d along the d -axis is sometimes used to reduce the magnetic flux amplitude $|\psi|$ [1]. The goal is to reach higher controllable speeds ω_d , assuming that the command voltage is maintained under the maximum voltage v_{max} supplied by the PWM-VSI. This is illustrated as follows. Neglecting resistive voltage drops, inverter nonlinearities and the eddy currents, the voltage \underline{v} at the machine terminals in the synchronous qd-reference-frame is:

$$\underline{v}|_{\text{qd}} \approx j\omega_d \underline{\psi}|_{\text{qd}} \Rightarrow |\underline{v}| \approx |\omega_d| \sqrt{(l_d \hat{i}_d - \hat{\psi}_{\text{PM}})^2 + (l_q i_q)^2} \quad (5.7)$$

While the speed increases, $\omega_d \nearrow$, the principle consists to increase the current $i_d \nearrow$ such that $|\underline{v}| < v_{\text{max}}$. The variations of i_d are therefore related to the speed ω_d and are slow regarding the variations of i_q performed by the torque control operations.

As we showed, all these operations are performed with space vectors in the synchronous qd-reference-frame, defined with respect to the PM-rotor position. The PM position can be measured by dedicated sensors, or using estimation methods such as the self-sensing methods described hereafter.

The expression of the PM contribution to the torque is complicated if $\underline{\psi}_{\text{PM}}$ is not oriented along the d -axis and (5.4) is not valid anymore. This is the case in our experimental BLDC motor, but experiments shown in chapter 2 that the fifth harmonic, that was the highest, represented only 1% of the fundamental amplitude. As a consequence, we could neglect the harmonics even in the case of our nonsynchronous BLDC motor. Another difference comes from the misalignment between the anisotropy and the synchronous frame. In that case, (5.5) is not valid anymore. As addressed in chapter 2, the misalignment can be due to space harmonics, but also to the increasing impact of \underline{i} on the magnetic state. This issue is not easy to handle since the value of the self-inductance is then required for any rotor position and any value of \underline{i} . Moreover, we can not rely on signal-injection methods since this method only identify the incremental part of the self-inductance, but not the self-inductance l regarding the total current \underline{i} .

Methods taking all these issues into account could certainly be developed, but this is not the topic of this study. We propose therefore to simply neglect the stator current contribution to the flux in the torque computation, and to assume the approximation of a synchronous flux for the control operations:

$$|i_d| \ll |i_q| \Rightarrow T \approx -\frac{3P}{2} \hat{\psi}_{PM} i_q \quad (5.8)$$

Note that there are also other sources of torque that are not controlled, such as the cogging torque or the torque due to the homopolar current. Controlling the homopolar current can increase the average torque produced during the rotation if we have access to the neutral connection [51]. They are however not studied in this document.

5.2.3 Conventional BLDC Control

The conventional control of BLDC-machines differs from FOC [2]. It is often described from the point of view of the phase values and assuming that the PM-fields can be approached by a trapezoidal function along the air-gap. It also neglects the anisotropy and its contribution to the torque. In that case, the torque should remain constant if opposite currents are injected in the two phases whose conductors are in front of the PM, while no current is injected in the third phase. The phase currents are therefore commutating during the rotation. Transposed in space vectors, we can define the torque axis along discrete positions of the PM. The current space vector is therefore not smoothly rotating with the PM, but jumps between these discrete positions. The commutations are usually initiated by hall-effect sensors that detect inversions of the magnetic field in the air-gap [29].

Our experimental machine is a BLDC motor. It would therefore make sense to use a conventional BLDC control method. Some experiments however showed us that the FOC produced a much smoother torque than the BLDC control. This issue was also introduced by [50].

5.2.4 Regulators in Closed-Loop Controls

Details about regulators and observers can be found in many publications [46, 134, 10, 11, 135, 36]. This work however does not focus on the regulation issues. All the regulations implemented in the experiments are based on simple discrete proportional-integral operations with anti-wind-up and limited output instructions. The operations are similar to those presented in [136]. Other type of operations exist, such as sliding-model regulators, but they are not studied in this work. For the position estimation filtering, simple *Luenberger* observers are used, as clearly described by Luenberger himself [137] and by [138], or in more recent publications [134].

Table 5.1: Comparison between the back-emf and the anisotropy as source of rotor-position information.

	1. back-EMF	2. Anisotropy
Speed range	Nonzero speed	Any from standstill
Load sensitivity	Low	Strong
Harmonic sensitivity	Medium	Strong

5.2.5 Sources of Position Information

As discussed previously, the vector controls require the knowledge of the rotor position. Two electromechanical phenomena in the PM machine model can contain rotor-position information:

- the back-electromotive force (back-EMF) ;
- a magnetic anisotropy.

They are compared in Table 5.2.5 and addressed in details hereafter. A huge number of different self-sensing strategies are found in the literature, with names that are very variable from one publication to the other. Often, the back-EMF-based methods are referred to as *fundamental model* methods [5, 139, 2]. But to our knowledge, the strategies found are all based on one or both of these sources of position information, sometimes with specific issues depending on the machine types.

5.2.6 Back-EMF-Based Self-Sensing

The back-EMF is the voltage induced by the time variation of the magnetic flux produced from the rotor-side and linked by the stator circuits. It is related to the rotor position in any machine having an independent magnetic source at the rotor, generally referred to as synchronous machine. The case of induction machines, also called asynchronous machines, is more complicated since the back-EMF is not induced from an independent rotor source, but related to a mutual flux and it is function of the shift between the rotor speed and the stator signal frequency. More details about back-EMF-based self-sensing methods in induction machines are given in [140] with analysis of parameter sensitivity and in [5, 2].

In case of PM, the back-EMF is written: $e_{PM} = d\psi_{PM}/dt$. In synchronous machines where the flux can be approached by its fundamental component, the PM flux is of constant amplitude and aligned with the d-axis: $\psi_{PM} = \hat{\psi}_{PM}e^{j\varphi_d}$. The back-EMF is then a reliable source to estimate the rotor position and speed without much effort [141]:

$$e_{PM} = \frac{d\psi_{PM}}{dt} = j\omega_d \hat{\psi}_{PM} e^{j\varphi_d} \Rightarrow \begin{cases} \omega_d = |e_{PM}|/\hat{\psi}_{PM} \\ \varphi_d = \angle(-je_{PM}) \end{cases} \quad (5.9)$$

If $\hat{\psi}_{\text{PM}}$ is known, the rotation speed ω_{d} is directly deduced. Otherwise, ω_{d} can be computed using an observer of the dynamic model (not developed here), and then $\hat{\psi}_{\text{PM}}$ could be deduced. Except in [142, 143], note that (5.9) is generally not explicitly mentioned in most of the publications, but it is integrated in an observer expression, such as described hereafter.

The back-EMF estimation can be based on one of the machine models developed in chapter 3. Let us analyze this issue from the continuous-time machine model without eddy currents in the stationary $\alpha\beta$ -frame (3.48):

$$\underline{e}_{\text{PM}} = \underline{v} - l_{\text{t}+} \frac{d\underline{i}}{dt} - l_{\text{t}-} \frac{d\underline{i}^*}{dt} - \left(r_{+} + \omega_{\text{q}} \frac{\partial l_{+}}{\partial \varphi_{\text{q}}} \right) \underline{i} - \left(r_{-} + \omega_{\text{q}} \frac{\partial l_{-}}{\partial \varphi_{\text{q}}} \right) \underline{i}^* \quad (5.10)$$

If the PWM-VSI nonlinearities are compensated, \underline{v} is known by its command value \underline{v}^* . The currents \underline{i} are measured. The computation of $\underline{e}_{\text{PM}}$ then requires accurate knowledge of all the parameters appearing in that expression. The expression (5.10) is generally not directly used to compute the back-EMF estimation. In order to reduce the noise impact and in order to eventually correct the parameter values, the use of an observer is advised. Most of the observers found in the literature assume no anisotropy and no variation of the self-inductances as a function of the position [5]. This is the case with [144] with a stator-flux-based methods using MRAS observer. Other publications take the anisotropy into account [79, 133, 142], or [145] using extended Kalman filters, but assuming constant parameters and assuming that the anisotropy is aligned with the synchronous frame. In [133], the method is improved including the dynamic model of the machine in the observation. In [133], the method is augmented by a signal-injection that identifies the resistance, that may vary with the temperature. It however neglects any anisotropic aspects. Taking the anisotropy into account in back-EMF-based methods is however not easy. Anisotropy misalignments can appear if the current load is significant or if the machine presents important harmonics. Moreover, the harmonics result in anisotropic relations oscillating at several times the rotation frequency. This strongly complicates the implementation of an observer. This is the case of the experimental BLDC motor. A review of the different types of methods is given by [5, 2].

As shown by (5.9), the back-EMF magnitude is directly related to the rotor speed. Therefore, the position estimation accuracy decreases with the speed reduction, and completely vanishes at standstill. This is the main drawback of the solutions compared to the anisotropy-based solutions, described hereafter. Some authors therefore propose methods switching between the two self-sensing solutions around a threshold speed [133, 143, 114].

5.2.7 Anisotropy-Based Self-Sensing

Terminal-based circuit model

We focused here on a model linking space vectors of the voltage and current terminals, that are sampled by the sensors used by the rotation-drive controller. Self-

sensing methods based on this model do therefore not require extra sensors, leading to a cost reduction and better reliability. The robustness is further improved by the possibility to place the terminal current sensors, and the DC-bus voltage sensor, distant from the rotor. They can thus be isolated from rotation vibrations and other environmental stresses [6].

The anisotropy of the incremental self-inductance is linked to geometry variations such as the air-gap length (rotor with salient poles) or to variations in magnetic saturation levels in the iron. It can be written using (2.81):

$$d\underline{\psi}_S = l_{t+}d\underline{i} + l_{t-}d\underline{i}^* e^{j2\varphi_x} \quad (5.11)$$

where the anisotropy angle φ_x is an estimator of the synchronous qd-frame angle φ_q linked to the rotor position. Misalignment between the anisotropy and the synchronous frame lead to position estimation errors, as discussed in Chapter 2.

A pronounced anisotropy, i.e. a significant l_{t-} regarding l_{t+} , is a benefit to achieve accurate estimations. The anisotropy ratio l_{t-}/l_{t+} tends to decrease with the load current \underline{i} in most of the machine designs. A map of the anisotropy with respect to the load, and feasibility operation regions are therefore established by some authors [60, 58, 59]. Special attention can be paid to the machine design in order to increase their anisotropy [40, 59, 146, 67]. On existing machines, it is sometimes possible to increase the anisotropy by adding a copper turn wound around the poles [68, 69]. Salient-poles machines, reluctance machines and many permanent-magnet (PM) machines, naturally present significant anisotropic properties. They are therefore appropriate candidates for the study of self-sensing methods based on anisotropies. The only anisotropy is related to the teeth between the slots containing the rotor coil. This results in small anisotropic amplitudes and in harmonics of much higher orders, that are not easy to identify. More details about anisotropy-based self-sensing methods in induction machines are given in [147, 139]. We focus here on PM machines.

The anisotropic relation (5.11) is independent to the speed and it can be used to estimate the rotor position from standstill up to the maximum speed. This is an important benefit compared to back-EMF-based self-sensing methods. The identification method can however carry some difficulties and drawbacks, that are discussed in this study. In practice, we do not have a direct access to $d\underline{\psi}_S$, since the relation is involved in the electrical circuit expression linking the stator currents \underline{i} with the supply voltage \underline{v} and the back-EMF \underline{e}_{PM} . Let us analyze this relation using the continuous-time machine model without eddy currents in the stationary $\alpha\beta$ -frame (3.48):

$$\underbrace{l_{t+} \frac{d\underline{i}}{dt} + l_{t-} \frac{d\underline{i}^*}{dt}}_{d\underline{\psi}_S/dt} + \underbrace{r_+ \underline{i} + r_- \underline{i}^*}_{\underline{v}_r} = \underline{v} - \underline{e}_{PM} - \underbrace{\left(\omega_q \frac{\partial l_+}{\partial \varphi_q} \underline{i} + \omega_q \frac{\partial l_-}{\partial \varphi_q} \underline{i}^* \right)}_{\text{neglected}} \quad (5.12)$$

The last term is due to harmonics in the self-inductance anisotropy, as explained in chapter 2. Being proportional to the current, it acts as an equivalent resistive

contribution, with the oscillating value, that could be mixed with the stator resistor. No publication found by the author manage this term, that is generally neglected [143]. We propose also to neglect it at this stage of the study, but its impact is quickly assessed at the end of this subsection.

As we can see in (5.12), the incremental self-inductance is not the only possible anisotropy source of this relation. Chapter 3 introduced the fact that the stator resistance can also present an anisotropy due to unbalancing between the different phase resistances, but this anisotropy is not linked to the rotor position. It was however showed that eddy currents, or any additional circuit placed in the rotor [68, 69], influence the apparent parameter values of the circuit model. In particular, the apparent resistance for high-frequency signals could largely increase in relation with a magnetic anisotropy linked to the rotor position. This effect is used in some publications to develop self-sensing methods based on resistance-anisotropy [148, 85, 149]. As discussed in chapter 3, this strategy should however be assessed with respect to discretization and PWM distortions. Assuming that the anisotropy angles of the incremental self-inductance and the resistance are equal, (5.12) can be written:

$$\left(l_{t+} \frac{d\underline{i}}{dt} + r_+ \underline{i} \right) + \left(l_{t-} \frac{d\underline{i}}{dt} + r_- \underline{i} \right)^* e^{j2\varphi_x} = \underline{v} - \underline{e}_{PM} \quad (5.13)$$

The low frequency signals used by the rotation-drive operations are generally not adequate to perform self-sensing estimations. In one hand, the current variations $d\underline{i}/dt$ are small compared to the measurements noise, leading to inaccurate estimations. On the other hand, the back-EMF is apriori unknown. In the vast majority of anisotropy-based methods, the solution to overcome these issues consists to use self-sensing estimations based on signals having higher frequencies than the rotation-drive operating signals (also sometimes referred to as “fundamental” operating signals) [5]. The self-sensing operations are then based on the relation between high-frequency signals, denoted here by hf. Higher the frequency, higher the contribution of $d\underline{i}_{hf}/dt$ with respect to \underline{i} and to the noise. As a consequence, a large number of methods found in publications neglect the resistive contribution. Moreover, the contribution of the high-frequency signals to the back-EMF tends to decrease, such that $\underline{e}_{PM,hf}$ is neglected in the high-frequency model. These points are further discussed in section 5.3. Therefore, (5.13) simply yields:

$$l_{t+} \frac{d\underline{i}_{hf}}{dt} + l_{t-} \frac{d\underline{i}_{hf}^*}{dt} e^{j2\varphi_x} \approx \underline{v}_{hf} \quad (5.14)$$

Since the injected high-frequency voltage \underline{v}_{hf} is known and since \underline{i}_{hf} can be measured, it is possible to identify the anisotropy angle φ_x . The method to extract φ_x depends on the type of signal. This is addressed in the next section 5.2. The impact of significant resistance on the self-sensing operations assuming this approximation is also addressed in this chapter.

Table 5.2: Comparison between solutions with extra sensors dedicated to the self-sensing operations and solutions using the terminal values.

	1. Terminal-based	2. Dedicated sensors
Type	Control sensors	Specifically selected
Accuracy	Lower	Increased
Reliability	Strong	Lower

Assessment of the impact from self-inductance variations

The impact of the neglected part in (5.12) is quickly assessed in the case of the experimental machine. For this, we assume that the harmonic content of the self-inductance should be lower in amplitude than the harmonic content of its incremental part. Therefore, the assessment is based on the incremental self-inductance, considered as an upper limit. Using the results of the experimental BLDC machine presented chapter 2, it was shown that $l_{t,+}$ is quite constant: $\partial l_{t,+}/\partial \varphi_q \approx 0$; and that $l_{t,-}$ only contains significant harmonics at $k = 2$ and $k = -4$. Neglecting the misalignment due to the current load, it yields:

$$l_{t,-} = l_{t,(2)}e^{j2\varphi_q} + l_{t,(-4)}e^{-j4\varphi_q} \quad (5.15)$$

$$\Rightarrow \omega_q \frac{\partial l_{t,-}}{\partial \varphi_q} = 2\omega_q l_{t,(2)}e^{-j4\varphi_q} - 4\omega_q l_{t,(-4)}e^{-j4\varphi_q} \quad (5.16)$$

where $|l_{t,(2)}| \approx 23 \mu\text{H}$ and $|l_{t,(-4)}| \approx 3 \mu\text{H}$. At the rated speed of the motor, $\omega_q = 2\pi \times 116 = 729 \text{ rad/s}$. Therefore:

$$\begin{cases} |2\omega_q l_{t,(2)}| \approx 0.034 \Omega \\ |4\omega_q l_{t,(-4)}| \approx 0.009 \Omega \end{cases} \quad (5.17)$$

These results are lower than resistance, that varies between 0.05Ω for DC signals and 0.15Ω for 3.33 kHz signals. We assume therefore that if the resistance contribution is small, then the self-inductive-variations contribution should also be small.

Dedicated-sensor solutions

Other solutions based on extra sensors are however possible. The drawback of extra sensors are always the same: additional source of possible failure, additional setup and cost. However, if dedicated to the self-sensing operations, the resolution of these extra sensors can be adapted to the small amplitude of the high-frequency signals used to identify the anisotropy angle [105]. This can be especially advised for machines presenting very small anisotropic properties, such as induction motors (IM). For example, [147, 139] use the zero-sequence current response flowing in a delta-connected stator circuit of IM. The main risk concerns the reliability because

Table 5.3: Comparison between different sources of high-frequency signals.

	1. DTC/PTC	2. PWM	3. Signal-Injection
Command	Subordinated	Subordinated	Free (*)
High-frequency	/	$\omega_c \ll \omega_s < \omega_{hf}$	$\omega_c \ll \omega_{hf} < \omega_s$
Measurements	Samples	Additional	Samples
Model sensitivity	High	Low	Low

Symbols: Usable high-frequencies ω_{hf} ; rotation-drive frequency ω_c ; sampling frequency ω_s . Note: (*) in the limit of the eligible voltages by the VSI and on the maximum current.

this sensor is placed in the stator circuit of the machine, and undergoes environmental stresses. It is also possible to use the zero-sequence voltage for self-sensing operations, as proposed in [150, 66, 105].

Note that some publications mention the use of current-slope sensors. These sensors can be dedicated [139, 151] or simply included in some newer sensors also used for the rotation-drive control operations. The issue of the noise in such current-slope measurements must however seriously be studied.

We also mentioned some alternative solutions: [77] proposes a solution based on an independent high-frequency supplier. This solution therefore requires also additional setup of the separated supply. [152] proposes to use a back-EMF detection circuit for the commutation of the currents in a BLDC motor control. [153] proposes a low cost solution by the measurement of the DC-bus current.

5.2.8 High-Frequency Sources

Let us analyze three sources of high-frequency signals that could be used for self-sensing operations. They are summarized in Table 5.2.8:

1. The high-frequency signals can be naturally produced by the rotation-drive operations, even if they are not used for the rotation drive. This is the case of the ripples in DTC and in PTC. The self-sensing operations can be performed using the current samples used for the control, without additional samplings. The high-frequency signal is however subordinated to the hysteresis method of the torque controller and it is therefore not independently commanded in time and amplitude. Moreover, that type of self-sensing strategy is significantly sensitive to the model parameters, such as the resistance and the back-EMF that must be known since they contribute to the current variations. Self-sensing methods using DTC signals or PTC signals are developed in [154, 155, 156]. Another type of controls such as the *Current Hysteresis Chopping Control* intended for switched reluctance motor (SRM) supplied by asymmetrical half bridge power converter may also provide high-frequency signals reliable for self-sensing operations, as proposed by [157].

2. It is also possible to use the high-frequency ripples due to the pulse-width modulation (PWM) of the voltage-source inverter (VSI) introduced in chapter 4. The main benefit is that the PWM is naturally present in the supplied voltage and that the frequencies are much larger than the rotation-drive frequencies [5]. The signal amplitudes are however generally small, especially at standstill and without load [143]. A solution to increase the ripple amplitude is proposed by [158] with the adjunction of a capacity at the neutral point of the three-phase circuit. Another drawback is that the high-frequency voltage is function of the modulation strategy and it is not independently commanded. Finally, this solution requires additional measurements, operating at higher frequencies than the sampling frequency used for the drive. Different solutions are possible: either measuring the current at specific instants [143], using current-derivative dedicated sensors [151] or using very high-frequency digital measurements systems.

3. The last proposed solution consist to inject additional high-frequency signals in the drive. The main benefit is that this signal is commanded, such that the high-frequency voltage amplitude can be adapted in order to compensate for noise and distortions, and the orientation can be modified in order to track the anisotropy. The self-sensing operations can also be performed using the current samples used for the rotation-drive operations also, and no extra sensor is thus required. The main drawback comes from the fact that this solution requires by principle the injection of addition signals, leading to additional vibrations and additional noise. Note however that some methods using signal injection use additional current samplings, such as in [159], but they are not further studied here. In that categorization, the methods based on PWM modifications are part of the signal-injection methods and not of PWM-ripple-based methods.

This study mainly focuses on the solution 3) using high-frequency signal injection that does not require additional measurements and allows an independent command of the injected voltage.

All these methods consist in the injection of high-frequency voltages in addition to the low-frequency voltage in output of the current controller, used for the rotation-drive. Another solution is proposed by [160] that inject current signal through the current instruction sent to the controller. This solution is however strongly limited by the performances of that controller.

Another particular method to be mentioned is proposed by [161], and consists to inject a very high-frequency signal during one subperiod of the PWM. By choosing a signal that does not modify the mean voltage, this solution removes any interaction with the rotation-drive, but it requires additional and very accurate samples.

Table 5.4: Comparison between permanent and intermittent signal injections, as generally met in the literature.

	1. Permanent	2. Intermittent
Self-sensing filtering	High-pass filtering	Response difference
Signal frequencies	$\omega_i \leq \omega_s/2$	$\omega_i = \omega_s/2$ (*)
Settling time	To be considered	Very short
Voltage amplitudes	Small	May be larger
Rotation-drive measur.	Low-pass filtering	Interruption
Remaining impact	None	To be considered

Symbols: signal-injection frequencies ω_i ; sampling frequency ω_s .

Note: (*) in case of asymmetrical modulation, the signal-injection frequency can reach the PWM frequency: $\omega_i = \omega_{\text{PWM}} = \omega_s/2$.

5.2.9 Types of Signal Injections

We propose to distinct two categories of injected signals:

1. Permanent signal-injection: the voltage-signal is continuously injected without interruption. The so-called *carrier*-based signal injections, rotating and pulsating, are part of this branch [115, 105, 54, 77, 55, 133, 56, 90, 7, 148, 91, 41, 162]. The high-frequency and low-frequency signals are separated using conventional low and high-pass filters, as further addressed. Many authors propose developments based on continuous-time models and continuous-time filtering, even if the operations are digital. In this chapter and in [126, 163], digital operations are however proposed. The main benefit of the permanent signal-injections are their simplicity.
2. Intermittent signal-injection: the voltage-signal is applied during limited period of times, generally after two sampling periods. The so-called trains of *test pulses* [79, 164, 159, 154, 165, 166, 7, 167] and certain *modified-PWM* [162, 168] are part of this branch, and are based on discrete-time machine models. The modified-PWM methods are generally based on asymmetrical modulation techniques, as introduced in chapter 3, and are equivalent to test pulse methods where the pulses are alternating on two half PWM-carriers, as in [166, 162]. In many of these methods, the low-frequency signal is filtered by the difference of the current response between two consecutive tests. The samples containing the high-frequency current response are generally removed for the rotation-drive operations. In some previous strategies, important distortions of the current remained after the test-pulse period, that affected the rotation-drive operations [159]. Improved solutions are introduced in [165] with adaptive test pulses that reduce the remaining current response after a test period. Compared to permanent signal-injection, test

pulses allow to modify the injected voltage after every signal-injection period and to cover the maximum supplied voltage [165]. The only drawback concerns the remaining impact of resistive voltage drops that may affect the rotation-drive operations, as explained in [169].

The distinction between permanent and intermittent signal-injections are not always obvious. The method proposed in the next chapter shows that, using discrete-time operations, finite-impulse response filters and some other considerations, both signal-injections are quite equivalent. A comparison between the rotating and pulsating permanent signal-injections is proposed by [66, 120].

Other uses of signal injections

The presence of an anisotropy is not required for double-fed IM. As proposed by [9], the rotor orientation can be deduced from the mutual inductance orientation. This is performed measuring the current response induced in the rotor by high-frequency signals injected in the stator (or inversely).

For information, signal-injection can be performed for other reasons than self-sensing position estimations, but to estimate the motor temperature, based on resistance variations during the drive operations, as proposed by [170, 171].

5.2.10 Position Estimation From The Anisotropy Angle

Initial polar ambiguity issue

The angle φ_x is defined on a period π , leading to an inherent ambiguity about the directions of the poles. Assuming that the orientation of the d-axis is known, the polar ambiguity can be initially removed by tracking small differences of the incremental self-inductance along opposite magnetizing directions: injecting a large test current along the positive direction of the d-axis should reduce the magnetic saturation in the machine (assuming that $\underline{\psi}_{PM}$ is oriented in the direction of negative values); while injecting a large test current along the negative direction should increase the magnetic saturation in the machine. The incremental self-inductance should therefore be slightly larger for positive currents than for negative currents along the d-axis. If that difference is larger than the noise, it is possible to remove the initial ambiguity. This strategy is proposed by [79, 164, 95, 172]. It is also performed by [173] for a brushless DC motor, comparing the difference between phase inductances with a position look-up table. In [174, 175, 176], large oscillating signals are used instead to test pulses.

Naturally the back-EMF-based self-sensing methods do not have problem of polar ambiguity, but are not working at standstill [79]. Combining both anisotropy-based with back-EMF-based self-sensing methods allow to guarantee that the polarity ambiguity is not lost at higher speeds [177].

Position error due to the load

Misalignment must be corrected if the contribution of the stator current to the magnetic state becomes significant. This contribution mainly comes from the current component along the quadratic q-axis, also called load current due to the relationship with the torque. Publications propose to compensate for this misalignment use look-up tables of angle corrections. These look-up tables however require initial and offline commissioning that are not always feasible in practice. Other recent methods combine simultaneously anisotropy-based and back-EMF-based self-sensing methods, in order to compensate for their respective error sources. Assuming that the back-EMF estimation is less sensitive to the load current, it can be used as an online commissioning of the anisotropy misalignment. The angle correction can then be performed online. These solutions are proposed in [57, 115, 167, 177].

Position error due to harmonics

A compensation method to the second harmonics in the anisotropy is proposed in [158]. This second harmonic is estimated during a commissioning, but not online. Methods of estimation based on feedback gains are proposed by [53, 56].

5.3 High-Frequency Signal Injection

We propose here the development of the required discrete-time model, the principle and the conditions for anisotropy-based self-sensing operations using high-frequency signal injections.

5.3.1 The Discrete-Time Model

We assume that the different operations are performed by digital controllers. A discretized model is therefore required. The current measurements are sampled with a frequency ν_s at instants $t^{[k]} = kT_s$, where $T_s = 1/\nu_s$ is the sampling period. For convenience, the pulse-width modulated signal (PWM) driving the voltage-source inverter (VSI) is synchronized with the sampling times. The mean value of the voltage supplied by the VSI between two sampling times was defined in (3.55) as follows:

$$\tilde{v}^{[k]} \triangleq \frac{1}{T_s} \int_{t^{[k-1]}}^{t^{[k]}} \underline{v}(t) dt \quad (5.18)$$

Assuming that the inverter nonlinearities are compensated, as described in chapter 4, the mean voltage supplied by the VSI should be equal to the command voltage sent to the PWM-VSI. Similarly, $\tilde{e}_{PM}^{[k]}$ is therefore the mean value of the back-EMF between two sampling times. The backward-difference of the current was defined in (3.57) as follows:

$$\delta \underline{i}^{[k]} \triangleq \underline{i}(t^{[k]}) - \underline{i}(t^{[k-1]}) \quad (5.19)$$

And finally the sampling average of the current was defined in (3.58) as follows:

$$\bar{i}^{[k]} \triangleq \frac{i(t^{[k]}) + i(t^{[k-1]})}{2} \quad (5.20)$$

Base on (5.13) and assuming constant parameters during the sampling periods, the discrete-time machine model without eddy currents in the stationary $\alpha\beta$ -frame yields:

$$\left(\frac{l_{t+}}{T_s} \delta \underline{i}^{[k]} + r_+ \bar{i}^{[k]} \right) + \left(\frac{l_{t-}}{T_s} \delta \underline{i}^{[k]} + r_- \bar{i}^{[k]} \right)^* e^{j2\varphi_x} = \underline{u}^{[k]} \quad (5.21)$$

where we defined $\underline{u} \triangleq \underline{v} - e_{PM}$.

5.3.2 The z -Transform of the Model

The operations can be described using the z -transform of the discrete-time model (5.21). In this chapter, the z -transform of a discrete-time space vector is written:

$$\underline{X}(z) \triangleq \mathcal{Z}\{x\} \quad (5.22)$$

where \underline{X} is therefore a function of the parameter z . This \underline{X} should not be confused with the matrix space vector introduced in Chapter 3, but not used here. Being used in the model, the z -transform of the conjugate value \underline{x}^* is [46]:

$$\mathcal{Z}\{\underline{x}^*\} = \underline{X}^*(z^*) \quad (5.23)$$

Assume in first approximation that φ_x is constant. Introducing the following z -transform $\tilde{\underline{U}}(z) \triangleq \mathcal{Z}\{\tilde{u}\}$, $\delta \underline{I}(z) \triangleq \mathcal{Z}\{\delta \underline{i}\}$ and $\bar{\underline{I}}(z) \triangleq \mathcal{Z}\{\bar{i}\}$, the z -transform of the model (5.21) yields:

$$\left(\frac{l_{t+}}{T_s} \delta \underline{I}(z) + r_+ \bar{\underline{I}}(z) \right) + \left(\frac{l_{t-}}{T_s} \delta \underline{I}^*(z^*) + r_- \bar{\underline{I}}^*(z^*) \right) e^{j2\varphi_x} = \tilde{\underline{U}}(z) \quad (5.24)$$

This expression can be further simplified using the relation between $\delta \underline{i}$ and \bar{i} that is deduced from (5.19) and (5.20). It can be shown that the relation between their z -transforms is linked by a transfer function $D(z)$:

$$\delta \underline{I}(z) = D(z) \bar{\underline{I}}(z) \quad \Rightarrow \quad D(z) \triangleq \frac{2(1 - z^{-1})}{1 + z^{-1}} \quad (5.25)$$

Observe that $D^*(z^*) = D(z)$. This relation allows to highlight the relation between $\tilde{\underline{U}}(z)$ and either 1) only $\delta \underline{I}(z)$ or only 2) $\bar{\underline{I}}(z)$ in (5.24), removing the other value. Most of the permanent signal-injection strategies are based on the choice 2) while most of the intermittent signal-injection strategies are based on the choice 1). This is choice is further addressed. We propose here to continue with the choice 1), and (5.24) can be written:

$$Z_+(z) \delta \underline{I}(z) + Z_-(z) e^{j2\varphi_x} \delta \underline{I}^*(z^*) = \tilde{\underline{U}}(z) \quad (5.26)$$

where we define two transfer-functions $Z_+(z)$ and $Z_-(z)$, that we respectively call positive and negative integral-impedances:

$$\begin{cases} Z_+(z) &= \frac{l_{t+}}{T_s} + \frac{r_+}{D(z)} \\ Z_-(z) &= \frac{l_{t-}}{T_s} + \frac{r_-}{D(z)} \end{cases} \quad (5.27)$$

In most of the drives, the voltage is the commanded input signal and the current is the measured output signal. It is therefore required to reverse the relation (5.26). As demonstrated in the annexes of [163] and hereafter, using some mathematical manipulations, it is shown that it can be written:

$$Y_+(z)\tilde{U}(z) + Y_-(z)e^{j2\varphi_x}\tilde{U}^*(z^*) = \delta I(z) \quad (5.28)$$

where we introduced two transfer-functions $Y_+(z)$ and $Y_-(z)$, that we respectively call positive and negative derivative-admittances, and that are computed as follows:

$$\begin{cases} Y_+(z) &\triangleq \frac{Z_+(z)}{Z_x(z)Z_y(z)} \\ Y_-(z) &\triangleq -\frac{Z_-(z)}{Z_x(z)Z_y(z)} \end{cases} \quad (5.29)$$

Note that $Z_x = Z_+ + Z_-$ and $Z_y = Z_+ - Z_-$ denote the integral-impedances along the xy-axes.

Demonstration of the inversion

It can be shown in (5.27) that $Z_+^*(z^*) = Z_+(z)$ and $Z_-^*(z^*) = Z_-(z)$. Using the complex conjugate of (5.26) yields:

$$\delta I^*(z^*) = \left(\tilde{U}^*(z^*) - Z_-(z)e^{-j2\varphi_x}\delta I(z) \right) / Z_+(z) \quad (5.30)$$

Replacing $\delta I^*(z^*)$ back in (5.26) yields:

$$Z_+(z)\tilde{U}(z) = (Z_+^2(z) - Z_-^2(z))\delta I(z) + Z_-(z)e^{j2\varphi_x}\tilde{U}^*(z^*) \quad (5.31)$$

Since $Z_+^2(z) - Z_-^2(z) = Z_x(z)Z_y(z)$, we obtain:

$$\frac{Z_+(z)}{Z_x(z)Z_y(z)}\tilde{U}(z) - \frac{Z_-(z)}{Z_x(z)Z_y(z)}e^{j2\varphi_x}\tilde{U}^*(z^*) = \delta I(z) \quad (5.32)$$

5.3.3 The Fourier-Transform of the Model

The signal injection is based on repetitive voltage sequences, generally at fixed frequencies. It is therefore convenient to use the discrete-time Fourier-transform (DTFT) of the space vector signals that is found replacing z by a unitary complex

value $e^{j\omega T_s}$ in the relations, where $\omega \leq \omega_s/2 = \pi/T_s$. It is shown that $D(z)$ defined in (5.25) yields:

$$D(e^{j\omega T_s}) = \frac{2(1 - e^{-j\omega T_s})}{1 + e^{-j\omega T_s}} = \frac{2(e^{j\omega T_s/2} - e^{-j\omega T_s/2})}{e^{j\omega T_s/2} + e^{-j\omega T_s/2}} = 2 \frac{\sin(\omega T_s/2)}{\cos(\omega T_s/2)} \quad (5.33)$$

It can also be written as follows:

$$D(e^{j\omega T_s}) = j\bar{\omega}T_s \quad \text{where} \quad \boxed{\bar{\omega} \triangleq \frac{2}{T_s} \tan(\omega \frac{T_s}{2})} \quad (5.34)$$

with $\bar{\omega}$ that tends to ω when $\omega \ll \omega_s$. Introducing (5.34) in (5.27) yields the DTFT of the positive and negative integral-impedances:

$$\begin{cases} Z_+(z) &= \frac{l_{t+}}{T_s} - j \frac{r_+}{\bar{\omega}} \\ Z_-(z) &= \frac{l_{t-}}{T_s} - j \frac{r_-}{\bar{\omega}} \end{cases} \quad (5.35)$$

Combining (5.29) with (5.35) yields the DTFT of the positive and negative derivative-admittances:

$$\begin{cases} Y_+(e^{j\omega T_s}) &= T_s \frac{l_{t+} - jr_+/\bar{\omega}}{(l_{tx} - jr_x/\bar{\omega})(l_{ty} - jr_y/\bar{\omega})} \\ Y_-(e^{j\omega T_s}) &= -T_s \frac{l_{t-} - jr_-/\bar{\omega}}{(l_{tx} - jr_x/\bar{\omega})(l_{ty} - jr_y/\bar{\omega})} \end{cases} \quad (5.36)$$

The resistance is often neglected in self-sensing operations and these parameters become very simple as the imaginary and frequency dependency vanish:

$$\left. \begin{matrix} r_x \ll \bar{\omega}l_{tx} \\ r_y \ll \bar{\omega}l_{ty} \end{matrix} \right\} \Rightarrow \begin{cases} Z_+(z) &= \frac{l_{t+}}{T_s} \\ Z_-(z) &= \frac{l_{t-}}{T_s} \end{cases} \quad \text{and} \quad \begin{cases} Y_+ &= T_s \frac{l_{t+}}{l_{tx}l_{ty}} \\ Y_- &= -T_s \frac{l_{t-}}{l_{tx}l_{ty}} \end{cases} \quad (5.37)$$

Let us define the inverse incremental self-inductances as follows: $y_{tx} \triangleq l_{tx}^{-1}$ and $y_{ty} \triangleq l_{ty}^{-1}$. The derivative-admittances therefore yields:

$$\begin{cases} Y_+ = T_s \frac{l_{t+}}{l_{tx}l_{ty}} = \frac{T_s}{2} \frac{l_{tx} + l_{ty}}{l_{tx}l_{ty}} = \frac{T_s}{2} (y_{ty} + y_{tx}) = T_s y_{t+} \\ Y_- = T_s \frac{l_{t-}}{l_{tx}l_{ty}} = \frac{T_s}{2} \frac{l_{tx} - l_{ty}}{l_{tx}l_{ty}} = \frac{T_s}{2} (y_{ty} - y_{tx}) = T_s y_{t-} \end{cases} \quad (5.38)$$

This is a common formalism found in some publications.

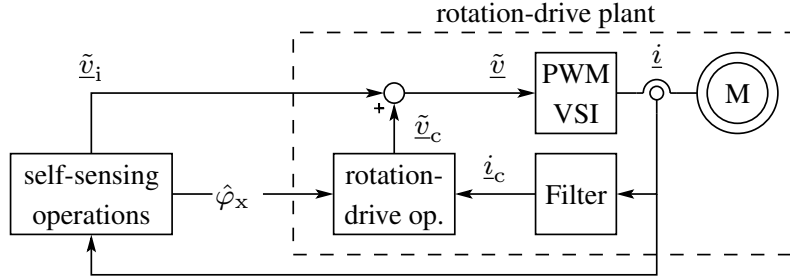


Figure 5.1: Flowchart of the rotation-drive plant including a signal-injection and a self-sensing computation

5.3.4 Principle and Assumptions

The principle is illustrated in Figure 5.1. It consists in the injection of a high-frequency voltage, written \tilde{v}_i and computed by the self-sensing operations, in addition to the low-frequency voltage, written \tilde{v}_c and computed by the rotation-drive operations: $\tilde{v} = \tilde{v}_c + \tilde{v}_i$. As a consequence, a high-frequency current response \hat{i}_i is added to the low-frequency current response \hat{i}_c controlled by the rotation-drive operations: $\hat{i} = \hat{i}_c + \hat{i}_i$.

In order to prevent or reduce disturbing interactions, the signal-injection operations and the rotation-drive operations should produce signals \underline{x}_i and \underline{x}_c covering separated frequency ranges $\{\omega_i\}$ and $\{\omega_c\}$ respectively. In terms of DTFT $\underline{X} = \mathcal{F}\{\underline{x}\}$, the condition is:

$$\begin{cases} |\underline{X}_c(\omega)| \ll |\underline{X}_i(\omega)| & \text{for } \omega \in \{\omega_i\} \\ |\underline{X}_c(\omega)| \gg |\underline{X}_i(\omega)| & \text{for } \omega \in \{\omega_c\} \end{cases} \quad (5.39)$$

Obviously, higher the signal-injection frequency, better is the separation [162, 147]. Note that the frequency content of the PWM is not considered in discrete-time operations and is, by consequence, excluded from the condition (5.39).

The high-frequency signals inevitably produce a high-frequency torque leading to high-frequency vibrations (that are audible under 20 kHz) and, by consequence, to a high-frequency back-EMF. The mechanical damping effects (due to the inertia plus the frictions of the machine and the coupled load) tend however to increase with the frequency, reducing the high-frequency back-EMF to a negligible value. In terms of DTFT of the back-EMF $\tilde{\underline{E}}_{\text{PM}} = \mathcal{F}\{\tilde{\underline{e}}_{\text{PM}}\}$ and of the PWM mean voltage $\tilde{\underline{V}} = \mathcal{F}\{\tilde{v}\}$, this leads to:

$$\left| \tilde{\underline{E}}_{\text{PM}}(\omega) \right| \ll \left| \tilde{\underline{V}}(\omega) \right| \quad \text{for } \omega \in \{\omega_i\} \quad (5.40)$$

The back-EMF can therefore be removed from the high-frequency electrical model and from self-sensing operations such that $\underline{U}_i(\omega) \approx \underline{V}_i(\omega)$. Introducing these assumptions (5.39) and (5.40), the relation (5.28) yields for the injected signals:

$$Y_+(e^{j\omega T_s})\tilde{\underline{V}}_i(e^{j\omega T_s}) + Y_-(e^{j\omega T_s})e^{j2\varphi_x}\tilde{\underline{V}}_i^*(e^{-j\omega T_s}) = \delta \underline{I}_i(e^{j\omega T_s}) \quad (5.41)$$

This expression is valid for any type of high-frequency injected signal based on digital operations, that can be permanent or intermittent.

5.3.5 Filtering Operations and Spectrum Dispersions

Concerning the self-sensing operations, apriori \tilde{V}_i in (5.41) is known, since it corresponds to the injected voltage. The difficulty is found in the implementation of an adequate filtering method that allows to extract $\delta \underline{I}_i$ at the desired frequencies $\omega \in \{\omega_i\}$, removing the contribution at other frequencies, in particular at the rotation-drive frequencies $\{\omega_c\}$. A widespread solution consists to perform a low-pass filtering (LPF) applied to the demodulated signal:

$$\delta \underline{I}_i(e^{-j\omega T_s}) \approx \text{LPF}(\delta \underline{i} e^{j\omega t}) \quad \forall \omega \in \{\omega_i\} \quad (5.42)$$

The band-pass of that filter should however not be too thin because of spectrum dispersion phenomena, explained as follows.

Until now, we assumed a constant anisotropy angle φ_x during the operations. In practice however, this angle varies $\omega_x = d\varphi_x/dt \neq 0$ due to the machine rotation and to possible harmonics in the anisotropy variations. Assume in first approximation that ω_x is constant. The following part of (5.21) can therefore be rewritten highlighting the exponential of this rotating term:

$$\left(\frac{l_{t-}}{T_s} \delta \underline{i}^{[k]} + r_{-} \bar{i}^{[k]} \right)^* e^{j2\varphi_x} = \left(\frac{l_{t-}}{T_s} (\delta \underline{i}^{[k]} e^{j2\omega_x t}) + r_{-} (\bar{i}^{[k]} e^{j2\omega_x t}) \right)^* e^{j2\varphi_{x,o}} \quad (5.43)$$

It can be shown that the z-transform of the conjugate value \underline{x}^* , where $\underline{x} \in \{\delta \underline{i}, \bar{i}\}$, multiplied by $e^{j2\omega_x t}$, where the values are sampled at instants $t^{[k]} = kT_s$, is:

$$\mathcal{Z} \{ \underline{x}^* e^{j2\omega_x t} \} = \underline{X}^* (z^* e^{j2\omega_x}) \quad (5.44)$$

Using the DTFT, this term leads to a spectrum shift of $2\omega_x$:

$$\mathcal{F} \{ \underline{x}^* e^{j2\omega_x t} \} = \underline{X}^* (e^{-j(\omega-2\omega_x)T_s}) \quad (5.45)$$

The inversion of the model relation (5.26) leading to (5.28) and therefore to (5.41) should include this shift. The computation is rather complicated and is thus not detailed here. We can however imagine that this shift results in a spectrum dispersion on the current response. It is negligible if $|2\omega_x| \ll |\omega_i|$, but this condition must be checked. Other spectrum dispersions are due to possible variations in the parameter values and to unmodelled phenomena, such as the angular variations of the self-inductance. A specific LPF implementation is further proposed considering the dispersion issue.

Note that some papers use pre-filtering with band-pass (BPF) or band-stop filters on the current signal in order to extract the signal-injection current response before the demodulation [178, 127, 179, 115, 147, 54, 180, 128, 77, 181, 90, 56, 182, 41, 120, 85, 162, 149, 114]: $\underline{i}_i = \text{BPF}(\underline{i})$. This is justified in [147] by the

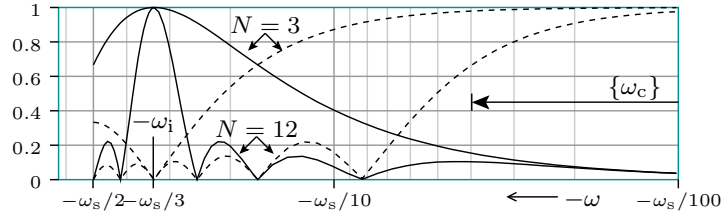


Figure 5.2: Filtering characteristics (magnitudes) of the moving average (dashed line) and the moving average shifted at $\omega_s/3$ (plain line) for $N = 3$ and $N = 12$, as a function of the signal frequency.

use of analog measurements that requires a notch filter in order to reject harmonics of the PWM frequency. But it is not required if the sampling is synchronized with the PWM. This is also not required since (5.53) naturally removes the frequency content outside $-\omega_i$. Moreover, the fact to use operations directly based on the ratio between the current and the high-frequency voltage removes lagging problems [128, 54, 183]. No prefiltering is performed by [105, 133].

5.3.6 Filter Implementation

We propose LPF operations based on the *moving average*, that is a finite impulse response (FIR) filter defined as the mean of the N previous discrete-time values \underline{x} , computed every sampling period k [46]:

$$\text{LPF}_N^{[k]}(\underline{x}) := \frac{1}{N} \sum_{n=0}^{N-1} \underline{x}^{[k-n]} \quad (5.46)$$

Its characteristic for the negative frequencies is illustrated in Figure 5.2 with dashed lines for the case $N = 3$ and $N = 12$. Note that the characteristic is symmetrical around zero. Assume that the considered high-frequency ω_i of the injected signals is an integer fraction $N_i \geq 3$ of the sampling frequency ω_s :

$$\omega_i = \omega_s/N_i \quad \Rightarrow \quad \omega_i T_s = 2\pi/N_i \quad (5.47)$$

The moving average (5.46) can then be used as a LPF for the operation (5.42) computed at $-\omega_i$, selecting an integer multiple N of N_i :

$$\delta \underline{I}_i(e^{-j\omega_i T_s}) \approx \frac{1}{N} \sum_{n=0}^{N-1} \left(\delta \underline{i}^{[k-n]} e^{j2\pi(k-n)/N_i} \right) \quad (5.48)$$

Considering the case $N_i = 3$, the characteristic of the moving averages shifted around $-\omega_i = -\omega_s/3$ is illustrated in Figure 5.2 with plain lines for $N = N_i = 3$ and $N = 4 \times N_i = 12$. The choice of N depends on the expanse of the low-frequency range $\{\omega_c\}$ to be removed. However, assuming that ω_i is much higher

than $\{\omega_c\}$, a higher N does not strongly improve the attenuation characteristic at low frequencies, while it requires more computational power. The choice of N also depends on the spectrum dispersions around $-\omega_i$. Higher N , higher the risk to filter beside the high-frequency current response. We propose therefore to use to lowest $N = N_i$ for the operations (5.53).

Apart from this, the moving average can also be used to remove the high-frequency current component in the samples $\underline{i}(t^{[k]})$ for the rotation-drive operations, possibly using a higher N to restrict the bandwidth:

$$\text{LPF}(\underline{i}_i) = 0 \quad \Rightarrow \quad \text{LPF}(\underline{i}_c) = \text{LPF}(\underline{i}) \quad (5.49)$$

If the rotation-drive controller bandwidth is much smaller than ω_i however, the filtering becomes unnecessary [128].

In many papers, operations are based on infinite impulse response (IIR) filters [176, 115, 105, 180, 128, 182, 120, 162, 149, 114]. The comparison between IIR and FIR filters would require further analysis, but apriori, the moving average provides a simple solution with good filtering characteristics and with good phase linearity. Moreover, the stabilization time of the FIR is not greater than N sampling periods, while it can be much longer with IIR filters for the same bandwidth.

5.3.7 Operations with Rotating Signals

The goal is to obtain a quick estimation of the angle φ_x from the model (5.41). An efficient solution, that does not require initial parameter knowledge, consists to inject a rotating voltage at one frequency ω_i [5]. The discrete-time expression of the injected rotating voltage is given as the rotating *modulation* of an initial voltage space vector $\underline{v}_{i,o}$:

$$\boxed{\hat{\underline{v}}_i^{[k]} := \underline{v}_{i,o} e^{j\omega_i k T_s}} \quad (5.50)$$

The DTFT of this voltage $\tilde{\underline{V}}_i = \mathcal{F}\{\hat{\underline{v}}_i\}$ is null except at $\omega = \omega_i$. In particular, it is null at $\omega = -\omega_i$. At $\omega = \omega_i$, it corresponds to its *demodulation*:

$$\tilde{\underline{V}}_i(e^{j\omega T_s}) = \begin{cases} \underline{v}_{i,o} & \text{if } \omega = \omega_i \\ 0 & \text{if } \omega \neq \omega_i \end{cases} \quad (5.51)$$

Thus at $\omega = -\omega_i$, (5.41) yields:

$$\underline{Y}_-(e^{-j\omega_i T_s}) e^{j2\varphi_x} = \delta \underline{I}_i(e^{-j\omega_i T_s}) / \underline{v}_{i,o} \quad (5.52)$$

The DTFT of the current difference at $-\omega_i$ can be approached using the filtering (5.42). Dividing (5.42) by $\underline{v}_{i,o}$ and using (5.50), (5.52) can be computed as follows:

$$\boxed{\hat{\underline{Y}}_-(e^{-j\omega_i T_s}) e^{j2\hat{\varphi}_x} := \text{LPF} \left(\delta \hat{\underline{i}}^{[k]} / \hat{\underline{v}}_i^{*[k]} \right)} \quad (5.53)$$

where the hat denotes estimated values.

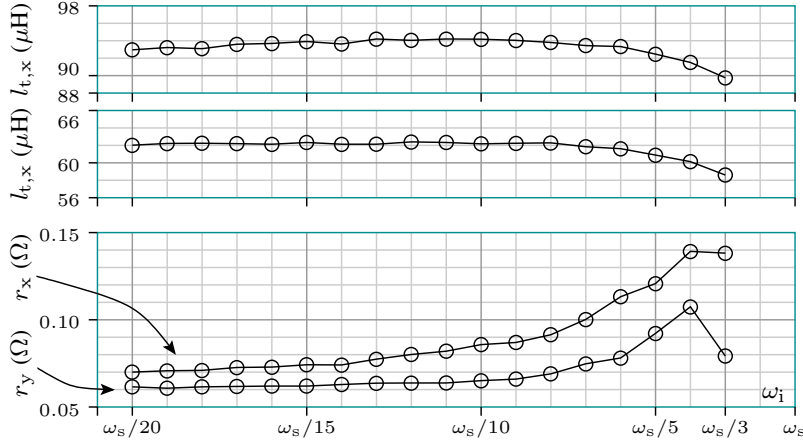


Figure 5.3: Apparent resistances and inductances of the experimental BLDC machine identified at different frequencies ω_i , assuming $\nu_s = 10$ kHz, with $\omega_s = 2\pi\nu_s$.

Position Estimation

As it is widely assumed in the literature, if the resistance impact is negligible compared to the inductance, the positive Y_+ and negative Y_- derivative-admittances are strictly real values: (5.37). Using (5.53), the angle is then easily extracted by:

$$\hat{\varphi}_x := \frac{\angle(-\text{LPF}(\delta \tilde{i}_i / \tilde{v}_i^*))}{2} \quad (5.54)$$

where \angle denotes the complex argument. The minus in front of $-\text{LPF}(\cdot)$ is required because $\hat{Y} < 0$. In practice however, the resistance is not always negligible, and Y_- is not strictly real, leading to angle estimation errors. Using (5.54), this error is the half complex argument of Y_- given in (5.36):

$$\begin{aligned} \hat{\varphi}_x|_{(5.54)} - \hat{\varphi}_x &= \frac{\angle(-Y_-(e^{-j\omega_i T_s}))}{2} \\ &= \frac{\angle(l_t + jr_-/\bar{\omega}_i) - \angle(l_{tx} + jr_x/\bar{\omega}_i) - \angle(l_{ty} + jr_y/\bar{\omega}_i)}{2} \end{aligned} \quad (5.55)$$

Note here that higher $\bar{\omega}_i$, lower the impact of the resistance. Except in [184, 90, 185, 183, 91, 148, 85, 149], the resistance impact is often neglected in signal-injection operations using rotating signal injections. This position error is addressed in [54, 90]. It is analyzed hereafter for experimental cases.

Experimental Cases

Figure 5.3 shows the apparent parameters of the experimental BLDC motor for different pulsating-signal frequencies along the x and y-axes, and with $\nu_s = 10$ kHz. These values are also in Figure 3.12 of chapter 3. Figure 5.4 shows the theoretical error due to the resistance, and computed using (5.55). The circles, joined by

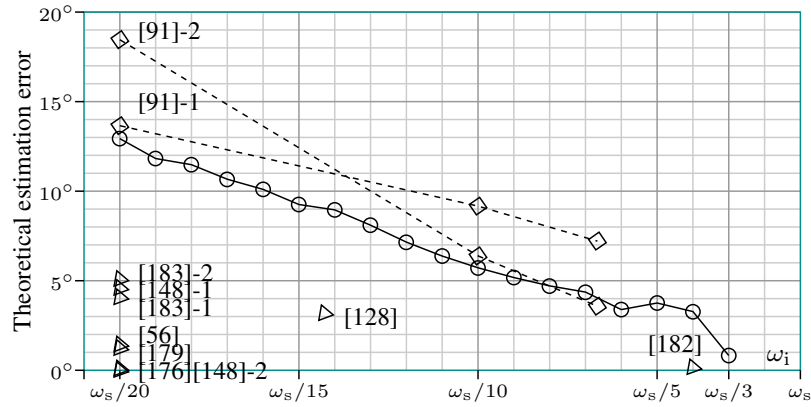


Figure 5.4: Theoretical estimation errors in experimental cases.

Table 5.5: Parameters of some machines found in the literature.

	ν_i (Hz)	$[r_y - r_x]$ (Ω) ^(*)	$[l_{t,y} - l_{t,x}]$ (H) ^(**)
[91]-1	0.5 k	[0.404 – 0.635]	[2.33 – 3.61] m
[91]-1	1 k	[1.339 – 1.959]	[2.33 – 3.61] m
[91]-1	1.5 k	[2.601 – 4.431]	[2.33 – 3.61] m
[91]-2	0.5 k	[0.259 – 0.436]	[2.17 – 2.83] m
[91]-2	1 k	[0.765 – 1.385]	[2.17 – 2.83] m
[91]-2	1.5 k	[1.48 – 2.791]	[2.17 – 2.83] m
[182]	2.5 k	0.15	[2.5 – 3.1] m
[128]	700	1.5	[5.15 – 7.35] m
[179]	500	0.0103	[101 – 306] μ
[56]	500	1.4	[10 – 76] m
[183]-1	500	2.2	[6.5 – 19.69] m
[183]-2	500	2.875	[8.5 – 12.75] m
[176]	500	8.4 m	[100 – 300] μ
[148]-1	500	[1.87 – 1.96]	[7.5 – 9.4] m
[148]-2	500	[0.76 – 0.88]	[420 – 440] μ

All machines are permanent-magnets, except [56] that is a switched reluctance machine. These parameters must be taken with care and as information only. ^(*) If the high-frequency resistance is not mentioned, the DC resistance is taken instead. ^(**) We take the inductances corresponding to the lowest load. The digital sampling frequency is $\nu_s = 10$ kHz for all drives, except in [56, 183] where this frequency is assumed because not specified. Note that $\omega = 2\pi\nu$.

plain lines, correspond to the error with our experimental BLDC machine, using the parameters of Figure 5.3. It is observed that, even if the apparent resistance tends to increase with the frequency, its relative impact is divided by $\bar{\omega}_i$ and tends

to decrease. This tends to confirm the benefits of using the highest frequency.

Results using the parameters of some machines found in the literature are shown by diamonds and triangles. The parameters can be found in Table 5.5. If there is more than one machine in one reference, the reference is followed by a numbering for each machine. In [91], parameters of two machines are given at three different frequencies. The corresponding errors are mentioned in Figure 5.4 by diamonds joined by dashed lines. A decrease of the resistance impact is also observed. The other machines are mentioned by triangles. We can see that many papers chose a frequency at $\nu_i = \nu_s/20 = 500$ Hz. Even if the error is typically not much larger than 5° , using higher frequencies could possibly further reduce the resistance impact.

5.3.8 Operations with Pulsating Signals

Another possibility to obtain an estimation of the angle φ_x from the model (5.41) consists to inject a pulsating voltage at one frequency ω_i [5]. The initial parameter knowledge must however be discussed. The discrete-time expression of the injected pulsating voltage can be given as the sum of two voltage space vectors rotating in opposition with respect to an fixed voltage $\underline{v}_{i,o}$:

$$\boxed{\tilde{v}_i^{[k]} := \underline{v}_{i,o} \frac{e^{j\omega_i k T_s} + e^{-j\omega_i k T_s}}{2} = \underline{v}_{i,o} \cos(\omega_i k T_s)} \quad (5.56)$$

The voltage $\underline{v}_{i,o}$ has a fixed amplitude \hat{V}_i and is oriented by an angle φ_i that may possibly vary at a lower frequency than ω_i , around ω_c :

$$\boxed{\underline{v}_{i,o} := \hat{V}_i e^{j\varphi_i}} \quad (5.57)$$

The DTFT of this voltage $\tilde{\underline{V}}_i = \mathcal{F}\{\tilde{v}_i\}$ is null except at $\omega = \pm\omega_i$ and yields in the case $\omega_i < \omega_s/2$:

$$\tilde{\underline{V}}_i(e^{j\omega T_s}) = \begin{cases} \underline{v}_{i,o}/2 & \text{if } \omega = \pm\omega_i \\ 0 & \text{if } \omega \neq \pm\omega_i \end{cases} \quad (5.58)$$

Due to this spectrum content, not null at two opposite frequencies, it is not possible to isolate the negative part of the relation (5.41) as done previously with rotating signals. But other strategies are possible using the property of $\tilde{\underline{V}}_i$ being equal at $\omega = \pm\omega_i$. We propose to sum the relation (5.41) at $\omega = \omega_i$ and at $\omega = -\omega_i$. Since:

$$Y_{\pm}(e^{-j\omega_i T_s}) = Y_{\pm}^*(e^{j\omega_i T_s}) \quad \Rightarrow \quad \frac{Y_{\pm}(e^{j\omega_i T_s}) + Y_{\pm}(e^{-j\omega_i T_s})}{2} = \Re(Y_{\pm}(e^{j\omega_i T_s})) \quad (5.59)$$

And since $\underline{v}_{i,o}^* = \underline{v}_{i,o} e^{-2j\varphi_i}$, it can be shown that it yields:

$$\Re(Y_{+}(e^{j\omega_i T_s})) + \Re(Y_{-}(e^{j\omega_i T_s})) e^{j2(\varphi_x - \varphi_i)} = \frac{\delta I_{+}(e^{j\omega_i T_s}) + \delta I_{-}(e^{-j\omega_i T_s})}{\underline{v}_{i,o}} \quad (5.60)$$

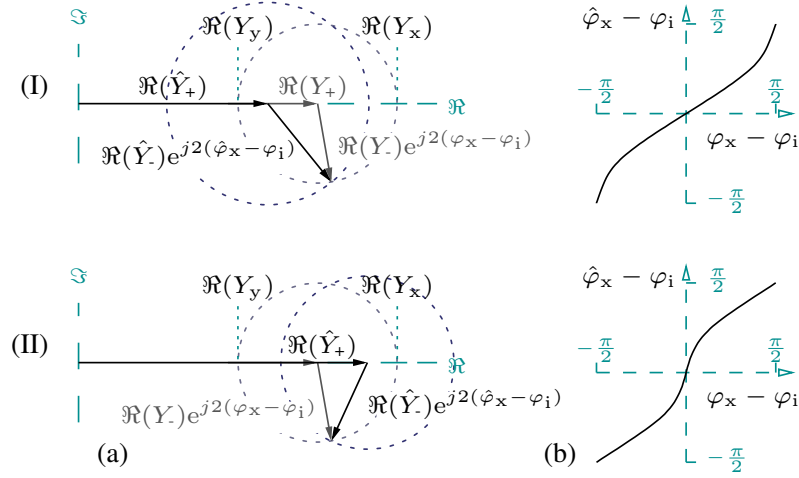


Figure 5.5: Illustration of (a) the approached locus of $\Re(\hat{Y}_+)e^{j2(\hat{\varphi}_x - \varphi_i)}$ compared to the correct one $\Re(Y_+)e^{j2(\varphi_x - \varphi_i)}$ assuming a faulty $\Re(\hat{Y}_+)$; and (b) approached angle between the anisotropy and the signal-injection $\hat{\varphi}_x - \varphi_i$ as a function of the correct one $\varphi_x - \varphi_i$. Case (I): $\Re(\hat{Y}_+) < \Re(Y_+)$; Case (II): $\Re(\hat{Y}_+) > \Re(Y_+)$.

The sum of DTFT of the current difference at the two frequencies can be approached using the filtering (5.42). Dividing by $v_{i,o}$, using (5.56) and (5.57), it yields:

$$\begin{aligned} \frac{\delta \underline{I}_i(e^{j\omega_i T_s}) + \delta \underline{I}_i(e^{-j\omega_i T_s})}{v_{i,o}} &\approx \frac{\text{LPF}(\delta \underline{i}(e^{j\omega_i t} + e^{-j\omega_i t}))}{v_{i,o}} = \frac{\text{LPF}(\delta \underline{i} 2 \cos(\omega_i t))}{v_{i,o}} \\ &= \frac{\text{LPF}(\delta \underline{i} \cos(\omega_i t) \underline{v}_{i,o}^*)}{v_{i,o} \underline{v}_{i,o}^* / 2} = \frac{\text{LPF}(\delta \underline{i} \tilde{v}_i^*)}{\hat{V}_i^2 / 2} \quad (5.61) \end{aligned}$$

$$\Rightarrow \boxed{\Re(\hat{Y}_+(e^{j\omega_i T_s})) + \Re(\hat{Y}_-(e^{j\omega_i T_s})) e^{j2(\hat{\varphi}_x - \varphi_i)} := \frac{\text{LPF}(\delta \underline{i} \tilde{v}_i^*)}{\hat{V}_i^2 / 2}} \quad (5.62)$$

where the hat denotes estimated values.

Position Estimation

In the case of a permanent signal, the possibilities to modify the angle φ_i are limited to slow variations, in order to limit the effect on spectrum dispersion, as previously discussed. A strategy, largely found in the literature, consists to track the anisotropy angle: $\varphi_i \rightarrow \varphi_x$. A shift between these angles leads to an estimation error $\hat{\varepsilon}_x$ that is used in a regulator (proportional-integral for instance) that computes the anisotropy angle estimation: $\hat{\varphi}_x = \text{REG}(\hat{\varepsilon}_x)$. Two possible computations of the estimation error are addressed hereafter. Note that there is a settling time related to the initially tracking of the anisotropy angle. This time depends on the regulator

bandwidth (or regulation poles) that is limited by the signal-injection period. By consequence, higher the signal-injection frequency, lower the minimum settling time. This settling time (in addition to settling times due to the noise filtering and due to any compensation method) is a drawback that does not exist in other self-sensing methods. Note that strategies using $\varphi_i \rightarrow \hat{\varphi}_y$ are also valid and result in similar operations.

1. Either the estimation error is computed taking the imaginary part of (5.62):

$$\hat{\epsilon}_x := \frac{\Im(\text{LPF}(\delta \underline{\tilde{v}}_i^*))}{\Re(\hat{Y}_-(e^{j\omega_i T_s})) \hat{V}_i^2} \quad (5.63)$$

This method is found in [186, 184, 59, 133, 68, 41, 85, 149, 114].

2. Or the estimation error is computed taking the angle of (5.62) reduced by the positive derivative-admittance estimation:

$$\hat{\epsilon}_x := \angle \left(-\frac{\text{LPF}(\delta \underline{\tilde{v}}_i^*)}{\hat{V}_i^2/2} + \Re(\hat{Y}_+(e^{j\omega_i T_s})) \right) / 2 \quad (5.64)$$

Both methods require at least an approximate knowledge of one parameter. For the method 1. it is: \hat{Y}_- ; and for the method 2. it is: \hat{Y}_+ . These methods are therefore not really parameter independent. Figure 5.5(a) illustrates the error on the angle estimation $\hat{\varphi}_x$ consequent to an error on $\Re(\hat{Y}_+)$ with respect to $\Re(Y_+)$ using (5.64). As illustrated in Figure 5.5(b), the impact of this error should vanish while $\varphi_i \rightarrow \hat{\varphi}_x$. It is therefore not required to have an accurate knowledge of $\Re(Y_+)$, but the only requirement is: $\Re(Y_y) < \Re(\hat{Y}_+) < \Re(Y_x)$. This is discussed in [126].

5.3.9 Operations with Alternating Signals

The operations (5.62) are simplified to their maximum with the case of an signal injected at half the sampling frequency: $\omega_i = \omega_s/2$. Using (5.47), it corresponds to $N_i = 2$ and \tilde{v}_i is purely alternating after every sampling period, as illustrated in Figure 5.6:

$$\tilde{v}_i^{[k]} := v_{i,o} e^{j\pi k} = (-1)^k v_{i,o} \quad (5.65)$$

This alternating signal can be handled as a pulsating signal, but the relation presents some differences that should be considered. The DTFT of this voltage differs compared to (5.58) due to frequency overlays:

$$\tilde{V}_i(e^{j\omega T_s}) = \begin{cases} v_{i,o} & \text{if } \omega = \pm\omega_i = \pm\omega_s/2 \\ 0 & \text{if } \omega \neq \pm\omega_i \end{cases} \quad (5.66)$$

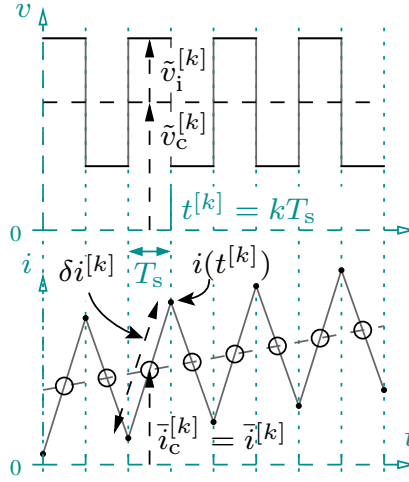


Figure 5.6: Illustration of the alternating signal-injection in addition to the rotation-drive operating signals (along $e^{j\varphi_i}$). The dots correspond to the current samples used for self-sensing operations. The circles correspond to the current value used as input for the rotation-drive control.

At the injected frequencies, using (5.34) we can compute that $\bar{\omega}_i = \infty$ and the condition to obtain (5.38) is met: $Y_{\pm} = T_s y_{t\pm}$. The filtering operations (5.46) are reduced to two sampling periods, i.e. three samples $\underline{i}(t)$, (including the initial, middle and last sample), such that (5.61) yields:

$$\text{LPF}_{N=2}^{[k]}(\delta \underline{i} 2 \cos(\pi k)) = \delta \underline{i}^{[k]} - \delta \underline{i}^{[k-1]} = \underline{i}(t^{[k]}) - 2\underline{i}(t^{[k-1]}) + \underline{i}(t^{[k-2]}) \quad (5.67)$$

The current back-differences are illustrated in Figure 5.6. Following the same steps as for the previous pulsating signal development, it yields:

$$\hat{y}_{t+} - \hat{y}_t e^{j2(\hat{\varphi}_x - \varphi_i)} := \frac{\underline{i}(t^{[k]}) - 2\underline{i}(t^{[k-1]}) + \underline{i}(t^{[k-2]})}{2 \underline{\hat{v}}_i^{[k]} T_s} \quad (5.68)$$

An equivalent form of this operation was proposed in [126].

Since $\bar{\omega}_i = \infty$, the signal-injection contribution to the current sample-average is null: $\bar{\underline{i}}_i = 0$. Therefore, the LPF operation (5.49) applied on the signal for the rotation-drive input can be reduced to only one sampling period, and it corresponds to:

$$\bar{\underline{i}}_c^{[k]} := \text{LPF}_{N=2}^{[k]}(\underline{i}) = \frac{\underline{i}(t^{[k]}) + \underline{i}(t^{[k-1]})}{2} = \bar{\underline{i}}^{[k]} \quad (5.69)$$

This value is illustrated by circles in Figure 5.6.

Position Estimation For Permanent Signals

The strategy differs if we use a permanent or an intermittent signal. The case of the intermittent signal is further discussed.

1. In the case of a permanent alternating signal, the operation (5.63) combined with (5.68) yields:

$$\hat{\varepsilon}_x := -\Im \left(\frac{\underline{i}(t^{[k]}) - 2\underline{i}(t^{[k-1]}) + \underline{i}(t^{[k-2]})}{\tilde{v}_i^{[k]} \hat{y}_{t-} T_s} \right) \quad (5.70)$$

where an approximate knowledge of \hat{y}_{t-} is required. This solution seems to be used by some authors [178, 181, 182]. However, all the developments are given under the form of continuous-time operations, leading to some interrogations about the filtering operations.

2. The operation (5.64) combined with (5.68) yields:

$$\hat{\varepsilon}_x := \angle \left(-\frac{\underline{i}(t^{[k]}) - 2\underline{i}(t^{[k-1]}) + \underline{i}(t^{[k-2]})}{2 \tilde{v}_i^{[k]} T_s} + \hat{y}_{t+} \right) / 2 \quad (5.71)$$

where an approximate knowledge of \hat{y}_{t+} is required. This second method was proposed in [126].

The choice of method 2. for the experiments on the BLDC motor in [126] was justified by the significant harmonics in the machine anisotropy, described in chapter 2. These harmonics produce strong variations of y_{t-} during the rotation, while y_{t+} was more stable, justifying the choice.

Position Estimation For Test Pulses

In the case of an intermittent signal, such as test pulses, the angle φ_i is easily changed after every test. The test pulses can be treated as alternating pulsating signals. Injection the test voltage at least following two different angles, denoted by I and II, and assuming that the anisotropy angle $\hat{\varphi}_x$ did not significantly change between the two tests, it can be estimated by subtraction the two results (5.68) as follows:

$$\hat{y}_{t-} e^{j2\hat{\varphi}_x} = \frac{\text{Eq.(5.68)}_I - \text{Eq.(5.68)}_{II}}{e^{-j2\varphi_{i,II}} - e^{-j2\varphi_{i,I}}} \quad (5.72)$$

Since \hat{y}_{t-} is strictly real and positive, the angle is found taking the complex argument \angle of (5.72):

$$\hat{\varphi}_x := \angle \left(\frac{\text{Eq.(5.68)}_I - \text{Eq.(5.68)}_{II}}{e^{-j2\varphi_{i,II}} - e^{-j2\varphi_{i,I}}} \right) / 2 \quad (5.73)$$

This is the solution proposed by [165], that is greatly simplified using quadratic signal injections. Note first of all that there is no angular error due to the resistance. The resistance can however lead to a remaining impact of the signal injection after the test period, that can disturb the rotation-drive operations. This problem was addressed in [169], however the solution was not perfect.

With test pulses, the rotation-drive current is generally not extracted through low-pass filtering. Instead, the current samples affected by the signal-injection are simply removed from the rotation-drive operations. As a consequence, lower the signal-injection period, lower is the number to affected samples. Typically, using methods such as adaptive test pulses proposed by [165], only one sample on two is removed. As explained in [165, 169], the issue of remaining test-pulses impact must however considered. This is not developed here.

5.3.10 Signal-to-Noise Ratio Issue

The noise in the current measurements is an important issue. We propose here a first approach based on the standard deviation σ , assuming a *Gaussian* noise. Using the space vector definition (2.71) given in chapter 2, it is shown that the variance (square of the standard deviation) on the space vector \underline{i} is related to the variance on the phase-current samples by: $\sigma^2(\underline{i}) = (2/3)^2 \sum_p \sigma^2(i_p) = (4/3)\sigma^2(i_p)$. From the definition (5.19), it is further shown that the variance on the current back-difference is: $\sigma^2(\delta\underline{i}) = 2\sigma^2(\underline{i}) = (8/3)\sigma^2(i_p) = 1.633\sigma^2(i_p)$.

The noise is firstly reduced through the LPF such, as (5.46) and depending on the number of values N on which the filter operates. In the case of a rotating signal, from (5.52) and assuming that the current measurements are the only source of noise, it is shown that the standard deviation of the identification (5.53), written σ_Y , yields:

$$\sigma_{Y|5.53}^2 \triangleq \sigma^2 \left(\frac{\text{LPF}(\delta\underline{i} e^{j\omega_i T_s})}{\underline{v}_{i,o}} \right) = \frac{\sigma^2(\delta\underline{i}) \frac{1}{N^2} \sum_{n=0}^{N-1} \overbrace{\left| e^{j2\pi(k-n)/N_i} \right|^2}^N}{\hat{V}_i} \quad (5.74)$$

$$\Rightarrow \sigma_{Y|5.53} = \frac{1}{\sqrt{N}} \frac{\sigma(\delta\underline{i})}{\hat{V}_i} \quad (5.75)$$

where N/N_i must be an integer. The result is similar for the case of an alternating signal (5.68). In the case of a pulsating signal, from (5.61), it is shown that the standard deviation of the identification (5.62):

$$\sigma_{Y|5.62}^2 \triangleq \sigma^2 \left(\frac{\text{LPF}(\delta\underline{i} 2 \cos(\omega_i t))}{\underline{v}_{i,o}} \right) = \frac{\sigma^2(\delta\underline{i}) \frac{4}{N^2} \sum_{n=0}^{N-1} \overbrace{\cos^2(2\pi(k-n)/N_i)}^{N/2}}{\hat{V}_i} \quad (5.76)$$

$$\Rightarrow \sigma_{Y|5.62} = \sqrt{\frac{2}{N}} \frac{\sigma(\delta\underline{i})}{\hat{V}_i} \quad (5.77)$$

Comparing (5.75) and (5.77), we see that the noise is a little bit stronger for pulsating than rotating (or alternating) signals, assuming the same voltage amplitude.

In practice, the voltage is not measured, but a noise exists in the PWM signals. The assessment of this noise would require further experiments. It is neglected here. In a second time, the remaining noise is inherited by the position estimation $\hat{\varphi}_x$ through one of the operations (5.54), (5.63), (5.64), (5.70), (5.71) or (5.73). This noise could be further filtered, as done in all the publications. Filtering solutions are detailed in [114]. A large description of position/speed/torque observers is addressed in [187] for PM machines.

There is however a limit in the admissible inherited noise due to the nonlinearity of the operation of position estimation: if the ratio between inherited noise and the negative derivative-admittance $\Re(\hat{Y}_c)$ is higher than 1, then some identification points could lead to π -turn estimation errors. The consequences can be dramatic because the polarity of the anisotropy can be lost. We propose therefore to select the minimum signal magnitude to be used for signal-injection methods as follows, based on two times σ_Y that should cover 94.5 % of the identification points:

$$2\sigma_Y < \Re(\hat{Y}_c) \quad \Rightarrow \quad \begin{cases} \hat{V}_i > \frac{2}{\sqrt{N}} \frac{\sigma(\delta i)}{\Re(\hat{Y}_c)} & \text{for rotating signals} \\ \hat{V}_i > 2\sqrt{\frac{2}{N}} \frac{\sigma(\delta i)}{\Re(\hat{Y}_c)} & \text{for pulsating signals} \end{cases} \quad (5.78)$$

We see that increasing N in the LPF reduce the lower limit of the injected voltage. This consideration however neglect the signal-to-noise on the supplied voltage, that decrease with the signal amplitude.

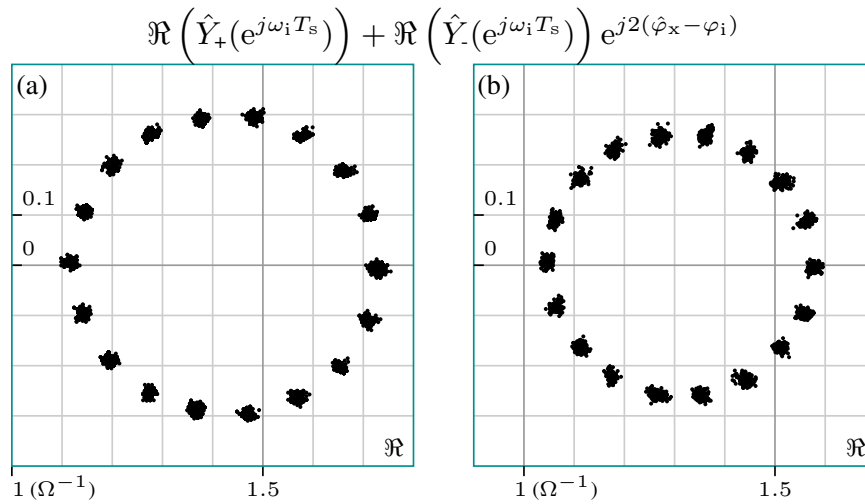
Further analysis of the noise is proposed by [105] from the point of view of *total harmonic distortion* (THD). ...Some authors proposed to draw maps of feasibility regions, representing the limit of the self-sensing accuracy as a function of [58, 59, 60]

Experimental example

The issue of the measurements noise is illustrated with experiments performed on a standstill uncoupled machine with PM oriented following $\varphi_d = 120^\circ$, equivalent to $\varphi_q = 30^\circ$. In that orientation, we have an overlay of the qd-frame and the xy-frame, as developed in chapter 2 and in [92]. The stator current has an amplitude of $\|\underline{i}\| = 25$ A and is oriented along the negative d-axis, i.e. $\angle \underline{i} = -60^\circ$. This stator current is chosen in order to prevent the effects of the zero-crossing inverter nonlinearities and in order to keep the rotor fixed in the desired position. The sampling frequency is $\nu_s = 10$ kHz. The identification is performed using pulsating high-frequency voltages between 5 kHz and 1.25 kHz, i.e. $N_i = 2$ up to 8, oriented along 18 different angles φ_i . There are 201 identification points for each condition, as shown in Figure 5.7 for the cases $N_i = 2$ and 8. The voltage amplitudes are adapted depending on the frequency, in order to produce a pulsating high-frequency current response with similar amplitudes. The moving average used for the LPF computation is based on $N = N_i$. The results are shown in Table 5.3.10.

Table 5.6: Experimental identification using pulsating high-frequency signals.

N_i	2	3	4	5	6	7	8
ν_i (Hz)	5000	3333	2500	2000	1667	1429	1250
\hat{V}_i (V)	11.5	10.0	8.2	6.8	5.8	5.0	4.4
$\Re(\hat{Y}_i)$ (Ω^{-1})	0.300	0.293	0.278	0.272	0.266	0.264	0.263
σ_Y (Ω^{-1})	0.010	0.012	0.011	0.011	0.010	0.010	0.010
$\sigma_{Y (5.62)}$ (Ω^{-1})	0.012	0.011	0.012	0.013	0.014	0.014	0.015
σ_{φ_x} (deg)	1.48°	1.60°	2.11°	1.63°	1.58°	1.60°	2.19°
$\hat{V}_{i (5.78)} >$ (V)	0.45	0.38	0.34	0.31	0.29	0.27	0.26

Figure 5.7: Experimental identification using pulsating high-frequency signals at (a) $\nu_i = 5$ kHz and (b) $\nu_i = 1.25$ kHz, along 19 angles $\varphi_i = 0^\circ, 10^\circ, \dots, 180^\circ$.

The resolution of the current measurements is 0.244 A, that is the main digital noise. This type of noise does unfortunately not satisfy to the Gaussian approximation. This has consequences on the noise computation: the standard deviation computed on 100 samples of the phase current is $\sigma(i_p) = 0.1213$ A, while the standard deviation on the corresponding current difference is $\sigma(\delta i) = 0.1350$ A, that is around the same result. The value $\sigma_{Y|(5.62)}$ in Table 5.3.10 is computed based on this $\sigma(\delta i)$ and shows a small increase with N_i . This is not observed with the experimental noise $\hat{\sigma}_Y$, that is quite constant. This is probably due to the fact that the noise is not Gaussian. The noise inherited by the estimated anisotropy angle is represented by σ_{φ_x} . It tends to increase mainly because $\Re(\hat{Y}_i)$ decreases with N_i . The condition (5.78) is met in all these experiments. The minimum voltage using that condition is shown in the table.

Choice of the current back-difference

In most of the papers dealing with rotating voltage injection, the self-sensing operations are based on the current samples instead of the current back-differences. The corresponding relation is simply found replacing the current back-difference using the relation (5.25) combined with the definition (5.34):

$$\delta \underline{I}(e^{j\omega T_s}) = j\bar{\omega}T_s \bar{\underline{I}}(e^{j\omega T_s}) \quad (5.79)$$

Our choice of the current back-differences is however justified as follows. Using the definitions (5.20) and (5.19), the standard deviation σ , that corresponds to the noise, yield:

$$\sigma(\delta \underline{i}) = 2\sigma(\underline{i}) \quad (5.80)$$

Assume a fixed voltage amplitude $|\tilde{V}|$ for the comparison and assume that the same filtering method (5.42) would be applied in both cases, it is shown that the signal-to-noise ratio of the current back-differences becomes favorable above:

$$2 \leq |\bar{\omega}T_s| \Rightarrow \sigma(\delta \underline{I}(e^{j\omega T_s})) \leq |\bar{\omega}T_s| \sigma(\bar{\underline{I}}(e^{j\omega T_s})) \quad (5.81)$$

Using (5.34), it corresponds to: $|\omega T_s| \geq \pi/2$. At first glance, since the maximum frequency for discrete-time signals is such that $|\omega_{\max}T_s| = \pi$, this condition strongly limit the frequencies at which the use of current back-differences is favorable. It is however further shown that many other benefits are found using high-frequencies in that range [163].

Note that the use of current back-differences is a benefic compared to the use of average current samples in terms of filtering. For the comparison, assume similar amplitudes for rotating-drive voltages and injected voltages. Using (5.79), we can say that the amplitude of δi_c is even reduced by its low frequency content ω_c regarding δi_i increased by the high-frequency content ω_i . This is a strong benefit compared to operations based on current samples or average current samples.

5.3.11 Issue regarding the PWM-VSI

We assume that the voltages are not measured but the command voltage is used instead. Dead-times in the pulse-width modulation (PWM) and voltage drops at the semiconductors of the voltage-source inverter (VSI) are common nonlinearities that must be managed. They can generally be linearized and compensated assuming fixed phase current flows [5, 121, 41, 114]. This is largely addressed in chapter 4. The frequency content of the compensation signal is mainly present in the low-frequencies and should therefore not affect the self-sensing operations.

As explained in chapter 4, when a phase current crosses zero however, non compensable dead-times and voltage drops discontinuities occur, referred to as *zero-crossing clamping* phenomenons. Even small, they may lead to significant estimation errors [169, 125, 120, 41]. The smaller N_i however, the smaller the number of estimations affected by the zero-crossing nonlinearity and better is the robustness of the self-sensing regarding the inverter nonlinearities. This is valid also regarding any other interruption in the measurements or in the signal injection.

Table 5.7: Comparison between 1. the permanent rotating voltage, 2. the permanent pulsating voltage, 3. the intermittent test pulses.

	1. Rotating	2. Pulsating ⁽⁰⁾	3. Test Pulses
Frequency ω_i	$\leq \omega_s/3$	$\leq \omega_s/2$	$= \omega_s/2$ ⁽¹⁾
Sensitivity to resistance	To be considered	None	None ⁽²⁾
Settling time ⁽³⁾	T_i	Several T_i ⁽⁴⁾	$2 \times T_i$ ⁽⁵⁾
Parameter knowledge	None	Approx.	None

Symbols: signal-injection frequency ω_i ; signal-injection period $T_i = 2\pi/\omega_i$; sampling frequency ω_s .

Notes: ⁽⁰⁾ Includes the alternating voltage injection corresponding to $\omega_i = \omega_s/2$. ⁽¹⁾ The test pulses can generally be treated as signals with a frequency of half the sampling frequency. ⁽²⁾ Beside the issue of the remaining signal-injection impact on the rotation-drive operations. ⁽³⁾ Excluding the effect of any additional noise filter and misalignment compensator. ⁽⁴⁾ Due to the initial anisotropy tracking. ⁽⁵⁾ The two distinct test pulses do not need to be consecutive, therefore the time can be longer.

5.3.12 Discussion on the Signal Characteristics

A summary comparing the properties of different types of injected voltage and their corresponding self-sensing operations, based on the developments in this section 5.3, is given in Table 5.3.12.

Discussion on the amplitude and frequency of the injected signal

The selection of the voltage signal amplitude is a compromise: on one hand, the amplitude of the current response should be the smallest possible in order to reduce the resistive loss, the vibrations and to limit the problems of possible zero-crossing nonlinearities [105]. On the other hand, the amplitude must be high enough in order to satisfy the condition (5.39) and in order to provide a good signal-to-noise ratio (5.78).

The higher the signal injection frequency, the higher the required injected voltage amplitude, assuming a fixed current response amplitude. This reduces the range of voltage allowable for the rotation-drive operations. Moreover, the audible nuisance and the eddy current loss increase with the frequency [7]. Assuming that these issues are managed otherwise, higher frequencies however present significant benefits. According to the different aspects highlighted in this section, they are:

1. reduction of frequency interactions (5.40) and decrease of the back-emf influence (5.39), that could lead to operation disturbances and affect the position estimation ;
2. lower computational requirements, since the computation steps of the moving average (5.46) is proportional to N_i ;

3. lower settling time at initialization and restart, due the stabilization time of only N_i sampling periods ;
4. robustness regarding inverter nonlinearities and other interruptions.

It is also beneficial regarding the resistance impact (5.55) for rotating signal injections, assuming that $r/\bar{\omega}_i$ decreases with the frequency ω_i . Note however that the contribution of eddy currents increases with the signal frequency [89, 90, 82, 91, 85] and augment the apparent value of the resistances, as addressed in chapter 3. This issue is analyzed experimentally hereafter. As a conclusion, the optimum frequency is the maximum satisfying (5.47). It is $N_i = 3 \Leftrightarrow \omega_i = \omega_s/3$ for rotating signals and $N_i = 2 \Leftrightarrow \omega_i = \omega_s/2$ for pulsating signals.

5.4 Experiments

5.4.1 Self-Sensing Using Rotating Signals

Experiments are performed on the experimental BLDC motor. Having 14 pole-pairs, its rated speed 500 rpm corresponds to a rotation frequency of $14 * 500/60 = 116$ Hz. This indicates the lower limit for the signal injection operations. The current controller bandwidth is around 400 Hz. A speed control is performed for the experiments, with a rather low bandwidth around 10 Hz. Note that the BLDC motors are generally not controlled in speed, but in torque only. The position is estimated using (5.54) and filtered through a third order observer, with a 62.6 Hz bandwidth, before it is used in the vector control of the rotation-drive. This observer also provides the speed estimation.

As explained in chapter 2, the anisotropy angle presents oscillations during the rotation, due to significant harmonics in the machine. No compensation is performed here, mainly due to lack of time, and they are therefore clearly visible on the results. Better results could therefore certainly be obtained if a compensation was implemented.

The zero-clamping inverter nonlinearity is very annoying in this type of machine: when a phase current crosses zero, the position is lost. As explained in chapter 4, in order to prevent this drawback, a current offset is added to the instruction to maintain a margin with respect to the zero-crossing phase lines. This offset is chosen in order to minimize its impact on the torque. As a consequence of the offset, the low-frequency current signal behaviour is far from a sinusoidal signal and the current instruction regularly jumps across the zero-crossing phase lines. This is clearly visible on the current signals. Since the position is lost, the self-sensing operations (but not the signal injection) are interrupted during the jumps. The lower the injected signal frequency, the longer the duration of the interruption.

Figures

From the top to the bottom, Figure 5.8, Figure 5.9, Figure 5.10 and Figure 5.11 are organized as follows: 1) a graph of the current samples of the first phase containing both high and low-frequency content (gray dots) and the filtered currents for the normal-drive operations (black dots) ; 2) the rotation speed (electrical frequency) measured by an external encoder (dashed lines) and the anisotropy speed estimated by the observer (black dots) ; 3) the rotor-PM angle (electrical degree) measured by an external encoder (dashed lines) and the estimated anisotropy angle (black dots) ; 4) the error (electrical degree) between the estimated angle and the rotor-PM angle ; 5) the frequency spectrum $|\underline{I}(e^{j\omega T_s})|$ of the current samples. As discussed previously, the position information is contained in the negative frequency $\nu = -\nu_i$.

Results

These results were published in [163].

The two first experiments compare the case $N_i = 20$, i.e. $\nu_i = 500$ Hz, in Figure 5.8 with the case $N_i = 3$, i.e. $\nu_i = 3333$ Hz, in Figure 5.9, for low-speed drives at 5 Hz that is 4.3% the rated speed. The voltage is chosen such that the peak values of the high-frequency current are equal in both cases, around 2 A that is 1.5% the rated current. For each case respectively it is 0.36 V, i.e. 1.4% of $v_{dc}/2$, and 2 V, i.e. 8% of $v_{dc}/2$. The drive operations are based on the encoder measurements and not on the estimated position in order to strictly assess the quality of the estimation and prevent feedback effects. The errors are around -10° for $N_i = 20$ and close to zero for $N_i = 3$, as theoretically predicted. An important problem with $N_i = 20$ is the interruption due to the zero-crossing, that becomes relatively long compared to the rotation period at higher speeds. The spectra illustrate the better frequency separation between signal injection and rotation-drive signals in the case of $N_i = 3$.

The two last experiments Figure 5.10 and Figure 5.11 show results of self-sensing operations, where the estimated position is used by the vector control. In Figure 5.10, the experiment starts at standstill with a speed ramp instruction up to 30 Hz at $t = 0.2$ s. In Figure 5.11, the experiment starts at standstill with the speed instruction step of 60 Hz at $t = 0$, that is 51.7% of the rated speed. Note that 0.2 s is quite short for such an acceleration in vehicle applications. At $t = 0.02$ s, larger errors on the position and the speed (negative) are observed, due to a phase current zero-crossing (inverter nonlinearity) that is not perfectly avoided. Such errors are repeated, especially at higher speeds. Above 60 Hz, the position estimation is strongly degraded because of the zero-crossings and the lower quantity of information, but this speed limitation is not inherent to the self-sensing. A clear spectrum dispersion is observed at $-\nu_i$. Despite the zero-crossing effects, the harmonic oscillations and the spectrum dispersion, these results are very satisfying for that type of machine. Note that the obtained resolution is much better than the one provided

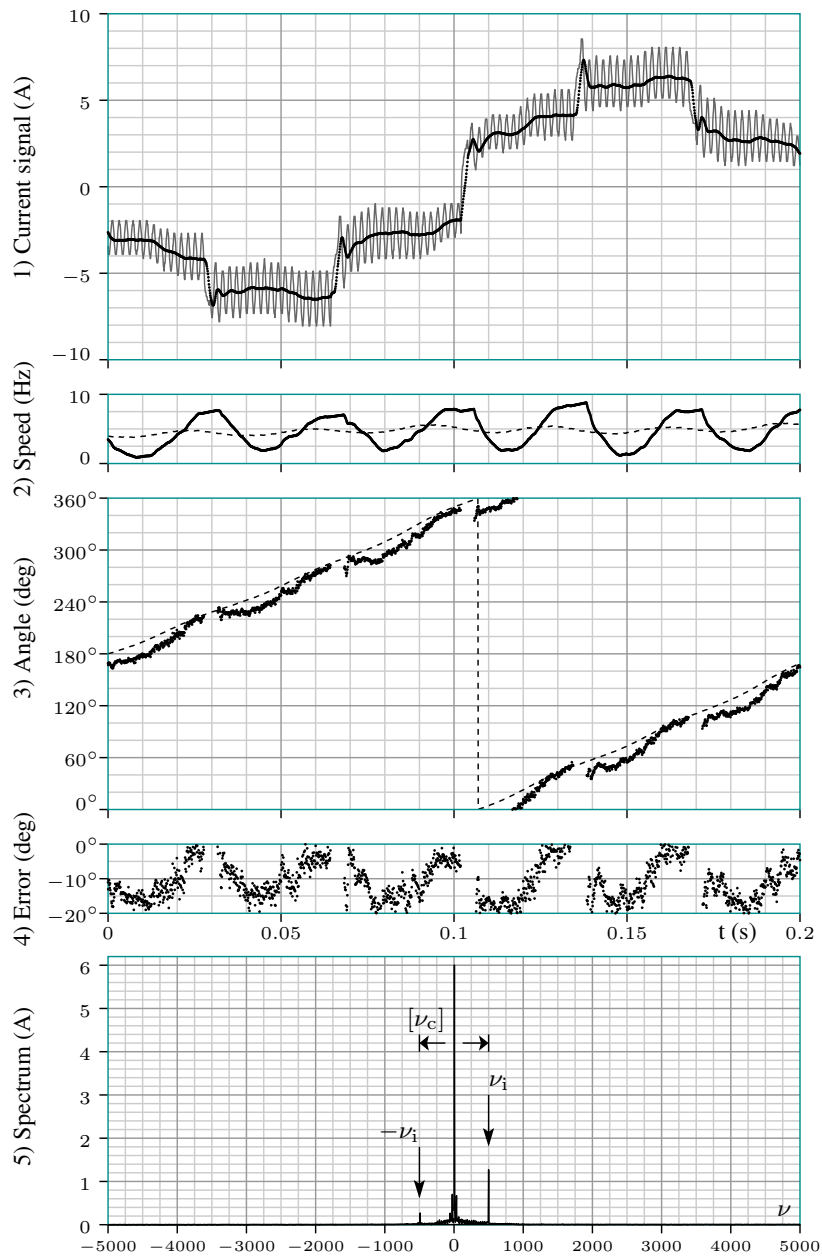


Figure 5.8: Experiments with a 0.36 V rotating voltage injection and $N_i = 20$, i.e. $\nu_i = 500$ Hz. Speed instruction at 5 Hz.

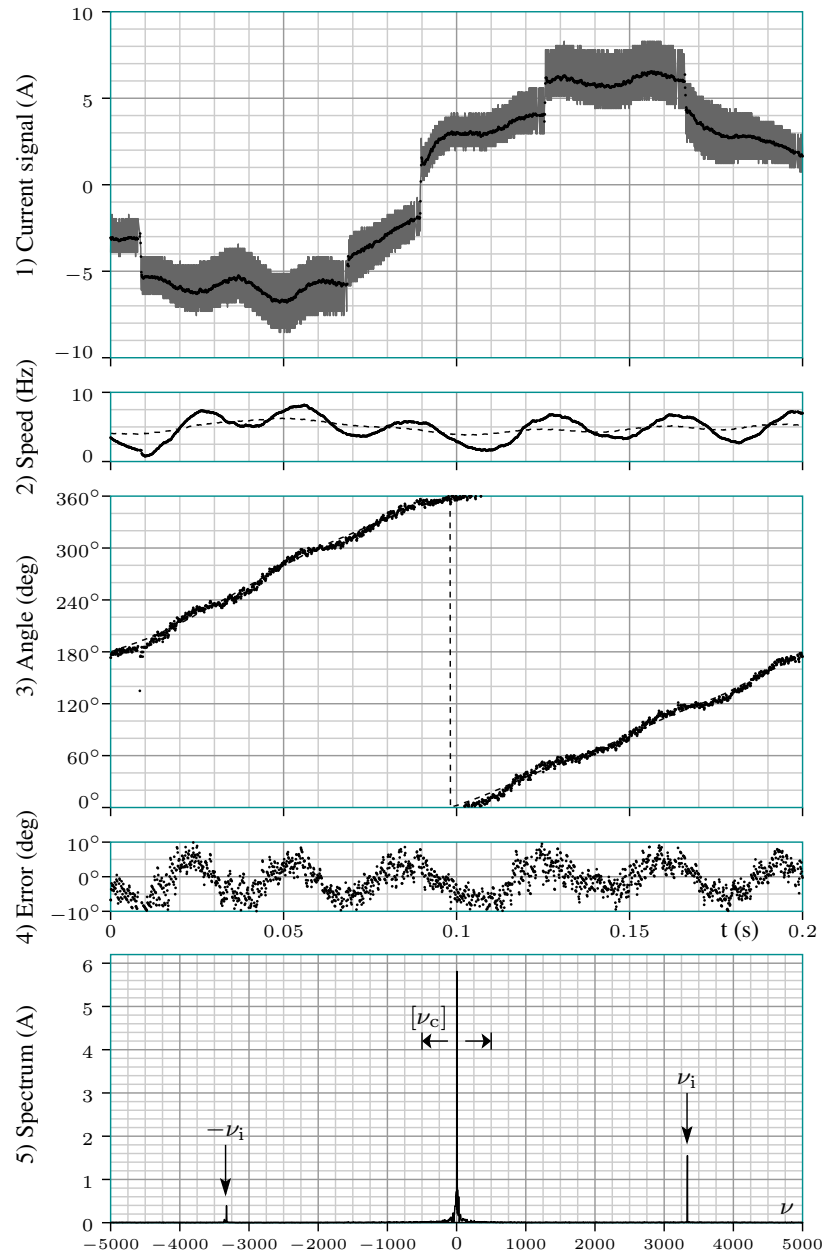


Figure 5.9: Experiments with a 2 V rotating voltage injection and $N_i = 3$, i.e. $\nu_i = 3333$ Hz. Speed instruction at 5 Hz.

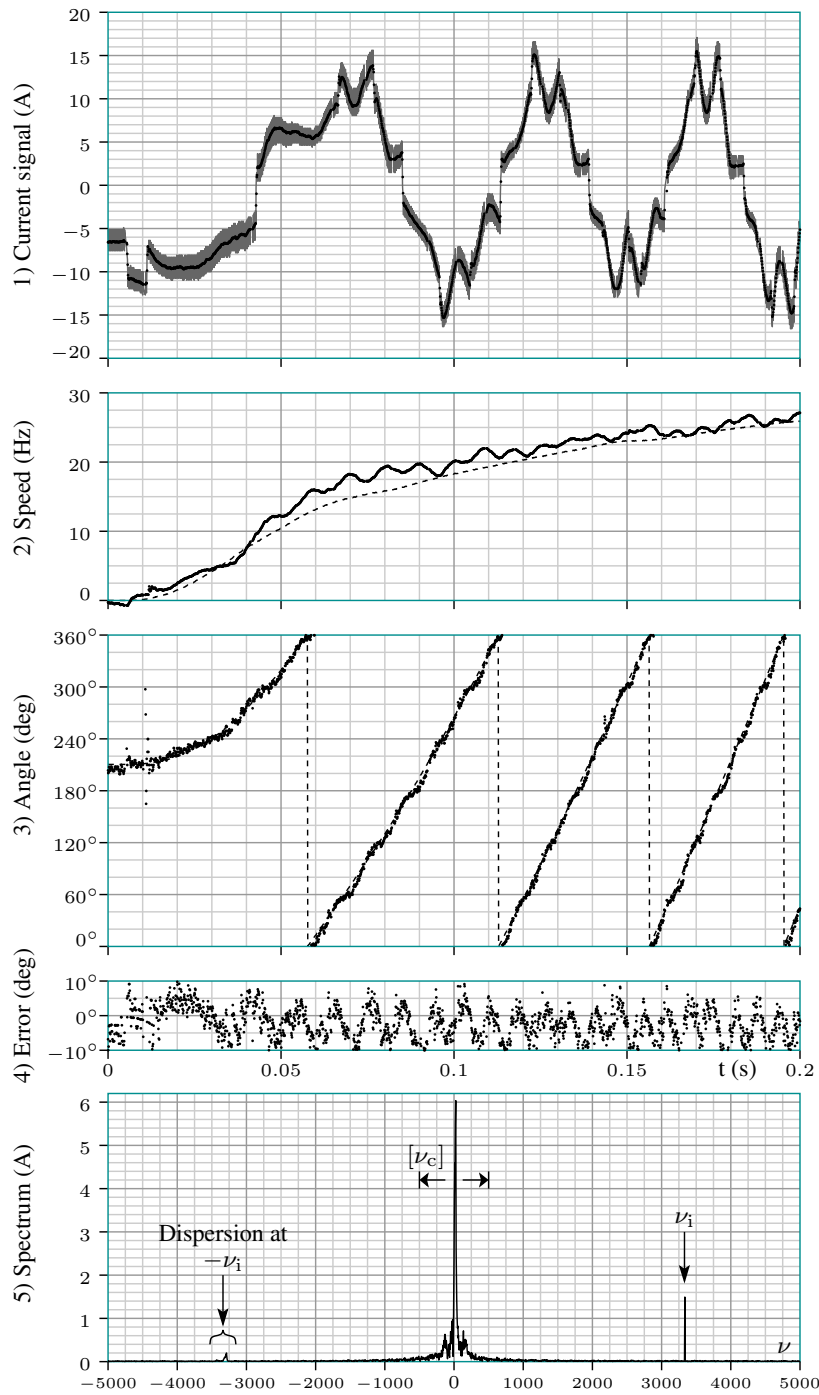


Figure 5.10: Experiments with a 2 V rotating voltage injection and $N_i = 3$. Ramp instruction from standstill to 30 Hz.

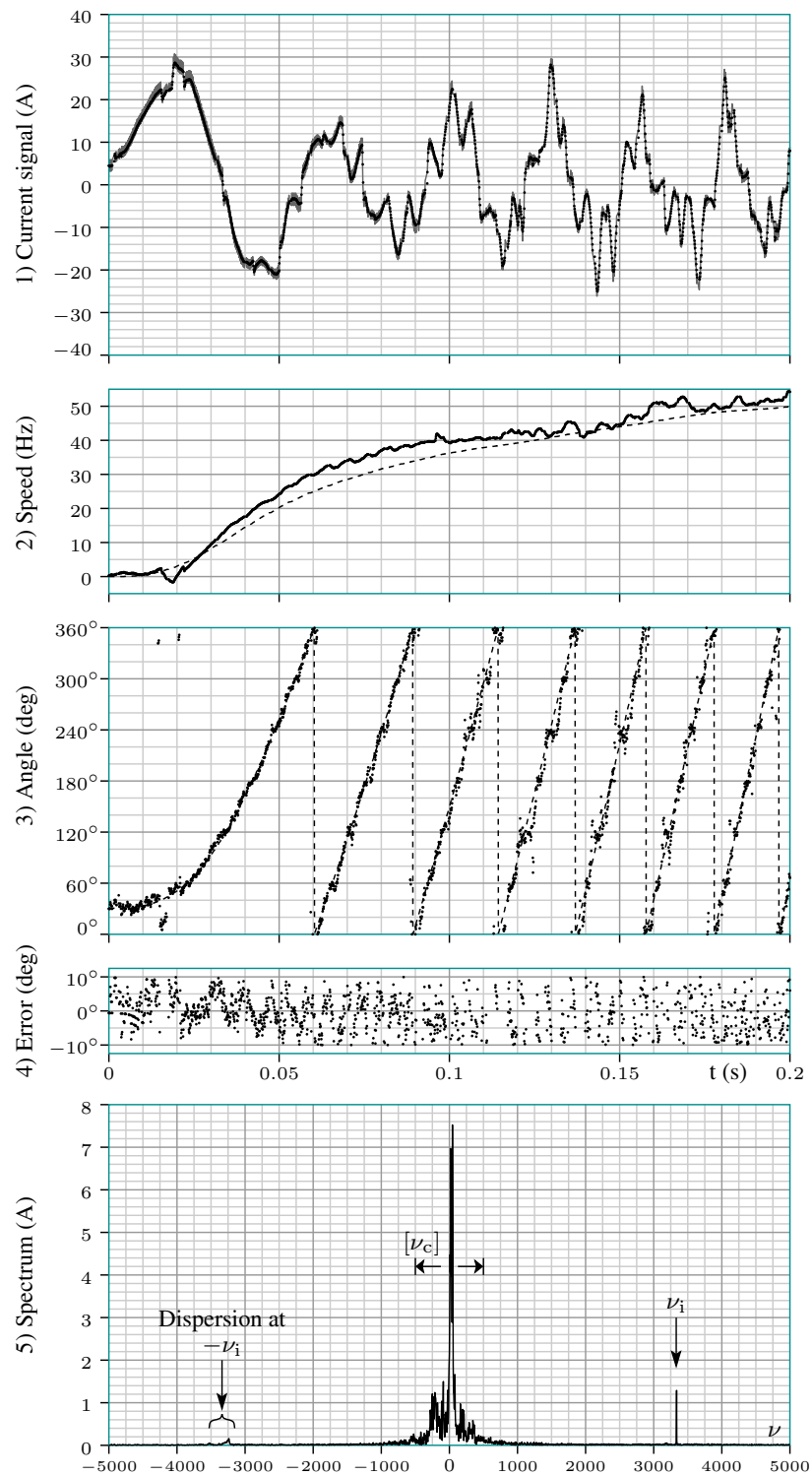


Figure 5.11: Experiments with a 2 V rotating voltage injection and $N_i = 3$. Step instruction from standstill to 60 Hz.

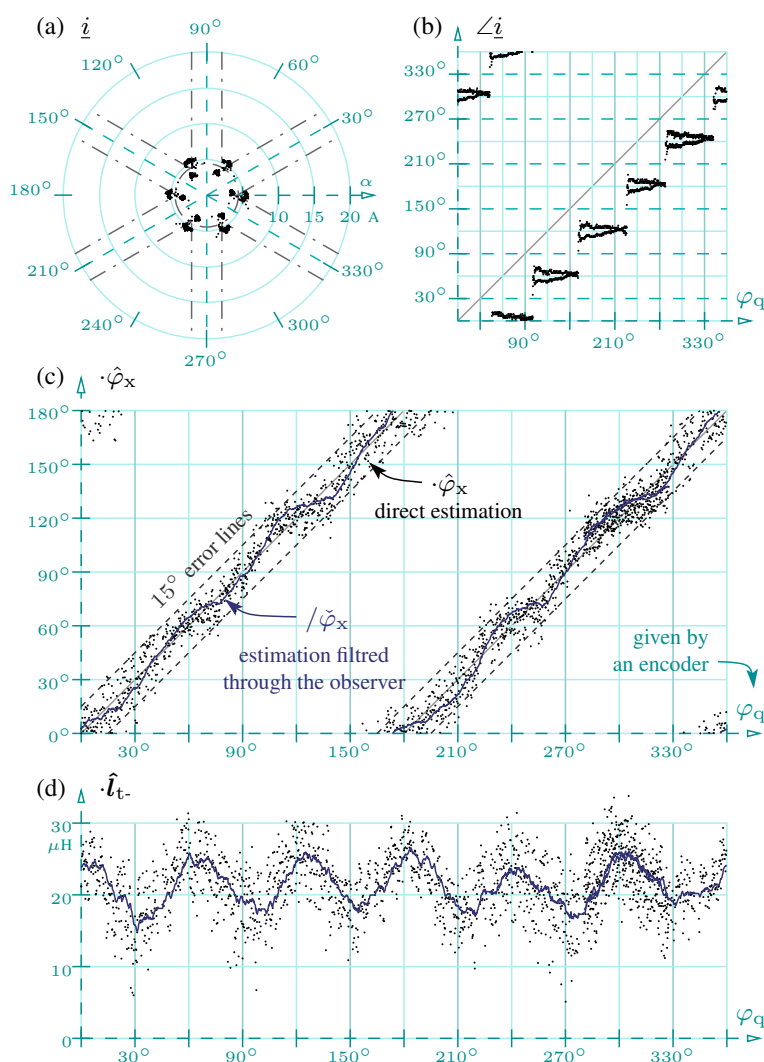


Figure 5.12: Experiments: machine unloaded and rotating at about 6 Hz.

by the hall-effect sensors traditionally used with BLDC machines [29].

5.4.2 Self-Sensing Using Alternating Signals

Experiments are performed on the experimental BLDC motor with the same program as for the rotating signal injection. The angle error ε_x is computed using a method similar to (5.71) using an approximate incremental self-inductance of $\hat{l}_{t+} = 80 \mu\text{H}$. More information can be found in [126]. The anisotropy angle is estimated using the third order observer, with a 62.6 Hz bandwidth.

We chose a signal-injection amplitude of approximately $V_i \approx 1.2 \text{ V}$, such that the current response is 2 A in the y direction. The experiments showed us that un-

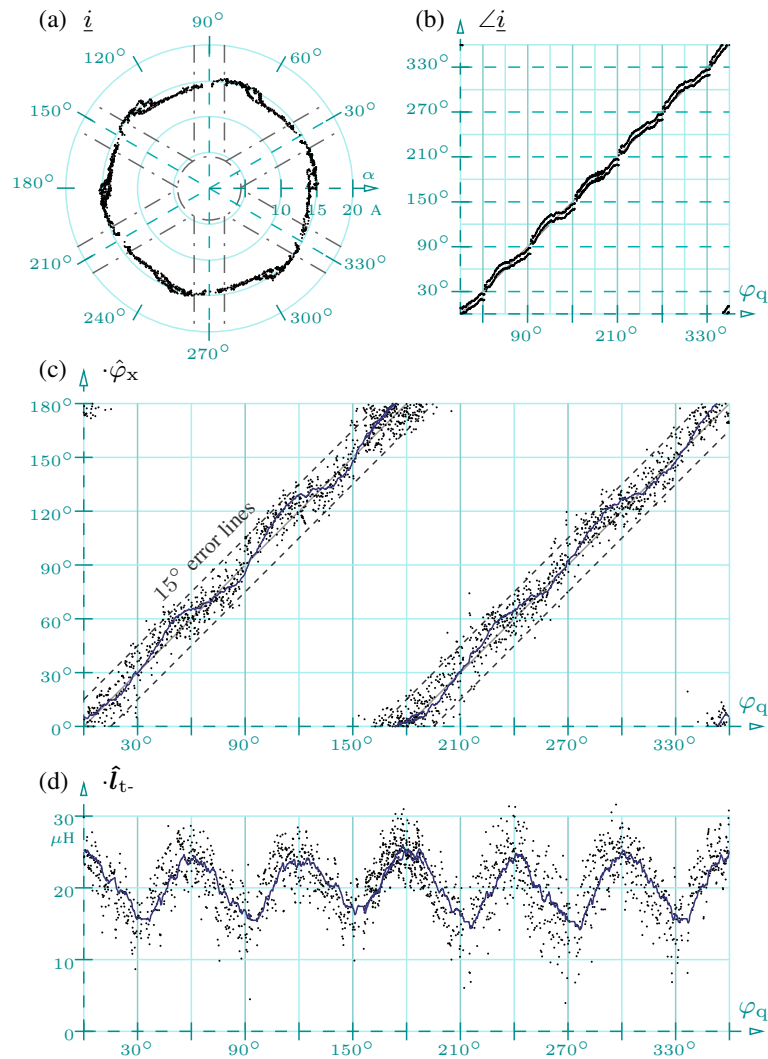


Figure 5.13: Experiments: machine loaded and rotating at about 6 Hz.

der 2 A amplitude, the position estimator isn't sufficiently accurate for the rotation-drive operations. Note that 2 A is only 1.5 % of the nominal current. The empirically zero-crossing margin is chosen here at a fixed $\Delta i_m = 2.1$ A.

Figures

The values $\check{\varphi}_x$ and \hat{l}_t are computed before their filtering (through the observer or the angle). While $\tilde{\varphi}_x$ and \tilde{l}_t are the filtered values.

The different figures are organized as follow: (a) the space vector of the current samples \underline{i} with the zero-crossing margins and (b) its angle $\angle \underline{i}$; (c) $\hat{\varphi}_x$ in black dots and $\check{\varphi}_x$ in blue lines ; (d) \hat{l}_t in black dots and \tilde{l}_t in blue lines. The angle φ_q is

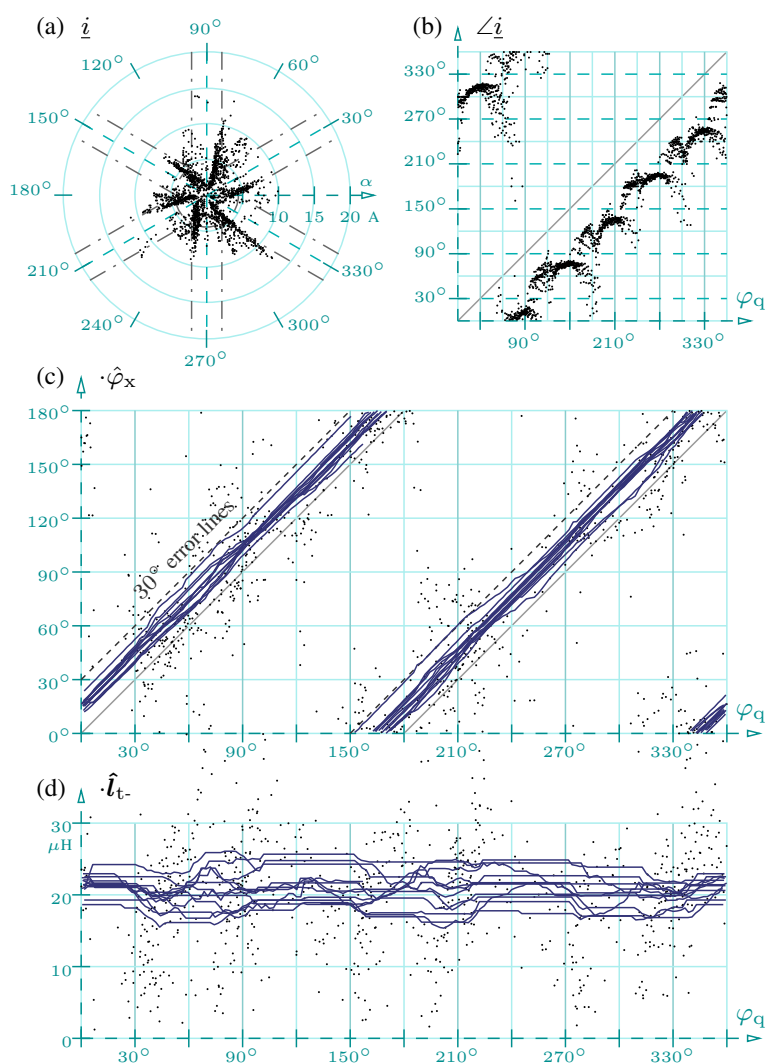


Figure 5.14: Experiments: machine unloaded and rotating at about 60 Hz.

measured by an encoder (not used in the control scheme).

Results

These results were published in [126].

The two first experimental results shown in Figure 5.12 and Figure 5.13 are performed with a low rotating machine around 6 Hz (5% of the nominal speed). The two next shown Figure 5.14 and Figure 5.15 are performed with a machine rotating around 60 Hz (51% of the nominal speed). The load corresponds to a current stator current of about 15 A amplitude (11% of the nominal current). The distortion on $\hat{\varphi}_x$ with respect to φ_d and the variations of \hat{l}_t are due to the harmonic

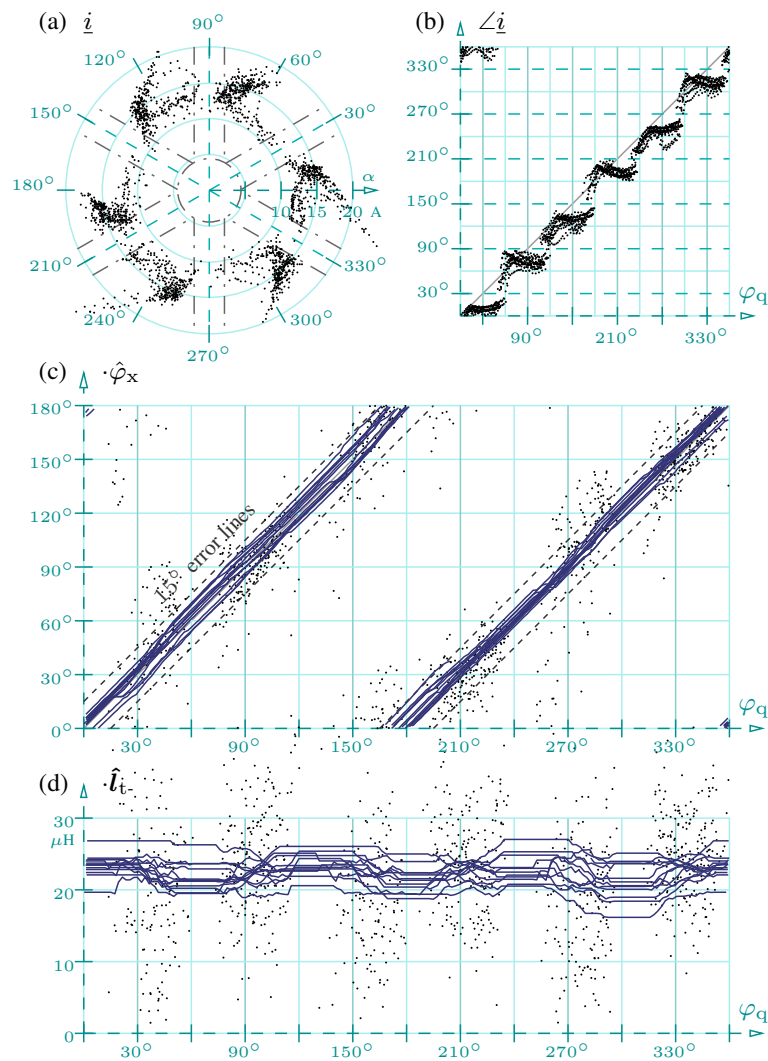


Figure 5.15: Experiments: machine loaded and rotating at about 60 Hz.

content in the anisotropy. No correction for the influence of this harmonic content on the estimated position is performed here. The distortions are only smoothed on $\hat{\varphi}_x$ and \hat{l}_t due to the observer filtering (bandwidth of 63 Hz).

The position estimation is satisfying at low speed, at no load as well as with a small load. At higher speed however, the current ripples are much larger than the margin size and the zero-crossings can not be avoided. This may explain the large dispersion of the estimations $\hat{\varphi}_x$ (dots). Nevertheless, the observer seems to filter these distortions since the filtered position $\hat{\varphi}_x$ (lines) is still reliable for the self-sensing control. It seems that a small load reduces the shift on the position estimation at higher speed, probably due to the fact that the current is farther from

the zero-crossing lines.

The oscillating behaviour of the current, specially in Figure 5.15, is far from a circle. This can be explained by the zero-crossing impact, since a similar behaviour is observed using the traditional BLDC-machine control with position sensors.

5.5 Summary

In this chapter, we firstly introduced the principle of the field-oriented control and we tried to categorize the numerous different self-sensing methods as follows:

- Back-EMF or Anisotropy-based methods ;
- Using terminal value measurements or extra dedicated sensors ;
- Anisotropy-based methods using the high-frequency signals of the rotation-drive operations, the high-frequency content of the PWM or methods using additional high-frequency injection ;
- Using permanent signal-injections or intermittent signal-injections ;

Solutions to the initial polar ambiguity, position error due to significant stator currents and estimation oscillations due to harmonics are addressed.

The next part focuses on the high-frequency signal injection. The discrete-time model of the transmittance to be identified is developed. The principle and the assumption required in order to separate the high-frequency operations of the self-sensing from the the low-frequency operations of the rotation-drive are detailed. The solution of the moving average for the filtering implementation is proposed and discussed. Among the types of signal-injections, we developed the operations of position estimations for the case of:

1. The rotating signal injection ;
2. The pulsating signal injection ;
3. And the so-called alternating signal injection.

The issue of the noise is quickly assessed. The issues regarding the frequency separation, the back-EMF impact, the resistance impact on the position estimation, the PWM-VSI nonlinearities, the settling time and the computation requirements are addressed for the case of rotating signal injection. The conclusions can be extended to the pulsating signal injection. It is shown that higher the frequency, better the operations regarding all these aspects. The optimal frequency is therefore third of the sampling frequency for rotating signals and half the sampling frequency for pulsating signals.

Experiments confirmed the considerations about the frequency and illustrate the high reliability of the high-frequency signal injection methods. It seems that rotating signal injections offer better accuracy than the pulsating signal injections,

but the experimental conditions were however not comparable. Further experiments would be require to compare them rigorously. A first comparison was proposed by [54], but it would require further analysis.

Chapter 6

Conclusions and Future Works

This chapter summarizes the main results and conclusions obtained in this thesis about self-sensing control, mentioning the contributions of our research work. It finishes by listing the large number of possible topics that could be addressed in continuation of that work.

6.1 Summary and Contributions

In the last chapter 5, we introduced how important was the knowledge of the rotor position regarding optimal field-oriented control operations for permanent-magnet machines. Firstly, an optimal torque production for a certain current amplitude is obtained by orienting the space vector of the current with respect to the permanent-magnets position. In first approximation, this orientation is found in quadrature regarding the axis of the permanent magnets. Secondly, the rotor position and the rotating speed are required in position and speed control operations.

As explained in chapter 1, the dedicated sensors used to obtain the position and the speed present many drawbacks. Instead of these sensors, it is possible to use some phenomena in the machine itself containing rotor position information. The position can therefore be extracted by on-line estimations of values modelling these phenomena, using only the phase current measurements and the DC-bus measurements. Other solutions using additional dedicated current/voltage sensors, additional samples or modifying the pulse-width modulated signal sent to the voltage-source inverter can be very efficient, but they present a relatively larger complexity and they are therefore not deeply addressed in this work. Among the phenomena, the back-EMF yields a simple and confident source of position information, except at low speeds and at standstill. The anisotropy, characterized by the variation of the incremental self-inductance as a function of the current space-vector orientation, is another source of position information valid for a wide speed range down to standstill. Back-EMF-based methods are already largely addressed in the literature. Therefore, this thesis work mainly focused on the anisotropy-based self-sensing methods.

Many publications assume an ideal sinusoidal variation of the anisotropic characteristics along the air-gap for their machine models. As introduced in chapter 2, if this simplification is valid, the incremental self-inductance should vary synchronously with the rotor position. In our experimental Brushless-DC motor however, important high-harmonic contents in the magnetic fields and in the stator conductor distributions create an oscillation of the anisotropy as a function of the rotor position. We referred to this as an “anisotropy misalignment”. An approached analytical model of the anisotropy highlighting this oscillating misalignment was published in [92]. Another misalignment, met in about all the machines, is due to the contribution of the currents along the quadratic axis. This contribution modifies the saturation levels in the machine in addition to the saturation due to the permanent-magnets fixed to the rotor. This misalignment is generally modeled as an error shift as a function of the currents. Another analytical model taking the currents into account was published in [39]. The chapter 2 of this thesis completed these models and provided tools to assess different impacts of the harmonics. For our experimental bench, it was firstly shown that the permanent-magnet contribution to the magnetic flux as a function of the rotor position mainly contains a fundamental component and only a small 5th rank harmonic. By consequence, this machine could reasonably be commanded as a synchronous machine, leading to a small oscillating torque related to the small 5th rank harmonic. Note that this oscillating torque is to be compared to the huge cogging torque due to the interaction between stator teeth and permanent magnets, that was not modelled. It was secondly shown that the anisotropic incremental self-inductances contain the 2th rank harmonic, expected to estimate the rotor position, plus a significant -4^{th} rank harmonic, sometimes referred to as “second saliency” and leading to the oscillating misalignment. Other harmonics were however negligible. The compensation solutions of the misalignment were addressed in chapter 5.

Upstream of this, methods to identify the incremental self-inductance and to estimate its anisotropy orientation are needed. All the identification methods require an accurate knowledge of the supplied voltage. For cost and reliability reasons however, the voltage is often not directly measured. In that case, self-sensing operations rely on the command voltage sent to the VSI. The behavior of the VSI is however not perfectly linear. In particular, the relation between the expected output voltage and the command voltage is strongly nonlinear when one phase current crosses zero. This is due to a phenomenon known as “zero-clamping” effect. Moreover, the current ripples due to the pulse-width modulation technique used to command most of the VSI are generally not measured and they complicate any attempt to compensate for the zero-clamping effect. This effect is very significant in our experimental bench because of the relatively low inductance of the machine, leading to large ripples and frequent zero-crossings. A first solution preventing zero-crossings, and thus reducing the zero-clamping impact, was published in [125]. Improvements were made and implemented in [126] and [163]. They are detailed in chapter 4. These solutions were absolutely required in the frame of our experiments, but they inevitably affect the performances of the con-

trol. For further researches, it is therefore advised to use other technologies and machine characteristics that do not present these problems.

We mainly focussed on self-sensing operations using signal injection at different high-frequencies, using current samples and based on discrete-time operations. A discrete-time model of the machine was therefore advised. In most of the publications, it is assumed that the discrete-time model can be represented as a first-order hold of the continuous-time model during the sampling periods. But experimentally, we observed unexpected variations of the model parameter values as a function of the injected signal frequency and as a function of the sampling frequency. The good understanding of these variations were required in order to eliminate any possible error in the implementation or to possibly discover any unmodelled phenomenon. A long development taking discretization effects and taking the pulse-width modulation into account was addressed in chapter 4, neglecting the eddy currents and taking the eddy currents into account. Comparing the theory with the experimental results at standstill, it was observed that the eddy currents have a significant impact on the apparent values of the discrete-time model of our experimental machine. These variations were however not dramatic for the performances of the self-sensing operations.

Many different types of high-frequency signals can be injected in the machine in order to identify the incremental self-inductance. They are overview and compared in chapter 5. Adaptive test signals were used in [169], permanent pulsating signals at half the sampling frequency were analyzed in [126] and permanent rotating signals up to one-third the sampling frequency were studied in [163]. In many aspects, the use of the maximum frequency in signal injection present important benefits. The first one is related to the error in the anisotropy estimation due to the presence of a resistance in the model for rotating signals (the pulsating signals do not experience that problem). Most of the self-sensing methods based on high-frequency signal-injections assume that the electrical-circuit of the machine behaves as a purely integrator (inductive behaviour): the variations of the currents are assumed directly proportional to the injected voltages, where the proportional factor is the incremental self-inductance. This assumption is however not valid in the experimental Brushless-DC motor due to significant resistive voltage drops, mainly due to eddy currents. Even if the eddy current contribution tends to increase with the frequency to some extent, as explained in chapter 4, it was however shown that their impacts on the self-sensing operations tend to decrease with the frequency of the injected signal. Other analyzed aspects are the separation between the self-sensing and the rotation-drive operations. This is of utmost importance in order to prevent mutual interactions and, possibly, to reduce the efficiency of the control. This separation is generally done by filtering operations. The quality of the filtering however depends on the gap between the frequencies used for both operations. Higher the injected-signal frequency, better is this gap. The optimal advised frequency is therefore the highest one. These conclusions concern the permanent signals. The test signals are equivalent to intermittent pulsating signals. Further issues concerning the remaining impact of the test signals on the control

operations, mainly due to the resistance, were addressed in [169].

The main conclusion concerning the experimental bench was that the use of such a Brushless-DC motor is not really advised in real applications requiring self-sensing, due to all the problems concerning the harmonics and the zero-clamping effects. It was however very interesting to implement self-sensing methods on that bench for scientific purposes in order to highlight all these undesired effects and to assess their impacts, since they exist anyway in all machines in a lesser extent and they could be considered to improve the control. For example, it allowed to demonstrate the robustness of the signal-injection techniques at the highest frequencies. It would now be recommendable to perform further analysis on other machines, with better characteristics, in order to assess the reachable accuracy.

6.2 Future Works

The final implementation of the self-sensing methods were very satisfying, but still incomplete to be transposed in industrial applications without further considerations and validations. Much work remains, but the numerous theoretical models and tools, plus the different proposed methods prepared the ground to future works and opens up the possibility of success in a short time. We suggest hereafter some topics for future works in the frame of this thesis:

- The impact of the load current on the anisotropy ratio and on the anisotropy misalignment have been theoretically analyzed. The theoretical model permitted to perform some observations on the experimental BLDC motor up to a reduced torque and a reduced speed. These limitations were inherited from hardware and power source capacities of the test bench. Experiments on the full ranges up to the rated values still remain to be performed in order to draw maps of feasibility regions. This could probably leads to new observations and conclusions about the experimental motor ;
- Some publications already drew maps of feasibility regions for anisotropy-based self-sensing operations as a function of the load current [66, 62, 63, 58, 59, 55, 65, 67, 60, 61, 64]. They are even computed using finite-element simulations, treating with variation of some small elements in order to highlight some benefits. Or they are proposing comparisons of different machine designs. This comparative methodology however takes much time and, by consequence, a lot of work remains with the many different possible machine designs. In order to accelerate this research, simple analytical models of the load impact, represented by the angular factor $m(\theta)$, could eventually be developed and coupled to the model of the incremental self-inductance proposed in the first chapter. We see some opportunities offered by that methodology in the selection of optimal designs. This is an open topic ;
- As explained in the last chapter, some authors already proposed angular corrections of the anisotropy misalignment as a function of the load current and

of the secondary anisotropy [53, 56, 158]. None of these methods, or any other method, were implemented and experimented in this work due to lack of time. This could however strongly increase the accuracy and improve the control, reducing the oscillations on the position estimation. A promising solution combines the back-EMF-based and the anisotropy-base self-sensing [57, 115, 167, 177]. Each of these source of position information could be used in order to mutually compensated for their errors. This is a significant evolution compared to hybrid solutions simply commutating between one to the other source of position over a speed threshold, as proposed in [133, 143, 114] ;

- The inverter nonlinearities were very annoying in this study. Due to the additional torque ripples and the computation complexity, the solution of zero-crossing prevention that we proposed could be discouraging for the industry and we have no great hope for the future of this solution. Other types of voltage source or other topologies, for instance using the neutral connection point, could possibly remove part of these problems and strongly improve the position estimation at higher speeds. This topic is however lying in fallow ;
- Between the different types of high-frequency signals were used in this work. Results suggested that rotating signal-injections presented better accuracy than pulsating signal-injection. Further experiments in comparable conditions should be performed in order to quantitatively assess this issue. It would also be interesting to further compare these permanent signal injections with intermittent signals injections, such as the test pulses proposed by [154]. This could probably be performed without much effort ;
- We mainly focused on the high-frequency injection using the controller sensors. Even if the use of extra dedicated sensors present some important drawbacks, it could however be interesting to compare their accuracy with the solution using controller sensors under similar conditions, since they could be more interesting for applications where the quality of the control is more important than the cost and the robustness ;
- Finally, the signal-injection method could be extended to multiphase machines (i.e. more than 3-phases). The theory presented in chapter 5 is independent to the number of phases and applications to multiphase machines were already published [188]. Possible interactions of the fundamental space-vectors, i.e. $\underline{x}_{(1)}$ with other harmonic orders in the machine, as described in chapter 2, should however be analyzed. The multiphase machines also present important benefits with respect to the fault-tolerance capacity, by maintaining drives under a smaller number of phases, even with reduced performances. Application to faulty three-phase machines was proposed by

[189]. But the case self-sensing methods applied to faulty multiphase machines could be a excellent topic of research.

Bibliography

- [1] I. Boldea, “Control issues in adjustable speed drives,” *IEEE Industrial Electronics Magazine*, vol. 2, pp. 32 – 50, Sept. 2008.
- [2] J. Finch and D. Giaouris, “Controlled ac electrical drives,” *IEEE Transactions on Industrial Electronics*, vol. 55, pp. 481 – 491, Feb. 2008.
- [3] C. Espanet, J.-M. Kauffmann, and R. Bernard, “Comparison of two in-wheel permanent magnet motors for military applications,” in *IEEE Vehicle Power and Propulsion Conference (VPPC)*, pp. 1 – 6, Sept. 2006.
- [4] G. Khalil, “Challenges of hybrid electric vehicles for military applications,” in *IEEE Vehicle Power and Propulsion Conference (VPPC)*, pp. 1 – 3, Sept. 2009.
- [5] J. Holtz, “Sensorless control of induction machines - with or without signal injection ?,” *IEEE Transactions on Industrial Electronics*, vol. 53, pp. 7 – 30, Feb. 2005.
- [6] P. Acarnley and J. Watson, “Review of position-sensorless operation of brushless permanent-magnet machines,” *IEEE Transactions on Industrial Electronics*, vol. 53, pp. 352 – 362, Apr. 2006.
- [7] M. Pacas, “Sensorless drives in industrial applications,” *IEEE Industrial Electronics Magazine*, vol. 5, pp. 16 – 23, June 2011.
- [8] E. Vazquez-Sanchez, J. Gomez-Gil, J. Gamazo-Real, and J. Diez-Higuera, “A new method for sensorless estimation of the speed and position in brushed dc motors using support vector machines,” *IEEE Transactions on Industrial Electronics*, vol. 59, pp. 1397 – 1408, Mar. 2012.
- [9] L. Xu, E. Inoa, Y. Liu, and B. Guan, “A new high-frequency injection method for sensorless control of doubly fed induction machines,” *IEEE Transactions on Industry Applications*, vol. 48, pp. 1556 – 1564, Sept. 2012.
- [10] P. Vas, *Electrical Machines and Drives: A Space-Vector Theory Approach*. United States: Oxford University Press, 1993.

- [11] J.-P. Caron and J.-P. Hautier, *Modélisation et commande de la machine asynchrone*. Méthodes et pratiques de l'ingénieur, 75737 Paris, France: Technip, 1995.
- [12] G. Sturtzer and E. Smigiel, *Modélisation et commande des moteurs triphasés*. Technosup, 75740 Paris, France: Ellipses Marketing, 2000.
- [13] M. Correvon, *Electronique de puissance*. France: Haute Ecole d'Ingénierie et de Gestion du Canton du Vaud, 2006.
- [14] R. H. Park, "Two-reaction theory of synchronous machines: Generalized method of analysis - part i," *American Institute of Electrical Engineers (AIEE)*, pp. 716 – 727, July 1929.
- [15] R. H. Park, "Two-reaction theory of synchronous machines-ii," *Transactions of the American Institute of Electrical Engineers*, vol. 52, pp. 352 – 354, June 1933.
- [16] I. H. Summers, "Vector theory of circuits involving synchronous machines," *Transactions of the American Institute of Electrical Engineers*, vol. 51, pp. 318 – 321, June 1932.
- [17] S. B. Crary, "Two-reaction theory of synchronous machines," *Transactions of the American Institute of Electrical Engineers*, vol. 56, pp. 27 – 36, Jan. 1937.
- [18] J. Holtz, "Pulsewidth modulation for electronic power conversion," *Proceedings of the IEEE*, vol. 82, pp. 1194 – 1214, Aug. 1994.
- [19] G. Maggetto, *Contribution A l'Etude Du Comportement Des Moteurs Asynchrones Alimentés Par Convertisseurs Statiques*. PhD thesis, Université Libre de Bruxelles, 1973.
- [20] H. Fudeh and C. Ong, "Modeling and analysis of induction machines containing space harmonics part i: Modeling and transformation," *IEEE Transactions on Power Apparatus and Systems*, vol. PAS-102, pp. 2608 – 2615, Aug. 1983.
- [21] H. Fudeh and C. Ong, "Modeling and analysis of induction machines containing space harmonics part ii: Analysis of asynchronous and synchronous actions," *IEEE Transactions on Power Apparatus and Systems*, vol. PAS-102, pp. 2616 – 2620, Aug. 1983.
- [22] H. Fudeh and C. Ong, "Modeling and analysis of induction machines containing space harmonics part iii: Three-phase cage rotor induction machines," *IEEE Transactions on Power Apparatus and Systems*, vol. PAS-102, pp. 2621 – 2628, Aug. 1983.

- [23] F. D. Belie, J. Melkebeek, K. Geldhof, L. Vandeveldel, and R. Boel, "A general description of high-frequency position estimators for interior permanent-magnet synchronous motors," in *International Conference on Electrical Machines (ICEM)*, Sept. 2004.
- [24] J. Faiz and I. Tabatabaei, "Extension of winding function theory for nonuniform air gap in electric machinery," *IEEE Transactions on Magnetics*, vol. 38, pp. 3654 – 3657, Nov. 2002.
- [25] H. Toda, Z. Xia, J. Wang, K. Atallah, and D. Howe, "Rotor eddy-current loss in permanent magnet brushless machines," *IEEE Transactions on Magnetics*, vol. 40, pp. 2104 – 2106, July 2004.
- [26] L. James and J. Kirtley, *6.685 Electric Machines*. Massachusetts - USA: Department of Electrical Engineering and Computer Science - Massachusetts Institute of Technology, 2005.
- [27] J. Gyselink, *ELEC269 Génie électrique*. Brussels - Belgium: Département Beams - Université Libre de Bruxelles, 2006.
- [28] J.-P. Vilain, A. Vauquelin, S. Vivier, and B. D. Nicolas Labbe, "Behavior analysis of a dc brush machine by space vector theory," in *International Conference on Electrical Machines (ICEM)*, Sept. 2010.
- [29] T. Jahns and W. Soong, "Pulsating torque minimization techniques for permanent magnet ac motor drives-a review," *IEEE Transactions on Industrial Electronics*, vol. 43, pp. 321 – 330, Apr. 1996.
- [30] J. Melkebeek, "Small signal dynamic modelling of saturated synchronous machines," in *International Conference on Electrical Machines (ICEM)*, no. 2, pp. 447 – 450, Sept. 1984.
- [31] F. De Belie, J. Melkebeek, L. Vandeveldel, R. Boel, K. Geldhof, and T. Vyncke, "A nonlinear model for synchronous machines to describe high-frequency signal based position estimators," in *IEEE International Conference on Electric Machines and Drives*, pp. 696 – 703, May 2005.
- [32] M.-J. Chung and D.-G. Gweon, "Modeling of the armature slotting effect in the magnetic field distribution of a linear permanent magnet motor," *Electrical Engineering (Archiv fur Elektrotechnik)*, vol. 84, pp. 101–108, 2002. 10.1007/s00202-001-0108-0.
- [33] T. Lubin, S. Mezani, and A. Rezzoug, "2-d exact analytical model for surface-mounted permanent-magnet motors with semi-closed slots," *IEEE Transactions on Magnetics*, vol. 47, pp. 479 – 492, Feb. 2011.
- [34] Z. Zhu and D. Howe, "Instantaneous magnetic field distribution in brushless permanent magnet dc motors. ii. armature-reaction field," *IEEE Transactions on Magnetics*, vol. 29, pp. 136 – 142, Jan. 1993.

- [35] Z. Zhu, D. Howe, E. Bolte, and B. Ackermann, "Instantaneous magnetic field distribution in brushless permanent magnet dc motors. i. open-circuit field," *IEEE Transactions on Magnetics*, vol. 29, pp. 124 – 135, Jan. 1993.
- [36] J. Chiasson, *Modeling and high performance control of electric machines*. USA: IEEE Computer Society Press, 2005.
- [37] I. A. Viorel and L. Hamemeyer, K. ; Strete, "On the carter's factor calculation for slotted electric machines," *Advances in Electrical and Computer Engineering*, vol. 7, no. 2, pp. 55 – 58, 2007.
- [38] K. Boughrara, R. Ibtouen, D. Z andarko, O. Touhami, and A. Rezzoug, "Magnetic field analysis of external rotor permanent-magnet synchronous motors using conformal mapping," *IEEE Transactions on Magnetics*, vol. 46, pp. 3684 – 3693, Sept. 2010.
- [39] F. Gabriel, F. De Belie, P. Sergeant, and X. Neyt, "Modelling the impact of the stator currents on inductance-based sensorless control of brushless dc-machines," in *Symposium on Sensorless Control for Electrical Drives (SLED)*, pp. 56 – 63, IEEE, Sept. 2011.
- [40] J.-I. Ha, "Analysis of inherent magnetic position sensors in symmetric ac machines for zero or low speed sensorless drives," *IEEE Transactions on Magnetics*, vol. 44, pp. 4689 – 4696, Dec. 2008.
- [41] S.-C. Yang, T. Suzuki, R. Lorenz, and T. Jahns, "Surface-permanent-magnet synchronous machine design for saliency-tracking self-sensing position estimation at zero and low speeds," *IEEE Transactions on Industry Applications*, vol. 47, pp. 2103 – 2116, Sept. 2011.
- [42] Z. Zhu and D. Howe, "Instantaneous magnetic field distribution in brushless permanent magnet dc motors. iii. effect of stator slotting," *IEEE Transactions on Magnetics*, vol. 29, pp. 143 – 151, Jan. 1993.
- [43] Y. Kano, T. Kosaka, and N. Matsui, "Simple nonlinear magnetic analysis for permanent-magnet motors," *IEEE Transactions on Industry Applications*, vol. 41, pp. 1205 – 1214, Sept. 2005.
- [44] B. Cassimere, S. Sudhoff, and D. Sudhoff, "Analytical design model for surface-mounted permanent-magnet synchronous machines," *IEEE Transactions on Energy Conversion*, vol. 24, pp. 347 – 357, June 2009.
- [45] L. Schreier, J. Bendl, M. Chomat, and M. Skalka, "Influence of space harmonics on properties of six-phase induction machine - part i. analysis," in *International Conference on Electrical Machines (ICEM)*, Sept. 2010.
- [46] A. V. Oppenheim and R. W. Schaffer, *Digital signal processing*. Prentice-Hall, 1975.

- [47] W. Wang, K. Nam, and S. young Kim, "Concentric winding bldc motor design," in *IEEE International Conference on Electric Machines and Drives*, pp. 157 – 161, May 2005.
- [48] Y. Wu, Z. Deng, X. Wang, X. Ling, and X. Cao, "Position sensorless control based on coordinate transformation for brushless dc motor drives," *IEEE Transactions on Power Electronics*, vol. 25, pp. 2365 – 2371, Sept. 2010.
- [49] J. Moreira and T. Lipo, "Modeling of saturated ac machines including air gap flux harmonic components," *IEEE Transactions on Industry Applications*, vol. 28, pp. 343 – 349, Mar. 1992.
- [50] H.-W. Lee, T.-H. Kim, and M. Ehsani, "Power density maximization of the brushless dc generator," in *IEEE Annual Conference of Industrial Electronics Society (IECON)*, vol. 3, pp. 2162 – 2166, Nov. 2003.
- [51] F. Meinguet, E. Semail, and J. Gyselinck, "Enhanced control of a pmsm supplied by a four-leg voltage source inverter using the homopolar torque," in *Proceedings of the XVIII International Conference on Electrical Machines (IEMDC)*, 2008.
- [52] P. Landsmann, D. Paulus, P. Stolze, and R. Kennel, "Saliency based encoderless predictive torque control without signal injection for a reluctance synchronous machine," in *International Power Electronics and Motion Control Conference (EPE/PEMC)*, pp. S1–10 – S1–17, Sept. 2010.
- [53] M. Degner and R. Lorenz, "Using multiple saliencies for the estimation of flux, position, and velocity in ac machines," *IEEE Transactions on Industry Applications*, vol. 34, pp. 1097 – 1104, Sept. 1998.
- [54] D. Raca, P. Garcia, D. Reigosa, F. Briz, and R. Lorenz, "A comparative analysis of pulsating vs. rotating vector carrier signal injection-based sensorless control," in *Applied Power Electronics Conference and Exposition (APEC)*, pp. 879 – 885, Feb. 2008.
- [55] S. Wu, D. Reigosa, Y. Shibukawa, M. Leetmaa, R. Lorenz, and Y. Li, "Interior permanent-magnet synchronous motor design for improving self-sensing performance at very low speed," *IEEE Transactions on Industry Applications*, vol. 45, pp. 1939 – 1946, Nov. 2009.
- [56] E. Kayikci and R. Lorenz, "Self-sensing methods extended to four phase switched reluctance machines," in *Power Electronics Conference (IPEC)*, pp. 2016 – 2023, June 2010.
- [57] I. Boldea, M. Paicu, and G.-D. Andreescu, "Active flux concept for motion-sensorless unified ac drives," *IEEE Transactions on Power Electronics*, vol. 23, pp. 2612 – 2618, Sept. 2008.

- [58] N. Bianchi, S. Bolognani, J.-H. Jang, and S.-K. Sul, "Comparison of pm motor structures and sensorless control techniques for zero-speed rotor position detection," *IEEE Transactions on Power Electronics*, vol. 22, pp. 2466 – 2475, Nov. 2007.
- [59] N. Bianchi and S. Bolognani, "Sensorless-oriented design of pm motors," *IEEE Transactions on Industry Applications*, vol. 45, pp. 1249 – 1257, July 2009.
- [60] Z. Zhu and L. Gong, "Investigation of effectiveness of sensorless operation in carrier-signal-injection-based sensorless-control methods," *IEEE Transactions on Industrial Electronics*, vol. 58, pp. 3431 – 3439, Aug. 2011.
- [61] L. Gong and Z. Zhu, "Saliency investigation of pm brushless ac motors for high-frequency carrier signal injection-based sensorless control," in *International Conference on Automation and Computing (ICAC)*, pp. 86 – 91, Sept. 2011.
- [62] P. Guglielmi, M. Pastorelli, and A. Vagati, "Cross-saturation effects in ipm motors and related impact on sensorless control," *IEEE Transactions on Industry Applications*, vol. 42, pp. 1516 – 1522, Nov. 2006.
- [63] Y. Li, Z. Zhu, D. Howe, and C. Bingham, "Modeling of cross-coupling magnetic saturation in signal-injection-based sensorless control of permanent-magnet brushless ac motors," *IEEE Transactions on Magnetics*, vol. 43, pp. 2552 – 2554, June 2007.
- [64] N. Limsuwan, Y. Shibukawa, D. Reigosa, and R. Lorenz, "Novel design of flux-intensifying interior permanent magnet synchronous machine suitable for self-sensing control at very low speed and power conversion," *IEEE Transactions on Industry Applications*, vol. 47, pp. 2004 – 2012, Sept. 2011.
- [65] P. Sergeant, F. De Belie, and J. Melkebeek, "Rotor geometry design of an interior permanent-magnet synchronous machine for more accurate sensorless control," in *International Conference on Electrical Machines (ICEM)*, pp. 1 – 6, Sept. 2010.
- [66] F. Briz, M. Degner, P. Garcia, and R. Lorenz, "Comparison of saliency-based sensorless control techniques for ac machines," *IEEE Transactions on Industry Applications*, vol. 40, pp. 1107 – 1115, July 2004.
- [67] I. Brown and R. Lorenz, "Induction machine design methodology for self-sensing: Balancing saliencies and power conversion properties," *IEEE Transactions on Industry Applications*, vol. 47, pp. 79 – 87, Jan. 2011.
- [68] A. Faggion, N. Bianchi, and S. Bolognani, "Ringed-pole permanent-magnet synchronous motor for position sensorless drives," *IEEE Transactions on Industry Applications*, vol. 47, pp. 1759 – 1766, July 2011.

- [69] M. Morandini, S. Bolognani, and A. Faggion, "Outer-rotor ringed-pole spm starter-alternator suited for sensorless drives," in *Symposium on Sensorless Control for Electrical Drives (SLED)*, pp. 96 – 101, Sept. 2011.
- [70] H. Mai, F. Dubas, D. Chamagne, and C. Espanet, "Optimal design of a surface mounted permanent magnet in-wheel motor for an urban hybrid vehicle," in *Vehicle Power and Propulsion Conference (VPPC)*, pp. 481 – 485, Sept. 2009.
- [71] Z. Zhu and D. Howe, "Instantaneous magnetic field distribution in permanent magnet brushless dc motors. iv. magnetic field on load," *IEEE Transactions on Magnetics*, vol. 29, pp. 152 – 158, Jan. 1993.
- [72] V. Donescu, A. Charette, Z. Yao, and V. Rajagopalan, "Modeling and simulation of saturated induction motors in phase quantities," *IEEE Transactions on Energy Conversion*, vol. 14, pp. 386 – 393, Sept. 1999.
- [73] H. Kim, M. Degner, J. Guerrero, F. Briz, and R. Lorenz, "Discrete-time current regulator design for ac machine drives," *IEEE Transactions on Industry Applications*, vol. 46, pp. 1425 – 1435, July 2010.
- [74] A. Navarrete, J. Rivera, J. Raygoza, and S. Ortega, "Discrete-time modeling and control of pmsm," in *Electronics, Robotics and Automotive Mechanics Conference (CERMA)*, pp. 258 – 263, Nov. 2011.
- [75] A. Loukianov, A. Navarrete, J. Rivera, and S. Ortega-Cisneros, "Discrete-time sensorless control of permanent magnet synchronous motors," in *Conference on Electrical Engineering Computing Science and Automatic Control (CCE)*, pp. 1 – 6, Oct. 2011.
- [76] I. Boldea and S. Nasar, "A general equivalent circuit (gec) of electric machines including cross-coupling saturation and frequency effects," *IEEE Transactions on Energy Conversion*, vol. 3, pp. 689 – 695, Sept. 1988.
- [77] D. Raca, P. Garcia, D. Reigosa, F. Briz, and R. Lorenz, "Carrier-signal selection for sensorless control of pm synchronous machines at zero and very low speeds," *IEEE Transactions on Industry Applications*, vol. 46, pp. 167 – 178, Jan. 2010.
- [78] B. Stumberger, G. Stumberger, D. Dolinar, A. Hamler, and M. Trlep, "Evaluation of saturation and cross-magnetization effects in interior permanent-magnet synchronous motor," *IEEE Transactions on Industry Applications*, vol. 39, pp. 1264 – 1271, Sept. 2003.
- [79] S. Ostlund and M. Brokemper, "Sensorless rotor-position detection from zero to rated speed for an integrated pm synchronous motor drive," *IEEE Transactions on Industry Applications*, vol. 32, pp. 1158 – 1165, Sept. 1996.

- [80] W. Roshen, "Iron loss model for permanent-magnet synchronous motors," *IEEE Transactions on Magnetics*, vol. 43, pp. 3428 – 3434, Aug. 2007.
- [81] J. Wang, K. Atallah, R. Chin, W. Arshad, and H. Lendenmann, "Rotor eddy-current loss in permanent-magnet brushless ac machines," *IEEE Transactions on Magnetics*, vol. 46, pp. 2701 – 2707, July 2010.
- [82] S.-C. Yang and R. Lorenz, "Analysis of iron and magnet losses in surface permanent magnet machines resulting from injection-based self-sensing position estimation," in *Energy Conversion Congress and Exposition (ECCE)*, pp. 630 – 637, Sept. 2011.
- [83] S. Moulahoum and O. Touhami, "A saturated induction machine model with series iron losses resistance," in *International Conference on Power Engineering, Energy and Electrical Drives*, pp. 156 – 161, Apr. 2007.
- [84] S. Bolognani, L. Peretti, M. Zigliotto, and E. Bertotto, "Commissioning of electromechanical conversion models for high dynamic pmsm drives," *IEEE Transactions on Industrial Electronics*, vol. 57, pp. 986 – 993, Mar. 2010.
- [85] S.-C. Yang and R. Lorenz, "Surface permanent magnet synchronous machine position estimation at low speed using eddy-current-reflected asymmetric resistance," *IEEE Transactions on Power Electronics*, vol. 27, pp. 2595 – 2604, May 2012.
- [86] M. R. Spiegel, *Formules et tables de mathematiques*. Série Schaum, 75014 Paris, France: Mac Graw Hill, 1992.
- [87] J. Holtz, "Pulsewidth modulation-a survey," *IEEE Transactions on Industrial Electronics*, vol. 39, pp. 410 – 420, Oct. 1992.
- [88] N. Urasaki, T. Senjyu, and K. Uezato, "Relationship of parallel model and series model for permanent magnet synchronous motors taking iron loss into account," *IEEE Transactions on Energy Conversion*, vol. 19, pp. 265 – 270, June 2004.
- [89] P. Sergeant, F. De Belie, L. Dupre, and J. Melkebeek, "Losses in sensorless controlled permanent-magnet synchronous machines," *IEEE Transactions on Magnetics*, vol. 46, pp. 590 – 593, Feb. 2010.
- [90] D. Reigosa, P. Garcia, F. Briz, D. Raca, and R. Lorenz, "Modeling and adaptive decoupling of high-frequency resistance and temperature effects in carrier-based sensorless control of pm synchronous machines," *IEEE Transactions on Industry Applications*, vol. 46, pp. 139 – 149, Jan. 2010.
- [91] N. Limsuwan, T. Kato, C.-Y. Yu, J. Tamura, D. Reigosa, K. Akatsu, and R. Lorenz, "Secondary resistive losses with high-frequency injection-based self-sensing in ipm machines," in *Energy Conversion Congress and Exposition (ECCE)*, pp. 622 – 629, Sept. 2011.

- [92] F. Gabriel, F. De Belie, P. Druyts, X. Neyt, and P. Lataire, "Sensorless drive of surface mounted permanent-magnet brushless dc machines with diametric windings based on inductance measurements," in *International Conference on Power Electronics (ICPE'11) - ECCE Asia*, vol. 1, pp. 1236 – 1243, IEEE, May 2011.
- [93] J. Verbeeck, *Standstill Frequency Response Measurement and Identification Methods for Synchronous Machines*. PhD thesis, Vrije Universiteit Brussel, Jan. 2000. <http://www.tw.vub.ac.be/elec/Papers>
- [94] Y.-K. Lin and Y.-S. Lai, "Dead-time elimination of pwm-controlled inverter/converter without separate power sources for current polarity detection circuit," *IEEE Transactions on Industrial Electronics*, vol. 56, pp. 2121 – 2127, June 2009.
- [95] J. Holtz, "Initial rotor polarity detection and sensorless control of pm synchronous machines," in *Industry Applications Conference (IAS)*, vol. 4, pp. 2040 – 2047, Oct. 2006.
- [96] Y. Inoue, K. Yamada, S. Morimoto, and M. Sanada, "Effectiveness of voltage error compensation and parameter identification for model-based sensorless control of ipmsm," *IEEE Transactions on Industry Applications*, vol. 45, pp. 213 – 221, Jan. 2009.
- [97] L. Peretti and M. Zigliotto, "Fpga-based voltage measurements in ac drives," in *International Conference on Electrical Machines (ICEM)*, pp. 1 – 6, Sept. 2010.
- [98] J. Verbeeck, R. Pintelon, and P. Lataire, "Influence of saturation on estimated synchronous machine parameters in standstill frequency response tests," *IEEE Transactions on Energy Conversion*, vol. 15, pp. 277 – 283, Sept. 2000.
- [99] A. Hava, R. Kerkman, and T. Lipo, "Simple analytical and graphical methods for carrier-based pwm-vsi drives," *IEEE Transactions on Power Electronics*, vol. 14, pp. 49 – 61, Jan. 1999.
- [100] J. Hobraiche, J.-P. Vilain, P. Macret, and N. Patin, "A new pwm strategy to reduce the inverter input current ripples," *IEEE Transactions on Power Electronics*, vol. 24, pp. 172 – 180, Jan. 2009.
- [101] D. Casadei, G. Serra, A. Tani, and L. Zarri, "A general approach for minimizing the current ripple in induction motor drives controlled by svm technique," in *IEEE International Symposium on Industrial Electronics*, vol. 1, pp. 247 – 252, 2000.

- [102] H. Krishnamurthy, G. Narayanan, R. Ayyanar, and V. Ranganathan, "Design of space vector-based hybrid pwm techniques for reduced current ripple," in *IEEE Applied Power Electronics Conference and Exposition*, vol. 1, pp. 583 – 588, Feb. 2003.
- [103] Y. Murai, T. Watanabe, and H. Iwasaki, "Waveform distortion and correction circuit for pwm inverters with switching lag-times," *IEEE Transactions on Industry Applications*, vol. 23, pp. 881 – 886, Sept. 1987.
- [104] A. Munoz and T. Lipo, "On-line dead-time compensation technique for open-loop pwm-vsi drives," *IEEE Transactions on Power Electronics*, vol. 14, pp. 683 – 689, July 1999.
- [105] P. Garcia, F. Briz, M. Degner, and D. Diaz-Reigosa, "Accuracy, bandwidth, and stability limits of carrier-signal-injection-based sensorless control methods," *IEEE Transactions on Industry Applications*, vol. 43, pp. 990 – 1000, July 2007.
- [106] D. Leggate and R. J. Kerkman, "Pulse-based dead-time compensator for pwm voltage inverters," *IEEE Transactions on Industrial Electronics*, vol. 44, pp. 191 – 197, Apr. 1997.
- [107] T. Summers and R. Betz, "Dead-time issues in predictive current control," *IEEE Transactions on Industry Applications*, vol. 40, pp. 835 – 844, May 2004.
- [108] G. Narayanan, V. Ranganathan, D. Zhao, H. Krishnamurthy, and R. Ayyanar, "Space vector based hybrid pwm techniques for reduced current ripple," *IEEE Transactions on Industrial Electronics*, vol. 55, pp. 1614 – 1627, Apr. 2008.
- [109] N. Urasaki, T. Senjyu, K. Uezato, and T. Funabashi, "Adaptive dead-time compensation strategy for permanent magnet synchronous motor drive," *IEEE Transactions on Energy Conversion*, vol. 22, pp. 271 – 280, June 2007.
- [110] J.-S. Choi, J.-Y. Yoo, S.-W. Lim, and Y.-S. Kim, "A novel dead time minimization algorithm of the pwm inverter," *IEEE Industry Applications Conference (IAS)*, vol. 4, pp. 2188 – 2193, 1999.
- [111] L. Ben-Brahim, "The analysis and compensation of dead-time effects in three phase pwm inverters," *Conference of the IEEE Industrial Electronics Society (IECON)*, vol. 2, pp. 792 – 797, Sept. 1998.
- [112] H.-S. Ryu, I.-H. Lim, J.-H. Lee, S.-H. Hwang, and J.-M. Kim, "A dead time compensation method in voltage-fed pwm inverter," vol. 2, pp. 911 – 916, Oct. 2006.

- [113] J.-W. Choi and S.-K. Sul, "Inverter output voltage synthesis using novel dead time compensation," *IEEE Transactions on Power Electronics*, vol. 11, pp. 221 – 227, Mar. 1996.
- [114] G. Wang, R. Yang, and D. Xu, "Dsp-based control of sensorless ipmsm drives for wide-speed-range operation," *IEEE Transactions on Industrial Electronics*, vol. 60, pp. 720 – 727, Feb. 2013.
- [115] C. Silva, G. Asher, and M. Sumner, "Hybrid rotor position observer for wide speed-range sensorless pm motor drives including zero speed," *IEEE Transactions on Industrial Electronics*, vol. 53, pp. 373 – 378, Apr. 2006.
- [116] J. Seung-Gi, L. Bang-Sup, K. Kyung-Seo, and P. Min-Ho, "The analysis and compensation of dead time effects in pwm inverters," vol. 3, pp. 667 – 671, Oct. 1988.
- [117] S.-G. Jeong and M.-H. Park, "The analysis and compensation of dead-time effects in pwm inverters," *IEEE Transactions on Industrial Electronics*, vol. 38, pp. 108 – 114, Apr. 1991.
- [118] V. Cardenas, S. Horta, and R. Echavarria, "Elimination of dead time effects in three phase inverters," pp. 258 – 262, Oct. 1996.
- [119] T. Wolbank, M. Vogelsberger, and M. Riepler, "Identification and compensation of inverter dead-time effect on zero speed sensorless control of ac machines based on voltage pulse injection," pp. 2844 – 2849, June 2008.
- [120] R. Raute, C. Caruana, C. Staines, J. Cilia, N. Teske, M. Sumner, and G. Asher, "A review of sensorless control in induction machines using hf injection, test vectors and pwm harmonics," in *Symposium on Sensorless Control for Electrical Drives (SLED)*, pp. 47 – 55, Sept. 2011.
- [121] L. Gong and Z. Zhu, "A novel method for compensating inverter nonlinearity effects in carrier signal injection-based sensorless control from positive-sequence carrier current distortion," *IEEE Transactions on Industry Applications*, vol. 47, pp. 1283 – 1292, May 2011.
- [122] L. Ben-Brahim, "On the compensation of dead time and zero-current crossing for a pwm-inverter-controlled ac servo drive," *IEEE Transaction on Industrial Electronics*, vol. 51, pp. 1113 – 1118, Oct. 2004.
- [123] N. Urasaki, T. Senjyu, K. Uezato, and T. Funabashi, "An adaptive dead-time compensation strategy for voltage source inverter fed motor drives," *IEEE Transactions on Power Electronics*, vol. 20, pp. 1150 – 1160, Sept. 2005.
- [124] C. Silva, G. Asher, and M. Sumner, "Influence of dead-time compensation on rotor position estimation in surface mounted pm machines using hf voltage injection," in *Power Conversion Conference (PCC)*, vol. 3, pp. 1279 – 1284, 2002.

- [125] F. Gabriel, F. De Belie, P. Druyts, and X. Neyt, "Strategy to detect and prevent the current zero-crossing for inverter powered drives," in *International Conference on Electrical Machines (ICEM)*, pp. 1 – 6, IEEE, Sept. 2010.
- [126] F. Gabriel, F. De Belie, and X. Neyt, "Inductance-based position self-sensing of a brushless dc-machine using high-frequency signal injection," in *Conference of the IEEE Industrial Electronics Society*, IEEE, Oct. 2012.
- [127] A. Consoli, G. Scarcella, and A. Testa, "Sensorless control of ac motors at zero speed," in *International Symposium on Industrial Electronics (ISIE)*, vol. 1, pp. 373 – 379, 1999.
- [128] R. Leidhold and P. Mutschler, "Interaction between the current controller and the injection of alternating carriers in sensorless drives," in *International Symposium on Power Electronics, Electrical Drives, Automation and Motion (SPEEDAM)*, pp. 262 – 267, June 2008.
- [129] M. Schroedl, "Detection of the rotor position of a permanent magnet synchronous machine at standstill," in *International Conference on Electrical Machines (ICEM)*, pp. 195 – 197, 1988.
- [130] S. Doki, Y. Kinpara, S. Okuma, and S. Sangwongwanich, "Unified interpretation of indirect and direct vector control," *Conference Record of the Power Conversion Conference Yokohama 1993*, pp. 297 – 302, Apr. 1993.
- [131] J. Rodriguez, R. Kennel, J. Espinoza, M. Trincado, C. Silva, and C. Rojas, "High-performance control strategies for electrical drives: An experimental assessment," *IEEE Transactions on Industrial Electronics*, vol. 59, pp. 812 – 820, Feb. 2012.
- [132] P. Landsmann, P. Stolze, and R. Kennel, "Optimal switching time calculation in predictive torque control," in *International Conference on Power Electronics and ECCE Asia (ICPE ECCE)*, pp. 923 – 930, June 2011.
- [133] A. Piippo, M. Hinkkanen, and J. Luomi, "Adaptation of motor parameters in sensorless pmsm drives," *IEEE Transactions on Industry Applications*, vol. 45, pp. 203 – 212, Jan. 2009.
- [134] K. Dutton, S. Thompson, and B. Barraclough, *The Art of Control Engineering*. England: Prentice Hall, 1st edition, 1997.
- [135] P. Vas, *Sensorless Vector and Direct Torque Control*. United States: Oxford University Press, 1998.
- [136] F. D. Belie, *Vector control of synchronous permanent-magnet machines without mechanical position sensor*. PhD thesis, Ghent University, Faculty of Engineering, Gent, Belgium, Mar. 2010.

- [137] D. G. Luenberger, "An introduction to observers," *IEEE Transactions on Automatic Control*, vol. 16, pp. 596–602, Dec. 1971.
- [138] G. Kreisselmeier, "Adaptive observers with exponential rate of convergence," *IEEE Transactions on Automatic Control*, vol. 22, pp. 2 – 8, Feb. 1977.
- [139] J. Holtz and J. Juliet, "Sensorless acquisition of the rotor position angle of induction motors with arbitrary stator windings," *IEEE Transactions on Industry Applications*, vol. 41, pp. 1675 – 1682, Nov. 2005.
- [140] S. Bolognani, L. Peretti, and M. Zigliotto, "Parameter sensitivity analysis of an improved open-loop speed estimate for induction motor drives," *IEEE Transactions on Power Electronics*, vol. 23, pp. 2127 – 2135, July 2008.
- [141] M. Tursini, C. Olivieri, and L. D. Leonardo, "Analysis of phase-detection algorithms for back-emf-based sensorless strategies through real-time simulations," in *Sensorless Control for Electrical Drives (SLED)*, pp. 129 – 137, Sept. 2011.
- [142] H. Kim, M. Harke, and R. Lorenz, "Sensorless control of interior permanent-magnet machine drives with zero-phase lag position estimation," *IEEE Transactions on Industry Applications*, vol. 39, pp. 1726 – 1733, Nov. 2003.
- [143] C. Wang and L. Xu, "A novel approach for sensorless control of pm machines down to zero speed without signal injection or special pwm technique," *IEEE Transactions on Power Electronics*, vol. 19, pp. 1601 – 1607, Nov. 2004.
- [144] R. Cardenas, R. Pena, J. Proboste, G. Asher, and J. Clare, "Mras observer for sensorless control of standalone doubly fed induction generators," *IEEE Transactions on Energy Conversion*, vol. 20, pp. 710 – 718, Dec. 2005.
- [145] Y. Shi, K. Sun, L. Huang, and Y. Li, "On-line identification of permanent magnet flux based on extended kalman filter for ipmsm drive with position sensorless control," *IEEE Transactions on Industrial Electronics*, vol. PP, no. 99, p. 1, 2011.
- [146] P. Sergeant, F. De Belie, and J. Melkebeek, "Effect of rotor geometry and magnetic saturation in sensorless control of pm synchronous machines," *IEEE Transactions on Magnetics*, vol. 45, pp. 1756 – 1759, Mar. 2009.
- [147] F. Briz, M. Degner, P. Fernandez, and A. Diez, "Rotor and flux position estimation in delta-connected ac machines using the zero-sequence carrier-signal current," *IEEE Transactions on Industry Applications*, vol. 42, pp. 495 – 503, Mar. 2006.

- [148] P. Garcia, F. Briz, D. Reigosa, C. Blanco, and J. M. Guerrero, "On the use of high frequency inductance vs. high frequency resistance for sensorless control of ac machines," in *Symposium on Sensorless Control for Electrical Drives (SLED)*, pp. 90 – 95, Sept. 2011.
- [149] S.-C. Yang and R. D. Lorenz, "Comparison of resistance-based and inductance-based self-sensing controls for surface permanent-magnet machines using high-frequency signal injection," *IEEE Transactions on Industry Applications*, vol. 48, pp. 977 –986, May 2012.
- [150] J. Moreira, "Indirect sensing for rotor flux position of permanent magnet ac motors operating over a wide speed range," *IEEE Transactions on Industry Applications*, vol. 32, pp. 1394 – 1401, Nov. 1996.
- [151] S. Bolognani, S. Calligaro, R. Petrella, and M. Sterpellone, "Sensorless control for ipmsm using pwm excitation: Analytical developments and implementation issues," in *Symposium on Sensorless Control for Electrical Drives (SLED)*, pp. 64 – 73, Sept. 2011.
- [152] S. Ogasawara and H. Akagi, "An approach to position sensorless drive for brushless dc motors," *IEEE Transactions on Industry Applications*, vol. 27, pp. 928 – 933, Sept. 1991.
- [153] U.-H. Rieder, M. Schroedl, and A. Ebner, "Sensorless control of an external rotor pmsm in the whole speed range including standstill using dc-link measurements only," *IEEE 35th Annual Power Electronics Specialists Conference*, vol. 2, pp. 1280 – 1285, June 2004.
- [154] F. De Belie, T. Vyncke, and J. Melkebeek, "Parameterless rotor position estimation in a direct-torque controlled salient-pole pmsm without using additional test signals," in *International Conference on Electrical Machines (ICEM)*, pp. 1 – 6, Sept. 2010.
- [155] P. Landsmann, D. Paulus, P. Stolze, and R. Kennel, "Saliency based encoderless predictive torque control without signal injection," in *Power Electronics Conference (IPEC), 2010 International*, pp. 3029 –3034, June 2010.
- [156] P. Landsmann, C. M. Hackl, and R. Kennel, "Eliminating all machine parameters in encoderless predictive torque control without signal injection," in *International Electric Machines and Drives Conference (IEMDC)*, pp. 1259 – 1264, May 2011.
- [157] J. Cai and Z. Deng, "Sensorless control of switched reluctance motor based on phase inductance vectors," *IEEE Transactions on Power Electronics*, vol. 27, pp. 3410 – 3423, July 2012.

- [158] R. Leidhold, "Position sensorless control of pm synchronous motors based on zero-sequence carrier injection," *IEEE Transactions on Industrial Electronics*, vol. 58, pp. 5371 – 5379, Dec. 2011.
- [159] E. Robeischl and M. Schroedl, "Optimized inform measurement sequence for sensorless pm synchronous motor drives with respect to minimum current distortion," *IEEE Transactions on Industry Applications*, vol. 40, pp. 591 – 598, Mar. 2004.
- [160] L. Ribeiro, M. Degner, F. Briz, and R. Lorenz, "Comparison of carrier signal voltage and current injection for the estimation of flux angle or rotor position," in *IEEE Industry Applications Conference*, vol. 1, pp. 452 – 459, Oct. 1998.
- [161] T. Wolbank and J. Machl, "A modified pwm scheme in order to obtain spatial information of ac machines without mechanical sensor," *IEEE Applied Power Electronics Conference and Exposition (APEC), Dallas, Texas*, vol. 1, pp. 310 – 315, Mar. 2002.
- [162] S. Kim, J.-I. Ha, and S.-K. Sul, "Pwm switching frequency signal injection sensorless method in ipmsm," *IEEE Transactions on Industry Applications*, vol. 48, pp. 1576 – 1587, Sept. 2012.
- [163] F. Gabriel, F. De Belie, X. Neyt, and P. Lataire, "High-frequency issues using rotating voltage injections intended for position self-sensing," *IEEE Transaction on Industrial Electronics*, Accepted in November 2012.
- [164] M. Schroedl, "Sensorless control of ac machines at low speed and standstill based on the "inform" method," in *Industry Applications Conference (IAS)*, vol. 1, pp. 270 – 277, Sept. 1996.
- [165] F. De Belie, P. Sergeant, and J. Melkebeek, "A sensorless drive by applying test pulses without affecting the average-current samples," *IEEE Transactions on Power Electronics*, vol. 25, pp. 875 – 888, Apr. 2010.
- [166] F. De Belie and J. Melkebeek, "Seamless integration of a low-speed position estimator for ipmsm in a current-controlled voltage-source inverter," in *Symposium on Sensorless Control for Electrical Drives (SLED)*, pp. 50 – 55, July 2010.
- [167] F. Demmelmayr, M. Susic, and M. Schroedl, "Sensorless control at high starting torque of a 4000 nm traction drive with permanent magnet synchronous machine," in *Conference on Power Electronics and Applications (EPE)*, pp. 1 – 8, Sept. 2011.
- [168] D. Paulus, P. Landsmann, and R. Kennel, "Sensorless field-oriented control for permanent magnet synchronous machines with an arbitrary injection

- scheme and direct angle calculation,” in *Symposium on Sensorless Control for Electrical Drives (SLED)*, pp. 41 – 46, Sept. 2011.
- [169] F. Gabriel, F. De Belie, P. Druyts, X. Neyt, J. Melkebeek, and M. Acheroy, “Compensating the influence of the stator resistor and inverter nonlinearities in signal-injection based sensorless strategies,” in *Vehicle Power and Propulsion Conference (VPPC)*, pp. 283 – 290, IEEE, Sept. 2009.
- [170] K.-R. Cho and J.-K. Seok, “Induction motor rotor temperature estimation based on a high-frequency model of a rotor bar,” *IEEE Transactions on Industry Applications*, vol. 45, pp. 1267 –1275, July 2009.
- [171] S. Kellner and B. Piepenbreier, “Identification of ohmic stator resistance based on low frequency current signal injection in permanent magnet synchronous machines,” in *Power Electronics and Motion Control Conference*, pp. T5–221 –T5–229, Sept. 2010.
- [172] P. Champa, P. Somsiri, P. Wipasuramonton, and P. Nakmahachalasint, “Initial rotor position estimation for sensorless brushless dc drives,” *IEEE Transactions on Industry Applications*, vol. 45, pp. 1318 – 1324, July 2009.
- [173] S. Shan, L. Qingfu, X. Wei, and W. Xinghua, “A novel starting method for the sensorless salient-pole brushless dc motors,” in *Conference on Electrical Machines and Systems (ICEMS)*, vol. 2, pp. 895 – 897, Aug. 2001.
- [174] T. Noguchi, K. Yamada, S. Kondo, and I. Takahashi, “Initial rotor position estimation method of sensorless pm synchronous motor with no sensitivity to armature resistance,” *IEEE Transactions on Industrial Electronics*, vol. 45, pp. 118 – 125, Feb. 1998.
- [175] H. Kim, K.-K. Huh, R. Lorenz, and T. Jahns, “A novel method for initial rotor position estimation for ipm synchronous machine drives,” *IEEE Transactions on Industry Applications*, vol. 40, pp. 1369 – 1378, Sept. 2004.
- [176] T. J. S.-K. S. Yu-seok Jeong, R.D. Lorenz, “Initial rotor position estimation of an interior permanent-magnet synchronous machine using carrier-frequency injection methods,” *IEEE Transactions on Industry Applications*, vol. 41, pp. 38 – 45, Jan. 2005.
- [177] P. Landsmann, D. Paulus, and R. Kennel, “Online identification of load angle compensation for anisotropy based sensorless control,” in *Symposium on Sensorless Control for Electrical Drives (SLED)*, pp. 80 – 84, Sept. 2011.
- [178] Y. doo Yoon, S. ki Sul, S. Morimoto, and K. Ide, “High bandwidth sensorless algorithm for ac machines based on square-wave type voltage injection,” in *Energy Conversion Congress and Exposition (ECCE)*, pp. 2123 – 2130, Sept. 2009.

- [179] H. Kim and R. Lorenz, "Carrier signal injection based sensorless control methods for ipm synchronous machine drives," in *Industry Applications Conference (IAS)*, vol. 2, pp. 977 – 984, Oct. 2004.
- [180] J. Hu, J. Liu, and L. Xu, "Eddy current effects on rotor position estimation and magnetic pole identification of pmsm at zero and low speeds," *IEEE Transactions on Power Electronics*, vol. 23, pp. 2565 –2575, Sept. 2008.
- [181] Y. doo Yoon and S. ki Sul, "Sensorless control for induction machines using square-wave voltage injection," in *Energy Conversion Congress and Exposition (ECCE)*, pp. 3147 – 3152, Sept. 2010.
- [182] C.-Y. Yu, J. Tamura, D. Reigosa, and R. Lorenz, "Position self-sensing evaluation of a fi-ipmsm based on high frequency signal injection methods," in *Energy Conversion Congress and Exposition (ECCE)*, pp. 3029 –3036, Sept. 2011.
- [183] W. Jianmin and G. Jianwei, "Analysis of position estimation error resulted from filter in carrier signal injection based sensorless control of pmsm," in *Conference on Electrical Machines and Systems (ICEMS)*, pp. 1 – 6, Aug. 2011.
- [184] J.-H. Jang, J.-I. Ha, M. Ohto, K. Ide, and S.-K. Sul, "Analysis of permanent-magnet machine for sensorless control based on high-frequency signal injection," *IEEE Transactions on Industry Applications*, vol. 40, pp. 1595 – 1604, Nov. 2004.
- [185] S.-C. Yang and R. Lorenz, "Surface permanent magnet synchronous machine self-sensing position estimation at low speed using eddy current reflected asymmetric resistance," in *Power Electronics and Applications (EPE)*, pp. 1 – 10, Sept. 2011.
- [186] J.-H. Jang, S.-K. Sul, J.-I. Ha, K. Ide, and M. Sawamura, "Sensorless drive of surface-mounted permanent-magnet motor by high-frequency signal injection based on magnetic saliency," *IEEE Transactions on Industry Applications*, vol. 39, pp. 1031 – 1039, July 2003.
- [187] S.-C. Yang and R. Lorenz, "Surface permanent-magnet machine self-sensing at zero and low speeds using improved observer for position, velocity, and disturbance torque estimation," *IEEE Transactions on Industry Applications*, vol. 48, pp. 151 – 160, Jan. 2012.
- [188] F. De Belie and J. Melkebeek, "Application of a voltage adaptive sensorless current controller to a multi-phase permanent-magnet synchronous machine," pp. 1 – 6, July 2009.

- [189] F. De Belie and J. Melkebeek, "Sensorless two-phase current control of a faulty three-phase salient-pole pmsm," in *International Conference on Electrical Machines and Systems (ICEMS)*, pp. 1 – 6, Nov. 2009.